Title

Observation-Informed Methodologies for Site Response Characterization in Probabilistic Seismic Hazard Analysis

Author

Afshari, Kioumars

Publication Date

2017

Peer reviewed|Thesis/dissertation

UNIVERSITY OF CALIFORNIA
Los Angeles

Observation-Informed Methodologies for Site Response Characterization in Probabilistic Seismic Hazard Analysis

A dissertation submitted in partial satisfaction of the requirements for the
degree Doctor of Philosophy in
Civil Engineering

by

Kioumars Afshari

2017

ABSTRACT OF THE DISSERTATION

Observation-Informed Methodologies for Site Response Characterization in Probabilistic Seismic Hazard Analysis

by

Kioumars Afshari

Doctor of Philosophy in Civil Engineering

University of California, Los Angeles, 2017

Professor Jonathan Paul Stewart, Chair

In this dissertation, I study the effects of site response on earthquake ground motions, the uncertainty in site response, and the means by which site-specific site response can be incorporated into probabilistic seismic hazard analysis. I contributed to the introduction of a guideline for evaluating non-ergodic (site-specific) site response using (a) observations from available recorded data at the site, (b) simulations from one-dimensional ground response analysis, or (c) a combination of both. Using non-ergodic site response is expected to be an improvement in comparison to using an ergodic model, which provides the average site response conditional on site parameters, as derived from a global dataset. The improvement in site response results from removal of bias from ergodic models by incorporating site-specific information. As a result of the site response being evaluated on a site-specific basis, when used in PSHA, the uncertainty can be reduced by removing site-to-site variability. The site-to-site variability is evaluated by partitioning

the residuals to different sources of variability. I illustrate application of these procedures for evaluating non-ergodic site response, and use examples to show how the reduction in site response uncertainty results in less hazard for long return periods.

I utilize a dataset of recordings from vertical array sites in California in order to study the effectiveness of one-dimensional ground response analysis in predicting site response. I use the California dataset for comparing the performance of linear ground response analysis to similar studies on a dataset from vertical arrays in Japan. I use surface/downhole transfer functions and amplification of pseudo-spectral acceleration to study the site response in vertical arrays. For performing linear site response analysis for the sites, I use three alternatives for small-strain soil damping namely (a) empirical models for laboratory-based soil damping; (b) an empirical model based on shear wave velocity for estimating rock quality factor; and (c) estimating damping using the difference between the spectral decay (κ) at the surface and downhole. The site response transfer functions show a better fit for California sites in comparison to the similar results on Japan. The better fit is due to different geological conditions at California and Japan vertical array sites, as well as the difference in the quality of seismic velocity data for the two regions. I use pseudo-spectral acceleration residuals to study the bias and dispersion of ground response analysis predictions. The results of our study shows geotechnical models for lab-based damping provide unbiased estimates of site response for most spectral periods. In addition, the between- and within-site variability of the residuals do not show a considerable regional between California and Japan vertical arrays.

In another part of this dissertation, we develop ground motion models for median and standard deviation of the significant duration of earthquake ground motions from shallow crustal earthquakes in active tectonic regions. The model predicts significant durations for 5-75%, 5-95%,

and 20-80% of the normalized Arias intensity, and is developed using NGA-West2 database with **M**3.0-7.9 events. I select recordings based on the criteria used for developing ground motion models for amplitude parameters as well as a new methodology for excluding recordings affected by noise. The model includes an **M**-dependent source duration term that also depends on focal mechanism. At small **M**, the data suggest approximately **M**-independent source durations that are close to 1 sec. The increase of source durations with M is slower over the range **M**5 to 7.2-7.4 than for larger magnitudes. I adopt an additive path term with breaks in distance scaling at 10 and 50 km. I include site terms that increase duration for decreasing V_{S30} and increasing basin depth. Our aleatory variability model captures decreasing between- and within-event standard deviation terms with increasing **M**. I use the model for validating the duration of ground motion time series produced by simulation routines implemented on the SCEC Broadband Platform. This validation is based on comparisons of median and standard deviation of simulated durations for five California events, and their trends with magnitude and distance, with our model for duration. Some misfits are observed in the median and dispersion of durations from simulated motions and their trend with magnitude and distance. Understanding the source of these misfits can help guide future improvements in the simulation routines.

The dissertation of Kioumars Afshari is approved.

Yousef Bozorgnia

Scott Joseph Brandenberg

Mladen Vucetic

Jonathan Paul Stewart, Committee Chair

University of California, Los Angeles

2017

CONTENTS

LIST OF FIGURES

LIST OF TABLES

ACKNOWLEDGMENTS

I would like to express my great appreciation to my advisor Professor Jonathan P. Stewart for his guidance and support during my research. His knowledge, support and patience helped me develop essential skills in the field of ground motion modeling, finishing this dissertation, and becoming a better engineer. I feel lucky to be one of his PhD students. I am also grateful to Professor Mladen Vucetic for his caring and support in the early stage of my presence at UCLA.

For this dissertation, I would like to thank my defense committee members: Professors Yousef Bozorgnia, Scott Brandenberg, and Mladen Vucetic for agreeing to be in this committee, and the committee for my PhD candidacy oral exam in 2013.

This research was supported by grants from the National Science Foundation through SCEC award number 36558820, the California Strong Motion Instrumentation Program (CSMIP) of the California Geological Survey (CGS) (agreement no. 1014-961), and the California Department of Transportation through the Pacific Earthquake Engineering Research Center (PEER) under subaward 8208. Partial support was also provided by the UCLA Civil & Environmental Engineering Department. This support is gratefully acknowledged.

I am also grateful to Christine Goulet, Emel Seyhan, Dong Youp Kwak, and Paolo Zimmaro for providing valuable guidance and sharing their scientific knowledge which helped me during the last five years.

I thank Tadahiro Kishida of PEER for providing access to data processing codes, Fabio Silva of SCEC for his assistance in accessing the ver. 15.3 simulated ground motions from SCEC servers, the PEER center staff for their invaluable roles in developing the data resources used in this study, and Kevin Milner of SCEC for his assistance with OpenSHA implementation. I would

also like to thank Hamid Haddadi of CSMIP for providing weak motion records from the Center for Engineering Strong Motion Data FTP folders, Javier Vargas Ortiz, Bahareh Heidarzadeh, and Jamison Steidle for providing geotechnical logs for vertical arrays sites used in this dissertation, and Eric Thompson and Adrian Rodriguez-Marek for providing data and valuable insight on their studies on vertical arrays.

This research could have not been possible without the support of my family and relatives who have always been there for me to provide all types of support during the last five years. I also grateful to UCLA faculty, staff, and students who helped providing a friendly and enjoyable environment for students and researchers at UCLA.

VITA

2009: Bachelor of Science in Civil Engineering, Sharif University of Technology, Tehran, Iran

2011: Master of Science in Civil Engineering (Geotechnical), Sharif University of Technology, Tehran, Iran

PUBLICATIONS

Afshari, K, Stewart, JP, 2016. Physically Parameterized Prediction Equations for Significant Duration in Active Crustal Regions, *Earthquake Spectra* 32 (4).

Afshari, K, Stewart, JP, 2016. Validation of Duration Parameters from SCEC Broadband Platform Simulated Ground Motions, *Seismological Research Letters* 87 (5).

Stewart, JP, Afshari, K, Goulet, CA, 2017. Non-ergodic site response in seismic hazard analysis, *Earthquake Spectra*, doi: https://doi.org/10.1193/081716EQS135M

Afshari, K and Stewart, JP, 2015. Uncertainty of site amplification derived from ground response analysis, *Proc. 6th Int. Conf. Earthquake Geotech. Eng.*, Christchurch, New Zealand, Paper No. 227.

Afshari, K and Stewart, JP, 2015. Effectiveness of 1D ground response analyses at predicting site response at California vertical array sites, Proc. *SMIP2015 Seminar on Utilization of Strong Motion Data, California Strong Motion Instrumentation Program*, Davis, CA.

Afshari, K and Stewart, JP, 2016. Implications of California Vertical Array Data for Modeling of Non-Ergodic Site Response, *Proc. SMIP2016 Seminar on Utilization of Strong Motion Data, California Strong Motion Instrumentation Program*, Irvine, CA.

Stewart, JP, Afshari, K, Hashash, YMA, 2014. Guidelines for Performing Hazard-Consistent One-Dimensional Ground Response Analysis for Ground Motion Prediction. Pacific Earthquake Engineering Research Center (PEER) report No. 2014/16, UC Berkeley, October 2014.

1 Introduction

This dissertation concerns two issues regarding earthquake ground motion prediction. (1) Site response: The issue of non-ergodic site response, its uncertainty, and it's implementation in probabilistic seismic hazard analysis (PSHA) as well as a validation study on site response using vertical array sites in California; (2) The duration of ground motions: developing a model for predicting the duration of ground motions, and using the model for validating the duration of a large number of simulated ground motions.

1.1 SITE RESPONSE

In ground motion prediction, several factors contribute to the characteristics of ground shaking at the surface of the earth during earthquakes. These factors are related to the earthquake source (fault), source-site path, and the site. Among source parameters, the most important parameter is the magnitude (**M**). There are also other parameters related to the source like stress drop. Stress drop is the amount of stress released when the fault ruptures, and this parameter is related to rupture area and earthquake duration. The second factor is the path through which the seismic waves will travel until reaching the site. The main parameter describing the path is the distance between the source and the site (R). The principal path effects are related to the geometric spreading of seismic energy away from the fault and anelastic attenuation effects associated with crustal damping. Both of these effects cause attenuation of ground motion with source-site distance. The third factor is the site. The seismic waves created by the source and traveled through

the path, have to propagate through the relatively shallow and softer geological structure before reaching the surface (shown schematically in Figure 1.1). Propagating through the site, the seismic waves can be amplified by soft soils, or deamplified because of damping effects. In site response, there are also different effects created by two or three dimensional propagation of waves like basin-edge effect, or the effect of surface waves.

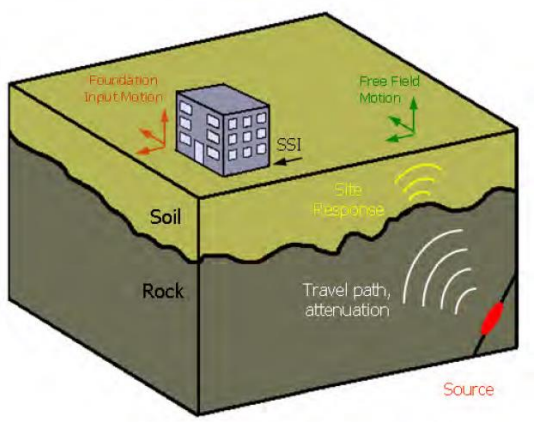

Figure 1.1. Schematic description of the three main components in ground motion prediction, namely source, path, and site (Goulet, 2008)

1.1.1 Site response in ground motion prediction

A Ground Motion Model (GMM) predicts the median and standard deviation of the intensity measure at the surface (Assuming log-normal distribution for ground motion intensity measure). The general form of a GMM is shown below:

$$\ln(IM) \propto f(source\ \ parameters_{(E)}) + f(path\ \ parameters_{(P)}) + f(Site\ \ parameters_{(S)}) + \varepsilon \qquad (1.1)$$

where the source, path, and site components are used to predict the ground motion at the surface. The GMM consists of different terms each relating to one component of ground motion prediction. In the general form of the equation, the site component represents the effect of amplification or

deamplification of the ground motion due to site response, and in empirical GMMs, the main parameters describing the site condition are the weighted average of shear wave velocity in the upper 30 meters and basin depth. The site terms are obtained empirically (using recorded data) or using a combination of simulation and recorded data and they are the easiest way to capture the effect of site response.

1.1.2 The effects of site response

In this section, a brief introduction is given about the physics of site response, and how site response affects ground motions. These effects are divided into three categories namely ground response, basin response, and topographic effects.

1.1.2.1 Ground response

Ground response is the effect of site on vertical traveling shear waves. Ground response effects, as produced by a model of a profile having a certain thickness, are only present for periods less than the soil column period. As these waves travel upwards, there are different phenomena affecting the characteristics of the waves. The first effect is Impedance Contrast. This phenomenon is due to the difference between shear wave velocity in different layers. As the wave travels from a stiff layer to a soft layer, the wave velocity drops. In order to have constant energy, the wave will have bigger amplitude. In other words, as the velocity drops, the amplitude increases. Therefore, the waves amplify as they reach a soft layer (soil).

Another important ground response effect is the effect of resonance. The soil column above the bedrock has a fundamental period of oscillation (first mode) which is related to the shear wave velocity. The relationship is as follows:

$$T_{site} = \frac{4H}{V_S} \tag{1.2}$$

where T_{site} is the first mode fundamental period of the soil column, H is the height of the soil column, and V_S is the weighted average shear wave velocity in the soil column. When seismic waves traveling through the soil column have a period close to the site period, resonance will happen. Resonance can cause considerable amplification of seismic waves at periods close to the site period.

The third ground response effect is the nonlinear behavior of soil. As shear waves travel through the soil, they cause shear strain. The behavior of soil is not linear elastic especially at high levels of strain (which are caused by strong motions). The nonlinear behavior of soil can be described by two parameters namely modulus reduction (G/G_{max}) and damping (D). Both parameters are dependent on shear strain. Some samples of modulus reduction and damping curves are shown in Figure 1.2. It can be seen that nonlinearity increases as the shear strain increases. Therefore, for strong motions, I should expect more nonlinearity, which is the cause of deamplification of strong motions at soft sites because of high level of damping. For weak motions, the behavior of soil is close to linear.

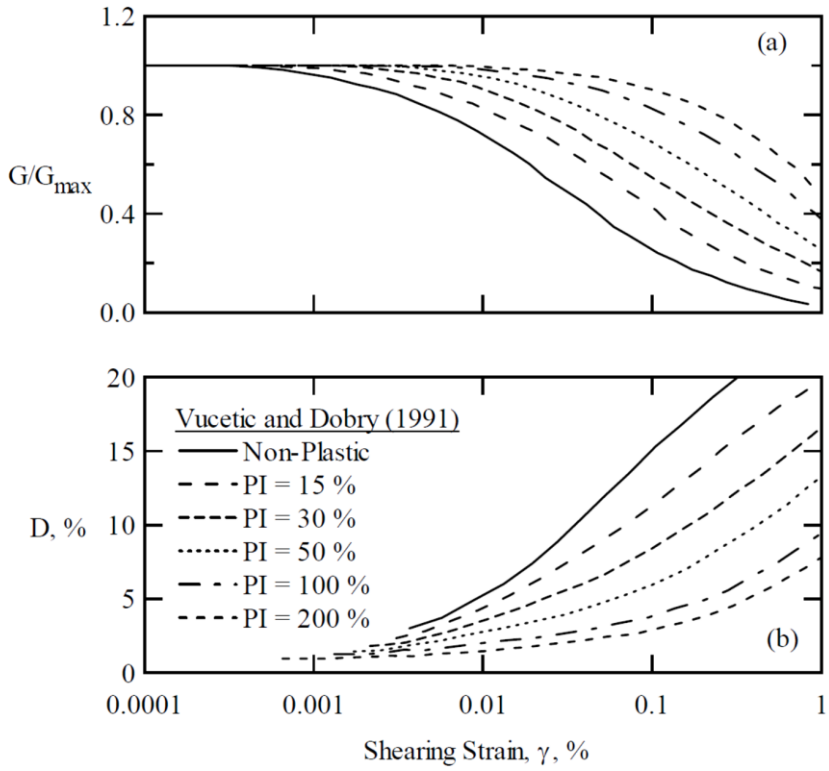

Figure 1.2. (a) Modulus reduction and (b) damping curves for soils with different Plasticity indexes (Vucetic and Dobry, 1991)

1.1.2.2 Basin response

Many regions are located on deep sedimentary basins (like Los Angeles basin or Seattle basin). Deep basins can affect the characteristics of seismic waves in two ways. The first one is basin edge effect. As the seismic waves reach the basin edge, according to Snell's law, they refract upwards towards the surface, after reaching the surface, they are reflected back towards the bottom of the basin. In some cases, the reflection angle of the reflecting wave is less than the critical reflection angle. Therefore, the wave reflects back again, and becomes trapped in the basin. This phenomenon creates surface waves which can be considerable especially at long periods.

Another basin response effect is the focusing of shear waves. The geometry of the bottom of the basin can affect vertical propagating shear waves. In some places, the waves can be

scattered, and in some regions they can converge. The convergence of the waves around a region is called focusing. This phenomenon can cause concentrated damage at some areas on the surface.

1.1.2.3 Topographic effects

Uneven topography of the ground surface can also affect the intensity of ground motion. Ground motion can be amplified at the top of slopes or on top of hills, because at these points, there is less horizontal restraint for the soil, making it easier to move by the seismic waves.

1.1.3 What is one dimensional ground response analysis?

One practical way of capturing the effect of ground response is simulating the vertical propagation of shear waves through the site. This approach is sometimes referred to as a 1D ground response analysis (GRA) because the soil layer boundaries are assumed to be horizontal and wave propagation is assumed to be vertical. In some cases, this method is satisfactory for periods less than the site period. However in many cases, the site period is ill-defined because of a gradual increase of stiffness with depth making it difficult to define the extent of the soil domain to be considered in the 1D model. Experience has shown that 1D GRA can work reasonably well for periods less than about 1.0 sec but seldom is effective at longer periods (Baturay and Stewart, 2003). In this period range, the wave type that dominates response spectral ordinates is generally shear waves. Therefore, modeling vertical propagation of shear waves is a reasonable assumption.

GRA can be performed using Linear, Equivalent linear (EL) analysis and Nonlinear (NL) methods. In the linear method, the differential wave equation is solved with the assumption of stress-independent linear elastic behavior of the material and constant damping ratio. In equivalent linear method, we solve the differential wave equation assuming linear soil behavior. This method works well when nonlinear behavior of the soil is not very strong. In cases where high levels of

shear strain (because of strong motion and weak soil) is expected, NL analysis is preferred because it can better simulate time-dependent and highly nonlinear soil response. Nonlinear methods of analysis solve for the response of a multi-degree-of-freedom lumped mass or finite element system when shaken at the base. There are numerous computer programs capable of performing 1D ground response analysis like DEEPSOIL (Hashash et al., 2016), STRATA, D-MOD 2 (Matasovic, 2006), OpenSees (McKenna and Fenves 2001), SHAKE (Youngs 2004) and SUMDES (Li et al. 1992). Some of the programs are capable of performing EL, some are able to perform NL, and some can do both of them.

For modeling the 1D propagation of shear waves through the site, the accurate cyclic stress-strain behavior of the material (soil) has to be known. In ground response analysis, the stress-strain behavior of the soil can be described by strain-dependent modulus and damping, which can be derived for a given depth from maximum shear modulus (G_{max}), modulus reduction, and damping relations. Modulus reduction curve describes the strain-dependent shear modulus of the soil. The G_{max} represents the maximum shear modulus of the backbone curve corresponding to very small strains, and damping curve represents the strain-dependent amount of energy dissipated in the soil mass in cyclic loading. In order to obtain G_{max}, the most typical way is measuring the velocity of shear waves in different layers of the soil profile, and using the equation below:

$$G_{\max} = \rho(V_S)^2 \tag{1.3}$$

where ρ is the density of the soil.

The velocity profile can be obtained in-situ by methods like spectral analysis of surface waves (SASW), downhole, or suspension logging. Modulus reduction and damping curves can be obtained by empirical relationships based on parameters like soil plasticity and overburden

pressure, or by site-specific laboratory tests. In Figure 1.3, a typical ground response analysis problem is shown schematically, in which the rock motion (or input motion), the soil column with its different properties (velocity profile and modulus reduction and damping (MRD) curves) are shown. The output motion or the surface motion will be obtained after the simulation of the rock motion propagating through the soil column towards the surface.

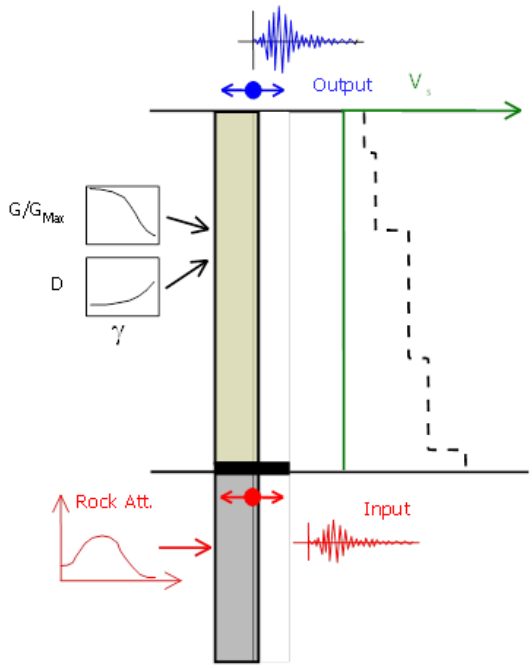

Figure 1.3. Schematic illustration of 1D ground response analysis (Goulet, 2008)

The method of 1D GRA is unable to capture two or three dimensional phenomena like surface waves or basin edge effect. These phenomena play a considerable role in the surface ground motion at long periods (usually more than 1.0-2.0 sec). Therefore, there is higher probability that 1D GRA gives unreliable results for predicting long period ground motion. However, short period motions are mainly controlled by 1D vertical propagation of shear waves, and the assumption of 1D GRA is more reasonable in predicting ground motion at short periods.

1.1.4 Site response and probabilistic seismic hazard analysis

The goal of earthquake engineering is designing structures capable of withstanding certain amounts of seismic loads without sustaining unacceptable damage. However, the seismic loads are always associated with different kinds of uncertainties. Probabilistic seismic hazard analysis enables us to quantify these kinds of uncertainties, so that the design loads for a certain probability of exceedance can be obtained. In probabilistic seismic hazard analysis, we are able to input the source, path, and site effects, and summarize the hazard over different combinations of sources and paths for the site.

A typical way of performing PSHA is the hazard integral. The equation of the hazard integral is shown in equation (1.4). The terms $f(\mathbf{M})$ and $f(R)$ are the probability density functions of magnitude (representing source), and probability density functions of distance (representing path). The term $P(IM > im|\mathbf{M},R)$ is the probability that the surface ground motion intensity measure exceeds a certain value conditioned on an earthquake with magnitude **M** at distance R ($im|\mathbf{M},R$). This term can be computed using a ground motion model (GMM). The GMM gives a median and a standard deviation in logarithmic units, by means of which the probability of exceedance for the surface ground motion can be obtained. Finally, by summarizing the hazard coming from a number of sources (faults), we can calculate the mean return period of the exceedance of ground motion intensity measure over a certain amount.

$$\nu(IM > im) = \sum_{i=1}^{N_{fault}} \nu_i \iint f(\mathbf{M}) f(R) P(IM > im|\mathbf{M}, R) d\mathbf{M} dR \tag{1.4}$$

After performing PSHA, the hazard calculated for a certain site can be represented in two ways, one is the uniform hazard spectrum which shows the response spectrum of an oscillator with certain damping ratio (usually 5%). The response spectrum is associated with a certain hazard level

(e.g. APE of 2% in 50 years). Another way of representing the hazard is the hazard curve, which shows the annual probability of exceedance (APE) vs. the amount of the intensity measure. Site response can affect the hazard curve as well as the shape of the uniform hazard spectra, and therefore, they can affect the results of hazard analysis. In Chapter 2, I am interested in the effect of site response, and how to represent this effect in probabilistic seismic hazard analysis. There are multiple approaches for incorporating site response in PSHA which are discussed in detail in a guideline report (Stewart et al., 2014). The report also discusses the benefits and the drawbacks of each method.

1.1.5 Scope of the research

The goal in this research is studying site response, and developing a guideline about using non ergodic or site-specific site response by geotechnical engineers. I propose methodologies about how to use available recordings at a site, results of GRA, or a combination of both in order to have a site-specific estimate of site response. Using non ergodic site response has a benefit of reducing the uncertainty which is discussed in detail in Chapter 2. I study the effect of the reduction in uncertainty in the results of PSHA using three example sites. I also study the question of to what extent 1D GRA can be trusted by a validation study in Chapter 4. I evaluate the effectiveness of 1D GRA, and estimate the uncertainties associated with 1D GRA using data from vertical array sites in California. The dataset that I compiled for this matter is discussed in Chapter 3, and the validation study on 1D GRA is discussed in Chapter 4.

1.2 DURATION OF GROUND MOTIONS

In ground motion prediction, there are several parameters representing the intensity of ground shaking called intensity measures (IM). The peak ground acceleration (*PGA*), spectral

acceleration at any oscillator period ($Sa(T)$), or the earthquake duration are some examples of earthquake intensity measures. Studies done on earthquake duration are relatively limited, while it has a considerable effect on some phenomena related to geotechnical earthquake engineering. For example, earthquake duration has a key role in estimating slope displacement in earthquakes, or in liquefaction analysis, the cyclic resistance ratio of the soil is affected by the number of loading cycles. The number of cycles are related to earthquake duration (The more the duration, the larger the number of cycles). The goal of the current study is on evaluating ground motion simulations from the Broadband Platform in terms of earthquake duration, and continuing on studying the effect of earthquake duration on geotechnical systems.

I consider significant duration parameters, which are the most often used duration metrics in engineering applications. Significant duration is defined from the time elapsed between various percentages of Arias intensity, which is computed as:

$$I_A = \frac{\pi}{2g}\int_0^{\infty}\left[\ddot{u}_g(t)\right]^2 dt \tag{1.5}$$

It is also needed to normalize the arias intensity:

$$NI_A(t) = \frac{\frac{\pi}{2g}\int_0^{t}\left[\ddot{u}_g(t)\right]^2 dt}{\frac{\pi}{2g}\int_0^{\infty}\left[\ddot{u}_g(t)\right]^2 dt} \tag{1.6}$$

where $\ddot{u}_g$ is the ground acceleration and g is acceleration of gravity. Figure 1.4 shows the accumulation of energy from zero to 100% of I_A along with times where various percentages are reached. Significant duration parameters considered here are time intervals for 0.05-0.75, 0.05-0.95, and 0.2-0.8 values of of NI_A (denoted $D_{5\text{-}75}$, $D_{5\text{-}95}$, and $D_{20\text{-}80}$, respectively).

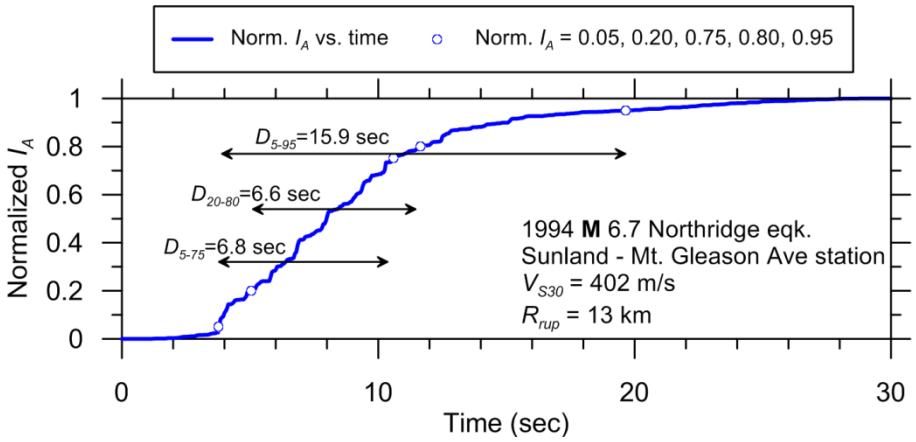

Figure 1.4. Normalized Arias intensity and illustration of three significant duration parameters D_{5-75}, D_{5-95}, and D_{20-80} for an example record.

Duration parameters have seen diverse application. The D_{5-75} and D_{5-95} parameters have been shown to correlate to collapse capacity of structures (Hancock and Bommer, 2007; Raghunandan and Liel, 2013, Chandramohan et al., 2015), with increased durations producing reduced capacities. Parameter D_{5-95} has been used in geotechnical applications including the seismic displacement of landslides (Bray and Rathje, 1998). Zhang et al. (2012) have studied the effects of D_{5-95} and D_{15-85} on the dynamic response and accumulated damage of concrete gravity dams. Duration parameters have been shown to correlate to damping scaling factors for horizontal and vertical elastic response spectra, with D_{5-75} and D_{5-95} adopted as predictive parameters by Stafford et al. (2008) and D_{5-75} considered but not adopted by Rezaeian et al. (2014a, 2014b). Parameter D_{20-80} has not been used in engineering applications to our knowledge, but is considered here because it is less impacted by noisy acceleration signals (details below), and as a result of work by Boore and Thompson (2014) (hereafter BT14), who found: (1) it captures the duration of S-wave motions better than other duration metrics by excluding intervals dominated by P-waves and surface waves, and (2) it is strongly correlated to D_{5-95} in their stochastic simulations (Boore, 2005) as $D_{5-95} \approx 2D_{20-80}$.

In this research, we intend to validate the duration of recordings from SCEC Broadband Platform as a part of the ground motion simulation validation (GMSV) task. Duration has been chosen as a validation parameter because it is less studied in comparison with spectral ordinates, and it has an important effect on geotechnical systems as discussed earlier in this section. I considered ground motion models available in the literature at the time (Kempton and Stewart, 2006, Bommer et al, 2008). Bommer et al., (2008) has a functional form which is not consistent with the physics of the problem as discussed in Chapter 5, therefore I did not use this model for the validation task. Kempton and Stewart (2006) model has a realistic functional form, however it is developed using a database which was about ten years old, and was much smaller than the most recent NGA-West2 database. Therefore, I felt the need for developing a new model based on NGA-West2 database, and use this model as a part of validation "gauntlet" for SCEC Broadband Platform simulated motions. The development of the model is discussed in Chapter 5, and the validation effort is discussed in Chapter 6 of this dissertation.

2 Non-Ergodic Site Response in Seismic Hazard Analysis

2.1 INTRODUCTION

The vast majority of the path length for seismic waves traveling from source-to-site occurs through rock in the earth's crust. As the waves approach the surface, they travel through geologic strata having progressively slower seismic velocities. This will tend to bend the wave propagation direction upward, per Snell's Law, and change the amplitude. These and other effects of the local geology and morphology of the site on the ground motions are collectively referred to as site effects. Several phenomena have the potential to contribute to site effects:

1. *Local ground response* describes the effects on ground motion of relatively shallow sediments (typically tens to hundreds of m in depth) having the slowest velocities. Because the dimensions of these soft sediments are limited, the affected frequencies are typically relatively high (>~1 Hz). Factors contributing to local ground response will include some combination of impedance effects, soil nonlinearity, and potentially resonance effects.

2. *Basin effects* are related to the deep structure of sediments that are present in many areas. Basins often include soft sediments near the surface that transition with depth to progressively stiffer sediments, including sedimentary rock, before basement conditions

(crystalline rock) are encountered. Because the dimensions of basins are often quite large (on the order of several km), the effected frequencies are relatively low (< ~ 1 Hz).

3. *Topographic effects* are related to irregularities in the ground surface morphology that can produce local amplification. The frequencies affected by topographic effects depend on the scale of the topographic features; a local steep hill will affect higher frequencies than large mountains.

Semi-empirical ground motion models (GMMs) are derived from recordings made at accelerograph sites having various combinations of these site response mechanisms. Accordingly, the effects of each mechanism are present in an average sense in GMM predictions, conditional on the considered site parameters, which are typically time-averaged 30 m shear wave velocity (V_{S30}) and some measure of basin depth. Site response predictions derived from global models conditional on such parameters are referred to as *ergodic* (Anderson and Brune, 1999).

Actual (or non-ergodic) site response will differ from this global average. When the decision is made to consider location-specific site effects, as is common for critical projects, one-dimensional (1D) ground response analyses (GRA) are the most frequently utilized approach. Guidelines for performing such analyses are available elsewhere (NCHRP, 2012; Stewart et al., 2014, hereafter Sea14). The point to be made here is that only some of the physical processes known to produce site effects (essentially, those related to local ground response) can be simulated in 1D GRA, hence error is likely for conditions where other site effects are appreciable. Errors of this sort bias the mean prediction of site response as estimated by GRA.

The standard deviation of ground motion estimates is also needed for probabilistic seismic hazard analysis (PSHA). Because ergodic analysis using GMMs consider conditionally averaged site effects, their within-event standard deviation terms include a component of site-to-site

variability (e.g., Al Atik et al. 2010). Non-ergodic site response allows this component of variability to be removed, which has been referred to as *single-station sigma* (Atkinson, 2006). As described further, when this reduction of standard deviation is taken, epistemic uncertainties in the site amplification model must be considered. A practical question facing many projects is whether site-specific GRA can be considered to reliably estimate non-ergodic site response, thereby justifying the use of a standard deviation model in which site-to-site variability is removed. This issue is discussed in this chapter, but I note here that such assumptions have been applied in PSHA for critical projects, including the Pegasos Refinement Project (Renault et al. 2010), the Thyspunt Siting Project (Bommer et al. 2015, Rodriguez-Marek et al. 2014), the Hanford site (Coppersmith et al. 2016), and the South Western US project (GeoPentech, 2015).

Ground motion analyses including site effects are performed with varying levels of sophistication. Most common is to perform PSHA for reference site conditions (typically rock), then to deterministically modify the rock motion using the mean site amplification. This is referred to as a hybrid analysis, due to its combination of probabilistic and deterministic methods, which produces a result with an unknown hazard level (e.g., Cramer, 2003; Goulet and Stewart, 2009). Convolution approaches (Bazzurro and Cornell, 2004a; Rathje et al., 2015) provide a more sophisticated modification of the rock hazard, but do not consider changes in standard deviation associated with non-ergodic site response nor differences in controlling sources that occur as site conditions are modified. The aforementioned projects in which non-ergodic site response was considered used convolution with simulation-based site amplification models; as such this approach effectively represents the state-of-practice for non-ergodic PSHA. The only approach for PSHA that rigorously incorporates site amplification effects is to modify the median and standard deviation of ground motion within the hazard integral. To date, this has generally only been

possible using GMMs with their site terms; the result is ergodic with its appurtenant issues of possible bias and large standard deviation.

In this chapter, we describe a methodology for PSHA that utilizes a site-specific (non-ergodic) GMM and illustrate its application using capabilities implemented in open-source hazard code OpenSHA (Field et al. 2003). I describe procedures for quantification of site-specific, nonlinear mean site response as derived using GRA results or on-site recordings (the use of which can overcome GRA bias). I describe analysis of within-event standard deviation considering nonlinear effects and removal of the site-to-site variability. Factors contributing to epistemic uncertainty are identified. I then illustrate the proposed approach, and its effect relative to more approximate procedures, on hazard curves and uniform hazard spectra. The findings and the explanations in this chapter are also published in a journal paper (Stewart et al., 2017). As a graduate student, I had a supporting role in this task, and my contributions were mostly in performing the analyses for the example sites, compiling literature for site response uncertainty, and developing the Bayesian/Frequentist approaches for evaluating site terms.

2.2 NOTATION AND PARTITIONING OF GROUND MOTION VARIABILITY

2.2.1 Probability Distribution for Site Amplification

I express site amplification factors (Y) as the ratio of a ground motion intensity measure (IM) on the ground surface (Z) to the value of the same IM on the reference site condition (typically rock), X:

$$Y = \frac{Z}{X} \text{ or } \ln Y = \ln Z - \ln X \tag{2.1}$$

The implementation of site amplification factors in PSHA requires a probability density function for *Y*, which is usually taken as log-normal. The mean in natural log units is defined using the following nonlinear expression that has proven to be effective for representing *X*-dependent amplification:

$$\mu_{\ln Y} = F_{lin} + F_{nl} = f_1 + f_2 \ln\left(\frac{x_{IMref} + f_3}{f_3}\right) \tag{2.2}$$

Where F_{lin} and F_{nl} indicate linear and nonlinear model components; f_1, f_2, and f_3 are model parameters; and x_{IMref} is the amplitude of shaking for the reference site condition. The intensity measure for x_{IMref} is often taken as the median, RotD50-component peak ground acceleration (PGA) for rock (where RotD50 refers to the median of all possible rotated horizontal components for a given ground motion; Boore, 2010). Ergodic versions of Eq. (2.2) include site terms in many GMMs (Abrahamson et al., 2014; Boore et al., 2014; Campbell and Bozorgnia, 2014; Chiou and Youngs, 2014). I use Eq. (2.2) to represent site-specific mean amplification.

2.2.2 Partitioning of Ground Motion Variability

A particular realization of earthquake ground motion from event *i* at site *j*, $\ln z_{ij}$, can be viewed as the sum of the mean from a GMM in natural log units, $(\mu_{lnZ})_{ij}$, and an error term,

$$\ln z_{ij} = \left(\mu_{\ln Z}\right)_{ij} + \varepsilon_{ij}\sigma_{\ln Z} \tag{2.3}$$

where ε is a standard normal variate, and σ_{lnZ} is the total standard deviation for *Z*. The GMM mean has mean (ergodic) terms for source or event (F_E), path (F_P), and site (F_S),

$$\left(\mu_{\ln Z}\right)_{ij} = F_{E,i} + F_{P,ij} + F_{S,ij} \tag{2.4}$$

The mean terms are written with indices *i* and *j* to indicate that they depend on characteristics of the event (e.g., magnitude, focal mechanism) and site (location and site parameters). For any given event and ground motion, the actual source, path, and site effects differ from the ergodic estimate by their respective random effects, denoted $\eta_{E,i}$, $\eta_{P,ij}$, and $\eta_{S,j}$. These random effects represent the bias of the ergodic model for the particular event, source-site path, and site that produced motion z_{ij}. Hence, the actual (or non-ergodic) site response is $F_{S,ij} + \eta_{S,j}$, and similar relations apply for the source and path terms.

Eq. (4.3) can be re-written as follows to help visualize the random effects (adapted from Al Atik et al., 2010 with some modification):

$$\ln z_{ij} = \left(\mu_{\ln Z}\right)_{ij} + \eta_{E,i} + \eta_{P,ij} + \eta_{S,j} + \varepsilon_{ij}\phi_{\ln Y} \tag{2.5}$$

where ε_{ij} has the same meaning as in Eq. (2.3) (although the values are now different) and $\phi_{\ln Y}$ is a standard deviation term reflecting the variability that remains when these random effects are considered. Effects of site amplification are more clearly expressed by re-writing Eq. (2.5) as

$$\ln z_{ij} = \left(\mu_{\ln X}\right)_{ij} + \eta_{E,i} + \eta_{P,ij} + \mu_{\ln Y,ij} + \varepsilon_{ij}\phi_{\ln Y} \tag{2.6}$$

in which $\left(\mu_{\ln Z}\right)_{ij} + \eta_{S,j}$ from Eq. (2.5) is replaced with $\left(\mu_{\ln X}\right)_{ij} + \mu_{\ln Y,ij}$, per Eq. (2.1).

Each of the event, path, and site terms has corresponding standard deviations. Following the notation introduced by Al Atik et al. (2010), the standard deviation of between-event terms, and for repeatable path and site terms are denoted τ, ϕ_{P2P}, and ϕ_{S2S}, respectively. These combine to produce the total standard deviation as follows:

$$\sigma_{\ln Z} = \sqrt{\tau^2 + \phi_{P2P}^2 + \phi_{S2S}^2 + \phi_{\ln Y}^2} \tag{2.7}$$

The site-to-site standard deviation (denoted ϕ_{S2S}) contributes to the within-event standard deviation ($\phi_{\ln Z}$) provided by GMMs with ergodic site terms, i.e.,

$$\phi_{\ln Z} = \sqrt{\phi_{P2P}^2 + \phi_{S2S}^2 + \phi_{\ln Y}^2} \tag{2.8}$$

Site-to-site variability is not needed when the site response model is non-ergodic, as discussed subsequently. The variability that remains when each of the random effects is accounted for is represented by the $\phi_{\ln Y}$ term in Eqs. (2.5-2.8). This term strictly represents variability in path and site effects when a non-ergodic model is used. However, prior studies summarized in the *Site Response Variability, ϕ_{lnY}* section below, indicate that $\phi_{\ln Y}$ is dominated by site amplification variability.

2.3 MEAN SITE RESPONSE

Eq. (2.2) is used herein to represent the natural log mean site response. Expressions of this type can be used in both ergodic and non-ergodic applications. In Eq. (2.2), the $F_{lin}=f_1$ term represents the weak-motion (visco-elastic) site amplification. The second term in the sum represents the effects of nonlinearity (F_{nl}); the physical meanings of the f_2 and f_3 parameters are depicted in Figure 1.4.

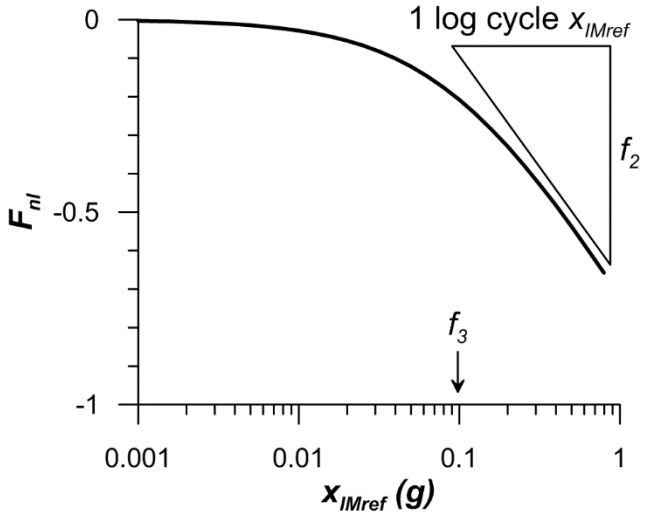

Figure 2.1. Schematic depiction of nonlinear component of mean site amplification function. Term f_2 represents the negative slope of F_{nl} for $x_{IMref} >> f_3$. Term f_3 represents the approximate center of the x_{IMref} range where amplification changes from visco-elastic (independent of x_{IMref}) to log-linearly dependent on x_{IMref}.

Ergodic site terms take f_1 as a function of V_{S30} and basin depth, while f_2 is a function of V_{S30} only. As discussed previously, such site terms can be in error due to site-specific geologic structure that is not captured by V_{S30} and basin depth parameters. Non-ergodic site terms can be developed from analysis of ground motion recordings made at the site of interest or GRA, as discussed below.

2.3.1 Evaluation from Recordings

Analysis of non-ergodic site response from recordings begins with the installation of seismic sensors (accelerometer or seismometer) at or near the target site. Ground motions are then recorded for regional earthquake events, which are of interest when they fall in the magnitude-distance range of applicable GMMs. In the case of active crustal regions, the NGA-West2 GMMs (Bozorgnia et al., 2014) are generally applicable for **M** > 3 and site-source distances < 400 km. The GMM selected should suitably capture average path effects, otherwise bias in the path term could map to erroneous assessments of site response.

Denoting the target site with index *j*, the intensity measure for event *i* (following suitable signal processing for noise effects; e.g., Boore and Bommer, 2005) is denoted z_{ij}. Residuals (R_{ij}) of these motions relative to a GMM applicable for the tectonic regime are then computed as:

$$R_{ij} = \ln z_{ij} - \left(\mu_{\ln Z}\right)_{ij} \tag{2.9}$$

The residuals in Eq. (2.9) contain random effects from each event *i* ($\eta_{E,i}$), which should be removed to evaluate the within-event residual (δW_{ij}),

$$\delta W_{ij} = R_{ij} - \eta_{E,i} \tag{2.10}$$

The evaluation of $\eta_{E,i}$ is non-trivial. For events considered in the development of GMMs, $\eta_{E,i}$ is a product of mixed-effects regression procedures, which are commonly used. For events not considered in GMM development, *a posteriori* estimates of $\eta_{E,i}$ (denoted $\hat{\eta}_{E,i}$) are needed using available recordings of event *i* (this requires data from multiple sites, which can typically be retrieved using local sensor networks such as Southern California Seismic Network and Berkeley Digital Seismic Network in southern and northern California, respectively). There are alternate procedures for this calculation, which consider a variety of factors including the relative sizes of τ and $\phi_{\ln Z}$, recording-to-recording correlation, and the number of records (N_i).

2.3.1.1 Analysis of Random Effect Terms

Two random effect terms are required when ground motion recordings from a site are used to develop a non-ergodic site term (Eq. 2.11). One is the random effect for source η_E, the other is the random effect for site η_S. The latter represents the difference between the actual site amplification and the estimate from an ergodic model.

There are three approaches for computing random effects:

(1) As part of a mixed-effects regression (Abrahamson and Youngs, 1992);

(2) Post-regression Bayesian inference;

(3) Post-regression frequentist inference.

Whereas (1) involves the estimate of random effects as part of the regression process, (2.11) and (3) use an existing model (GMM) and new data that was not considered in model development.

2.3.1.1.1 Bayesian Inference

Bayesian inference takes a prior distribution for a parameter of interest, which is then updated into a posterior distribution as a result of conditioning on data. Expressed in a generic form, this takes the form (Gelman et al. 2014):

$$p(\theta \mid y) \propto p(\theta)\, p(y \mid \theta) \tag{2.11}$$

where p indicates a distribution, θ indicates the parameters being estimated and y indicates the data. In the present application, θ represents the random effect being estimated and y represents residuals, which are total residuals R (Eq. 2.9) for the estimation of η_E and within-event residuals δW (Eq. 2.10) for the estimation of η_S. When applied to the present problem, term $p(y \mid \theta)$ indicates residuals conditioned on a prior realization of parameter θ. Values of θ produced by Bayesian inference are intermediate between the prior and those implied directly by data, with more weight given to the data as the size of the data set increases and the data dispersion decreases.

The prior distribution $p(\theta)$ for a random effect has zero mean and standard deviations of τ and ϕ_{S2S} for random effects related to event and site, respectively. The posterior distribution $p(\theta \mid y)$ is described by a mean estimate of the random effect $\hat{\eta}$ and standard deviation of that

estimate $\sigma_{\hat{\eta}}$. In the case of uncorrelated data, these estimates can be written as follows for the cases of event and site terms (adapted from Gelman et al., 2014):

For event terms:

$$\hat{\eta}_E = \frac{\frac{N_i}{\phi^2_{\ln Z}}\overline{R_i}}{\frac{1}{\tau^2}+\frac{N_i}{\phi^2_{\ln Z}}} \tag{2.12}$$

$$\sigma^2_{\hat{\eta}_E} = \frac{1}{\frac{1}{\tau^2}+\frac{N_i}{\phi^2_{\ln Z}}} \tag{2.13}$$

For site terms:

$$\hat{\eta}_S = \frac{\frac{n_j}{\phi^2_{\ln Y}}\overline{\delta W_{ij}}}{\frac{1}{\phi^2_{S2S}}+\frac{n_j}{\phi^2_{\ln Y}}} \tag{2.14}$$

$$\sigma^2_{\hat{\eta}_S} = \frac{1}{\frac{1}{\phi^2_{S2S}}+\frac{n_j}{\phi^2_{\ln Y}}} \tag{2.15}$$

where N_i is the number of recordings of event i (all sites) and n_j is the number of recordings at site j (all events). Terms $\overline{R_i}$ and $\overline{\delta W_{ij}}$ are means of total residuals for event i and within-event residuals for site j, respectively.

The assumption of uncorrelated data behind Eqs. (2.12-2.15) is appropriate for the site term calculation, but not for event terms (earthquake recordings exhibit spatial correlation, as given for example by Jayaram and Baker, 2009). Expressions similar to Eqs. (2.12-2.13) that account for recording-to-recording spatial correlations are given by Stafford (2012), modified to match the present notation as:

$$\hat{\eta}_E = \frac{\mathbf{1}_{n,1}^T \boldsymbol{C}_c^{-1} \boldsymbol{R}_i}{\frac{1}{\tau^2} + \mathbf{1}_{n,1}^T \boldsymbol{C}_c^{-1} \mathbf{1}_{n,1}} \tag{2.16}$$

$$\sigma_{\hat{\eta}_E}^2 = \frac{1}{\frac{1}{\tau^2} + \mathbf{1}_{n,1}^T \boldsymbol{C}_c^{-1} \mathbf{1}_{n,1}} \tag{2.17}$$

where R is the vector of total residuals, and C_c is a covariance matrix given by:

$$\boldsymbol{C}_c = \begin{bmatrix} \phi_1^2 & \rho_{12}\phi_1\phi_2 & \cdots & \rho_{1N_i}\phi_1\phi_{N_i} \\ \rho_{21}\phi_2\phi_1 & \phi_2^2 & \cdots & \rho_{2N_i}\phi_2\phi_{N_i} \\ \vdots & \vdots & \ddots & \vdots \\ \rho_{N_i1}\phi_{N_i}\phi_1 & \rho_{N_i2}\phi_{N_i}\phi_2 & \cdots & \phi_{N_i}^2 \end{bmatrix} \tag{2.18}$$

where ϕ_j is the within-event standard deviation for site *j*. If we assume within-event standard deviation is the same for all sites, ϕ_j terms will be replaced by constant ϕ. The spatial correlation between residuals at sites *j* and *k* is denoted ρ_{jk}. Jayaram and Baker (2009) developed a distance-dependent model for estimating ρ_{jk}:

$$\rho_{jk} = \rho\left(x_j, x_k\right) = \exp\left(-\frac{3\left\|x_j - x_k\right\|}{b}\right) \tag{2.19}$$

where *b* is a model parameter, and $\left\|x_j - x_k\right\|$ is the distance between sites.

2.3.1.1.2 Frequentist Inference

Frequentist inference involves analysis of data in a way that emphasizes the frequency or proportion of the data. The principle behind this approach is that a given data sample is one of an infinite sequence of statistically independent realizations of an underlying physical process (Everett, 2002). If the distribution of the data (residuals) is normal with an unknown mean and

standard deviation, the maximum likelihood estimator of the mean is the sample average and the maximum likelihood estimator of the standard deviation is the sample's standard deviation. The standard error of the mean is the sample's standard deviation divided by square root of the number of data observations. This produces the following estimates for event and site terms:

For event terms:

$$\hat{\eta}_{E,i} = \overline{R_i} \tag{2.20}$$

$$\sigma^2_{\hat{\eta}_E} = \frac{s_i^2}{N_i} \tag{2.21}$$

For site terms:

$$\hat{\eta}_{S,j} = \overline{\delta W_{ij}} \tag{2.22}$$

$$\sigma^2_{\hat{\eta}_S} = \frac{s_j^2}{n_j} \tag{2.23}$$

where s_i and s_j are the sample standard deviations. As explained in the main text, frequentist inference provides unbiased estimates of the mean, which is a desirable attribute for assessment of site-specific (non-ergodic) site response.

2.3.1.1.3 Comparison between Bayesian and frequentist inference

I present two examples to compare the Bayesian and frequentist approaches. The first pertains to the random effect for event ($\hat{\eta}_{E,i}$) and uses data from the 1994 **M**6.7 Northridge, California earthquake. The second pertains to the random effect for site ($\hat{\eta}_{S,j}$) and uses data recorded at the

Los Angeles, California, Obregon Park site. The calculations are for *PGA*, and I show the effect of the number of available observations for the selected event and site.

The Northridge mainshock event has 147 records in the NGA-West2 database passing the Boore et al. (2014) criteria for ground motion selection. The event term as developed in the original regression is 0.251. To investigate the effect of different numbers of recordings, I randomly select N_i records from the 147 available records, with N_i ranging from 1 to 147. For each random sample, I estimate the event term and its standard error following the Bayesian and frequentist approaches. Moreover, for each N_i, I repeat the calculations for every possible combination of N_i from the set of 147, and compute average results, which has the effect of smoothing the dependence on N_i. The resulting event terms (and their standard errors) are shown in Figure 2.2, which are based on τ = 0.364, and ϕ_{lnZ} = 0.552 (Boore et al., 2014). From trial and error, I found a small effect of spatial correlation on the outcome of the calculations; the values in Figure 2.2 are for zero between-site correlation.

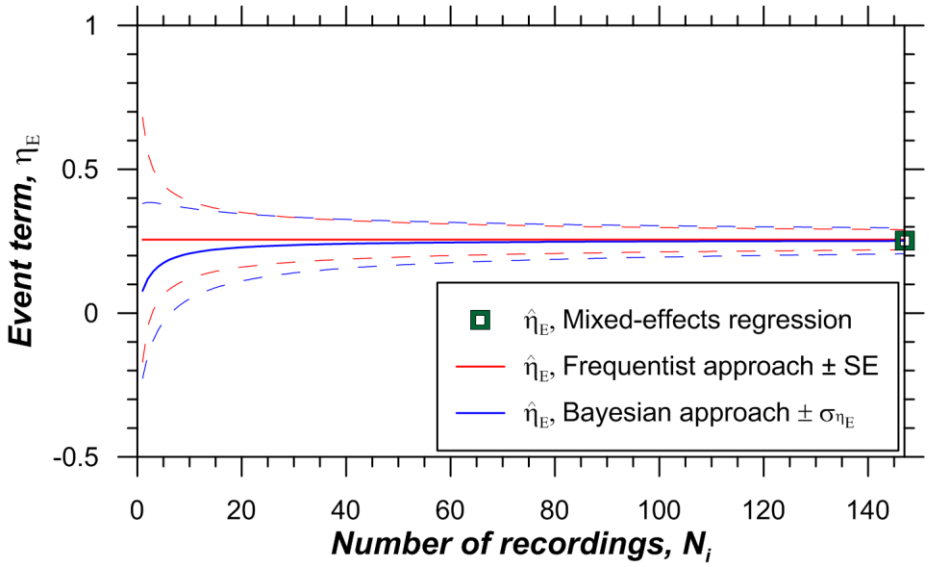

Figure 2.2. Different estimates of the mean and standard deviation of the Northridge earthquake event term ($\hat{\eta}_{E,i}$), as derived from GMM regression (mixed-effects regression) and as computed using Bayesian and frequentist approaches.

Figure 2.2 shows that the uncertainty of the mean decreases with N_i for both approaches. For small N_i, the Bayesian estimate of $\sigma_{\hat{\eta}_E}$ is close to the prior standard deviation, which is τ. The frequentist approach produces larger values of $\sigma_{\hat{\eta}_E}$ (in proportion to inverse-square root of N_i), without any effects from a prior distribution. Moreover, the Bayesian approach has a "shrinking" effect on the mean for small N_i (< ~ 30 in this case). According to the Bayes theorem, the Bayesian inference for $\hat{\eta}_{E,i}$ is a compromise between a prior distribution (which has a mean of zero in this case), and the observations. For small N_i, less weight is given to the observations, and the posterior distribution is dominated by the prior distribution, causing the estimate of the mean to shrink and be closer to zero. This shrinking of the mean is not present with the frequentist approach.

The Obregon Park site has 13 available observations for estimating site term ($\hat{\eta}_{S,j}$). I use ϕ_{S2S} = 0.4 and ϕ_{lnY} = 0.35 for the computations. I sample subsets of the available data in the manner described above, with the results shown in Figure 2.3. Similar effects of n_j on the estimates of the mean and standard error are observed as described previously for the case of event terms. In the case of the site term computation, the data are too limited to achieve convergence between the estimates of $\hat{\eta}_{S,j}$ at the largest values of n_j.

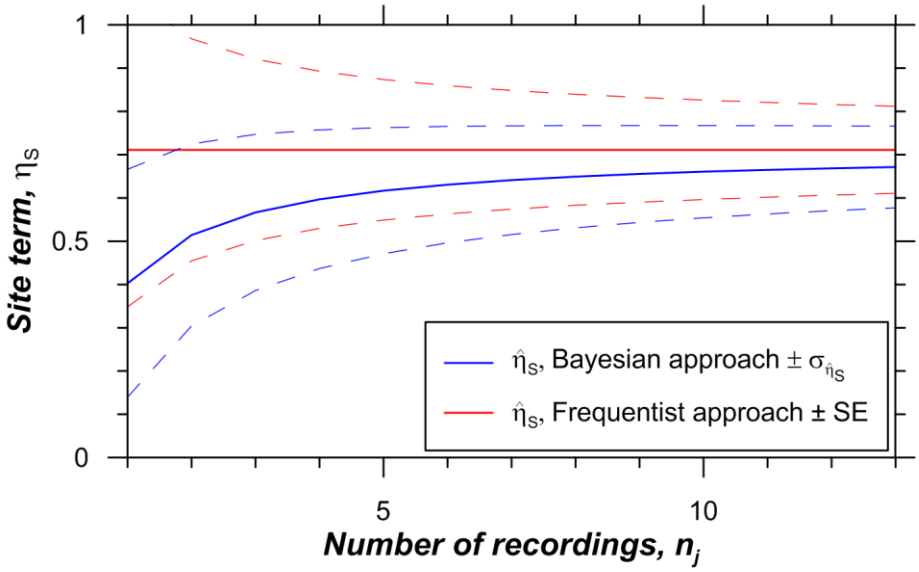

Figure 2.3. Different estimates of the mean and standard error of the Los Angeles Obregon Park site term ($\hat{\eta}_{S,j}$) using Bayesian and frequentist approaches.

2.3.1.1.4 Recommendations for mean site response from recordings

We recommend computation of $\hat{\eta}_{E,i}$ using a Bayesian inference approach (Eq. 2.16, modified from Stafford 2012). As illustrated in Figure 2.2, $\hat{\eta}_{E,i}$ from Eq. (2.16) nearly matches the mean of event residuals when the number of observations N_i > ~30.

Figure 2.4 shows example results for 13 recordings made at the Obregon Park site, which has station sequence number SSN 337 in the NGA-West2 site database (Seyhan et al., 2014). Residuals were computed using the Boore et al. (2014) GMM (BSSA14 hereafter). This site has large positive residuals, indicating that the site response is stronger than anticipated from the ergodic site term.

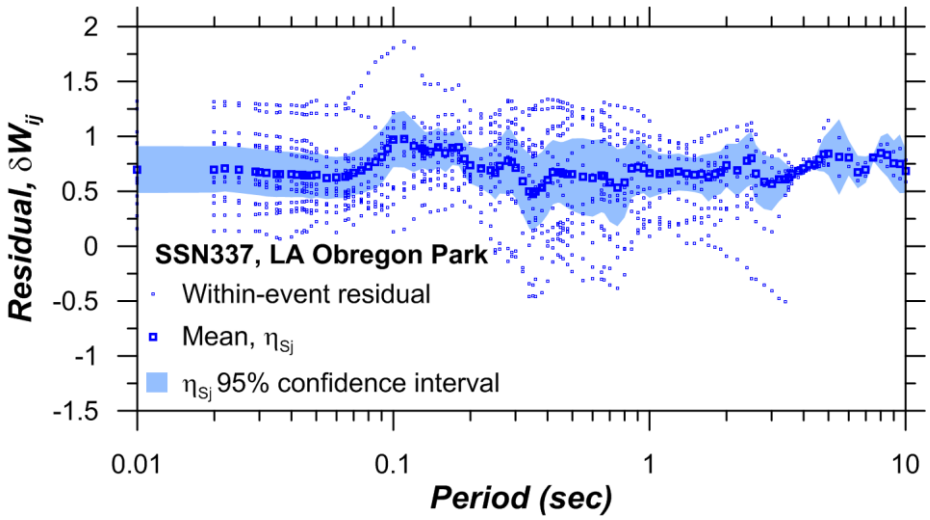

Figure 2.4. Within-event residuals and their mean for Obregon Park site. The large positive bias indicates under-estimation of site response from the ergodic site term used in the calculation (in this case, BSSA14). SSN indicates the station sequence number for the site in the NGA-West2 flatfile (Seyhan et al. 2014).

I recommend that random effect $\eta_{S,j}$ be taken as the mean of δW_{ij} (Eq. 2.22, denoted $\hat{\eta}_{S,j}$). This follows a frequentist inference approach, which is recommended because it provides an unbiased (though uncertain) estimate of $\eta_{S,j}$. Alternate Bayesian methods (Eq. 2.14) provide a biased mean estimate. Our preference for the unbiased mean is to provide the most accurate possible site response. Uncertainty in the mean estimate, $\sigma_{\hat{\eta}_S}$ is considered within the epistemic uncertainty characterization (explained further below).

I recommend using the observations as reflected through site term $\eta_{S,j}$ to set the F_{lin}=f_1 term in the non-ergodic site amplification model (Eq. 2.2) (nonlinear parameters will typically be set from simulations, next section). A first estimate of f_1 can be taken as:

$$(f_1)_j = F_{lin}^{erg} + \eta_{S,j} \tag{2.24}$$

where F_{lin}^{erg} is the ergodic (V_{S30}- and depth-based) linear site amplification. Eq. (2.24) is effective if the recordings from which $\eta_{S,j}$ is derived are sufficiently weak that the nonlinear component of

the GMM site term is not exercised in the residuals calculation (Eq. 2.9) or if the nonlinear site-specific amplification is well represented by the ergodic model. When the ground motions used to evaluate $\eta_{S,j}$ are strong enough to produce nonlinearity and the site-specific and ergodic nonlinear models are dissimilar, site residuals can be re-computed by taking site response as the sum of F_{lin}^{erg} and site-specific F_{nl}. The resulting $\eta_{S,j}$ values are then used with Eq. (2.24) to set site-specific f_1.

The linear amplification for the Obregon Park site is shown in Figure 2.5 in arithmetic units (expf_1). The amplification is relative to the reference site condition in the ergodic model, in this case 760 m/s.

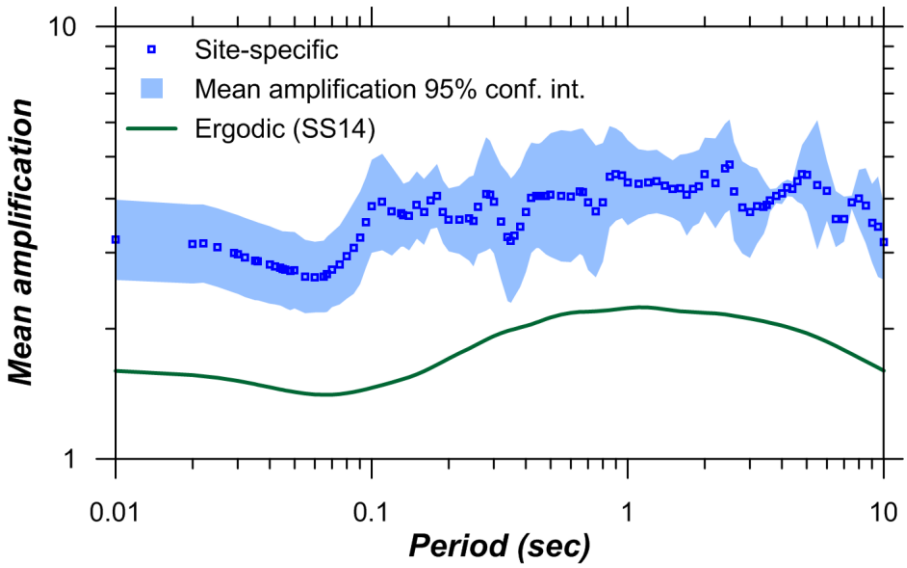

Figure 2.5. Ergodic (BSSA14) and non-ergodic (site-specific) linear site amplification relative to 760 m/s for Obregon Park site.

2.3.2 Evaluation from Simulations

When GRAs are used to estimate site amplification, they should follow recommended practices for selecting an appropriate computational framework, developing dynamic material properties and their uncertainties, and identifying hazard-appropriate input motions. As described in the

Introduction, such recommendations are provided in NCHRP (2012) and Sea14; we assume GRA results compatible with these recommendations in the discussion that follows.

GRA produces a series of discrete results, consisting of period-dependent amplification Y given a particular set of dynamic soil properties and a particular input motion with amplitude x_{IMref}. In most cases, Eq. (2.2) is used to predict the RotD50-component of ground motion Z, in which case, per Baker and Cornell (2006) x_{IMref} should be similarly computed for a pair of input motions using the RotD50 component, which is well estimated by the geometric mean (Shahi and Baker 2014). Hence, even when only one scaled component of an input record is used in ground response simulations, a combination of the two original components (as RotD50 or geometric mean) should be used to represent its amplitude as x_{IMref}.

For the three example sites shown in Figure 2.6, two alternative approaches are used for small-strain damping (D_{min}): (1) Darendeli (2001) and Menq (2003) models based on soil damping measured in laboratory; (2) estimating damping based on V_S using Campbell (2009) model for rock quality factor, Q_{ef} (See Section 4.2.2) which is ovrepredicting soil damping (See Section (4.3.1). When multiple input motions are used, potentially also with multiple realizations of uncertain soil properties, a distribution of x_{IMref}-Y results is obtained as shown in Figure 2.6. This distribution can typically be fit reasonably well using the mean amplification function in Eq. (2.2). Routines for performing these regression fits are provided in electronic supplements to Sea14. When the reference site ground motions are derived for a single hazard level, usually that prescribed for design purposes (e.g., 475 year return period), values of amplification Y are computed for a relatively narrow range of x_{IMref}. In such cases, it is not possible to regress each of the parameters f_1, f_2, and f_3; Sea14 (Section 2.6) suggest several options for addressing this situation and the aforementioned routines can accommodate this case.

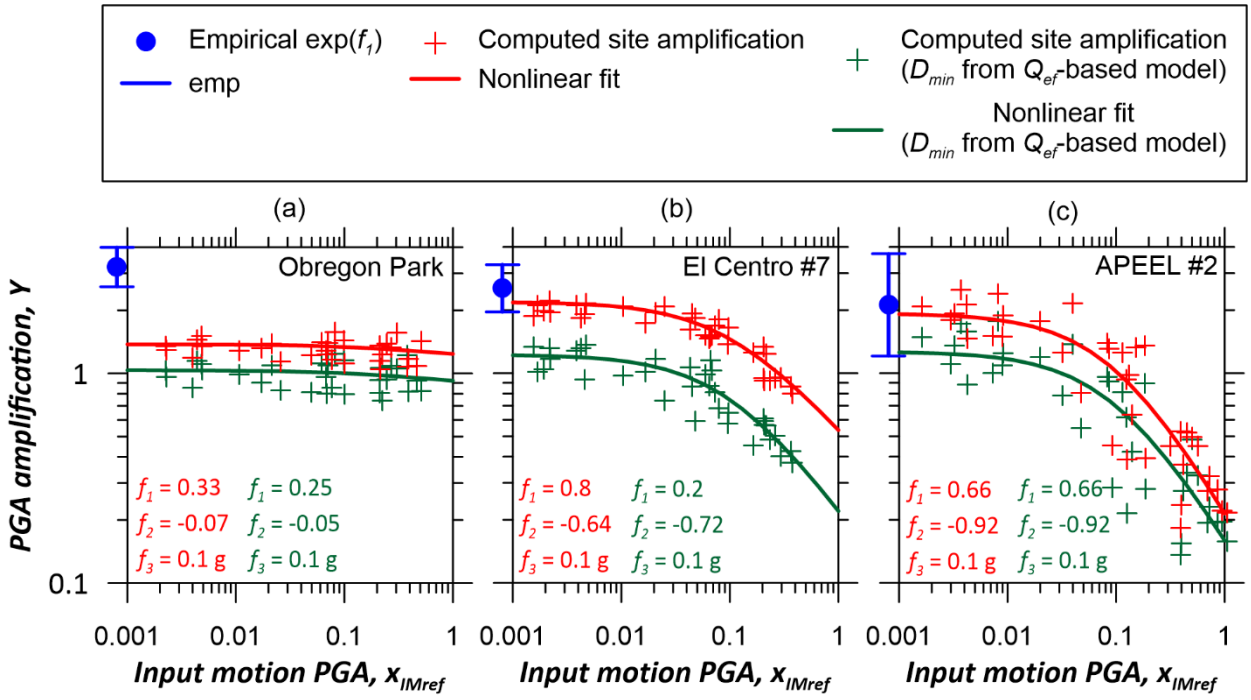

Figure 2.6. Intensity measure amplification levels from individual GRAs (symbols) using two models for small-strain damping following reference site adjustment, fit curves from Eq. (2.2), and regression coefficients. The x_{IMref} values used in the figures are the RotD50-component. Amplification levels reflect record-to-record variability only (mean soil properties used in the GRA). Empirical site amplification (derived from recordings) is shown as a mean amplification with 95% confidence intervals beyond the limits of the abscissa, to indicate that this amplification is not associated with any specific value of x_{IMref}.

The example GRA results in Figure 2.6 are for amplification of PGA at one stiff and two soft soil sites (Obregon Park, El Centro #7, and APEEL #2; site attributes are presented in Figures 2.12-2.13, and details on the example results are given subsequently). These results are from nonlinear GRA performed using DEEPSOIL (Hashash et al., 2016) following guidelines for parameter selection in Sea14. The trend of site amplification with the input motion PGA demonstrates weak nonlinearity for Obregon Park and strong nonlinearity for APEEL #2. These are typical patterns that reflect the larger strains that develop in soils at soft sites.

The site amplification directly provided by the GRA result reflects the surface IM relative to the IM for the site condition at the base of the profile, which is 540 m/s for Obregon Park,

508 m/s for El Centro #7, and 1525 m/s for APEEL #2. These conditions are different than the GMM reference condition for *X*, which is typically 760 to 1100 m/s, hence the GRA-based amplification requires modification to represent *Y* per Eq. (2.1). If we denote the V_{S30} value corresponding to conditions at the base of the profile as V_{S30}^{B} and the ground motion IM for that condition (corresponding to the GRA input motions) is X^B, then the GRA-based site amplification is:

$$Y^B = \frac{Z}{X^B} \tag{2.25}$$

The site amplification relative to the reference condition for *X* can then be evaluated as

$$\ln(Y) = \ln\left(Y^B\right) + \mu_{\ln Y}\left(V_{S30}^{B}\right) \tag{2.26}$$

where $\mu_{\ln Y}\left(V_{S30}^{B}\right)$ is the mean site amplification from an ergodic model for the base-of-profile site condition. Likewise the ground motion amplitude used in the nonlinear site term computation is taken as:

$$\ln\left(x_{IMref}\right) = \ln\left(x_{IMref}^{B}\right) - \mu_{\ln Yref}\left(V_{S30}^{B}\right) \tag{2.27}$$

where x_{IMref}^{B} is the corresponding value of that IM for the base-of-profile site condition and $\mu_{\ln Yref}\left(V_{S30}^{B}\right)$ is the ergodic amplification of that reference IM for the site condition represented by V_{S30}^{B}. The site amplification and x_{IMref} values shown in Figure 2.6 were adjusted in this manner. These procedures carry elevated epistemic uncertainty when V_{S30}^{B} is near or beyond the limits of empirical models (i.e., > 1500-2000 m/s).

An important consideration in the interpretation of GRA results is that the computed mean amplification may be biased relative to the true (generally unknown) mean site amplification.

Studies that investigate the effectiveness of GRA are most robust when the input motions are known, which only applies for vertical arrays. While numerous studies of data from vertical arrays at individual sites have found reasonably good fits to GRA results (e.g., Borja et al., 1999; Elgamal et al., 2001; Lee et al., 2006; Tsai and Hashash, 2009; Yee et al., 2013; Kaklamanos et al. 2014), other studies that systematically examine a broad set of such arrays generally find misfits for a substantial subset (Thompson et al. 2012; Afshari and Stewart, 2015a). This bias occurs because GRA does not capture some of the physical mechanisms that contribute to site response, especially for geologic conditions that cannot be reasonably represented as 1D. The three example sites (Figure 2.6) illustrate the issue – amplification levels observed from recordings (using procedures from previous section) are shown in the figure along with the simulation fits. Underprediction bias for PGA amplification occurs for Obregon Park; the bias is statistically significant in that the simulation mean is outside the 95% confidence interval for the empirical amplification. The El Centro #7 and APEEL #2 weak motion amplification levels from the data and simulations are relatively compatible.

For situations where amplification is evaluated from recordings and the resulting f_1 differs from the GRA-based estimate, I recommend adopting the empirical f_1 value while maintaining the nonlinear function from GRA (coefficients f_2 and f_3). This amounts to a vertical shift of the simulation-based amplification function to the empirical value (e.g., to 3.2 in Figure 2.6a).

When ground motion recordings are not available for a site, simulations are the only viable option for developing site-specific amplification functions. The suitability of simulation results derived from 1D analysis requires judgement on the part of the analyst, and is subject to significant epistemic uncertainty, as discussed next. However, a situation for which the inadequacy of GRA is clear is at periods higher than the fundamental-mode period of the soil column considered in the

simulations (e.g., Baturay and Stewart, 2003), which is typically tens to perhaps hundreds of meters in thickness. At these long periods, essentially no site response is computed because the quarter wavelength is longer than the profile dimension; in the limit the site displaces in an essentially rigid body manner. In contrast, long-period site response is empirically known (from ergodic models) to be pronounced, which is due to macroscopic features of the geologic column, and perhaps three-dimensional basin structure, that may be several km in dimension. As discussed subsequently (*Implementation* section), we recommend transitioning from simulation-based non-ergodic coefficients to ergodic coefficients at these long periods.

2.3.3 Epistemic uncertainty of mean site response

PSHA with a site-specific (non-ergodic) GMM requires consideration of epistemic uncertainties in the mean site amplification model (this section) and aleatory uncertainty model (next section), typically following a logic tree framework (Abrahamson and Bommer, 2005; Bommer and Scherbaum, 2008). I suggest to characterize uncertainties in the mean model in two ways: (1) uncertainty in f_1 (Eq. 2.2), which reflects the overall level of amplification; and (2) uncertainty in the nonlinear model (F_{nl}), potentially affecting parameters f_2 and f_3 (Eq. 2.2).

Uncertainty in the overall amplification level (parameter f_1 in Eq. 2.2) should be characterized differently when the model is derived partly from recordings versus being entirely GRA-based. When f_1 is set from recordings, epistemic uncertainty is represented by the standard error of the mean of $\eta_{S,j}$ (Eq. 2.23). When f_1 is set by GRA, epistemic uncertainties should reflect the degree to which the physical processes modeled in 1D analysis capture the true site response given the local geologic structure. For example, sites having a large impedance contrast might be well characterized by GRA for oscillator periods below the site period. For such conditions,

epistemic uncertainty could be taken from the range of simulation results given alternate input motions and variable V_S profiles (details for considering such uncertainties are given in Chapter 2 of Sea14). If geologic complexities not captured by GRA could reasonably be expected to influence site response (e.g., sites within large sedimentary basins with gradually increasing V_S with depth), epistemic uncertainty is driven more by the (admittedly subjective) impacts of those complexities.

Characterization of epistemic uncertainty in the nonlinear model (F_{nl}) is directly related to uncertainty in the soil properties that produce this response, which are the modulus reduction and damping versus shear strain relations. Sea14 (Sections 2.2.2 and 2.3) summarize current models for such uncertainties. The influence of these uncertainties on mean site amplification can be readily considered in appropriate suites of GRA.

2.4 WITHIN-EVENT STANDARD DEVIATION

Our objective in this section is to develop an expression for the within-event standard deviation of surface ground motion, $\phi_{\ln Z}$, appropriate for use with a site-specific natural log mean in non-ergodic PSHA. Epistemic uncertainty in within-event standard deviations models are also discussed. We note that $\phi_{\ln Z}$ is not required when using convolution approaches, which instead use the within-event standard deviation for reference rock, $\phi_{\ln X}$, as well as the standard deviation of site amplification, $\phi_{\ln Y}$.

2.4.1 Effect of Soil Nonlinearity

Bazzurro and Cornell (2004a) showed that when the mean site amplification is described as,

$$\mu_{\ln Y} = c_1 + c_2 \ln(x) \tag{2.28}$$

the standard deviation for *Z* can be computed as follows:

$$\sigma_{\ln Z} \approx \sqrt{(c_2 + 1)^2 \sigma_{\ln X}^2 + \phi_{\ln Y}^2} \tag{2.29}$$

where $\sigma_{\ln X}$ represents the total standard deviation of input motions (as used in GRA) and $\phi_{\ln Y}$ is as defined previously (dispersion of site amplification). An important feature of Eq. (2.29) is that values of $c_2 < 0$ (caused by nonlinearity) reduce the ground motion variance. This feature of ground motion has a physical explanation. Consider a distribution of reference ground motion *X* of sufficient amplitude to produce nonlinearity. The mean realization (μ_{lnX}) produces a particular level of amplification according to Eq. (2.2). Considering now the tails of the *X* distribution, a low realization (negative epsilon) produces less nonlinearity and hence more amplification than at μ_{lnX}, which has the effect of 'squeezing' the below-mean tail of the *Z* distribution. A high *X* realization produces the opposite effect (more nonlinearity, less amplification), squeezing the above-mean *Z* distribution tail. These reductions in the *Z* distribution width require reduction of $\phi_{\ln Z}$, which is accommodated by the c_2 term in Eq. (2.29); such effects of decreased within-event variability for soft soil sites are also observed empirically (e.g., Boore et al., 2014).

The use of total standard deviation $\sigma_{\ln X}$ in Eq. (2.29) indicates that both the between- and within-event components of variability are affected by site nonlinearity (per Eq. 2.7). Depending on how between-event terms are computed, it may or may not be appropriate to reduce τ using the slope term as in Eq. (2.29). Al Atik and Abrahamson (2010) take the position that between-event variability τ represents the standard deviation of random effects terms $\eta_{E,i}$ for rock conditions only, which implies that nonlinear site response is not reflected in the data used in their computation.

The effects of nonlinearity are therefore added subsequent to the GMM regression, and appear because of the impact of between-event variability on x_{IMref}. Interestingly, the effects of between-event variability on x_{IMref} are not considered in forward application (median values are used – discussed further in the *Correlation Issues* section below). Among GMMs, this approach is used by Abrahamson et al. (2014) and Campbell and Bozorgnia (2014). I take a different position that τ is based on $\eta_{E,i}$ terms for as-recorded conditions including rock and soil sites. In this case, the average site effect represented by the site term in the GMM affects the event terms and hence their variability. Following this approach, between-event dispersion for application is taken as that implied by the data and is not modified for site nonlinearity, nor is it considered in the specification of x_{IMref}. Among recent GMMs, this approach is used by Boore et al. (2014) and Chiou and Youngs (2014). While I adopt the latter approach, I acknowledge the former could also be applied in combination with appropriate GMMs.

Because I take τ as a source attribute and site-independent, I modify Eq. (2.29) for applicability to within-event variability:

$$\phi_{\ln Z} \approx \sqrt{\left(c_2 + 1\right)^2 \phi_{\ln X}^2 + \phi_{\ln Y}^2} \tag{2.30}$$

The approximation in Eqs. (2.29-2.30) is used because its derivation assumed Y and X as uncorrelated, which is not strictly correct. These equations also apply for the case that the IMs for X and x_{IMref} match; I provide in Section 2.4.3 expressions for the case that the X and x_{IMref} IMs are different.

In the present work, I use a nonlinear function for mean amplification (Eq. 2.2), requiring revision of Eq. (2.30) to account for nonlinear site effects. I replace c_2 in Eq. (2.30) with the slope of Eq. (2.2) in log-space,

$$\frac{d\left(\mu_{\ln Y}\right)}{d\left(\ln x_{IMref}\right)} \tag{2.31}$$

The numerator in Eq. (2.31) can be written as:

$$d\left[\, f_2 \ln\left(x_{IMref} + f_3\right)\right] = \frac{f_2 dx_{IMref}}{x_{IMref} + f_3} \tag{2.32}$$

The denominator is

$$d\left(\ln x_{IMref}\right) = \frac{dx_{IMref}}{x_{IMref}} \tag{2.33}$$

Combining, the slope from Eq. (2.31) becomes,

$$\frac{d\left(\mu_{\ln Y}\right)}{d\left(\ln x_{IMref}\right)} = \frac{f_2 x_{IMref}}{x_{IMref} + f_3} \tag{2.34}$$

Replacing c_2 in Eq. (2.30) with the slope in Eq. (2.34), I obtain the following expression for within-event standard deviation:

$$\phi_{\ln Z} \approx \sqrt{\left(\frac{f_2 x_{IMref}}{x_{IMref} + f_3} + 1\right)^2 \phi_{\ln X}^2 + \phi_{\ln Y}^2} \tag{2.35}$$

A similar version of Eq. (2.35) was originally derived by Goulet (2008), and subsequently given by Papaspiliou et al. (2012). As before, Eq. (2.35) applies for matching X and x_{IMref} IMs; App. C presents equivalent expressions for non-matched IMs. Below I describe the evaluation of $\phi_{\ln X}$ and $\phi_{\ln Y}$.

2.4.2 Removing Effects of Site-to-Site Variability

The term $\phi_{\ln X}$ in Eq. (2.35) represents the within-event variability of IMs for reference site condition *X*, prior to modification for nonlinear site effects. Per Eq. (2.8), the principal contributor to this standard deviation for non-ergodic applications is path-to-path variability (ϕ_{P2P}). Site-to-site variability (ϕ_{S2S}) would also contribute for ergodic site response. Our challenge is that the within-event standard deviation terms published with GMMs generally do not include this partitioning (exceptions are Kotha et al. 2016 & Landwehr et al. 2016), hence only the total within-event standard deviation is typically known (with contributions from ϕ_{P2P}, ϕ_{S2S}, and $\phi_{\ln Y}$). When these dispersions are taken from a GMM for the reference site condition *X*, they are referred to as $\phi_{\ln Xm}$, where '*m*' in the subscript indicates its source is a model (GMM or a stand-alone standard deviation model). Some contemporary GMMs are heteroskedastic, in the sense they include site-dependent standard deviation terms (Abrahamson et al., 2014; Boore et al., 2014; Campbell and Bozorgnia, 2014; Chiou and Youngs, 2014), making them well-suited to estimating $\phi_{\ln Xm}$.

For ergodic applications, the problem is trivial – the $\phi_{\ln X}$ term in Eq. (2.35) is taken as $\phi_{\ln Xm}$. For non-ergodic applications, I propose two alternate procedures:

Approach 1: Subtract some fraction of variance ϕ_{S2S}^2 from published values of $\phi_{\ln Xm}^2$, i.e.,

$$\phi_{\ln X}^2 = \phi_{\ln Xm}^2 - F\phi_{S2S}^2 \tag{2.36}$$

The term ϕ_{S2S} has been evaluated in prior work (Figure 2.7) using ground surface stations with multiple recordings, most of which are of sufficiently low amplitude that the nonlinear effects from the prior section are modest-to-negligible. It typically ranges between 0.3-0.5 and is regionally variable (Rodriguez-Marek et al., 2013; Kaklamanos et al. 2013; Lin et al. 2011). Results in Figure

2.7 by Rodriguez-Marek et al. (2014) are for downhole records and have lower ϕ_{S2S} than the surface data, indicating much of the variability is from shallow portions of these KiK-net sites. The term F in Eq. (2.36) ranges from zero to one. A value of $F = 0$ indicates no confidence that the site amplification factors remove site-specific effects beyond the capability of an ergodic model. A value of $F = 1$ is fully non-ergodic. I recommend use of $F = 1$ when f_1 is inferred from recordings; when the site amplification model is derived solely from simulations, F should be selected in consideration of the degree to which GRA could be expected to capture the most important site response physics (such considerations are discussed in the *Epistemic Uncertainty of Mean Site Response* section). In developing Eq. (2.36), I considered whether the subtraction of $F\phi_{S2S}^2$ could alternatively be applied to the product of $\phi_{\ln X}^2$ and the nonlinear term in brackets in Eq. (2.35); the present choice reflects the concept that the reference site ground motions are partially non-ergodic, which are then further modified for nonlinear site effects.

Approach 2: Take $\phi_{\ln X}$ from so-called 'single station' models (ϕ_{SSm}) developed for region-specific applications, as available.

$$\phi_{\ln X} = \phi_{SS,m} \tag{2.37}$$

One such set of models is shown in Figure 2.8 along with an ergodic model (GeoPentech, 2015).

While site-specific within-event standard deviations are typically reduced relative to ergodic models (as provided by Approaches 1 or 2), there is a possibility of especially high variability for particular sites (e.g., Bradley, 2015). I am currently unable to predict such conditions in the absence of recordings.

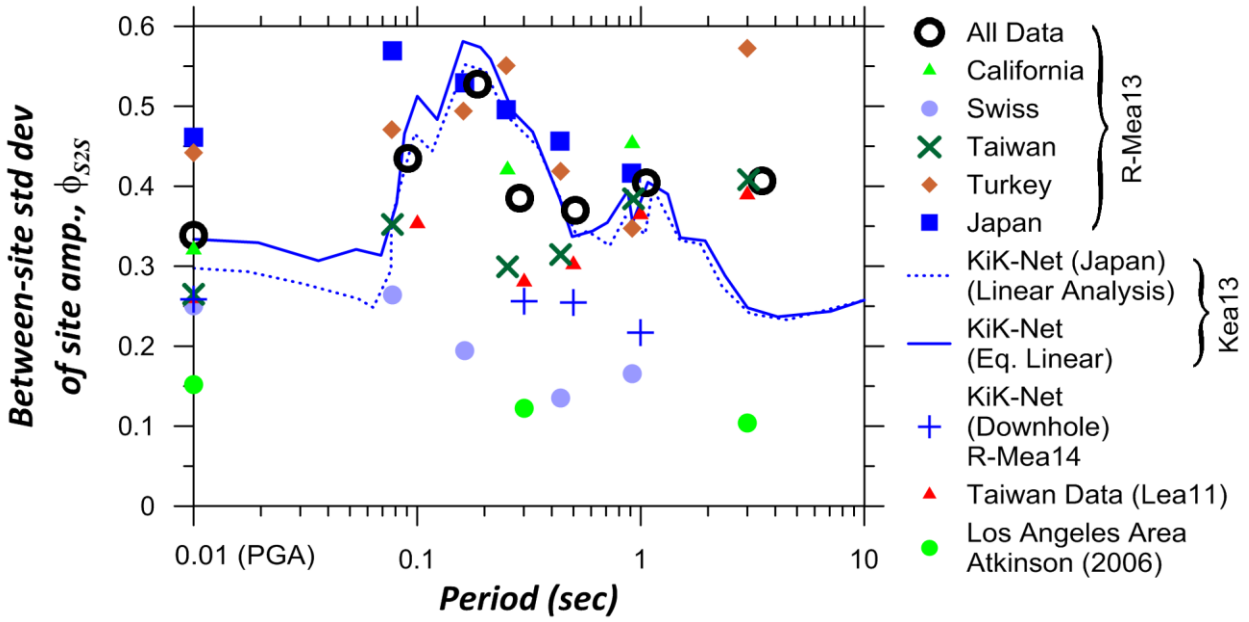

Figure 2.7. Site-to-site standard deviation (ϕ_{S2S}) findings from prior studies. R-Mea13, 14 = Rodriguez-Marek et al. (2013, 2014); Kea13 = Kaklamanos et al. (2013); Lea11 = Lin et al. (2011). All results based on ground surface recordings except R-Mea14, which is based on downhole recordings.

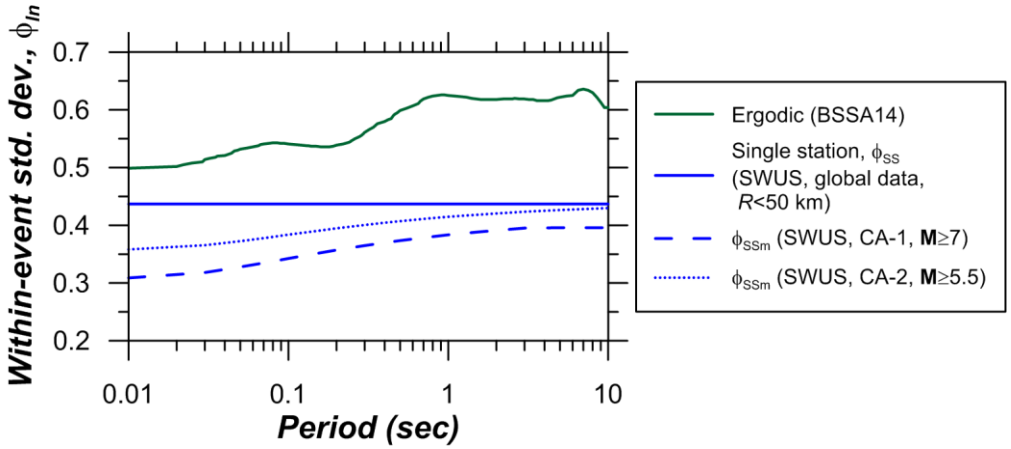

Figure 2.8. Single-station standard deviation models (ϕ_{SSm}) developed for South-Western US (SWUS) project (GeoPentech, 2015). Three alternate models are shown, one derived from global data with rupture distances < 50 km, and the other two derived from California data using different magnitude cutoffs (CA-1, CA-2). BSSA14 ergodic model shown for comparison (plotted results applicable for M > 5.5, R_{jb} < 79 km, and V_{S30} > 300 m/s).

2.4.3 Standard Deviation Equations for Non-Matching *X* and x_{IMref} IMs

In Section 2.4.1, the standard deviation equations that account for the effects of site nonlinearity is derived for the case that the IM for which ground motions are being predicted (used for *X* and *Z*) matches that used to represent the amplitude of shaking for the nonlinear operator, x_{IMref}. Here we generalize these expressions for the case that these IMs are distinct.

I begin by generalizing the total standard deviation expression from Bazzurro and Cornell (2004) (Eq. 2.29) using relations from Montgomery and Runger (2005) for the variance of the sum of correlated variables as derived using a bivariate normal density function. The counterpart expression to Eq. (2.29) is:

$$\sigma_{\ln Z} \approx \sqrt{c_2^2 \sigma_{\ln IMref}^2 + 2c_2 \rho_{\ln X,\ln IMref} \sigma_{\ln X} \sigma_{\ln IMref} + \sigma_{\ln X}^2 + \phi_{\ln Y}^2} \tag{2.38}$$

where $\sigma_{\ln IMref}$ is the standard deviation of x_{IMref}, $\rho_{\ln X,\ln IMref}$ is the correlation between *X* and x_{IMref}, and other variables are as described in the main text.

The corresponding expression for within-event variability terms (counterpart to Eq. 2.30) is:

$$\phi_{\ln Z} = \sqrt{c_2^2 \phi_{\ln IMref}^2 + 2c_2 \rho_{\ln X,\ln IMref} \phi_{\ln X} \phi_{\ln IMref} + \phi_{\ln X}^2 + \phi_{\ln Y}^2} \tag{2.39}$$

where $\phi_{\ln IMref}$ is the within-event standard deviation of x_{IMref}. I now substitute the expression in Eq. (2.34) for c_2 into Eq. (2.39), in order to adapt the model for the form of the site amplification relation from Eq. (2.2). This provides:

$$\phi_{\ln Z} = \sqrt{\left(\frac{f_2 x_{IMref}}{x_{IMref} + f_3}\right)^2 \phi_{\ln IMref}^2 + 2\left(\frac{f_2 x_{IMref}}{x_{IMref} + f_3}\right) \rho_{\ln X,\ln IMref} \phi_{\ln X} \phi_{\ln IMref} + \phi_{\ln X}^2 + \phi_{\ln Y}^2} \tag{2.40}$$

In the case that the IMs for X and x_{IMref} match, their respective ϕ_{ln} terms are identical, $\rho_{\ln X,\ln IMref}$ = 1.0, and Eq. (2.40) reverts to Eq. (2.35).

Both Approaches 1 and 2 for the non-ergodic estimation of ϕ_{lnX} can be applied with Eq. (2.40). In Approach 1, the reduction of model-based dispersions (ϕ_{lnXm}) is applied as in Eq. (2.40) to the ϕ_{lnX} term. For the $\phi_{\ln IMref}$ term the corresponding expression is:

$$\phi^2_{\ln IMref} = \phi^2_{\ln IMref,m} - F\phi^2_{S2S,IMref} \tag{2.41}$$

where $\phi_{\ln IMref,m}$ is the model-based within-event variability for the IM used for x_{IMref}, and $\phi_{S2S,IMref}$ is the site-to-site variability (e.g., from Figure 2.7) for that IM.

For Approach 2, Eq. (2.37) is used for the ϕ_{lnX} term in Eq. (2.39), and $\phi_{\ln IMref}$ is taken as:

$$\phi_{\ln IMref} = \phi_{SS,IMref,m} \tag{2.42}$$

Where $\phi_{SS,IMref,m}$ is the single-station variability (e.g., from Figure 2.8) for the x_{IMref} IM.

2.4.4 Site Response Variability, $\phi_{\ln Y}$

Prior studies have investigated site response variability based on sensitivity analyses using GRA and based on analysis of ground motion data. The findings of this work have been synthesized by Afshari and Stewart (2015b) and provide a basis for estimation of ϕ_{lnY}.

Suites of GRAs can evaluate the effects of random realizations of input motions, randomness in V_S profiles, randomness in modulus reduction and damping (MRD) curves, and model-to-model variability (through the use of alternate codes). Sources of variability that are not captured comprise epistemic uncertainties associated with limitations of GRA with respect to

geologic structure and 3D wave propagation effects. Figure 2.9 presents a compilation of period-dependent site-amplification dispersion values (ϕ_{lnY}) from Kwok et al. 2008, Rathje et al. 2010, Bazzurro and Cornell 2004b, and Li and Assimaki 2011. These studies all considered V_S profile and MRD uncertainties, but were inconsistent in their consideration of other sources. Nonetheless, the results exhibit broadly similar features, namely: (1) the level of variability at short periods is quite high at about 0.5-0.6; (2) there is an increased variability near the inelastic period of the soil column considered in the analysis (e.g., about 0.15 sec at the Turkey Flat site considered by Kwok et al. 2008, 1.2 sec at the La Cienega site considered by Li and Assimaki 2011); and (3) beyond the soil column period, the dispersion drops markedly.

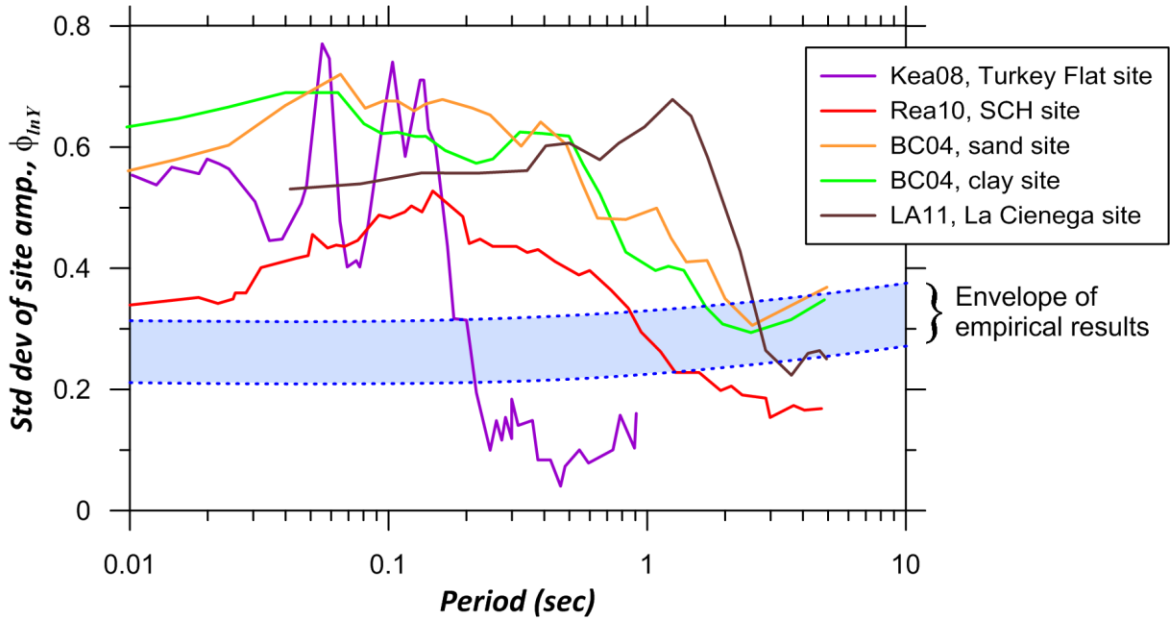

Figure 2.9. Synthesis of standard deviations of site amplification from GRA-based studies (Kea08=Kwok et al. 2008; Rea10=Rathje et al. 2010; BC04=Bazzurro and Cornell 2004b; LA11=Li and Assimaki 2011) and empirical studies based on recordings (R-Mea13, Kea13, Lea11).

For sites having ground motion recordings from multiple earthquakes, ϕ_{lnY} has been estimated in two general ways. One approach is to partition GMM residuals as in Eq. (2.5), which requires only ground surface records (Lin et al. 2011). In this case, ϕ_{lnY} is affected by randomness

in path and site response. The second approach uses vertical array data in which site amplification (and its variability) is evaluated empirically using surface and downhole recordings (Rodriguez-Marek et al. 2011, Kaklamanos et al. 2013); in such studies, ϕ_{lnY} reflects site response variability only. Afshari and Stewart (2015b) explain how we have inferred values of ϕ_{lnY} from this prior work.

Figure 2.9 envelopes results from these studies for ϕ_{lnY}, which are remarkably consistently within a band of width ~ 0.1 centered over the period range of interest at ~0.26–0.32, despite significant differences in the source data types and regions. Importantly, at periods below the site period, this variability is less than suggested by GRA, whereas it is greater at long periods. Our interpretation is that V_S profile variability may be overestimated in the Toro (1995) model used in the prior GRA-based studies and that GRA cannot capture site response variability beyond the site period. Based on currently available information, I suggest that ϕ_{lnY} can reasonably be estimated as falling in the range 0.26-0.32. Moreover, the relative consistency of ϕ_{lnY} as evaluated from surface recordings (affected by site and path variability) and from surface/downhole recordings (site variability only) suggest that ϕ_{lnY} is dominated by site amplification variability, as noted previously.

2.4.5 Epistemic uncertainty

Epistemic uncertainty of the within-event standard deviation model should be considered in PSHA along with uncertainties in the mean model (previous section). Considerations affecting this epistemic uncertainty are:

- Uncertainty in nonlinear parameters f_2 and f_3 from the mean model, which impacts ϕ_{lnZ} per Eq. (2.35).
- Uncertainty in the non-ergodic, reference-site within-event standard deviation per Eq. (2.36) or (2.37). If Approach 1 is used (Eq. 2.36), epistemic uncertainty should include alternate values of parameter F (subjective) and ϕ_{S2S} (regionally variable, Figure 2.9). Epistemic uncertainty with Approach 2 involves consideration of alternate values of $\phi_{SS,m}$.

2.5 IMPLEMENTATION

The preceding sections present procedures for evaluating site-specific natural log mean site amplification and within-event standard deviation. When combined with a reference site GMM, the result is a site-specific GMM suitable for non-ergodic PSHA. This approach has been implemented in the open-source hazard code OpenSHA (Field et al. 2003). Here I describe several details required for this implementation including correlation issues and an algorithm for interpolation of coefficients between periods. I then describe input fields required for the OpenSHA routines and currently enabled outputs.

2.5.1 Correlation Issues

PSHA provides one hazard curve for each IM at the surface (Z). The multi-variate hazard integral includes an integration across possible values of this ground motion conditional on **M**, site-source distance, and potentially other controlling variables. The IM for Z is characterized by its mean, $\mu_{\ln Z}$, and total standard deviation, $\sigma_{\ln Z}$, and an individual realization (z) within the hazard integral can be written as:

$$\ln z = \mu_{\ln Z} + \varepsilon_{\ln Z}\sigma_{\ln Z} \tag{2.43}$$

where $\varepsilon_{\ln Z}$ is the standard normal variate used in the integration for Z. Expanding upon Eq. (2.1), the mean $\mu_{\ln Z}$ depends on X as follows:

$$\mu_{\ln Z} = \mu_{\ln X} + \mu_{\ln Y} \mid x_{IMref} \tag{2.44}$$

where $\mu_{\ln X}$ is the natural log mean returned by a GMM for the reference site condition and $\mu_{\ln Y} \mid x_{IMref}$ is the mean site response model from Eq. (2.2). The quantity x_{IMref} has its own distribution, and a particular realization within that distribution can be written as:

$$\ln x_{IMref} = \mu_{\ln IMref} + \varepsilon_{\ln IMref}\sigma_{\ln IMref} \tag{2.45}$$

where $\mu_{\ln IMref}$ is the natural log mean and $\sigma_{\ln IMref}$ is the standard deviation of x_{IMref} .

Correlation issues arise because the IM controlling nonlinear site response (x_{IMref}) differs from the IM being predicted (Z) in two possible respects, even when both are for the RotD50 component of ground motion: (1) they apply for different site conditions and (2) they may be different IMs (e.g., PGA for x_{IMref} and pseudo-spectral acceleration, PSA, for Z). These correlations affect the relationship between $\varepsilon_{\ln Z}$ and $\varepsilon_{\ln IMref}$; since $\varepsilon_{\ln Z}$ is the hazard integrand, I seek to estimate $\varepsilon_{\ln IMref}$ given $\varepsilon_{\ln Z}$.

When the IM for Z and x_{IMref} match, the conditional mean of $\varepsilon_{\ln IMref}$ (given $\varepsilon_{\ln Z}$) can be computed using the Z-X correlation coefficient $\rho_{\ln Z,\ln X}$:

$$\bar{\varepsilon}_{\ln IMref} = \varepsilon_{\ln Z}\rho_{\ln Z,\ln X} \tag{2.46}$$

A conditional standard deviation would in principle apply as well, but I do not consider this source of dispersion, which would require another loop in the hazard integral. For the present implementation I take $\varepsilon_{\ln IMref}$ as its conditional mean and subsequently drop the overbar notation. When the *Z* and x_{IMref} IMs do not match, a more general relationship is applied,

$$\varepsilon_{\ln IMref} = \varepsilon_{\ln Z} \rho_{\ln Z, \ln IMref} \tag{2.47}$$

where correlation coefficient $\rho_{\ln Z, \ln IMref}$ reflects the effects of *Z*-*X* correlation and correlation between intensity measures $\rho_{\ln IM_1, \ln IM_2}$ (previously investigated by Baker and Jayaram, 2008 and Bradley, 2011).

Neither $\rho_{\ln Z, \ln X}$ nor $\rho_{\ln Z, \ln IMref}$ is presently known. I include this term in the formulation to offer flexibility to users and because its effects are significant (next section). Correlations $\rho_{\ln Z, \ln X}$ and $\rho_{\ln Z, \ln IMref}$ are generally assumed as null in practice, which has the effect of taking x_{IMref} as its mean value ($\varepsilon_{\ln IMref}$=0). In future work, it should be possible to develop models for these correlations from array data.

2.5.2 Coefficient Interpolation Between Periods

In practice, it may be cumbersome to perform the fitting operations for parameters f_1, f_2, and f_3 (as in Figure 2.6) for all of the periods used to construct a response spectrum. In lieu of this, it is possible for the analyst to compute these parameters for a selected number of periods over the range where GRA results are considered valid (usually this would be periods below the soil column period, elongated for effects of nonlinearity). With these established, values at intermediate periods

can be interpolated in a way that captures features of the data while mimicking known trends from ergodic models.

Equations implementing such an interpolation scheme have been developed using the Boore et al. (2014) ergodic model, and are presented in Section 2.6.3 of Sea14. For brevity, the details are not presented here, but example results of such an interpolation are given in Figure 2.10. As shown in the figure, the routines provide the option of transitioning coefficients to ergodic values beyond a user-specified period (denoted T_{site} in Figure 2.10; this is general taken as the elongated site period). The transition occurs over a range T_{site}:NT_{site}, where $N > 1$.

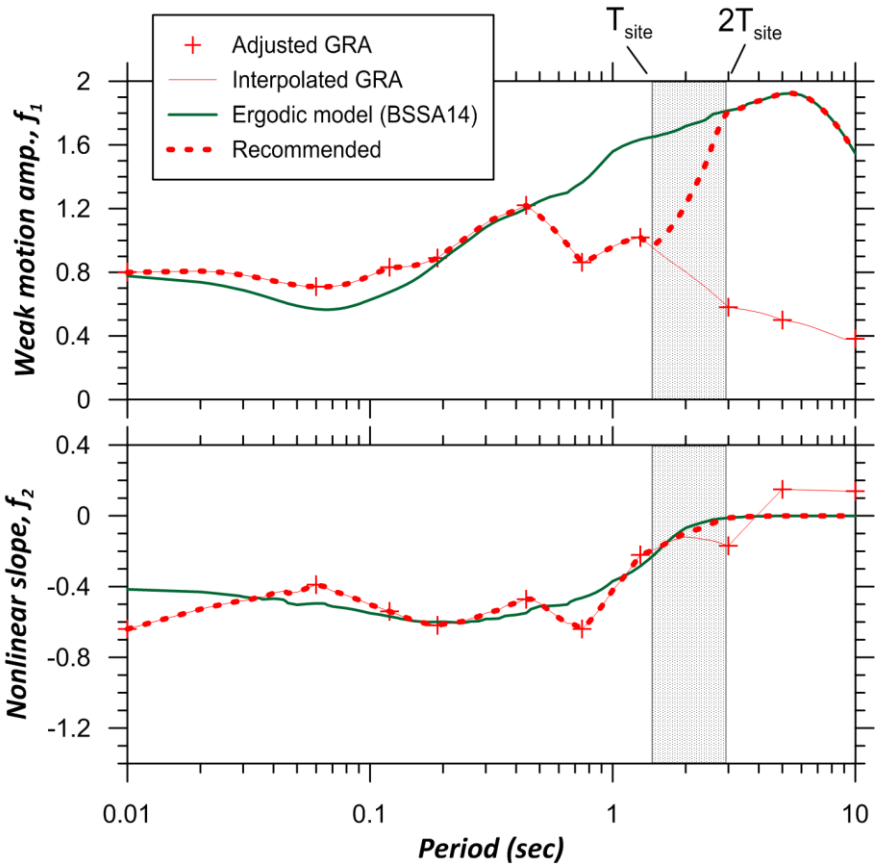

Figure 2.10. An example of interpolation for calculating f_1 and f_2 values between GRA-based values of f_1 and f_2 at 10 periods for example of El Centro #7 site. For f_1, the ergodic model is taken as the sum of V_{S30}-based term and basin depth term from Boore et al. (2014) (BSSA14). Basin depth taken as $z_{1.0}$ = 1.54 km (depth to 1.0 km/s shear wave isosurface). GRA results adjusted for compatibility with reference condition in BSSA14 (760 m/s) (Eq. 2.26).

2.5.3 OpenSHA Input Fields and Output Options

The OpenSHA routines for developing a site-specific GMM as described above are given in the *Non-ergodic site response GMPE* option as an intensity measure relation (along with a series of ergodic models, i.e., GMMs). Users enter the following information:

- GMM for the reference site condition (i.e., for analysis of ground motions denoted *X*). The reference site condition is defined as that for which the site factor in the GMM is null (in natural log units).
- Site parameter corresponding to conditions at base of profile (V_{S30}^{B}) – needed when GRA are used to estimate site effects. This would typically be a relatively firm soil or rock condition corresponding to velocities at some depth in the profile. This condition is often different from the reference site condition in the GMM.
- The V_{S30} and depth parameter appropriate for surface conditions (used in the interpolation algorithm).
- Coefficients for the mean site amplification model (f_1, f_2, f_3) and standard deviation model ($\phi_{\ln Y}$, and either ϕ_{SS} or ϕ_{S2S} and F).
- Option for upper bound limit to site amplification, Y_{max} (default is expf_1).
- Definition of the IM used for x_{IMref} (PGA or PSA at oscillator period of interest).
- Correlation coefficient $\rho_{\ln Z,\ln IMref}$ (default is zero).
- Option to adjust coefficients to ergodic model at long periods.

OpenSHA outputs using this intensity measure relation are the same as with other GMMs – deterministic medians and standard deviations for specified conditions, hazard curves, uniform hazard spectra, and disaggregation.

2.6 EXAMPLE HAZARD RESULTS

Figures Figure 2.11-Figure 2.13 present site location maps, geologic logs, and shear wave velocity (V_S) profiles for three sites in California – Obregon Park (OP), El Centro #7 (EC7), and APEEL #2 (A2). Geotechnical conditions at the three selected sites are given in Table 2.1. We perform PSHA for these sites to (1) illustrate the differences between ergodic and non-ergodic site response as implemented in PSHA; (2) demonstrate differences between non-ergodic amplification functions and associated PSHA results derived solely from GRA vs. those derived from the semi-empirical approach (weak motion amplification from recordings combined with nonlinearity from GRA); (3) illustrate the significance of *X-Z* correlation (described in preceding section) on hazard results; and (4) demonstrate differences between site-specific PSHA and more approximate convolution approaches. For brevity, I do not show the different results obtained from site-specific PSHA and hybrid approaches, which has been shown previously (e.g., Cramer, 2003; Bazzurro and Cornell, 2004a; Goulet and Stewart, 2009). GRA are performed using Deepsoil version 6.1 (Hashash et al., 2016) following the protocols for ground motion selection and parameter selection in Sea14 with one exception – small-strain soil damping D_{min} is taken from geotechnical models (Darendeli, 2001; Menq, 2003) without modification.

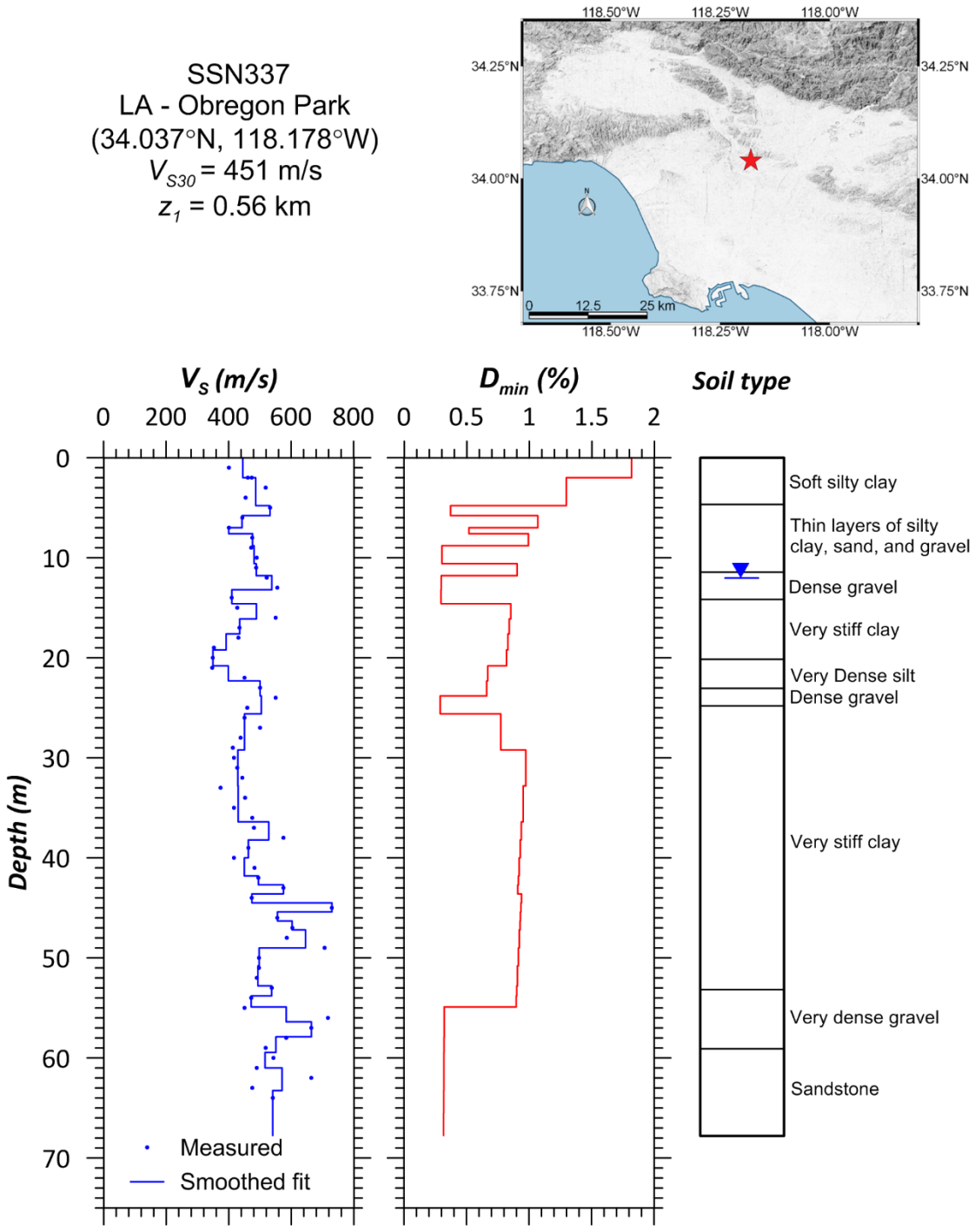

Figure 2.11. Location map, geologic log, and profiles of shear-wave velocity and small-strain damping (D_{min}) for the site LA – Obregon Park (V_S data and geotechnical log from ROSRINE).

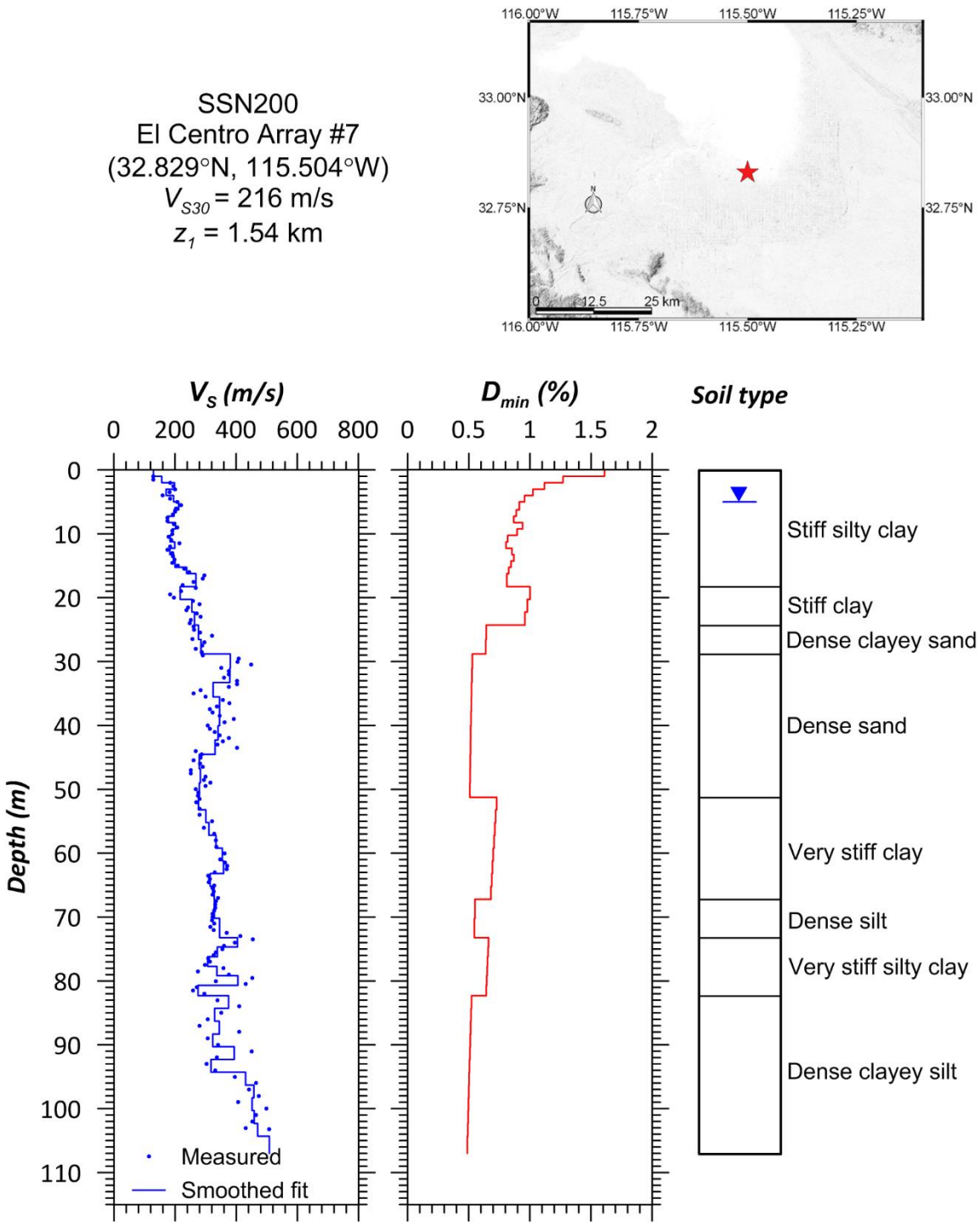

Figure 2.12. Location map, geologic log, and profiles of shear-wave velocity and small-strain damping (D_{min}) for the site El Centro array #7 (V_S data and geotechnical log from KAJIMA).

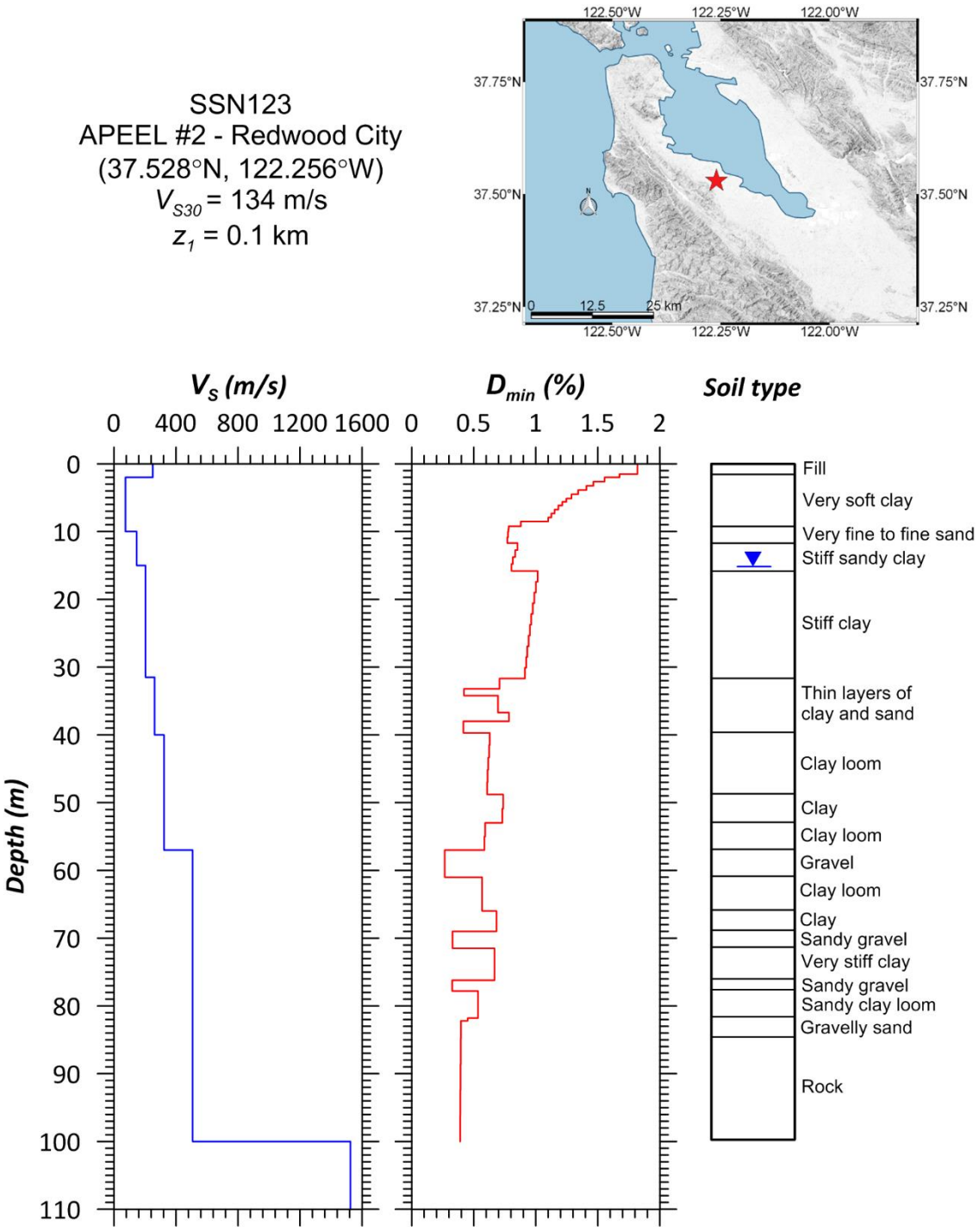

Figure 2.13. Location map, geologic log, and profiles of shear-wave velocity and small-strain damping (D_{min}) for the site APEEL #2-Redwood City (V_S data and geotechnical log from USGS).

Table 2.1. Geotechnical conditions at example sites selected for analysis

Site	Description	V_{S30}^{B} (m/s)	V_{S30} (m/s)	$z_{1.0}$ (km)	T_{site} (sec)
Obregon Park (OP)	stiff soil overlying weathered rock, lacking appreciable impedance contrast over the depth of exploration	540	449	0.56	0.57
El Centro #7 (EC7)	very deep soil with soft near-surface sediments, without a pronounced impedance contrast over depth of exploration	508	211	1.54	1.5
APEEL #2 (A2)	soft clay (Bay Mud) overlying stiffer sediments and rock, and having large impedance contrasts at the base of the soft clay and at the soil-rock interface	1525	133	0.09	1.6

Figure 2.14(a) shows the variation of linear PSA amplification with oscillator period for the three sites. Results are shown from the interpretation of recordings (Eq. 2.25), GRA, and an ergodic model (BSSA14). The empirical results are shown as a median and 95% confidence interval, which reflect the uncertainty of site term $\eta_{S,j}$ associated with the finite number of recordings. The GRA results are fit using Eq. (2.2) for each IM as shown in Figure 2.6; the result plotted here is exp(f_1) (small-strain amplification). There is no increase of D_{min} for performing GRA which is computed using Darendeli (2001) model for clays and Menq (2003) for granular soils. The ergodic results reflect V_{S30}-scaling and basin effects from BSSA14. For the OP site, the GRA underprediction bias for PGA originally shown in Figure 2.6 is seen to persist across the full period range. The ergodic model also underpredicts, but is less biased for $T > 1$ sec than GRA. EC7 has relatively modest underprediction bias for $T <$ ~0.3 sec, but substantial bias at longer periods including near an apparent site period at 4 sec (possible fundamental mode for the deep sediment column in this part of the Imperial Valley). The match of GRA to observations is quite good for A2, including amplification near the site period of 1 sec. The ergodic model improves upon GRA predictions at long periods for EC7 but not for A2. Figure 2.14(b) shows results for a

nonlinear case in which $x_{IMref} = 5f_3$; as such, the difference from the linear result reflects the size of the f_2 term. Nonlinear effects are small for OP, but pronounced for EC7 and A2 for periods $T <$ ~ 2 sec. Nonlinearity increases the site period for A2.

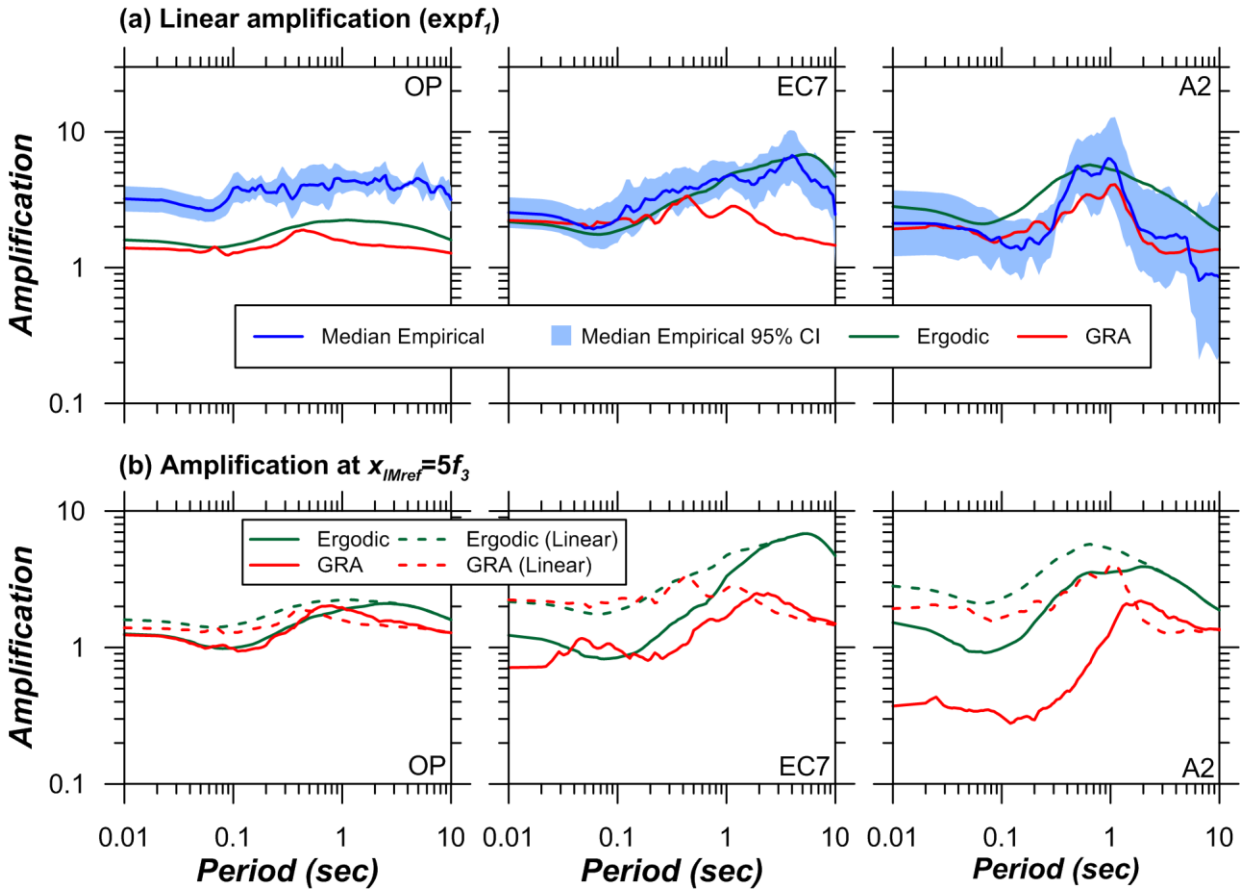

Figure 2.14. (a) Linear amplification vs. period as inferred from recordings and as estimated from GRA and ergodic model. (b) Amplification for nonlinear condition in which $x_{IMref}/f_3 = 5$ for ergodic and GRA-based models.

Figure 2.15 shows uniform hazard spectra (UHS) for 2475 year return period computed by OpenSHA with alternate site models: non-ergodic site response based on GRA alone, semi-empirical non-ergodic (f_1 set empirically, F_{nl} from GRE results), the ergodic site model, and ergodic reference site. The analyses using GRA for site response are applied across the full period range (no transition to empirical model at long period, as described in previous section), so as to highlight differences from other modeling approaches. The reference site GMM is taken as

BSSA14 and the source model is UCERF3 FM3.1 (Field et al. 2014). The hazard results presented in Figure 2.15 and subsequently are based on the site-specific natural log mean amplification and standard deviation models.

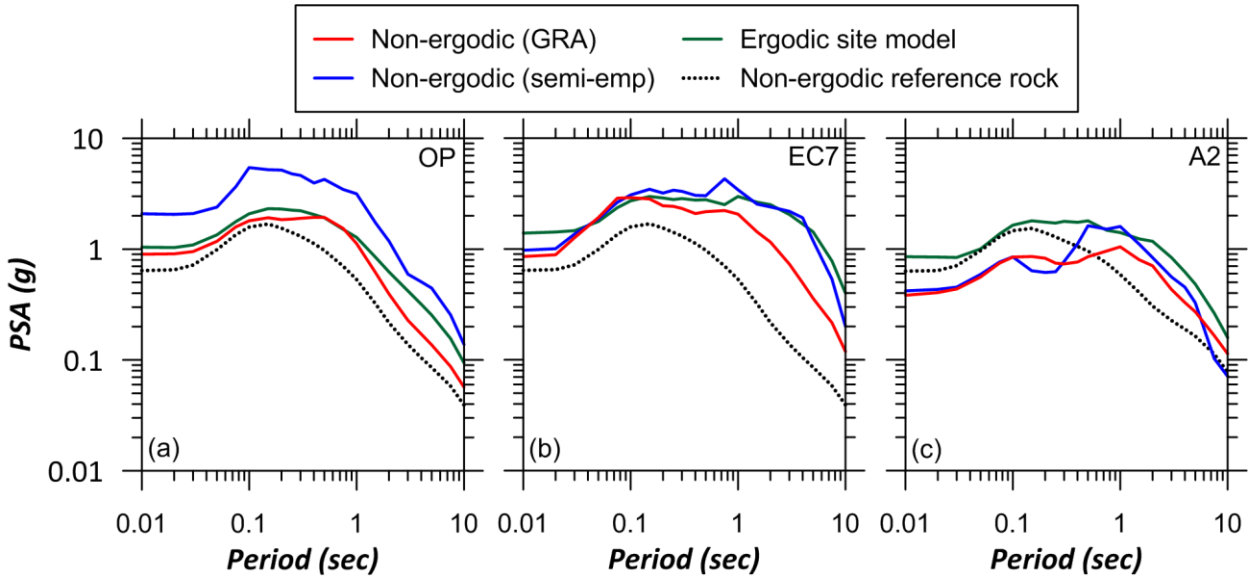

Figure 2.15. Uniform hazard spectra 2475 year return period for example sites using ergodic and non-ergodic site amplification models. Reference site hazard computed using reduced within-event standard deviation (ϕ_{S2S} removed), in conformance with standard-of-practice for non-ergodic hazard analysis with convolution approach. Non-ergodic models use F=1, and ϕ_{S2S} =0.4. No transition to ergodic model at long periods applied. The jagged appearance of non-ergodic spectra result from a limited number of GMM periods implemented in OpenSHA.

For the OP site (Figure 2.15a), the effect of the underprediction bias from the ergodic model and GRA is clear, as is the more favorable performance of the ergodic model at long periods. For EC7 (Figure 2.15b), the GRA under-predicts long-period (> ~ 0.7 sec) site amplification associated with deep basin structure. Those long period site effects are reasonably well captured by the ergodic model; results of this sort motivate the use of the ergodic model transition (Figure 2.10). The non-ergodic UHS for A2 (Figure 2.15c) exhibits a peak in the spectrum near the site period (~ 1 sec) that is captured by GRA – the ability to capture features of this sort is an advantage of non-ergodic site response procedures. The large impedance contrast at A2 causes ground response

to dominate the site response, which is demonstrated by the similarity of the GRA and semi-empirical results in Figures Figure 2.14 and Figure 2.15.

Figure 2.16 shows example hazard curves for the three example sites derived using the reference site condition, the semi-empirical non-ergodic site model, and the ergodic site model. The sort and long period IMs were selected to illustrate results for cases with nonlinearity varying from strong (PGA) to weak but non-zero (0.5 sec PSA for OP). The non-ergodic site model is applied using both the convolution approach and the recommended site-specific GMM implementation. For the latter, I show results computed with $\rho_{\ln Z,\ln X}$ set to 0 (default), 0.5, and 1.0. Per typical practice on recent projects (as described in *Introduction*), the convolution approach is applied with reduced within-event standard deviation, per Eq. (2.36). Two key findings from these hazard curves are:

- As $\rho_{\ln Z,\ln X}$ increases, the nonlinear component of the site term becomes more pronounced, which reduces the hazard (PGA, Figure 2.16a). Where the site nonlinearity is not significant (1.5 sec PSA, Figure 2.16b), the effect of $\rho_{\ln Z,\ln X}$ on hazard disappears.
- For IMs subject to strongly nonlinear site response (Figure 2.16a), the use of convolution produces lower hazard at long return periods than site-specific PSHA when applied with the default zero correlation. This occurs because the amplitude of shaking driving the nonlinear site term (x_{IMref}) in convolution is taken from the reference (X) hazard, which is 'positive epsilon' (exceeds the mean). When nonlinearity effects are modest (Figure 2.16b), the differences between convolution and site-specific PSHA results are small.

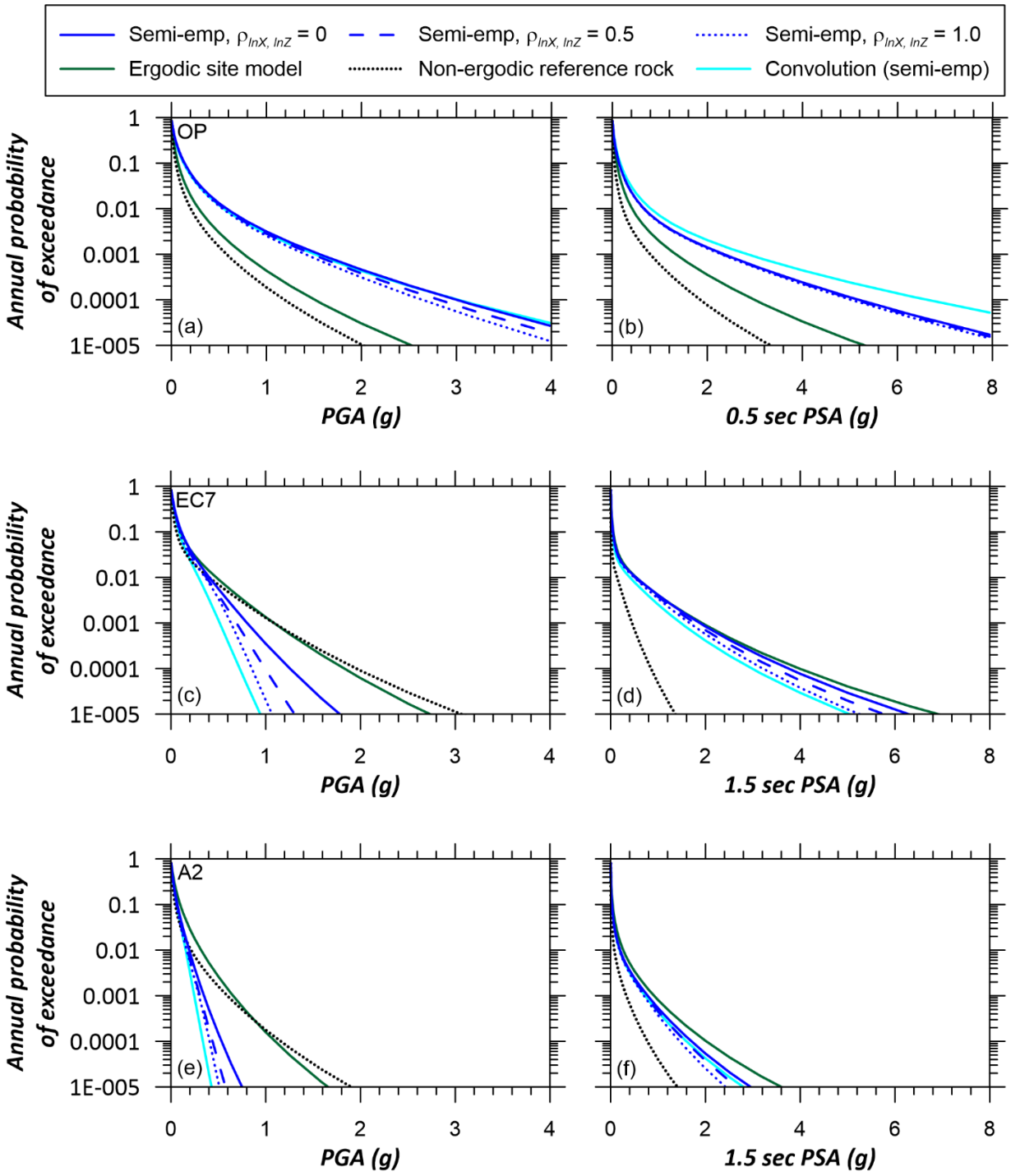

Figure 2.16. Hazard curves for OP (a and b), EC7 (b and c) and A2 (e and f) site derived using non-ergodic and ergodic site amplification models. The non-ergodic (semi-empirical) model is applied in hazard computations with varying levels of reference-to-site correlation. The model is also applied through convolution with the non-ergodic reference rock hazard.

2.7 CONCLUSIONS AND RECOMMENDATIONS

We seek to explain the meaning of non-ergodic site response and the manner by which it can be applied to develop site-specific GMMs for use in hazard analyses. The concept of using site-specific GMMs in PSHA has been proposed previously (McGuire et al., 2001), but a specific methodology has not been described in the open literature and such approaches have seldom been applied in practice. I describe a methodology and demonstrate its use (in a module within the OpenSHA hazard code), from which several benefits are evident relative to the use of ergodic models:

- Non-ergodic mean site response is estimated using truly site-specific information that improves the accuracy and reliability of hazard estimates and related outcomes (e.g, disaggregation results) relative to ergodic models.
- The standard deviation of ground motion is reduced, which tends to lower ground motion estimates for hazard levels of interest in design (return periods of 500 years or more).

I show how non-ergodic (i.e., site-specific) site response can be evaluated using on-site ground motion recordings in combination with GRA simulations, or by using GRA simulations alone. The former is preferred when practicable, because GRA results may be biased, particularly at long periods (i.e., beyond the fundamental period of the 1D model). These errors arise from physical processes that affect site response (e.g., surface waves, basin effects) but that cannot be readily incorporated into typical GRA simulations performed for engineering purposes.

The methodology presented in this chapter can be distilled to the following steps:

1. Perform detailed site characterization, including geotechnical borehole logging and geophysical logging (details in Sections 2.2-2.3 of Sea14).

2. (Optional, but recommended): Install ground motion instrumentation at the site of interest (accelerometers or seismometers) and record data over time. When such data is unavailable, it may be possible to use recordings from instruments in the vicinity of the site of interest. Future research will investigate the viability of this approach, which will depend on the spatial correlations of random effect terms η_S.
3. Analyze ground response using suitable equivalent-linear or nonlinear procedures (NCHRP, 2012; Sections 2.4 of Sea14). Compute amplification values using Eq. (2.25) (Y^B) for each simulation outcome (combination of dynamic soil properties and input motion).
4. Adjust computed amplification values as needed to correct for incompatibility between the reference condition in the GMM and the base of profile condition (V_{S30}^B) using Eqs. (2.13-2.14). Adjusted amplification values are denoted as *Y*.
5. Select the IM for the reference site condition to use for x_{IMref}. Fit Eq. (2.2) to adjusted amplification values (*Y*) over the range of x_{IMref} considered in the simulations.
6. (Optional): Compute empirical site response from ground motions recorded at the site using Eq. (2.24); adjust coefficient f_1 from Step 5 as needed to match these results.
7. Evaluate the extent to which the computed site response is non-ergodic, which is often subjective. If on-site ground motions are used, I posit that the site response is non-ergodic, which implies that the within-event standard deviation should be taken using Eq. (2.35) with $\phi_{\ln X}$ taken using either Eq. (2.36) (with $F = 1$) or Eq. (2.37) (alternate expressions for unmatched IMs for *X* and x_{IMref} given in Section 2.4.3). If recordings are not used, $\phi_{\ln X}$ is best taken using Eqs (2.36) with *F* set by judgement (when site response is judged to be

dominated by ground response, F can be nearly unity; when this is not the case, F should be less than one).

8. Consider Z-X and between-IM correlation effects as explained in the *Correlation Issues* section. These correlations affect the implementation of the mean amplification function per Eqs (2.27-2.29).
9. The mean site amplification function (Eq. 2.2) and within-event standard deviation terms (Eq. 2.35) are combined with regionally appropriate ground motion models to define site-specific GMMs for use in hazard analyses. It is common for results of such calculations in active regions like California to lower ground motion estimates at long return periods (e.g., 475 or 2475 years) by 20% or more, due in large part to standard deviation reductions.
10. Repeat hazard analyses to consider epistemic uncertainties of the mean amplification function, alternate representations of standard deviation (e.g., due to variations in F), and alternate correlation models (especially for Z-X correlation). It is not appropriate to take the standard deviation reduction associated with the use of a non-ergodic model without considering these site response uncertainty effects.

Clearly the level of effort involved in developing a non-ergodic site amplification model (with corresponding site-specific GMMs) is greater than the use of relatively simple ergodic models. While conceding that point, our view is that the profession should continue to move in this direction, at least for critical projects. The increased effort provides additional knowledge, which lowers aleatory variability and frequently reduces hazard.

Moreover, the proposed approach using a site-specific GMM in the hazard integral offers advantages relative to convolution methods that comprise the current state of practice for non-ergodic PSHA. These advantages include consideration of nonlinear effects on within-event

standard deviation terms, consideration of rock-soil and between-IM correlation issues as described above, and the identification of controlling sources (through disaggregation) in a manner than considers the site response. I show that the use of convolution methods tends to underestimate hazard when the site response is nonlinear.

As described in this chapter, two technical challenges will affect projects utilizing the proposed approach: (1) difficulty in identifying *a priori* when GRA results provide an unbiased estimate of site effects and (2) lack of knowledge regarding surface-reference (Z-X) correlations. Future progress on these subjects will affect specific steps in the proposed procedure, but not the framework itself.

3 California Vertical Array Dataset

3.1 INTRODUCTION

Vertical arrays are valuable tools for distinguishing the effects of shallow site conditions from the other effects (source, path, etc.) on ground motions. They allow for the observation of ground motions from the same source both at the surface and the depth at which the downhole sensor is installed. Therefore, a vertical array directly reveals the effects of site response between surface and downhole instruments. In addition to allowing for direct observation of site response effects, a well characterized vertical array site, which includes a high quality shear wave velocity (V_s) profile and possibly a geotechnical log, allows for validating numerical site response models.

In this study, I compile a database of recordings from vertical arrays owned and operated by the California Strong Motion Instrumentation Program (CSMIP) and University of California at Santa Barbara (UCSB). A similar database from Japan has been compiled by Dawood et al. (2015), which utilized data from the Kiban-Kyoshin network (KiK-net) (Aoi et al., 2001). The Dawood et al. database updates an earlier KiK-net database by Pousse (2005). In order to compile the large database of about 157,000 recordings, Dawood et al. (2015) developed a step-by-step automated protocol to systematically process the data, and produce a flatfile which is available at NEEShub (https://nees.org/resources/7849). Other major vertical array networks are operated in Taiwan (Downhole Earthquake Monitoring Network, http://scweb.cwb.gov.tw/Twenty.aspx?ItemId=41&loc=en) and Greece (EuroSeis test, Raptakis et al., 2000, Chavez-Garcıa et al., 2000 at http://euroseisdb.civil.auth.gr/).

3.2 ARRAY ATTRIBUTES

We have collected site data for 39 vertical arrays in California as listed in Table 3.1. Our main source of site properties and ground motion data is the Center for Engineering Strong Motion Data (CESMD) website (http://www.strongmotioncenter.org/). Velocity profile data is available for 30 sites, and ground motion time series can be downloaded through a search engine. In addition, CESMD maintains an FTP folder containing a database of weaker motions for all vertical array and surface-only sites. I have also considered four sites owned and maintained by the University of California at Santa Barbara (UCSB). The site information and recorded motions for these sites are available at http://nees.ucsb.edu/.

Interestingly, a major factor limiting the inventory of usable vertical array sites in California is the availability of V_S profile data; of the 39 vertical arrays, I have been able to collect usable V_S profile data for 30 sites (26 CESMD, 4 UCSB), and boring logs are available for 24 sites (20 CESMD and 4 UCSB). Given the relative cost of array installation (high) vs V_S profile development (low), a priority in future work should be to fill this data gap.

Boring logs for the sites were obtained from multiple sources. For two of the four sites owned by UCSB, the boring logs were available at http://nees.ucsb.edu/. For the Hollister Digital Array site and Borrego Valley Downhole Array site, boring logs were provided by J. Steidel (*personal communication*, Feb, 2016). For 17 CESMD sites located at California Department of Transportation bridges, I obtained logs from Javier V. Ortiz (personal communication, July, 2015). Three of CESMD sites have been part of calibration sites for validation of nonlinear geotechnical models project for which high quality boring logs are available. The V_S profiles and the details of boring logs is shown in Figures 4.5-4.25.

For our study, I utilize vertical array sites with measured V_S profiles and having at least four pairs of surface/downhole recordings to increase the statistical significance of the results. These data selection criteria resulted in 21 sites, of which 17 have available boring logs. The locations of those vertical array sites are shown in Figure 3.1. Figure 3.2 shows the histograms of V_{S30} for the KiK-net sites used by Thompson et al. (2012), all California sites listed in Table 3.1, and the California sites selected to be used in this study with a measured V_S profile and at least four surface/downhole recording pairs. The median V_{S30} is 413 m/s for the KiK-net sites, 309 m/s for all California sites, and 321 m/s for the California sites used in this study. The median values as well as the shape of the histograms in Figure 3.2 indicates that KiK-net sites are generally stiffer than the California sites. This is due to the fact that KiK-net arrays were installed with the primary purpose of source detection, for which installation of the base instrument in rock is preferred. This led to a large number of KiK-net vertical arrays being located on geology consisting of weathered rock or shallow soil overlying rock, often in mountainous areas. In contrast, most of the California sites are located next to bridges, which are mostly located in topographically flat areas with relatively soft soils near the surface of deep sedimentary basins.

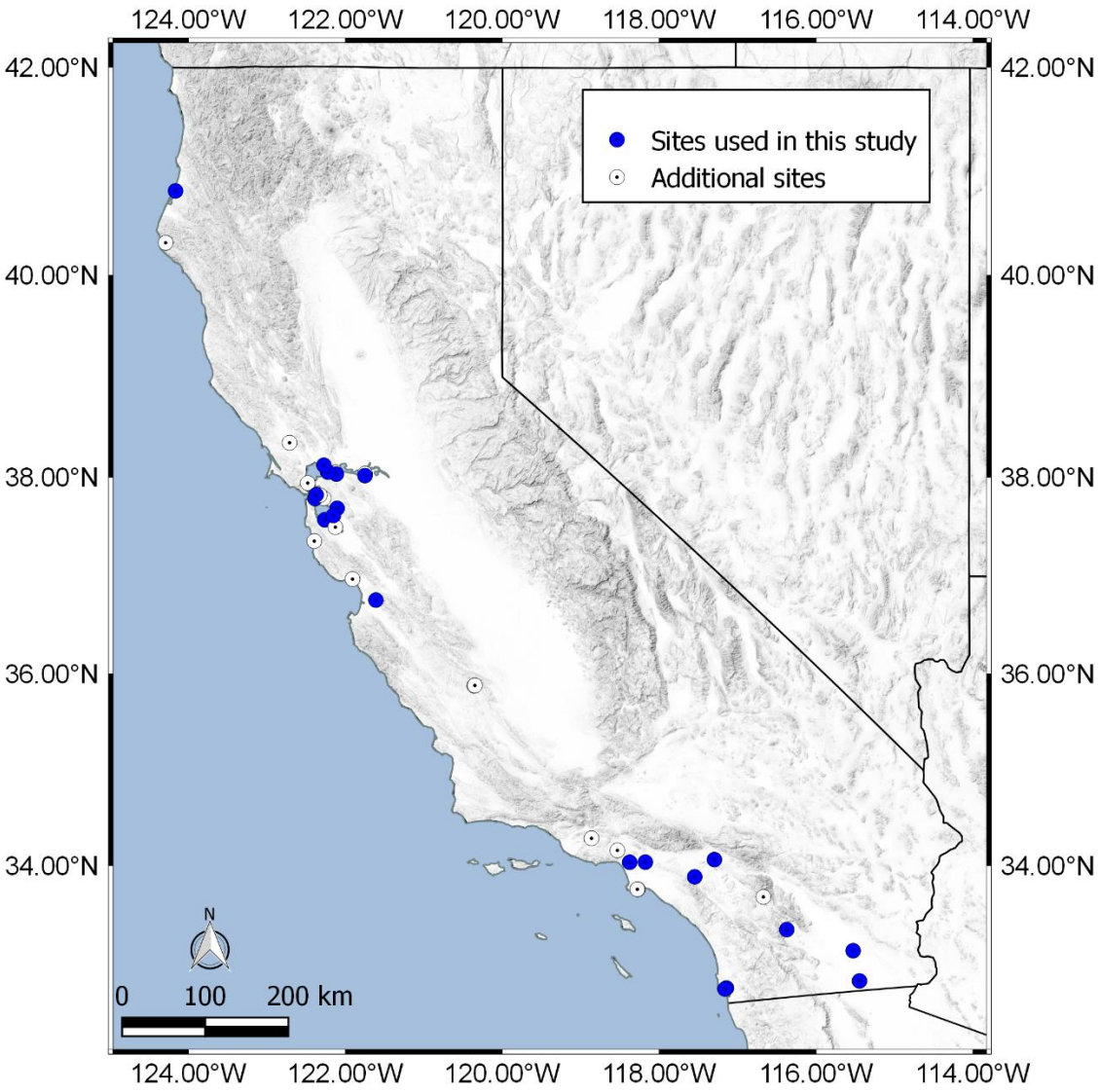

Figure 3.1. The location of vertical array sites in California (The sites used in this study are shown in blue)

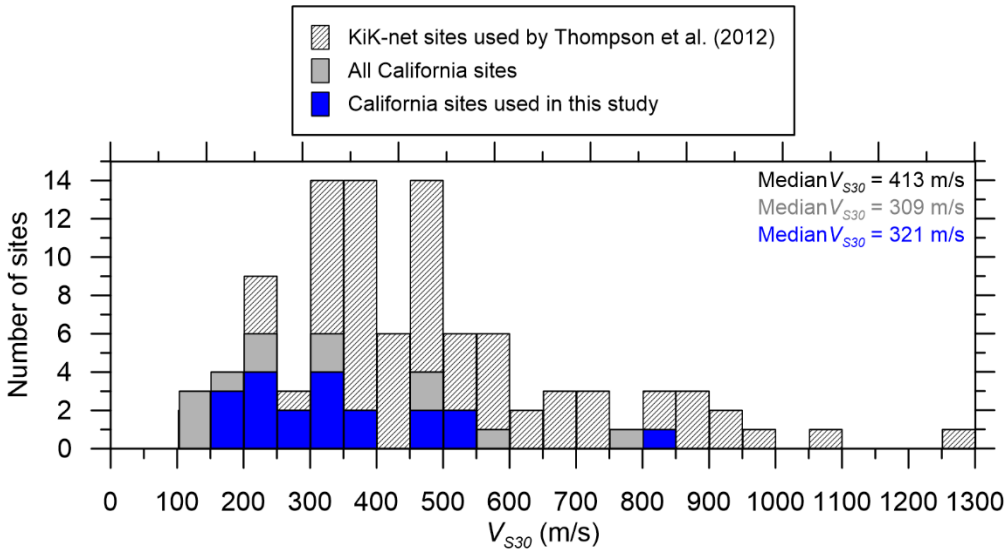

Figure 3.2. Histograms of V_{S30} for vertical array sites from Table 3.1, vertical array sites selected to be used in this study, and vertical arrays from KiK-net used by Thompson et al. (2012).

Table 3.1. Summary of site characteristics for California vertical arrays. Sites considered in present work are bolded

Site	Station NO (CSMIP)	Owner	No. of Rec	Latitude	Longitude	Site geology	V_{S30} (m/s)	$R_V = \frac{V_{SDH}}{V_{S5}}$	V_S profile available ?	Boring log available?	Source of boring log
Alameda - Posey & Webster	58137	CGS - CSMIP	7	37.790	-122.277	Deep alluvium	208 (inferred)	NA	N	Y	Caltrans[1]
Antioch-San Joaquin N	67265	CGS	4	38.0377	-121.7515	Deep Alluvium	Problematic Measurements	NA	top 20 m missing	N	NA
Antioch-San Joaquin S	**67266**	**CGS**	**4**	**38.018**	**-121.752**	**Deep Alluvium**	**253**	**3.76**	**Y**	**Y**	**Caltrans**
Aptos - Seacliff Bluff	47750	CGS - CSMIP	4	36.972	-121.910	Alluvium	463 (profile not available)	NA	N	N	NA
Benicia North	68321	CGS - CSMIP	2	38.051	-122.128	Shallow fill over bay mud	582	Not measured	Y	Y	Caltrans
San Francisco - Bay Bridge	**58961**	**CGS - CSMIP**	**9**	**37.787**	**-122.389**	**Thin alluvium over soft rock**	**391**	**6.58**	**Y**	**N**	**NA**
Benicia-Martinez South	**68323**	**CGS - CSMIP**	**10**	**38.033**	**-122.117**	**Sediments underlain by slightly more competent rock**	**547**	**1.48**	**Y**	**Y**	**Caltrans**
Borrego Valley Digital Array	**NA**	**UCSB**	**16**	**33.322**	**-116.376**	**Shallow alluv over rock (granodiorite)**	**340**	**12.22**	**Y**	**Y**	**Jamison Steidle[2]**
Crockett-Carquinez Br #2	68259	CGS - CSMIP	4	38.055	-122.226	Shallow clay over rock (sed.)	--	NA	N	Y	Caltrans
Corona I15/Hwy 91	**13186**	**CGS - CSMIP**	**31**	**33.882**	**-117.549**	**Shallow clay over soft rock**	**321**	**16.68**	**Y**	**Y**	**Caltrans**
Coronado East	**3192**	**CGS - CSMIP**	**10**	**32.698**	**-117.145**	**Deep alluvium**	**329**	**1.89**	**Y**	**Y**	**Caltrans**
Coronado West	**3193**	**CGS - CSMIP**	**21**	**32.688**	**-117.164**	**Deep alluvium**	**214**	**4.53**	**Y**	**Y**	**Caltrans**
Half Moon Bay - Tunitas	58964	CGS - CSMIP	2	37.358	-122.398	Shallow alluv over rock (chert/greenstone)	309	Not measured	Y	Y	Caltrans

Site	Station NO (CSMIP)	Owner	No. of Rec	Latitude	Longitude	Site geology	V_{S30} (m/s)	$R_V = \frac{V_{SDH}}{V_{S5}}$	V_S profile available ?	Boring log available?	Source of boring log
Crockett-Carquinez Br #1	**68206**	**CGS - CSMIP**	**8**	**38.054**	**-122.225**	**Alluvium over soft rock (granite)**	**335**	**3.08**	**Y**	**Y**	**Caltrans**
El Centro - Meloland	**1794**	**CGS - CSMIP**	**19**	**32.774**	**-115.449**	**Alluvium over soft rock (siltstone)**	**238**	**4.45**	**Y**	**Y**	**Calibration sites[3]**
Eureka	**89734**	**CGS - CSMIP**	**14**	**40.819**	**-124.166**	**Deep alluvium**	**160**	**6.31**	**Y**	**Y**	**Caltrans**
Foster City-San Mateo	**58968**	**CGS - CSMIP**	**7**	**37.573**	**-122.264**	**Deep alluvium**	**810**	**22.40**	**Y**	**N**	**Caltrans**
Los Angeles – Vincent Thm Geo Array W1	14783	CGS - CSMIP	3	33.750	-118.275	Alluvium over crystalline rock	149	Not measured	Y	N	NA
Los Angeles – Vincent Thm Geo Array W2	14784	CGS - CSMIP	3	33.750	-118.278	Deep alluvium	149	Not measured	Y	N	NA
Los Angeles – Vincent Thos W	14786	CGS - CSMIP	2	33.750	-118.280	Deep alluvium over rock (sandstone)	149	Not measured	Y	Y	Caltrans
Moorpark - Hwy118/Arroyo Simi	24185	CGS - CSMIP	1	34.288	-118.865	Deep alluvium	--	NA	N	Y	Caltrans
Oakland – Bay Bridge	58204	CGS - CSMIP	3	37.821	-122.327	Deep alluvium	--	Not measured	top 20 m missing	N	NA
Palo Alto – Dumbarton Br W	58526	CGS	1	37.499	-122.129	Deep alluvium	--	Not measured	missing in website	Y	Caltrans
Parkfield – Turkey Flat #1	36529	CGS - CSMIP	1	35.878	-120.359	Shallow alluvium rock (sandstone)	907	Not measured	Y	N	NA
Parkfield – Turkey Flat #2	36520	CGS - CSMIP	0	35.882	-120.351	Alluvium (fill)	467	Not measured	Y	N	NA
Petrolia - Downhole [abandoned]	89289	CGS - CSMIP	1	40.317	-124.292	Deep alluvium	--	NA	N	N	NA
Rohnert Park - Hwy 101	68797	CGS - CSMIP	2	38.347	-122.713	Rock (sandstone)	223	Not measured	Y	N	NA

Site	Station NO (CSMIP)	Owner	No. of Rec	Latitude	Longitude	Site geology	V_{S30} (m/s)	$R_V = \frac{V_{SDH}}{V_{S5}}$	V_S profile available ?	Boring log available?	Source of boring log
Garner Valley	**NA**	**UCSB**	**10**	**33.669**	**-116.674**	**Shallow alluvium over rock (sandstone)**	**241**	**14.08**	**Y**	**Y**	**NEES @ UCSB Website[4]**
Hayward-580W	**58487**	**CGS**	**5**	**37.689**	**-122.107**	**Shallow alluvium over rock (greywacke)**	**489**	**0.94**	**Y**	**N**	**NA**
Hayward-San Mateo	**58798**	**CGS**	**5**	**37.617**	**-122.154**	**Alluvium**	**185**	**3.10**	**Y**	**N**	**NA**
Hollister Digital Array	**NA**	**UCSB**	**23**	**36.758**	**-121.613**	**Deep alluvium**	**385**	**10.36**	**Y**	**Y**	**Jamison Steidle**
San Rafael – Richmond Brdg	58267	CGS	1	37.943	-122.481	Shallow alluvium over soft rock (sandst)	921	Not measured	Y	N	NA
Tarzana – Cedar Hill B	24764	CGS - CSMIP	4	34.161	-118.535	Thin fill/alluv over soft rock (sandst)	302	NA	N	N	NA
La-Cienega	**24703**	**CGS - CSMIP**	**20**	**34.036**	**-118.378**	**Fill over shallow alluv over soft rock**	**242**	**3.62**	**Y**	**Y**	**Calibration sites**
Obregon Park	**24400**	**CGS - CSMIP**	**23**	**34.037**	**-118.178**	**Thin Alluvium over weathered rock (Franciscan)**	**452**	**1.28**	**Y**	**Y**	**Calibration sites**
San Bernardino	**23792**	**CGS - CSMIP**	**5**	**34.064**	**-117.298**	**Thin alluvium over shale**	**252**	**4.85**	**Y**	**Y**	**Caltrans**
Treasure Island	**58642**	**CGS - CSMIP**	**11**	**37.825**	**-122.374**	**Shallow fill over deep alluvium (Bay mud)**	**157**	**16.00**	**Y**	**Y**	**Caltrans**
Vallejo - Hwy 37/Napa River	**68310**	**CGS - CSMIP**	**17**	**38.122**	**-122.275**	**Bay mud**	**528**	**1.54**	**Y**	**Y**	**Caltrans**
Wildlife Liquefaction Array	**NA**	**UCSB**	**21**	**33.097**	**-115.530**	**Silty clay with a granular layer**	**200**	**1.44**	**Y**	**Y**	**NEES @ UCSB Website**

[1] Caltrans: California Department of Transportation (Javier V. Ortiz, personal communication).
[2] Jamison Steidle: Personal communication with Jamison Steidle of UCSB.

[3] Calibration sites: Calibration sites for validation of nonlinear geotechnical models project (http://www.seas.ucla.edu/~jstewart/CalibrationSites/Webpage/main.htm).

[4] NEES @ UCSB Website: http://nees.ucsb.edu/

The sites as shown in Figure 3.1 are primarily located in the San Francisco Bay Area in northern California, and the Los Angeles, San Diego, and Imperial Valley regions of southern California. Due to the diverse geological conditions at the sites, the vertical arrays selected for this study cover site classes from rock (NEHRP class B) to soft soil (NEHRP class E). There are also differences in the stiffness of the soil/rock at the depth of the downhole instrument, as well as difference in the relative change in the stiffness between surface and downhole. In order to quantify the latter conditions, I define a surface/downhole shear wave velocity ratio (R_V) as the ratio of the time-averaged V_S at the top 5 meters (V_{S5}) to the time-averaged V_S at the 5 meter interval below the downhole instrument (V_{SDH}):

$$R_V = \frac{V_{SDH}}{V_{S5}} \tag{3.1}$$

A high value of R_V indicates a large change of stiffness from downhole to surface, which is indicative of either a steep gradient in the V_S profile and/or a large impedance contrast, either of which causes large ground response. Low values of R_V (close to 1) indicate a small gradient and lack of impedance contrast, which in turn should produce little amplification. Small R_V values tend to occur when the downhole instrument in a vertical array is within the sediment stack and not within underlying bedrock materials, which is typical of arrays in deep basins (e.g., Los Angeles, Imperial Valley). A histogram of R_V values is shown in Figure 3.3, and the spatial distribution of R_V is shown in Figure 3.4.

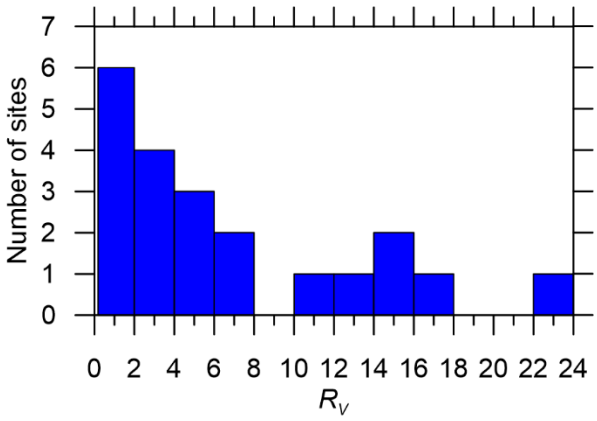

Figure 3.3. Histograms of R_V for vertical array sites used in this study.

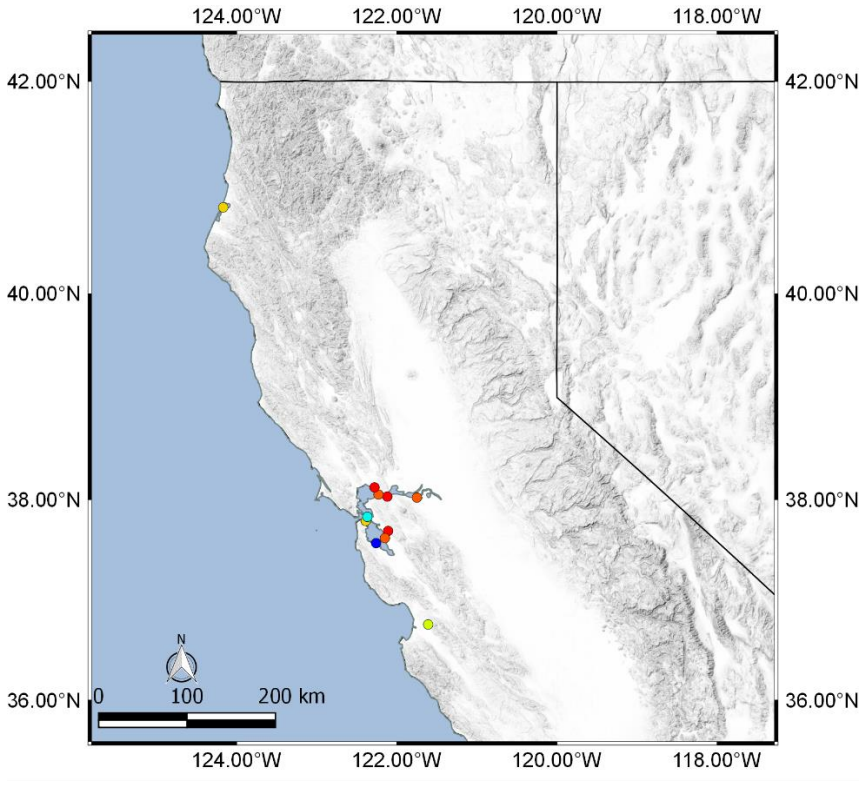

a)

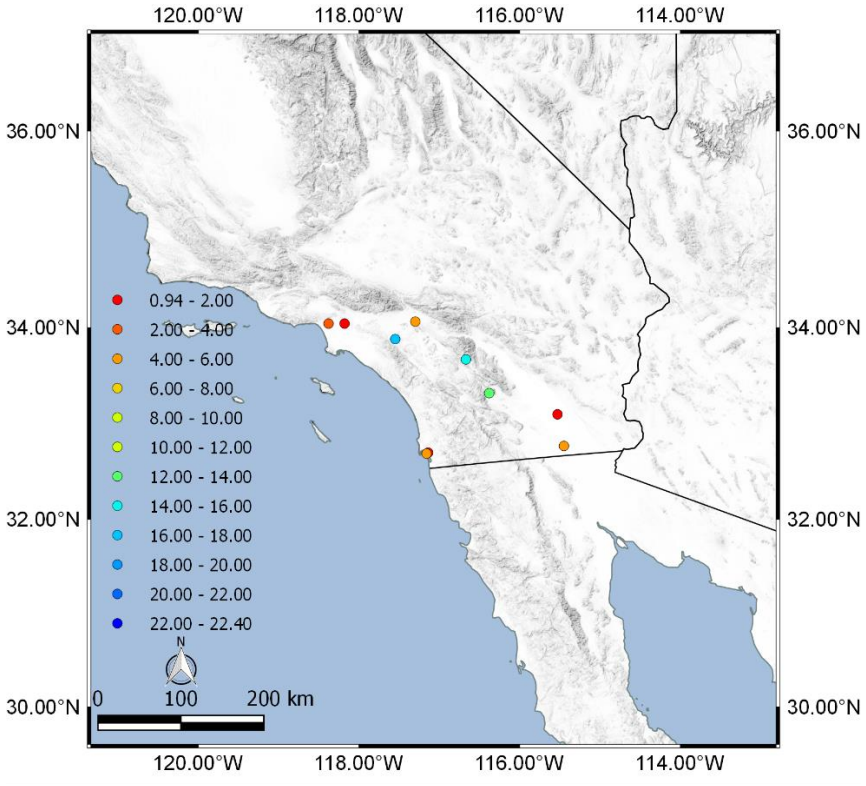

b)

Figure 3.4. The location of vertical array sites in California used for this study in (a) northern California and (b) southern California (Red: Low values of R_V, blue: High values of R_V).

3.3 DATA ATTRIBUTES

In this section, I describe a dataset of 287 surface/downhole processed recording pairs from 207 events. The times of the events have been extracted from the unprocessed data files, and the characteristics of the events (magnitude and epicenter location) are found on a USGS website (https://earthquake.usgs.gov/earthquakes/search/). Event magnitudes vary from small (**M**2.5) to large (**M**7.2 El Mayor Cucapah earthquake). Epicenter locations are shown in Figure 3.5 with circle diameters proportional to magnitude. Also shown in Figure 3.5 are station locations.

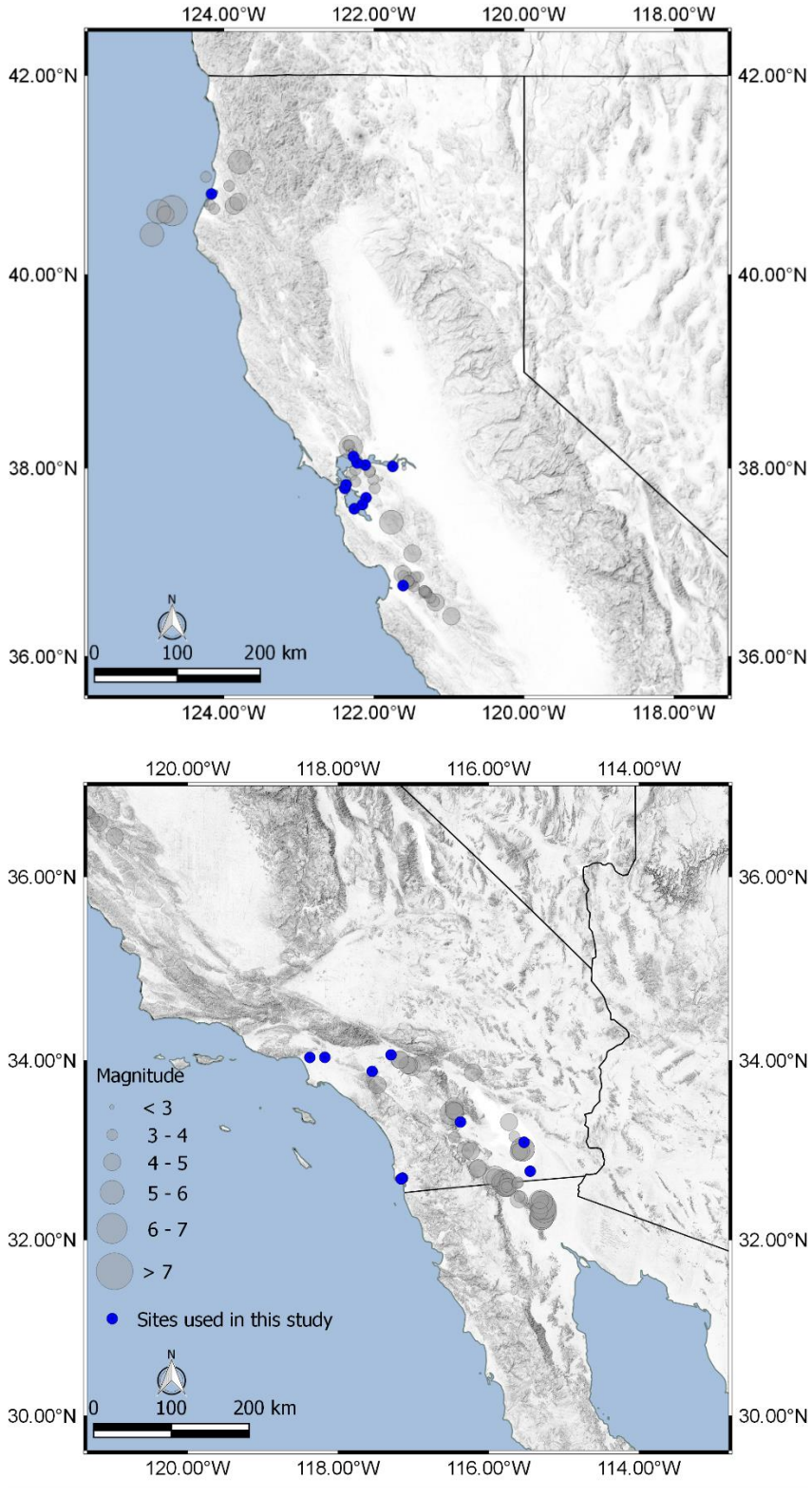

Figure 3.5. The location of vertical array sites in California used for this study in (a) Northern California and (b) Southern California (Red: Low values of R_V, blue: High values of R_V).

3.3.1 Available recordings

The 287 surface/downhole recording pairs used in this study include two horizontal components recorded at the surface and two horizontal components recorded downhole (total of four individual recordings). The vertical array sites often have instruments at multiple levels to record ground motions at different depths. In the case of multiple downhole instruments, we have chosen the deepest level in order to capture the effects of site response over a longest path for upcoming shear waves, therefore the recordings at the intermediate depths were not processed for inclusion in this database. Figure 3.6 shows the distribution of the data with respect to magnitude and epicenteral distance, with the plot symbol size being proportional to the RotD50 peak ground velocity (*PGV*) at the surface. I choose (*PGV*) because it can be related to maximum shear strain in the profile caused by the ground motions (Kim et al., 2016).

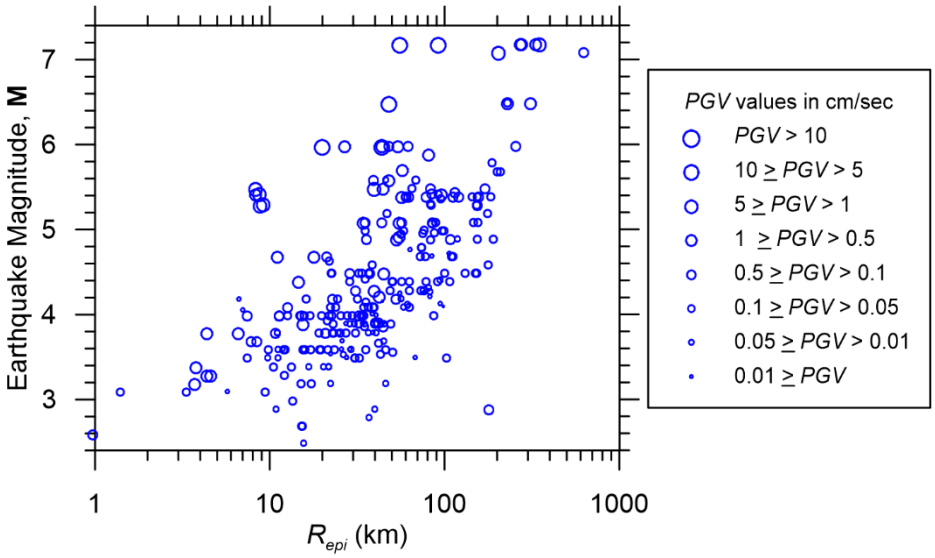

Figure 3.6. Magnitude and distance distribution of data used in the current work; the size of the symbols represent the *PGV* of the surface recording.

3.3.2 Data processing

Unprocessed records for the sites identified in the previous section were downloaded from CESMD and the nees.ucsb websites. Acceleration time series were visually inspected to identify and exclude low-quality, noise-dominated records. The data were processed using procedures developed in the NGA-West2 research project (Ancheta et al., 2014) and coded into an R routine (T. Kishida, *personal communication*, 2015). Low-cut and high-cut corner frequencies have been identified for each record by visual inspection, and low- and high-pass acausal Butterworth filters are used for filtering high and low frequency noise in the frequency domain. Baseline correction is also applied as needed.

Figure 3.7 shows an example of a record processed using these procedures, including time series (acceleration, velocity, displacement for processed record) and Fourier amplitude spectra and pseudo-acceleration response spectra at 5% damping for the unprocessed and processed versions of the record. Based on the records I have been able to access and process thus far, the usable database currently includes 21 sites and 288 record pairs. Figure 3.8 shows the number of usable records as a function of period; the decrease as period increases is due to application of low-cut corner frequencies in the record processing. The longest usable period is taken as $(0.877/f_c)$, where f_c is the low-cut corner frequency selected in record processing.

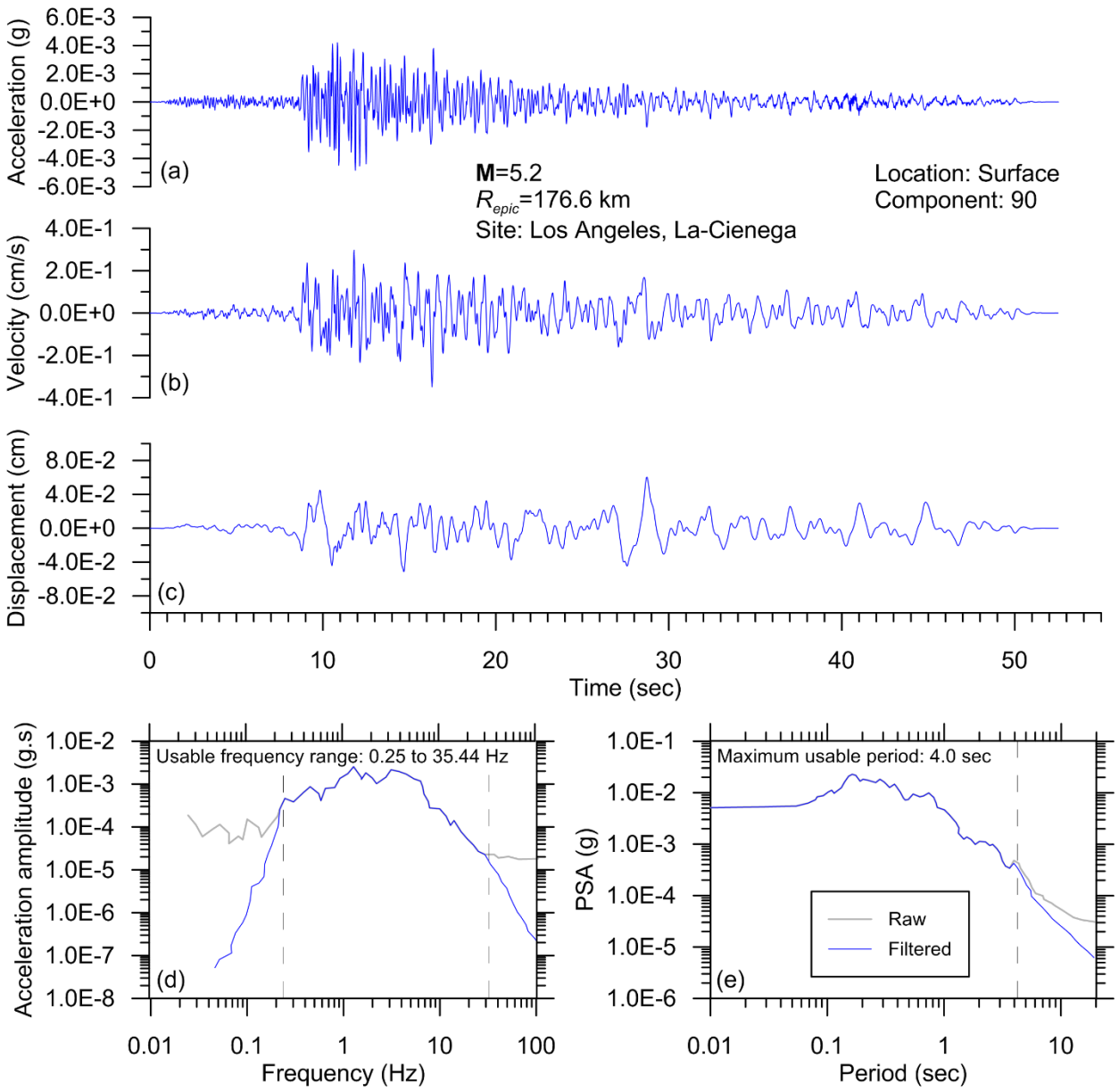

Figure 3.7. Example of record processed using PEER protocols developed in NGA-West2 project (Ancheta et al., 2014), including (a) acceleration time series, (b) velocity time series, (c) displacement time series, as well as (d) Fourier amplitude spectra and (e) pseudo-acceleration response spectra (*PSA*) at 5% damping for raw and filtered records.

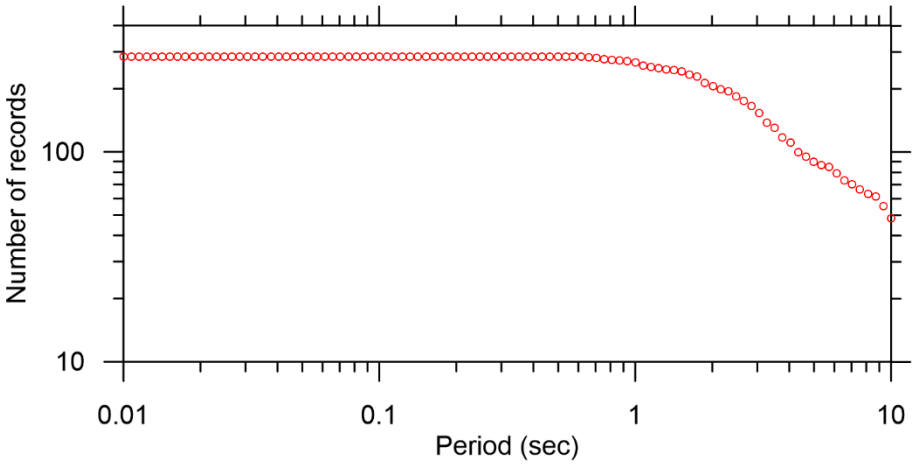

Figure 3.8. Number of available record pairs in the database according to their longest usable periods.

4 Effectiveness of 1D Ground Response Analysis at Predicting Site Response at California Vertical Array Sites

4.1 INTRODUCTION

Evaluating the role of local site conditions on ground shaking is an essential part of earthquake ground motion prediction, which can be done using ergodic models or site-specific (non-ergodic) analyses. One-dimensional (1D) simulation of shear waves propagating vertically through shallow soil layers, also known as ground response analysis (GRA), is a common approach for capturing the effects of site response on ground shaking. In GRA, different approaches have been used for modeling soil behavior, namely linear, equivalent-linear (EL), and various nonlinear (NL) methods. Much attention has been directed in recent research to which of these approaches is best suited to a particular problem, with the intention of guiding the selection of an appropriate method of analysis (e.g., choosing when NL is preferred to EL) (e.g., Kim et al., 2015; Kaklamanos et al, 2013, 2015; Zalachoris and Rathje, 2015). However, a crucial issue that has received much less attention is the degree to which 1D simulations (the essential assumption behind all GRA methods) are effective. While site response can include important contributions from the wave propagation mechanics simulated in GRA, site response as a whole is considerably more complex. True site response represents the difference between ground motions for a given site condition and what would have occurred had the site had a reference condition (typically rock with a particular

V_{S30}). Aside from ground response, processes that can affect site response include surface waves, basin effects (including focusing and basin edge-generated surface waves), and topographic effects. Because GRA only simulates a portion of the physics controlling site response, there should be no surprise that it is not always effective at accurately predicting site effects.

When GRA are performed for engineering projects, it is usually with the expectation that they provide an unbiased, site-specific estimate of site response. The site response computed in this manner can be interpreted in the form of a site-specific amplification function, which in turn can be implemented in probabilistic seismic hazard analysis (PSHA) (e.g., Chapter 2 and references therein). If the ground response computed in this manner accurately reflects the primary physical mechanisms controlling site response, it provides the basis for a non-ergodic hazard analysis, which has appreciable benefits with regard to standard deviation and hazard reduction, as discussed in Chapter 2. The essential question in this process is whether GRA is indeed effective at predicting site response? While numerous studies of data from vertical arrays at individual sites have found reasonably good fits of data to GRA results (e.g., Borja et al., 1999; Elgamal et al., 2001; Lee et al., 2006; Tsai and Hashash, 2009; Yee et al., 2013; Kaklamanos et al., 2014, 2015), another study that systematically examined a broad set of KiK-net vertical array sites found misfits for about 80% of the investigated sites (Thompson et al. 2012). In this Chapter, I use California vertical array data in order to further examine this issue. As described in Chapter 3, the geologic conditions and seismic velocities represented at the California vertical array sites differ from those at Japanese KiK-net sites, so some differences in the effectiveness of GRA might be expected.

Validation and testing of 1D GRA is possible by studying recordings from vertical array sites. The KiK-net array in Japan provides a large inventory of vertical arrays that has been extensively used for validation purposes (Thompson et al., 2012; Kaklamanos et al, 2013, 2015;

Zalachoris and Rathje, 2015). When viewed as a whole, these KiK-net data challenge the notion that 1D GRA provides a reliable estimate of site response. Were this result found to be widely applicable, it would upend a good deal of current practice that relies on GRA to estimate first-order site response. The objective of this study is to utilize the growing body of vertical array data from California to investigate applicability of 1D GRA to predict observed site response. In short, I seek to answer the question – are the poor matches of 1D GRA from the KiK-net array a product of predominant geological conditions at sites in that array, which may be different from conditions in California, hence limiting the applicability of those results in California? I also seek to quantify uncertainty in the prediction of site response as estimated from GRA. This is of interest for PSHA in which site terms are taken from the results of GRA, in which case epistemic uncertainties in the site response should be considered using a logic tree (or similar) framework (Bommer et al. 2005). I present a methodology for quantifying these uncertainties, present results as derived from the California data, and compare to comparable results obtained previously for KiK-net sites (Kaklamanos et al., 2013).

The data from California used for this work is presented in Chapter 3, and is not discussed further here. This chapter is organized as follows. First, I describe how the ground response analyses were performed, including the selected analysis platform and the manner by which small-strain hysteretic damping was assigned. Next, I compare observed and predicted transfer functions, which are amplitudes of surface/downhole Fourier spectra. I consider several metrics regarding fit of observation to data, and contrast our approach with that used previously (Thompson et al. 2012). I then perform similar comparisons of observation to prediction using 5% damped pseudo spectral acceleration (*PSA*), which also facilitates the aforementioned uncertainty quantification exercise.

4.2 GROUND RESPONSE ANALYSIS PROCEDURES

4.2.1 Ground Response Analysis Platform

There are many options for performing 1D GRA as explained in chapter 1. Studies in the literature have used different programs for GRA depending on the level of nonlinearity that is expected in the profile (as discussed in Chapter 1) and capability of each code to perform Linear (more specifically, visco-elastic), Equivalent-Linear (EL), or Nonlinear (NL) analysis. As one example, Thompson et al. (2012) used the program NRATTLE, which is a part of the ground motion simulation program SMSIM (Boore, 2005). NRATTLE performs linear GRA using NRATTLE is Thomson–Haskell matrix. Kaklamanos et al. (2013) used NRATTLE for linear and SHAKE for EL GRA, and Kaklamanos et al. (2015) used SHAKE for EL and DEEPSOIL for NL analysis to compare the effectiveness of different methods for site response problems involving different levels of nonlinearity. In a similar study, Zalachoris and Rathje (2015) used STRATA for EL and DEEPSOIL for NL analysis.

In this study, I model the soil as linearly visco-elastic because almost all of the recordings compiled in our database are not strong enough to cause soil nonlinearity, as discussed further below. Therefore, I only perform linear analysis similar to Thompson et al. (2012) in order to validate GRA under small levels of ground shaking. I have chosen to use the Linear option in Frequency Domain Analysis module in DEEPSOIL for linear analysis. I acknowledge there are several other GRA programs which are capable of performing linear GRA, including NRATTLE, SHAKE, and STRATA. All of these programs are freely available and were tried at some point by the author (with exception of SHAKE). I selected DEEPSOIL in consideration of its user-friendliness. For parameter selection in GRA, I apply protocols recommended by Stewart at al.

(2014), with the exception of small strain damping (D_{min}). The issue of D_{min} is discussed in Sections 4.2.2-4.2.3.

Methods of analysis for EL and NL are familiar to geotechnical engineers and are well documented elsewhere (e.g., NCHRP, 2012; Stewart et al. 2014). Hence, I do not describe such methods here. I next describe quarter-wavelength theory, because this approach is less familiar to engineers (although it is well documented, Joyner et al. 1981, Boore, 2013).

The most simple and efficient approach for evaluating linear GRA is quarter wave length theory. This theory is based on a simple equation for evaluating amplification of Fourier Amplitude Spectra for a vertical ray path:

$$A_0(f) = \left(\frac{\rho_R V_R}{\bar{\rho}\bar{V}} \right)^{0.5} \tag{4.1}$$

where A_0 is the amplification, ρ_R and V_R are density and shear wave velocity at the reference (downhole condition), and $\bar{\rho}$ and $\bar{V}$ are average density and shear wave velocity for a depth interval corresponding to the top quarter wavelength of the profile. While this method is simple and efficient, it cannot capture the effects of resonance and nonlinearity. Moreover, in the form represented by Eq. (4.1), it does not include the effects of damping, which is evident by the amplification value at high frequencies approaching a plateau of unrealistic large values as shown in Figure 4.1.

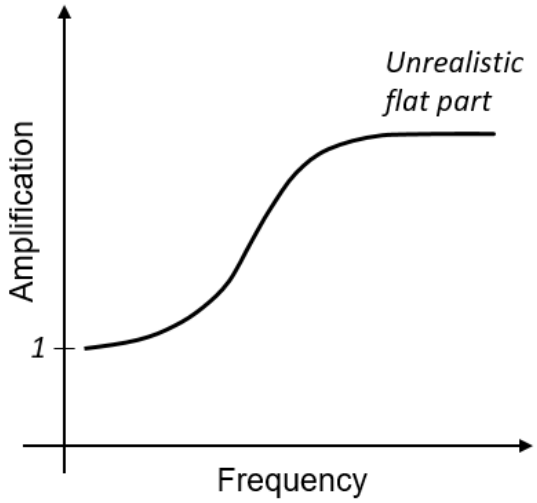

Figure 4.1. Unrealistic plateau of amplification at high frequencies when using quarter wave length theory without proper use of κ.

In order to overcome this problem, a spectral decay parameter (κ) is used in order to introduce a decay in FAS space, which reduces the amplification function at high frequencies (Anderson and Hough, 1984). The application of κ is schematically shown in Figure 4.2, and will modify the amplification as:

$$A(f) = A_0(f) \times \exp(-\pi \kappa f) \tag{4.2}$$

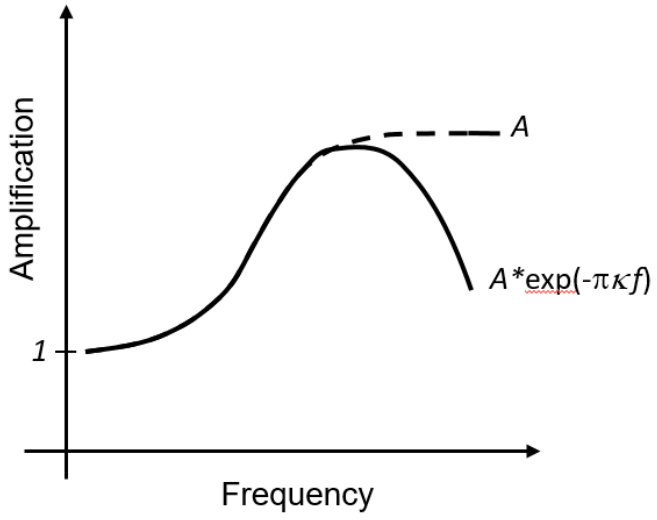

Figure 4.2. Modifying amplification from quarter wave length theory at high frequencies by introducing κ.

I do not intend to use quarter wave length theory for GRA, however I will use κ for estimating small strain damping, as described further below.

4.2.2 Small Strain Damping from Models

I consider two classes of models for small strain hysteretic damping in soils. The first class of models are collectively referred to as geotechnical models, because they are derived from advanced cyclic testing performed in geotechnical labs. The second are V_S-based models originally developed for stochastic ground motion simulations in central and eastern North America.

The geotechnical models relate small-strain damping as measured from geotechnical laboratory cyclic testing, denoted $D_{\min}^{L}$, to various predictor variables related to soil type and confining pressure. I estimate laboratory-based $D_{\min}^{L}$ using Darendeli (2001) relations for clays and silts, and Menq (2003) relations for granular soils. The input parameters for the $D_{\min}^{L}$ models are plasticity index (*PI*), overconsolidation ratio (*OCR*), and effective stress for Darendeli (2001), and mean grain size (D_{50}), coefficient of uniformity (C_u), and effective stress for Menq (2003). The $D_{\min}^{L}$ relations can only be used when geotechnical log and/or description of soil conditions are available for the site.

The second class of models for D_{min} draw from the seismology literature. Seismological simulations often convolve ground motions derived from source and path models, which apply for a reference rock site condition, with a site amplification function derived from an assumed (or measured) soil column V_S profile. The site amplification function is typically derived using quarter wavelength procedures (Sec. 4.2.1) that evaluate impedance effects from the V_S profile (Eq. 4.1)

and damping effects from the κ_0 diminutive parameter (Eq. 4.2). The κ_0 parameter represents the cumulative effect of damping through the soil column, which is commonly represented by (Hough and Anderson 1988; Chapman et al. 2003; Campbell 2009):

$$\kappa_0 = \int_0^z \frac{dz}{Q_{ef}(z)V_S(z)} \tag{4.3}$$

where z is the soil column depth and Q_{ef} is the depth-dependent effective material quality factor, representing both the effects of frequency-dependent wave scattering and frequency-independent soil damping. Quantity Q_{ef} can be readily converted to soil damping as follows (Campbell, 2009):

$$D_{\min}(\%) = \frac{100}{2Q_{\text{ef}}} \tag{4.4}$$

In order to facilitate ground motion prediction in central and eastern U.S., several investigators have developed models for either depth-dependent Q_{ef} or κ_0 in particular regions (e.g., Boore and Joyner 1991, Gomberg et al. 2003, Cramer et al. 2004). Campbell (2009) reviewed many of these studies and proposed a suite of models relating Q_{ef} to V_S, one of which is given by

$$Q_{\text{ef}} = 7.17 + 0.0276V_S \tag{4.5}$$

Eq. (4.2) is one of four models proposed by Campbell (2009) and has seen application in a number of subsequent studies (Hashash et al., 2014; E. Rathje, personal communication) (more so than the other three models). I choose to use this model over an older model by Olsen et al. (2003) which works for long periods (>2 sec). An advantage of this approach for modeling D_{min} is that it is only based on V_S as an input parameter, and therefore it does not require a geotechnical log. I apply this approach for all 21 sites used in this study.

4.2.3 Kappa-Informed Small Strain Damping

The use of site diminutive parameter κ in ground response prediction was introduced in Section 4.2.1. Here I describe in more detail conceptual background information for this parameter and how it can be used for sites with ground motion recordings to adjust values of small-strain damping derived from models like those in Section 4.2.2 to represent site-specific effects. Whether such adjustments are effective for ground motion prediction is investigated in Section 4.4.1.

As it was shown in Eq. (4.2), κ is the controlling spectral decay parameter for amplification of Fourier Amplitude Spectra. The value of κ applicable to a particular ground motion recording can be partitioned into two components, namely a zero distance κ or site κ (κ_0), and the attenuation with distance ($\kappa_R R$) (adapted from Anderson, 1991):

$$\kappa = \kappa_0 + \kappa_R R \tag{4.6}$$

where R is the source-site distance, and κ_R is the slope by which the decay parameter (κ) increases with distance capturing the effects of anelastic attenuation. Adopting notation from Hough and Anderson (1988), the site damping parameter κ_0 can be taken as (Campbell, 2009):

$$\kappa_0 = \kappa_{0,ref} + \int_0^z Q_{ef}(z)^{-1} V_S(z)^{-1} dz \tag{4.7}$$

where $\kappa_{0,ref}$ is the attenuation parameter for the bedrock and the integral represents the contribution from the soil column (Eq. 4.3). Note that $\kappa_{0,ref}$ as used in simulations may not match the site condition at the downhole sensor. However, for the present application, I take $\kappa_{0,ref}$ as applying for the downhole geologic condition. Adopting this definition and using Eq. (4.4) to convert Q_{ef} to D_{min}, I re-write Eq. (4.7) as:

$$\kappa_0 = \kappa_{0,ref} + \int_0^z \frac{2D_{\min}(z)}{100} V_S(z)^{-1} dz \tag{4.8}$$

The following sub-sections describe how vertical array data can be used to estimate the integral in Eq. (4.3), which in turn can be used to adjust model-based D_{min} to reflect site-specific conditions.

4.2.3.1 Inference of profile contribution to κ_0 from vertical array data

Using recordings from vertical arrays, κ_0 and $\kappa_{0,ref}$ cannot be measured directly because the source-site distance component ($\kappa_R R$) still exists in κ measured from the surface and downhole recordings. However, if I take the distance component ($\kappa_R R$) as identical for the surface and downhole κ as observed for a given event, the difference ($\Delta\kappa$) in total κ becomes a profile attribute:

$$\Delta\kappa = \kappa - \kappa_{ref} = \left(\kappa_0 + \kappa_R R\right) - \left(\kappa_{0,ref} + \kappa_R R\right) = \kappa_0 - \kappa_{0,ref} \tag{4.9}$$

where κ_{ref} is the total κ for the downhole recording. Combining Eqs (4.8) and (4.9), I can relate $\Delta\kappa$ to D_{min} as:

$$\Delta\kappa = \int_0^z \frac{2D_{\min}(z)}{100} \frac{dz}{V_S(z)} \tag{4.10}$$

The conceptually simplest way to estimate $\Delta\kappa$ from vertical array recordings is to evaluate κ_{ref} and κ from the recorded Fourier amplitude spectra (FAS) of downhole and surface recordings, and take the difference (per Eq. 4.9). It is recognized that the downhole recording is a 'within' record that contains attributes of reflected waves from the ground surface, and hence is different from the outcropping condition at the surface. In other words, comparing κ and κ_{ref} may not be exactly apples-to-apples comparison. However, the differences between outcropping and within

motions are localized at site frequencies, and hence are unlikely to significantly affect the downhole κ_{ref} measurement.

I measure κ using procedures introduced by Anderson and Hough (1984), in which a line is fit to the decaying part of the FAS, as shown for example recordings in Figure 4.3. As shown in the figure, it is necessary to pick a frequency range over which the line is fit. The lower and upper limit of the fit frequency range are denoted f_1 and f_2, respectively. I adopt the criteria below for choosing the frequency range (similar to Cabas and Rodriguez-Marek, 2017). It is acknowledged that there are other approaches for measuring κ in the literature (Ktenidou et al., 2014).

- Avoid the 1st site response peak in the transfer function.
- Avoid the flat part of the high frequency ETF which is not expected to be dominated by shear waves.
- Avoid frequencies outside of the usable frequency rage chosen for filtering in the processing stage.

In order to select f_1 and f_2 values producing the most stable κ, I initially select a reasonable range for both f_1 and f_2 based on the above criteria, and then use a search module to pick the combination of f_1 and f_2 producing the least variability with azimuth for $\Delta\kappa$ (Eq. 4.9). Note that one set of f_1 and f_2 is chosen for all four components of a recording (two horizontal components each for surface and downhole). In order to compute variability with azimuth, the search module uses the two horizontal components of $\Delta\kappa$ for a range of orientations, and then computes the coefficient of variation (COV) across $\Delta\kappa$ values from all orientations. The COV is computed for every combination of f_1 and f_2 inside the introduced range, and the combination that generates the smallest COV for $\Delta\kappa$ is selected and then applied to all four components. The summary of findings on measuring $\Delta\kappa$ from surface and downhole recordings in our dataset as the difference between

κ and κ_{ref} is shown in Table 4.1. In the table, the average and limits of f_1 and f_2 chosen for κ measurements are summarized for each site.

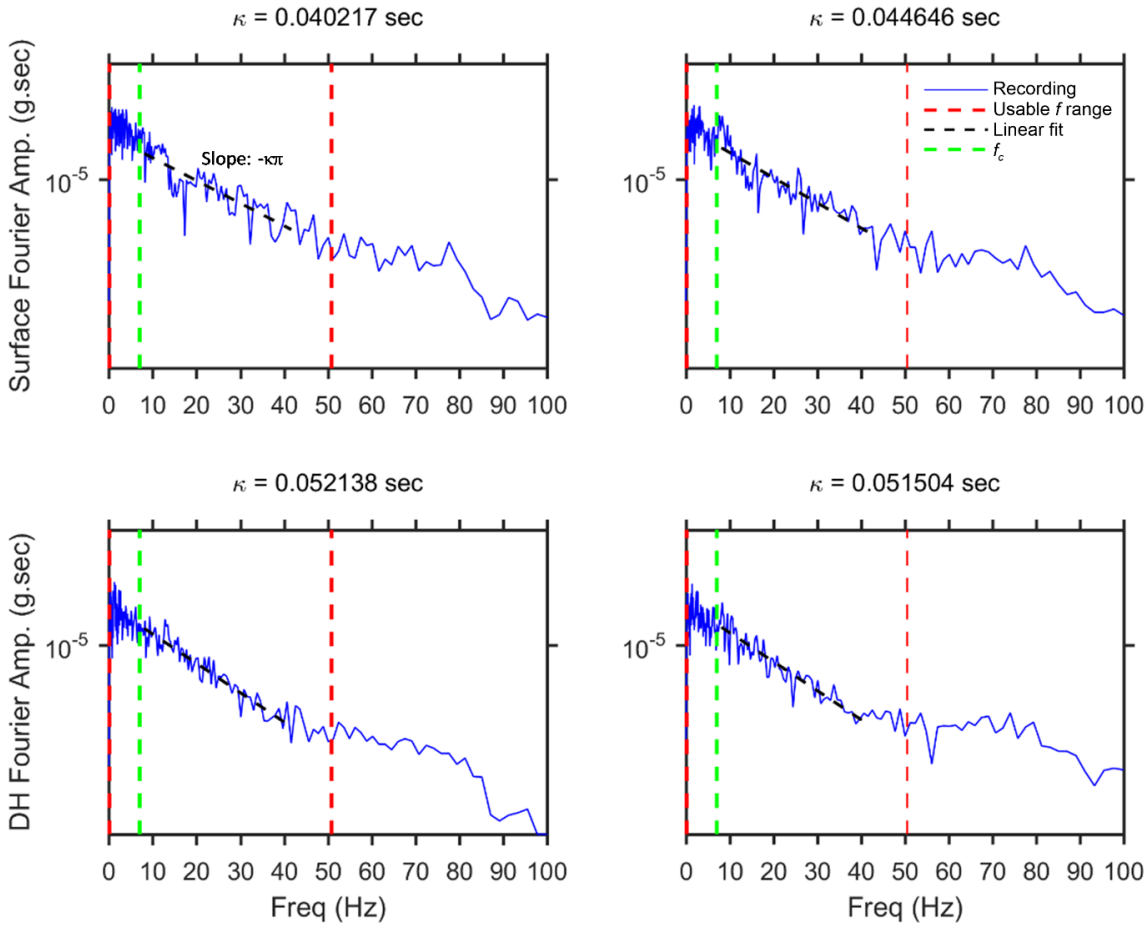

Figure 4.3. The customary approach of measuring $\Delta\kappa$ by directly fitting a line to the two components of surface (top) and downhole (bottom) FAS, where f_c is the corner frequency of the event.

Although the above approach of separately evaluating κ for surface and downhole records was applied, the measurements are somewhat 'noisy' due to sensitivities to limiting frequencies, and the differences between surface and downhole κ is often small. As a result of these issues, $\Delta\kappa$ values were negative for a surprising number of cases (35% of recordings) as shown in Table 4.1, which is clearly a spurious result. Accordingly, I considered a different approach in which $\Delta\kappa$ is evaluated directly from surface/downhole transfer functions. Because the line is fit in semi-

logarithmic space, the slope of the transfer function is the difference between the slopes of respective FAS. An advantage of this approach is that the transfer function lacks peaks and valleys due from effects other than surface-downhole site response, which allows the line to be fit over lower frequency ranges than is possible for κ measurements (Figure 4.3.). An example of $\Delta\kappa$ inference from a transfer function is shown in Figure 4.4.

I measure $\Delta\kappa$ by directly fitting a line to the ETF over a frequency range that is expected to be dominated by shear waves. The protocols for selecting that frequency range are similar to those described above (for FAS). However, in addition to those criteria, I find the surface/downhole ratio of FFT for background noise useful in order to find the frequency ranges less dominated by noise and more dominated by seismic shear waves. For this purpose, I compute the FFT ratio for the first 5 seconds of the raw recordings, which I found to comprise a pre-event time window (before seismic shaking). For the example in Figure 4.4, for frequencies above approximately 22 Hz, the FFT ratio for the noise becomes similar to the FFT ratio for the actual seismic event (ETF). Although this cannot lead to a definite conclusion that for f > ~22Hz the transfer function is dominated by noise, the visual comparison of the shape and the amplitude of spectral ratios for noise and the seismic event can be helpful for identifying frequency ranges dominated by seismic shear waves and not surface waves, which are expected to more dominate the noise spectrum.

Summary results obtained by measuring $\Delta\kappa$ in this manner are shown in Table 4.2. Summary statistics of directly measuring Δκ for the vertical array sites from transfer functions.

In this case, only two sites (less than 10%) produced negative $\Delta\kappa$. Comparing the limiting frequencies in Tables 4.1 and 4.2, the ETF-fitting approach produces lower ranges for f_1 and f_2.

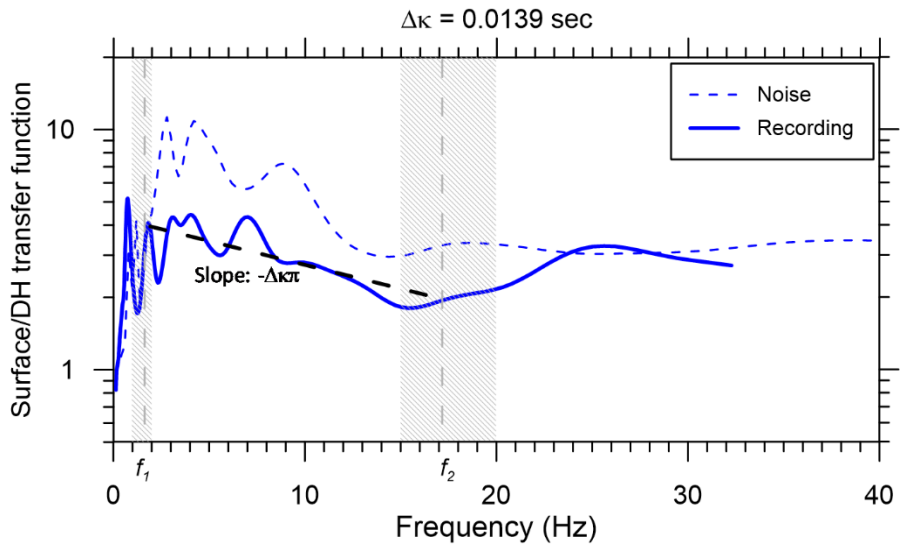

Figure 4.4. This study's approach of measuring $\Delta\kappa$ by directly fitting a line to ETF for each recording. The shaded areas show the frequency ranges used for choosing f_1 and f_2.

Table 4.1. Summary statistics of measuring $\Delta\kappa$ for the vertical array sites as the difference between κ and κ_{ref}.

Site	Station NO (CSMIP)	No. of Rec	$\overline{f_1}$ (Hz)	$\overline{f_2}$ (Hz)	f_1 range (Hz) min, max	f_2 range (Hz) min, max	$\overline{\kappa}$ (sec)	κ range (sec) min, max	$\overline{\kappa_{ref}}$ (sec)	κ_{ref} range (sec) min, max	$\overline{\Delta\kappa}$ (sec)	$\Delta\kappa$ range (sec) min, max
Antioch-San Joaquin S	67266	4	3.1	13.0	2.0, 5.0	10, 17	0.121	0.105, 0.133	0.109	0.092, 0.133	0.0119	-0.0005, 0.0213
Bay Bridge	58961	9	7.9	21.4	5.5, 10	15.3, 27.2	0.069	0.038, 0.113	0.051	0.03, 0.074	0.0184	0.0034, 0.0387
Benicia South	68323	10	8.6	28.8	6.1, 10	21.9, 44.7	0.049	0.026, 0.085	0.050	0.023, 0.104	-0.0006	-0.0183, 0.0162
Borrego Valley	NA	16	8.1	33.4	4.0, 20.9	20.0, 50.5	0.042	0.016, 0.069	0.048	0.028, 0.0616	-0.0057	-0.0147, 0.0084
Corona	13186	31	10.4	55.2	4.0, 23.7	10.0, 79.5	0.024	0.009, 0.084	0.028	0.009, 0.0987	-0.0035	-0.0354, 0.0181
Coronado East	3192	10	8.0	29.6	2.9, 16.6	23.9, 51.3	0.040	0.019, 0.055	0.048	0.025, 0.073	-0.0080	-0.0321, 0.0236
Coronado West	3193	21	6.4	23.5	3.3, 14.5	10.8, 45	0.063	0.025, 0.096	0.057	0.014, 0.094	0.0060	-0.0214, 0.0459
Crockett-1	68206	8	10.6	31.7	5.3, 14.7	21.1, 46.8	0.041	0.027, 0.052	0.056	0.024, 0.072	-0.0150	-0.0276, 0.0227
El Centro-Meloland	1794	19	10.0	31.6	5.5, 14.8	17.3, 51.3	0.049	0.013, 0.074	0.049	0.035, 0.073	0.0004	-0.0253, 0.0185
Eureka	89734	14	7.3	24.3	2.0, 9.5	15.0, 30.0	0.073	0.046, 0.093	0.045	0.026, 0.057	0.0285	0.0018, 0.0502

Site	Station NO (CSMIP)	No. of Rec	$\overline{f_1}$ (Hz)	$\overline{f_2}$ (Hz)	f_1 range (Hz) min, max	f_2 range (Hz) min, max	$\overline{\kappa}$ (sec)	κ range (sec) min, max	$\overline{\kappa_{ref}}$ (sec)	κ_{ref} range (sec) min, max	$\overline{\Delta\kappa}$ (sec)	$\Delta\kappa$ range (sec) min, max
Foster City	58968	7	7.2	25.7	3.0, 12.0	13.2, 42.6	0.034	0.008, 0.069	0.052	0.003, 0.114	-0.0173	-0.0445, 0.0043
Garner Valley	NA	10	12.6	53.4	7.1, 19.5	42.6, 70.0	0.028	0.018, 0.046	0.011	0.001, 0.030	0.0178	0.0146, 0.0223
Hayward-580W	58487	5	11.9	44.4	5.8, 26.8	25.0, 63.2	0.042	0.015, 0.084	0.038	0.018, 0.065	0.0040	-0.0120, 0.0185
Hayward-San Mateo	58798	5	8.0	22.1	6.9, 9.7	18.0, 32.4	0.051	0.024, 0.079	0.043	0.002, 0.073	0.0080	-0.049, 0.072
Hollister digital	NA	23	10.9	28.3	5.7, 22.4	17.0, 47.9	0.060	0.013, 0.111	0.048	0.009, 0.0100	0.0122	-0.0576, 0.0554
La-Cienega	24703	20	13.0	43.6	5.0, 35.8	22.0, 80.0	0.040	0.007, 0.096	0.032	0.008, 0.084	0.0076	-0.0162, 0.0179
Obregon Park	24400	23	12.9	34.0	4.8, 19.5	16.2, 75.0	0.067	0.032, 0.118	0.046	0.019, 0.101	0.0214	0.0089, 0.0380
San Bernardino	23792	5	7.6	23.8	2.0, 11.8	12.0, 32.0	0.059	0.025, 0.130	0.060	0.031, 0.119	-0.0008	-0.0171, 0.0111
Treasure Island	58642	11	9.9	38.4	9.5, 10.0	20.0, 60.0	0.049	0.029, 0.072	0.033	0.021, 0.068	0.0157	0.0036, 0.0332
Vallejo	68310	17	12.1	31.2	5.5, 19.3	20.0, 45.0	0.053	0.035, 0.077	0.049	0.025, 0.059	0.0043	-0.0139, 0.0180
Wildlife Liquefaction	NA	21	7.4	38.1	5.0, 10.0	7.0, 63.2	0.043	0.000, 0.079	0.049	0.029, 0.066	-0.0051	-0.0665, 0.0244

Table 4.2. Summary statistics of directly measuring $\Delta\kappa$ for the vertical array sites from transfer functions.

Site	Station NO (CSMIP)	No. of Rec	$\overline{f_1}$ (Hz)	$\overline{f_2}$ (Hz)	f_1 range (Hz) min, max	f_2 range (Hz) min, max	$\overline{\Delta\kappa}$ (sec)	$\Delta\kappa$ range (sec) min, max
Antioch-San Joaquin S	67266	4	2.8	12.8	2.0, 3.0	8.0, 17.0	0.0116	-0.0014, 0.0197
Bay Bridge	58961	9	7.4	18.3	7.0, 8.0	17.0, 20.0	0.0085	-0.0023, 0.0174
Benicia South	68323	10	4.4	24.3	4.0, 5.0	17.0, 35.0	0.0044	0.0005, 0.0120
Borrego Valley	NA	16	1.5	16.3	1.0, 2.0	8.0, 20.0	0.0053	0.0003, 0.0159
Corona	13186	31	3.8	18.2	3.0, 5.0	15.0, 22.9	0.0078	-0.0223, 0.0264
Coronado East	3192	10	1.6	15.8	1.0, 2.5	10.0, 24.5	0.0133	0.0044, 0.0295
Coronado West	3193	21	2.0	14.9	1.0, 3.0	4.0, 21.9	0.0063	-0.0175, 0.0490
Crockett-1	68206	8	3.2	16.2	2.0, 5.0	6.0, 19.9	0.0016	-0.0094, 0.0154
El Centro-Meloland	1794	19	1.1	12.0	1.0, 2.0	5.0, 24.1	0.0013	-0.0053, 0.0119
Eureka	89734	14	1.4	18.1	1.0, 1.8	8.1, 19.9	0.0203	0.0115, 0.0276

Site	Station NO (CSMIP)	No. of Rec	$\overline{f_1}$ (Hz)	$\overline{f_2}$ (Hz)	f_1 range (Hz) min, max	f_2 range (Hz) min, max	$\overline{\Delta\kappa}$ (sec)	$\Delta\kappa$ range (sec) min, max
Foster City	58968	7	1.5	14.6	1.0, 2.0	6.9, 21.4	-0.0033	-0.0475, 0.0148
Garner Valley	NA	10	1.9	21.2	1.3, 3.0	12, 24.5	0.0136	-0.0185, 0.0239
Hayward-580W	58487	5	2.3	16.1	1.0, 3.0	11.8, 20.0	0.0234	0.0126, 0.0304
Hayward-San Mateo	58798	5	1.4	12.9	1.0, 2.0	4.0, 24.5	0.0330	0.0053, 0.0802
Hollister digital	NA	23	1.5	16.6	1.0, 3.0	15.0, 19.5	0.0236	0.0097, 00413
La-Cienega	24703	20	2.1	18.2	1.0, 3.0	5.0, 23.9	0.0042	-0.1216, 0.0354
Obregon Park	24400	23	2.1	23.4	1.0, 3.0	17.0, 24.5	0.0074	-0.0200, 0.0156
San Bernardino	23792	5	2.7	22.6	2.2, 3.0	20.0, 24.5	0.0000	-0.0162, 0.0168
Treasure Island	58642	11	2.6	17.8	1.0, 3.0	15.0, 20.0	0.0118	0.0040, 0.0182
Vallejo	68310	17	5.3	23.9	4.0, 6.0	15.0, 29.5	-0.0080	-0.0191, 0.0046
Wildlife Liquefaction	NA	21	1.7	16.5	1.5, 2.0	15.0, 18.7	0.0167	0.0068, 0.0309

4.2.3.2 Modifying damping profiles based on measured $\Delta\kappa$

I begin with the laboratory-based estimate of the D_{min} profile ($D^L_{\min}$) and multiply it by a constant value (F_D) at all layers. Eq. (4.10) is modified as:

$$\overline{\Delta\kappa} = \int_0^z \frac{2D^L_{\min}(z) \times F_D}{100} V_S(z)^{-1} dz \tag{4.11}$$

where $\overline{\Delta\kappa}$ is the mean $\Delta\kappa$ for all recordings at the site and F_D is the multiplicative modification factor. For sites without a geotechnical log we do not have the $D^L_{\min}$ profile – in these cases I assume $D^L_{\min}$ = 1% for use with the above procedures. This application as well as the other two approaches for estimation of damping are shown for all sites in Figure 4.5-4.25. In the figures the damping profiles are shown even if they are available for that site.

Table 4.3 summarizes for each site values of $\overline{\Delta\kappa}$ as measured from ETFs, $\Delta\kappa$ implied by the $D^L_{\min}$ profile without any modification (F_D=1), and F_D values computed using Eq. (4.11). The later two are not shown for sites without a geotechnical log.

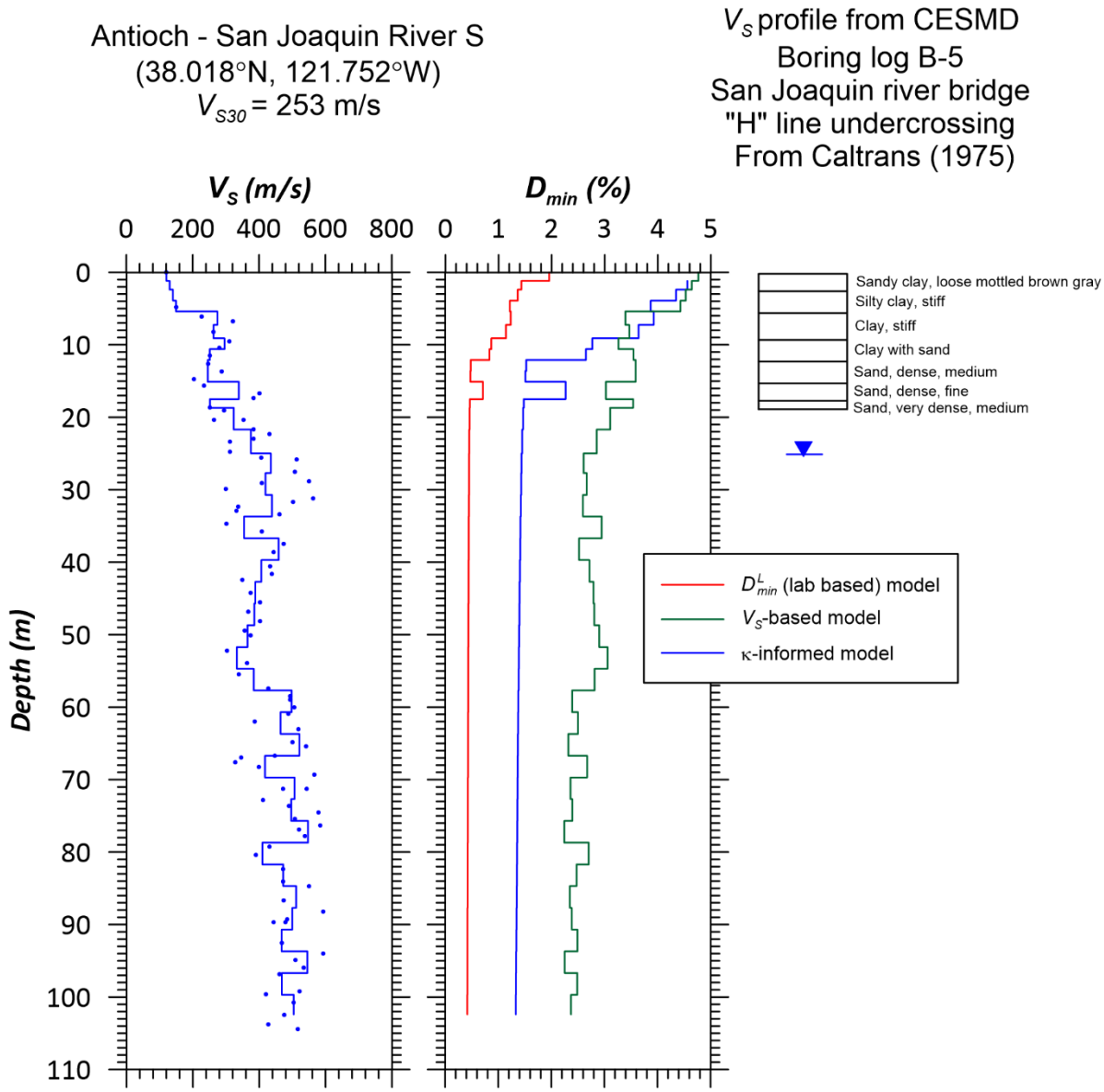

Figure 4.5. V_S profile and D_{min} profiles based on geotechnical models for laboratory damping ($D^L_{\min}$), Campbell (2009) model for Q_{ef}, and $\Delta\kappa$ for Antioch-San Joaquin site.

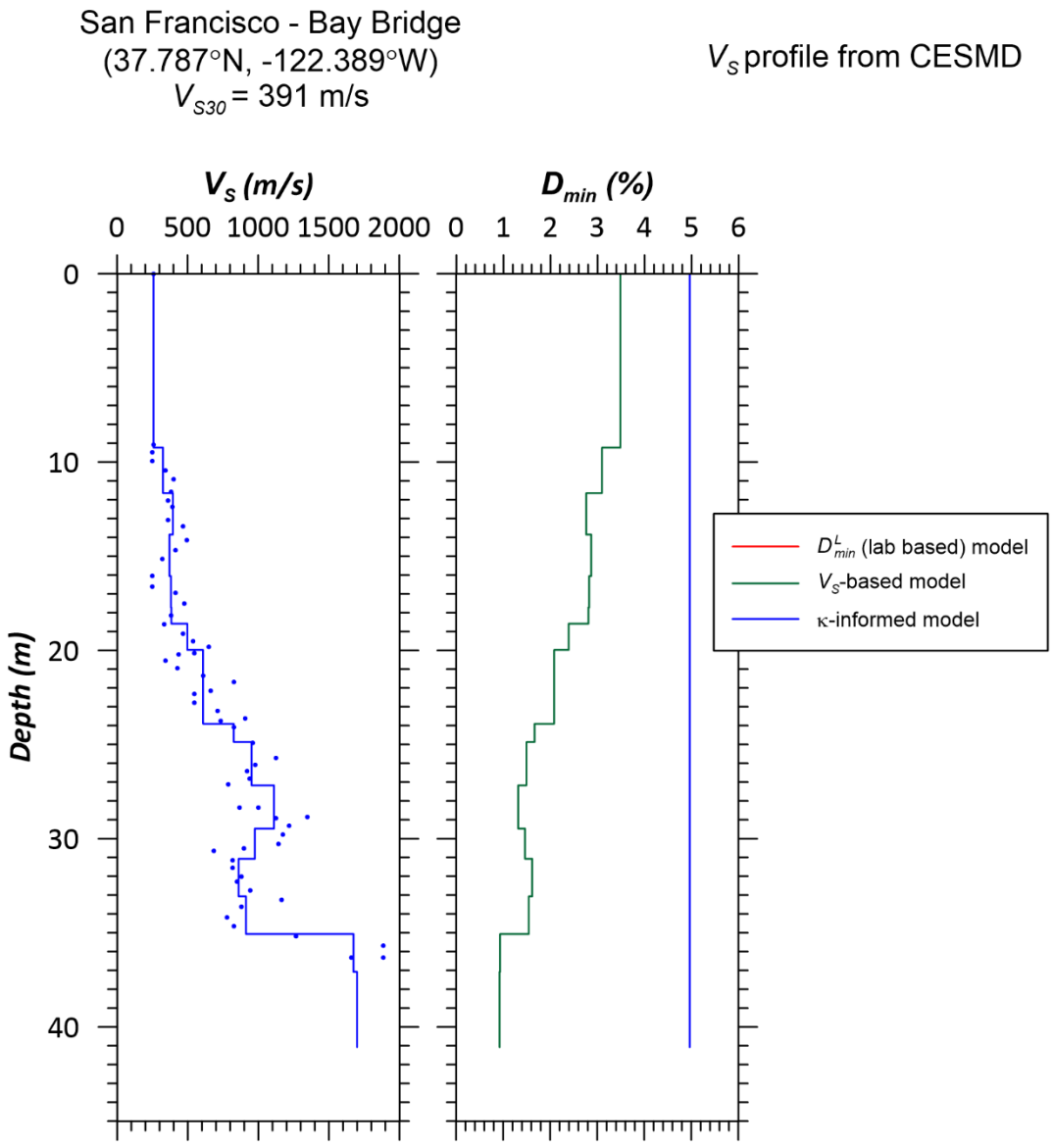

Figure 4.6. V_S profile and D_{min} profiles based on geotechnical models for laboratory damping ($D^L_{\min}$), Campbell (2009) model for Q_{ef}, and $\Delta\kappa$ for San Francisco Bay Bridge site.

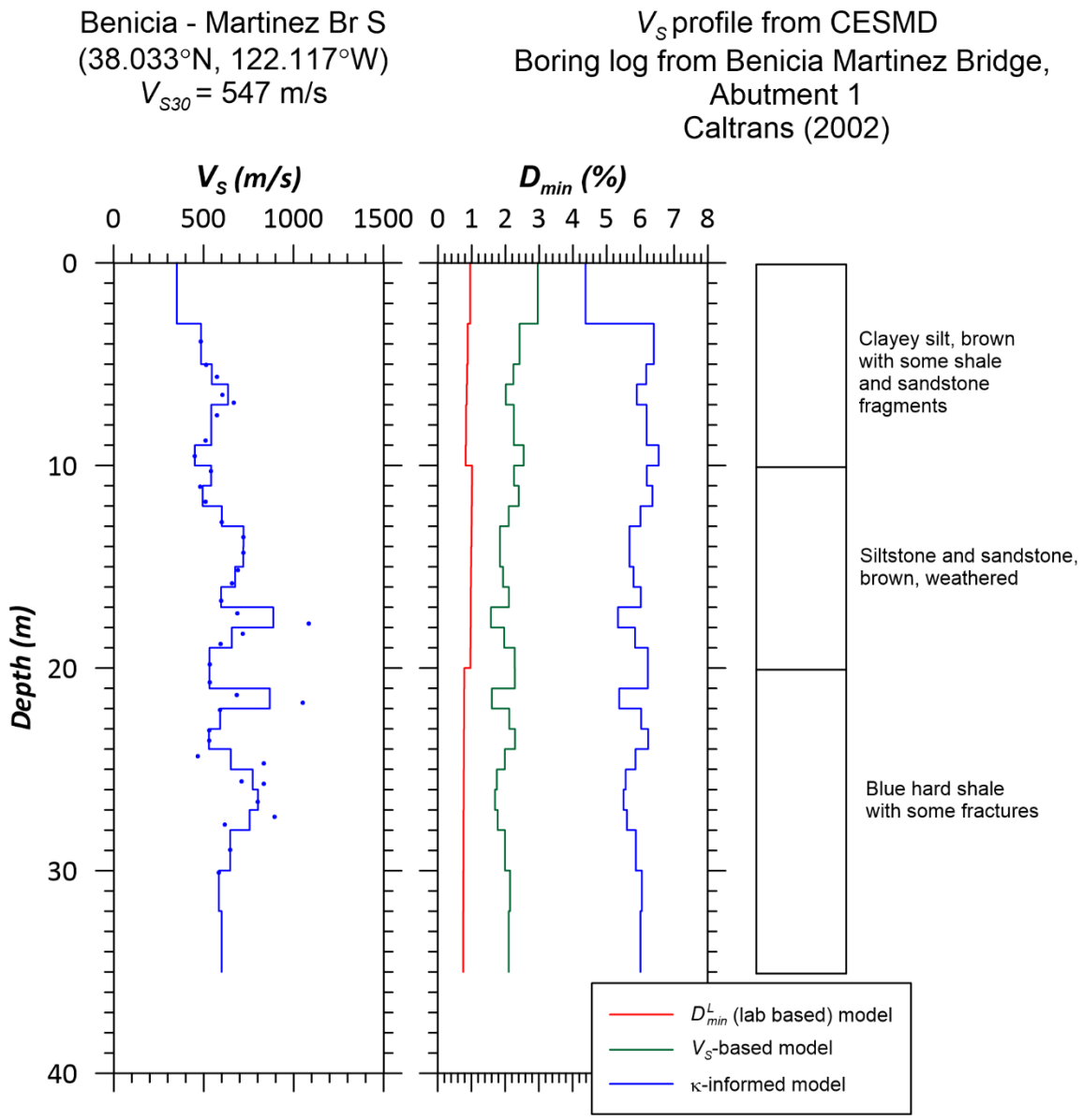

Figure 4.7. V_S profile and D_{min} profiles based on geotechnical models for laboratory damping (D^L_{min}), Campbell (2009) model for Q_{ef}, and $\Delta\kappa$ for Benicia-Martinez South site.

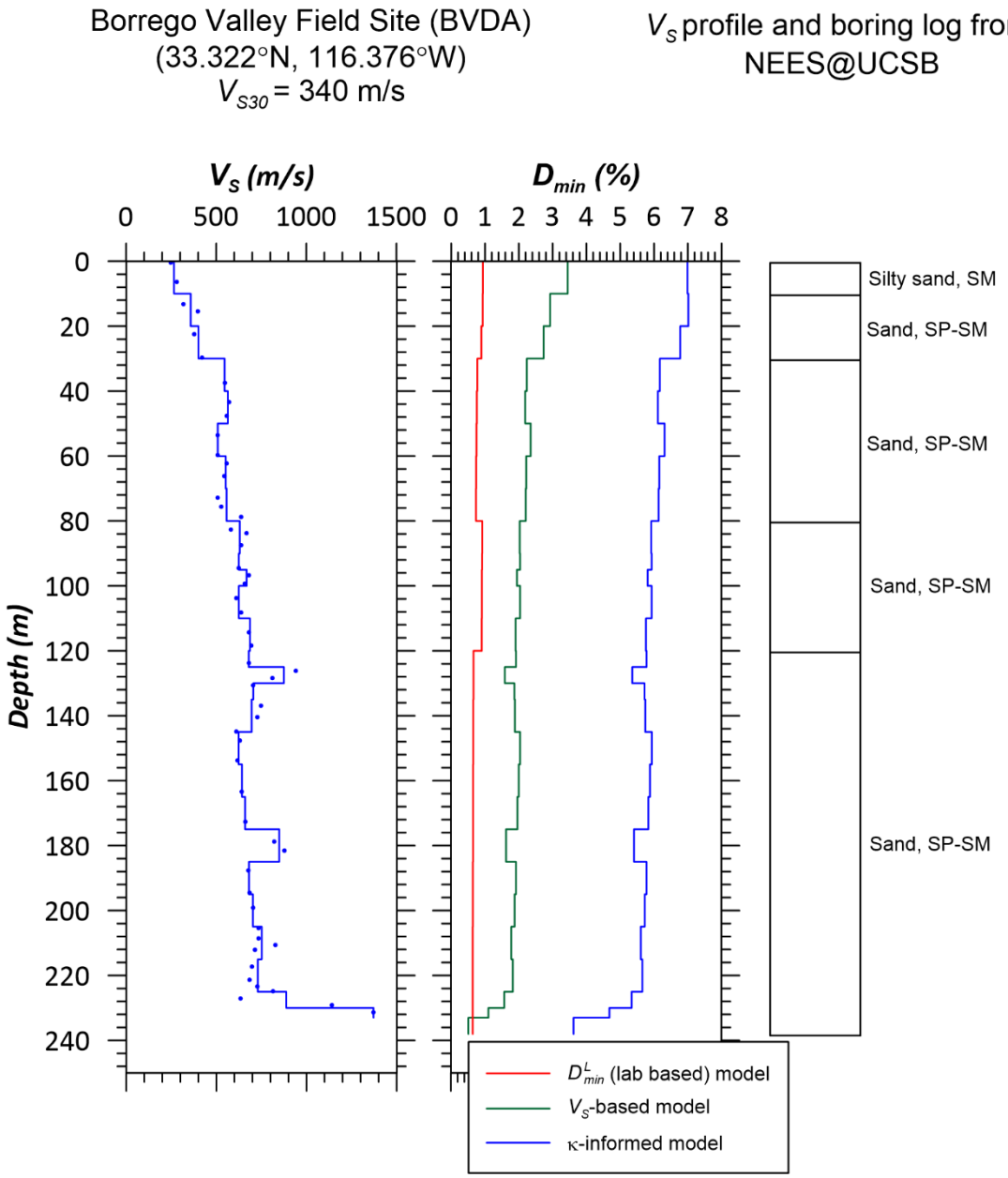

Figure 4.8. V_S profile and D_{min} profiles based on geotechnical models for laboratory damping (D^L_{min}), Campbell (2009) model for Q_{ef}, and $\Delta\kappa$ for Borrego Valley Downhole Array site.

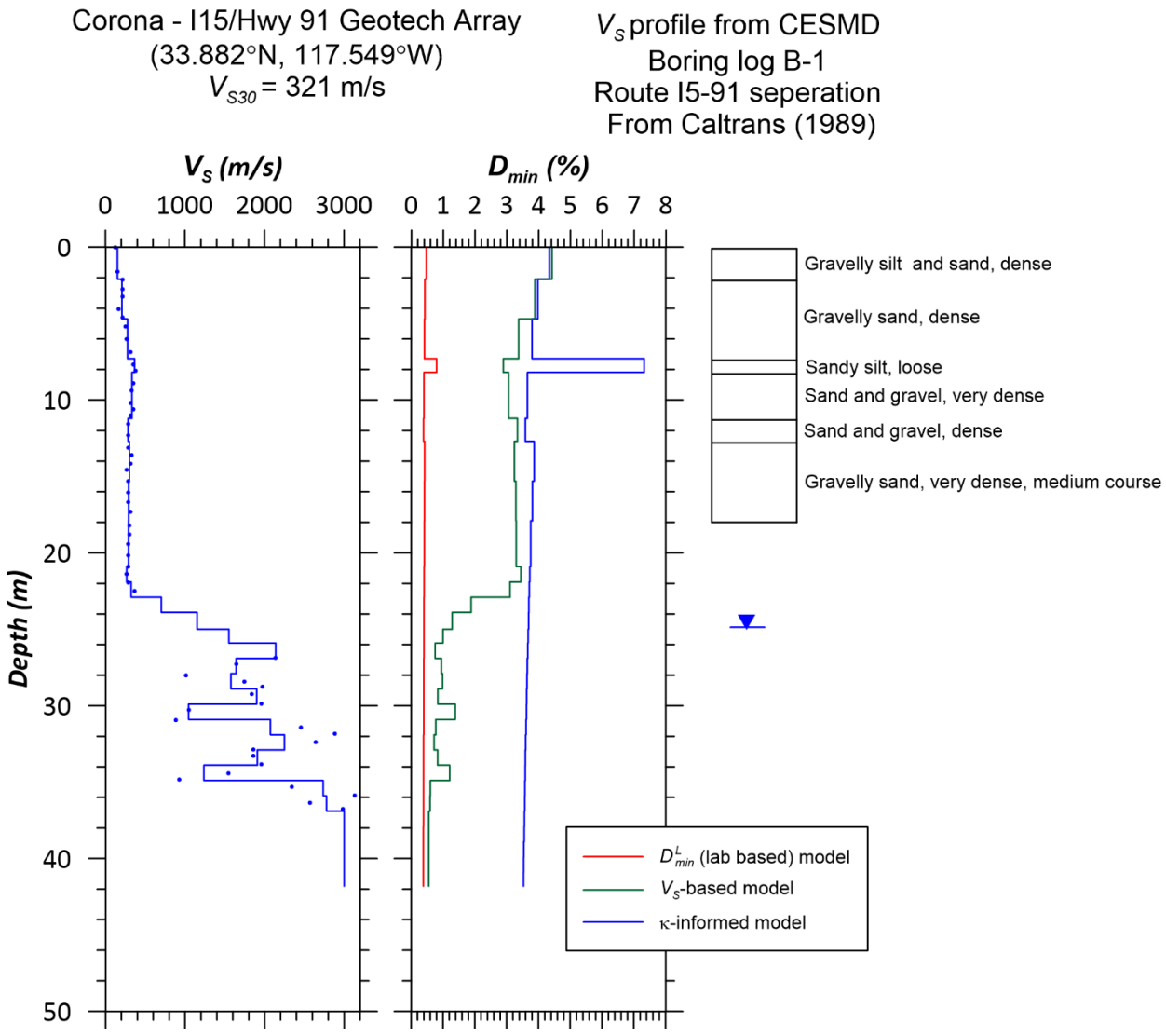

Figure 4.9. V_S profile and D_{min} profiles based on geotechnical models for laboratory damping ($D^L_{\min}$), Campbell (2009) model for Q_{ef}, and $\Delta\kappa$ for Corona vertical array site.

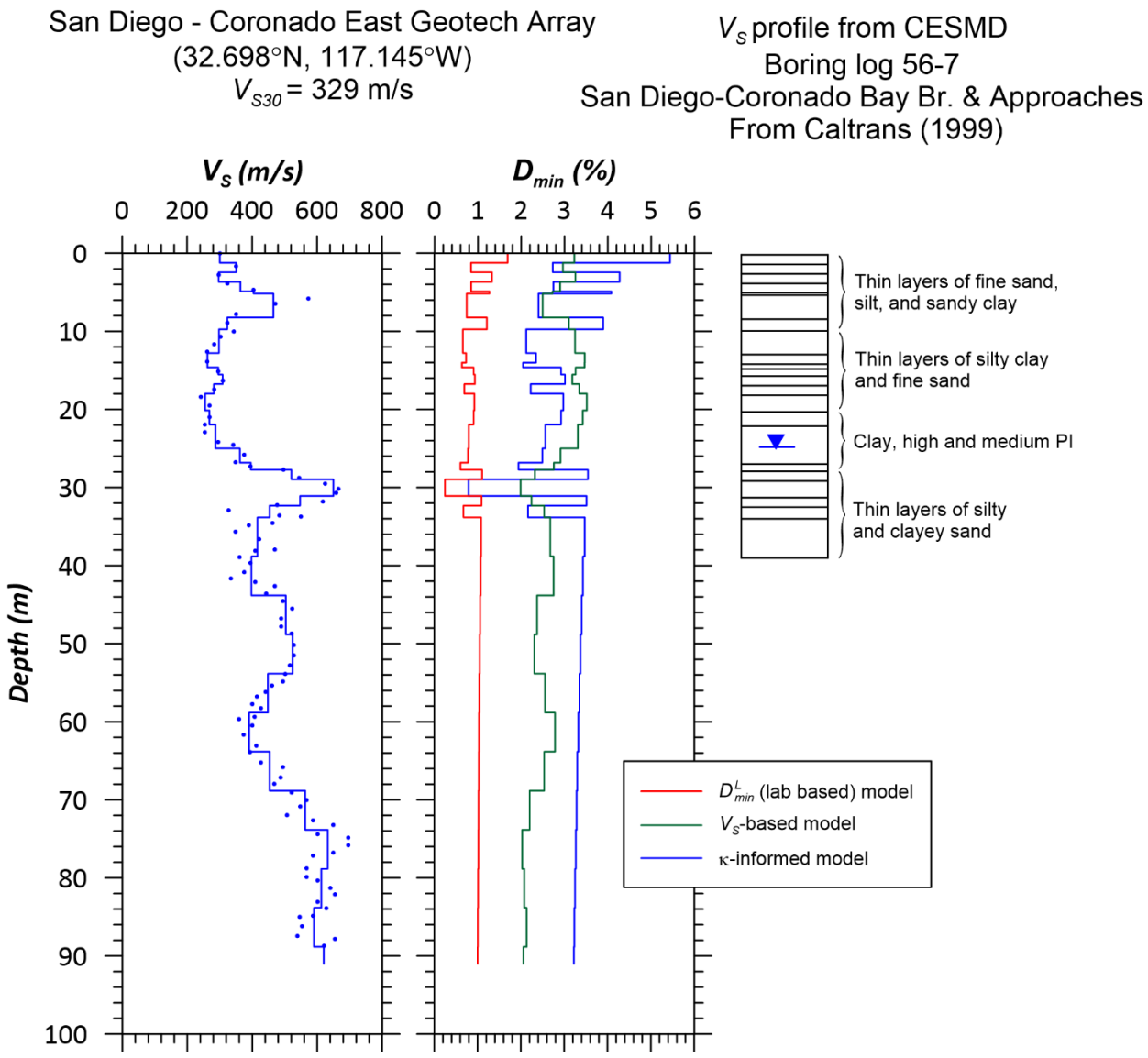

Figure 4.10. V_S profile and D_{min} profiles based on geotechnical models for laboratory damping ($D^L_{\min}$), Campbell (2009) model for Q_{ef}, and $\Delta\kappa$ for Coronado East site.

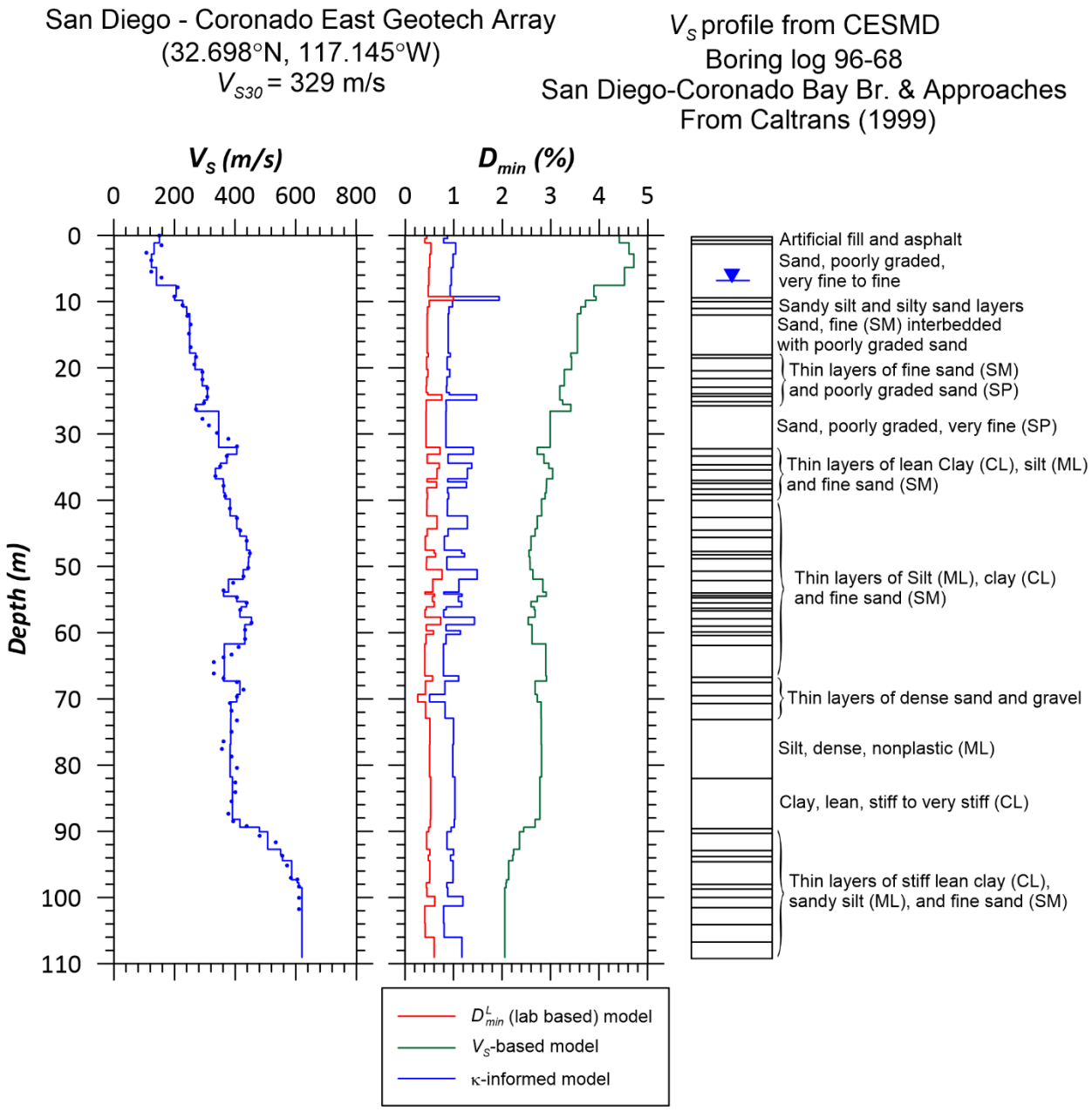

Figure 4.11. V_S profile and D_{min} profiles based on geotechnical models for laboratory damping ($D^L_{\min}$), Campbell (2009) model for Q_{ef}, and $\Delta\kappa$ for Coronado West site.

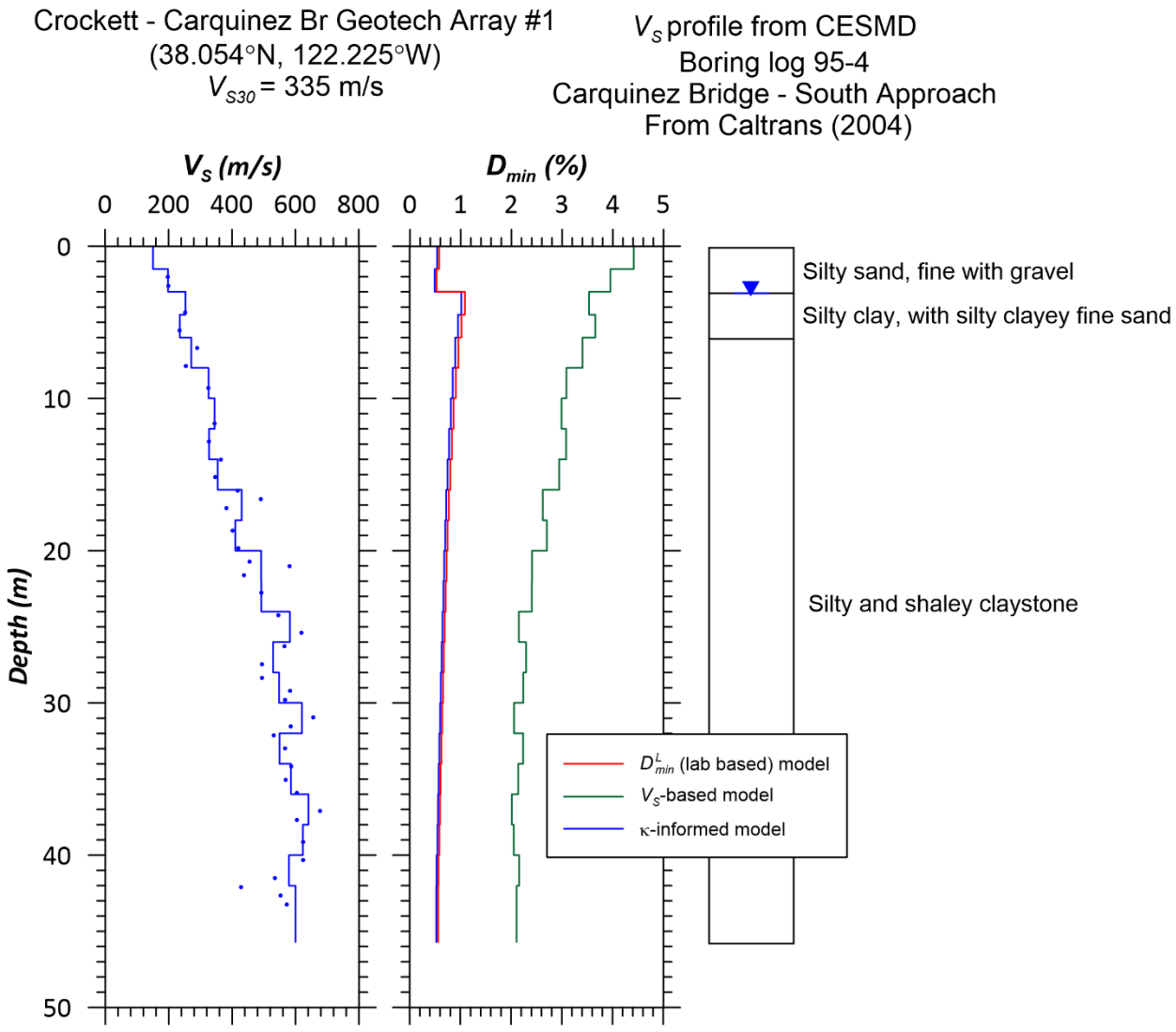

Figure 4.12. V_S profile and D_{min} profiles based on geotechnical models for laboratory damping (D^L_{min}), Campbell (2009) model for Q_{ef}, and $\Delta\kappa$ for Crockett-Carquinez Br site.

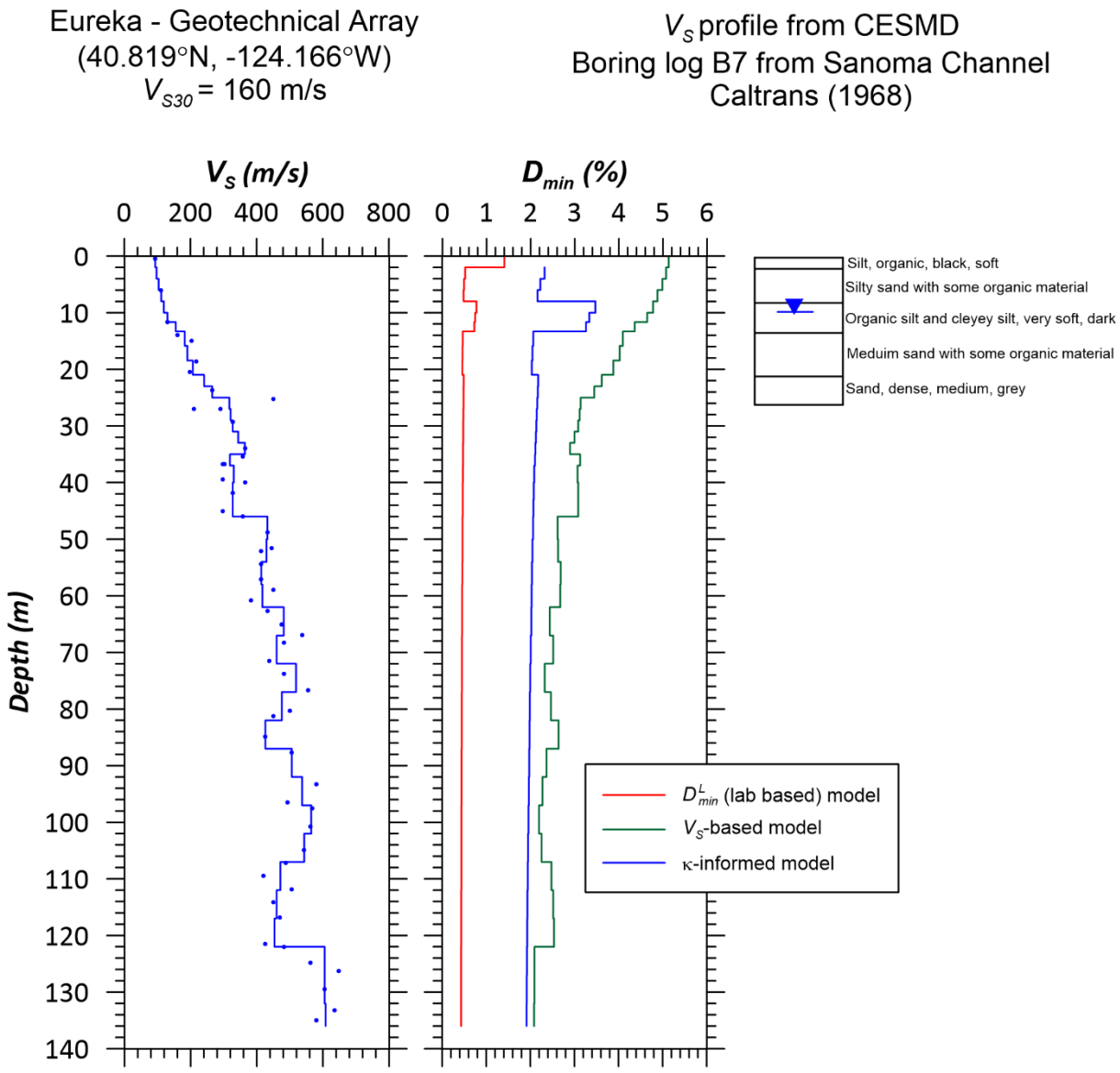

Figure 4.13. V_S profile and D_{min} profiles based on geotechnical models for laboratory damping ($D^L_{\min}$), Campbell (2009) model for Q_{ef}, and $\Delta\kappa$ for Eureka site.

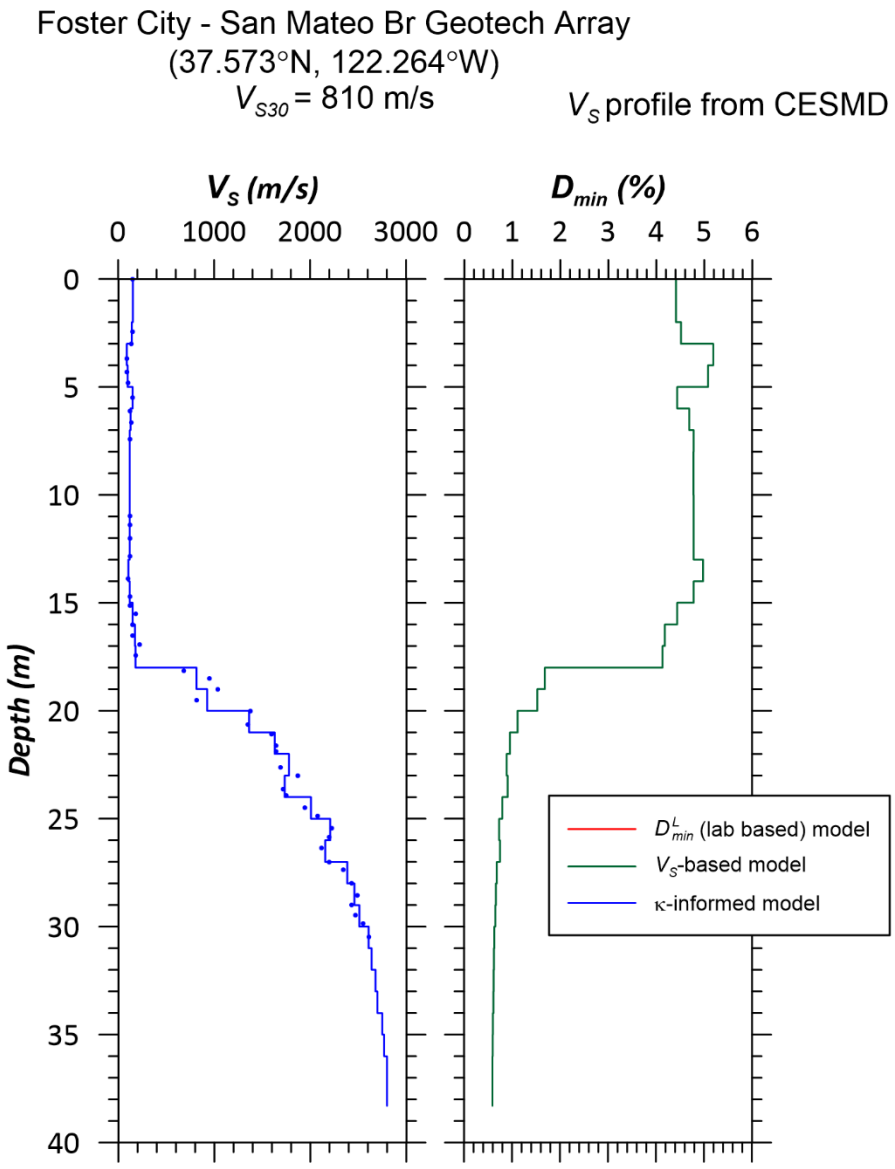

Figure 4.14. V_S profile and D_{min} profiles based on geotechnical models for laboratory damping ($D^L_{\min}$), Campbell (2009) model for Q_{ef}, and $\Delta\kappa$ for Foster City-San Mateo site.

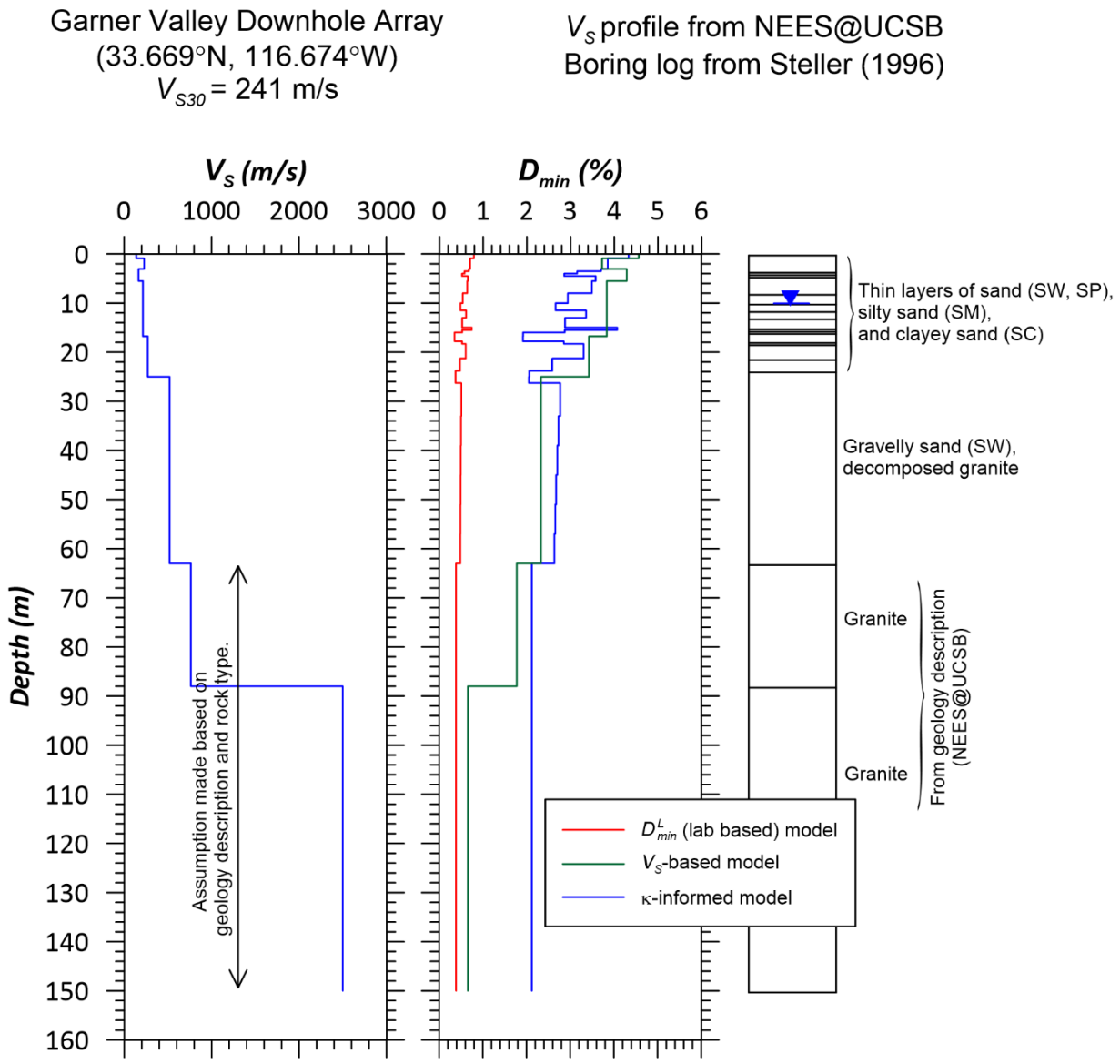

Figure 4.15. V_S profile and D_{min} profiles based on geotechnical models for laboratory damping (D^L_{min}), Campbell (2009) model for Q_{ef}, and $\Delta\kappa$ for Garner Valley site.

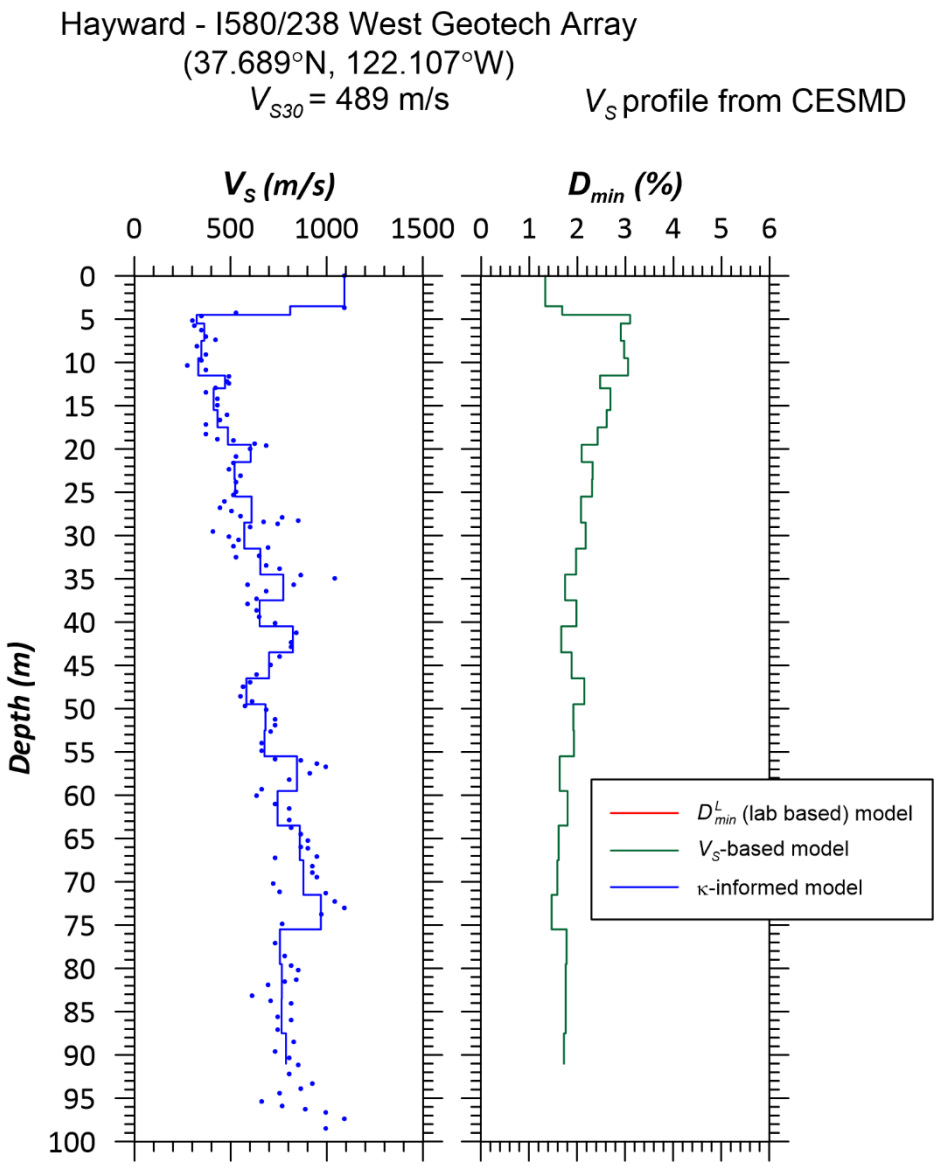

Figure 4.16. V_S profile and D_{min} profiles based on geotechnical models for laboratory damping ($D^L_{\min}$), Campbell (2009) model for Q_{ef}, and $\Delta\kappa$ for Hayward-I580/238 site.

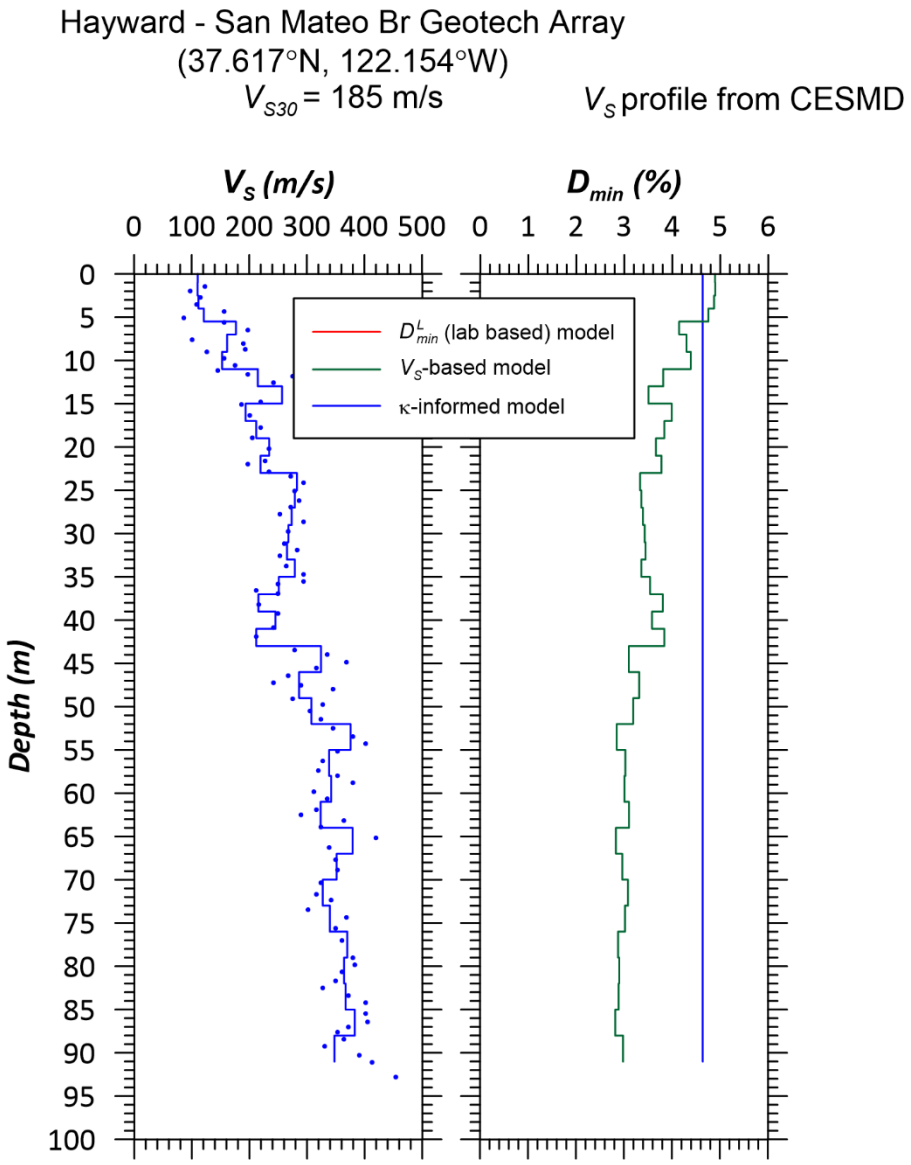

Figure 4.17. V_S profile and D_{min} profiles based on geotechnical models for laboratory damping ($D^L_{\min}$), Campbell (2009) model for Q_{ef}, and $\Delta\kappa$ for Hayward-San Mateo site.

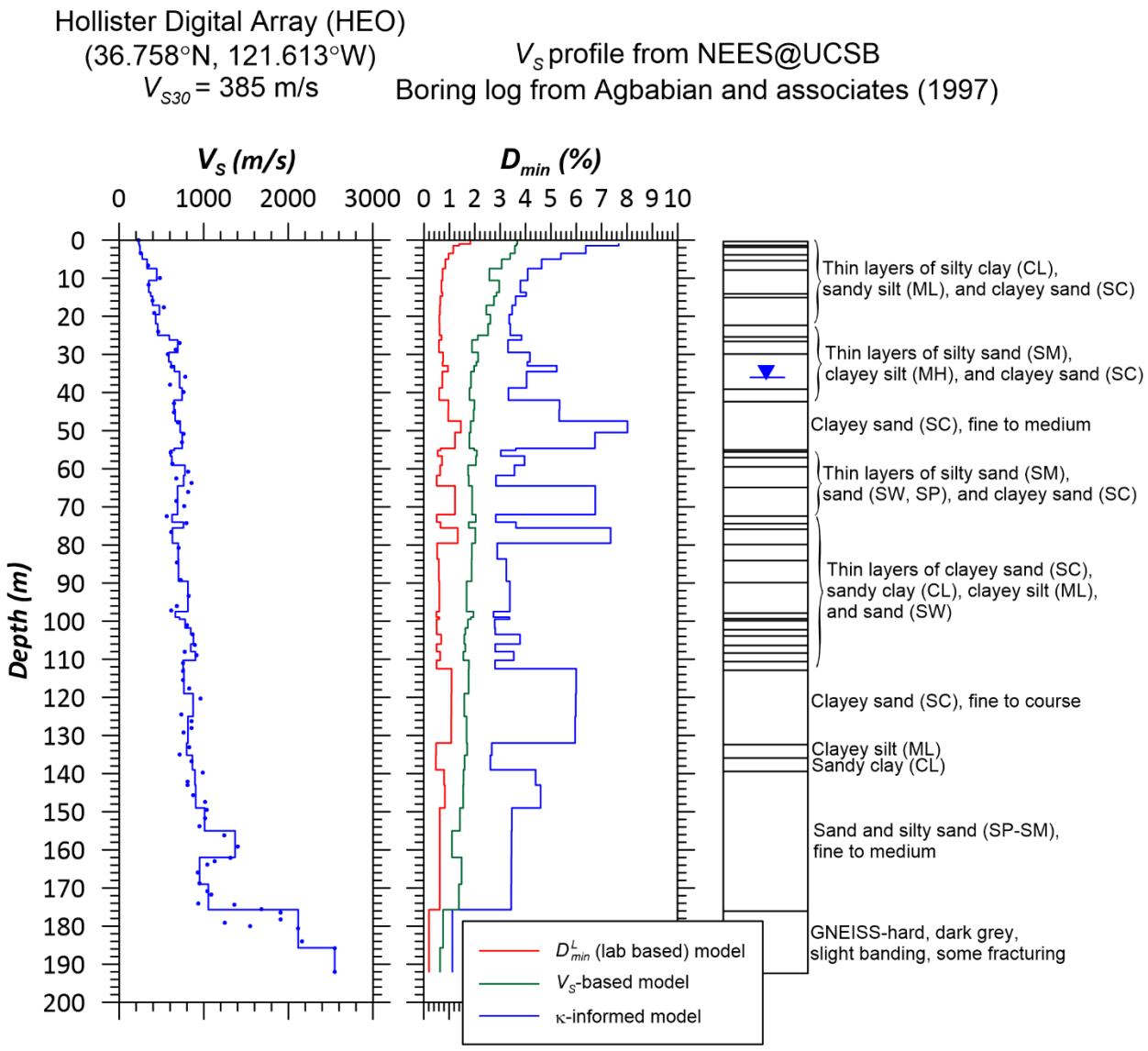

Figure 4.18. V_S profile and D_{min} profiles based on geotechnical models for laboratory damping (D^L_{min}), Campbell (2009) model for Q_{ef}, and $\Delta\kappa$ for Hollister Digital Array site.

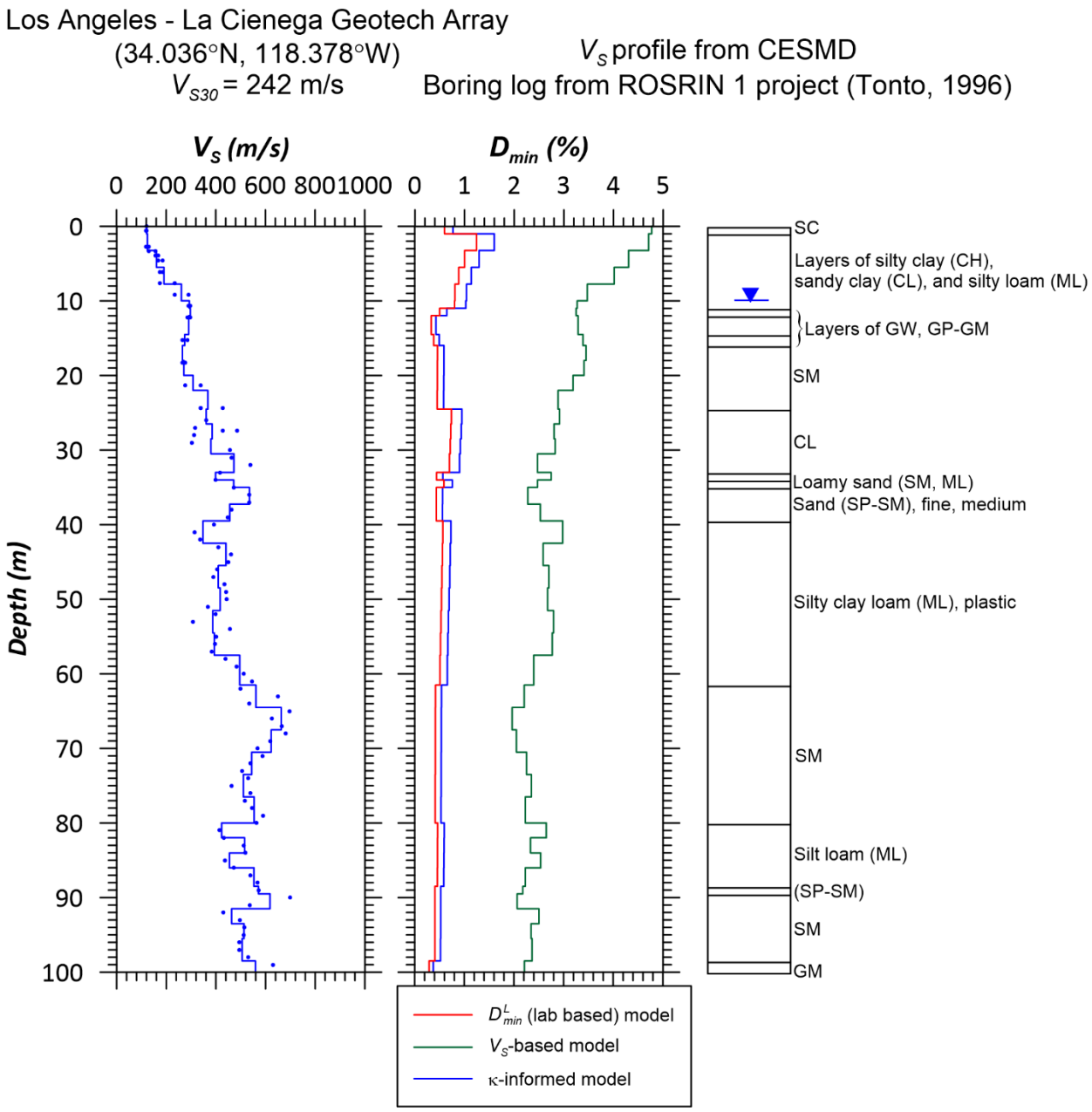

Figure 4.19. V_S profile and D_{min} profiles based on geotechnical models for laboratory damping (D^L_{min}), Campbell (2009) model for Q_{ef}, and $\Delta\kappa$ for Los Angeles-La Cienega site.

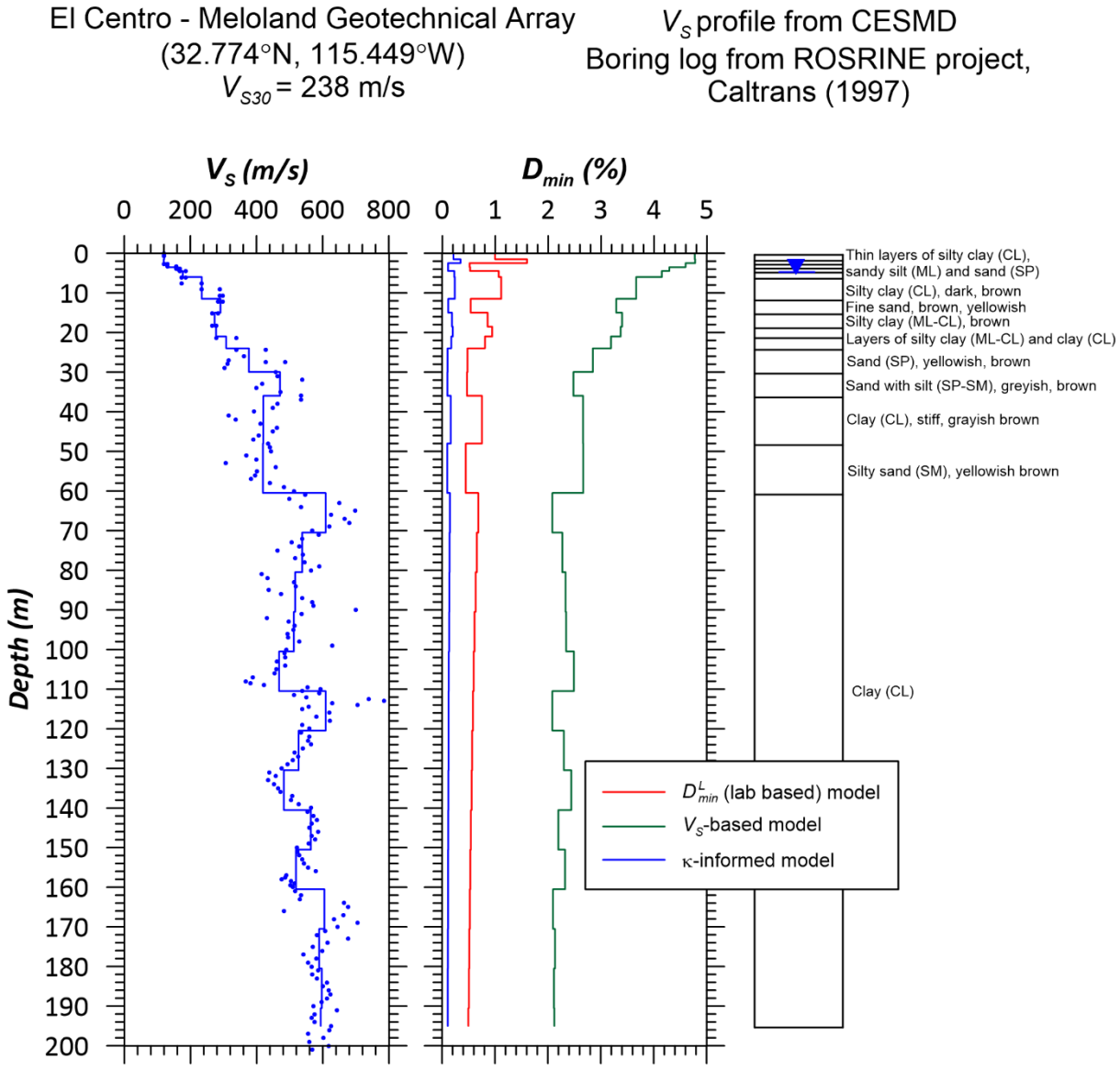

Figure 4.20. V_S profile and D_{min} profiles based on geotechnical models for laboratory damping ($D^L_{\min}$), Campbell (2009) model for Q_{ef}, and $\Delta\kappa$ for El Centro-Meloland vertical array site.

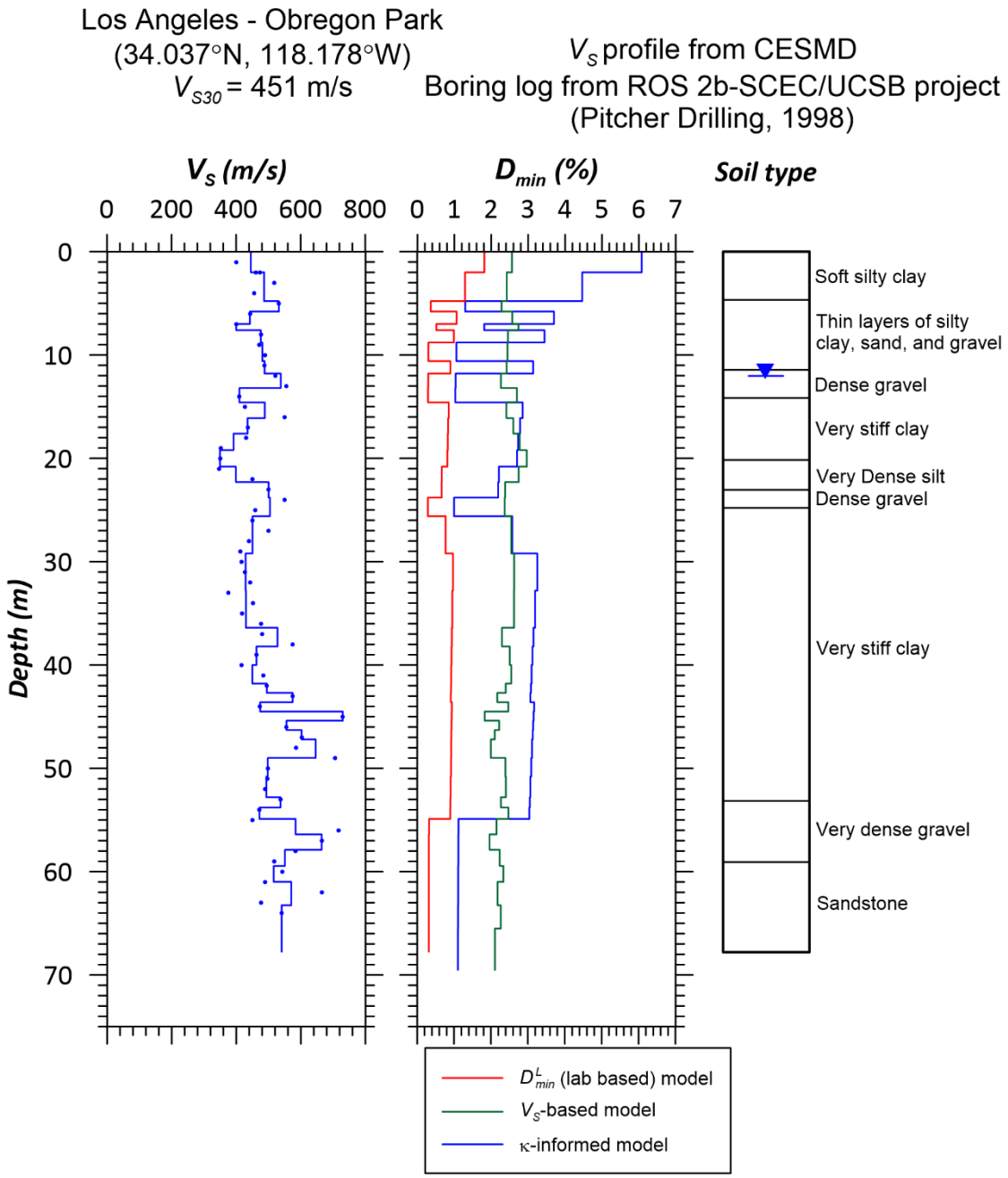

Figure 4.21. V_S profile and D_{min} profiles based on geotechnical models for laboratory damping ($D^L_{\min}$), Campbell (2009) model for Q_{ef}, and $\Delta\kappa$ for Los Angeles-Obregon Park site.

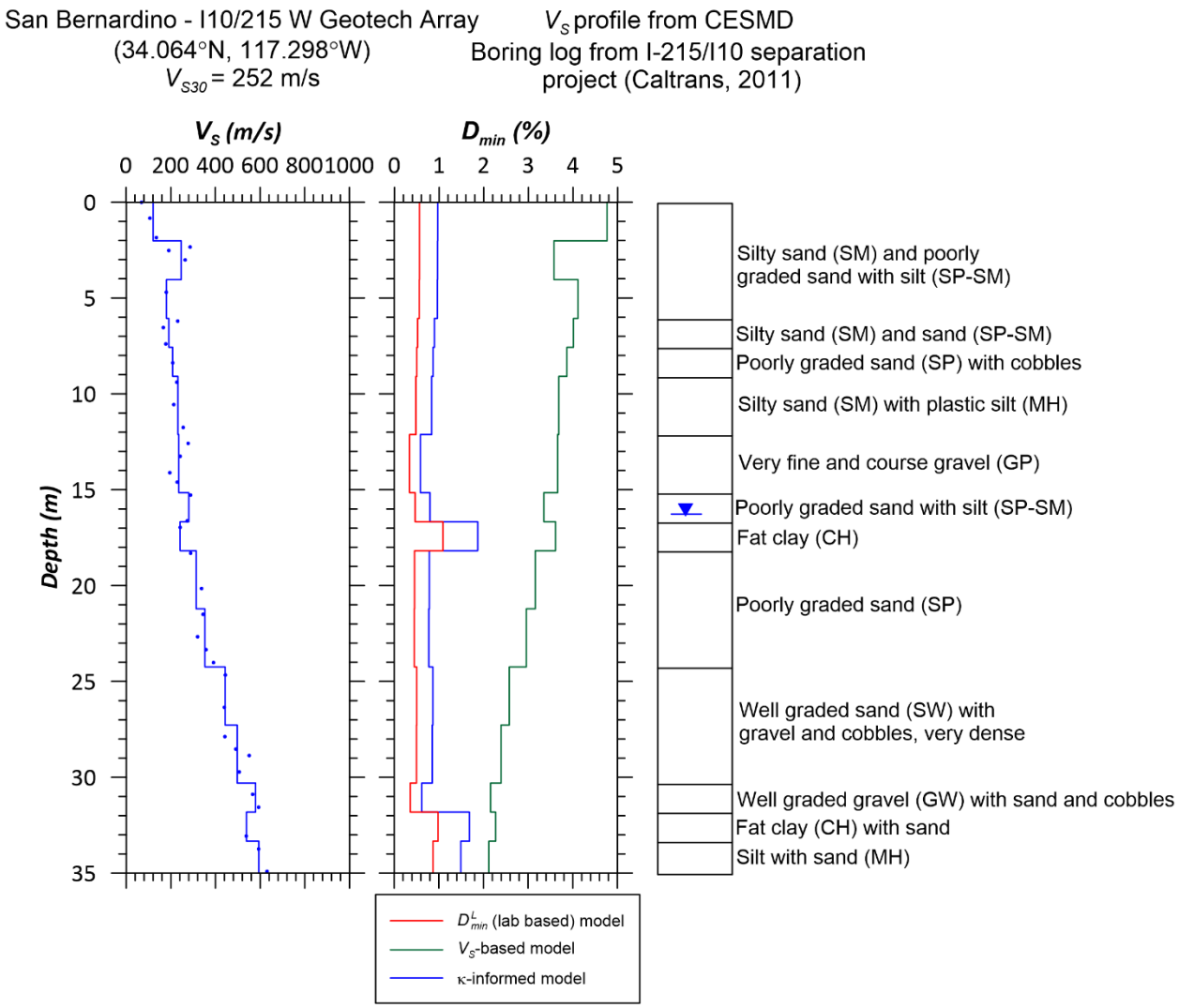

Figure 4.22. V_S profile and D_{min} profiles based on geotechnical models for laboratory damping ($D^L_{\min}$), Campbell (2009) model for Q_{ef}, and $\Delta\kappa$ for San Bernardino vertical array site.

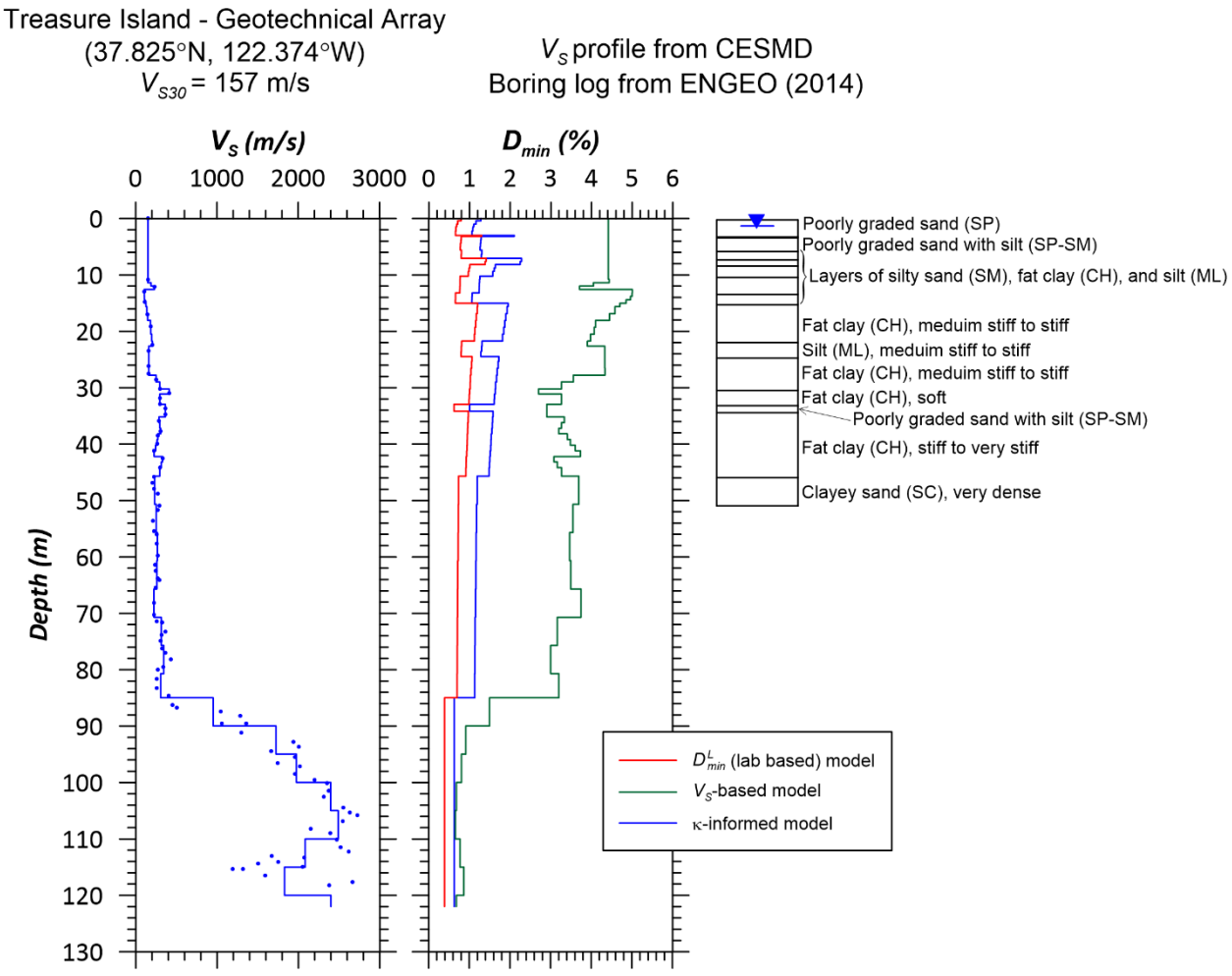

Figure 4.23. V_S profile and D_{min} profiles based on geotechnical models for laboratory damping ($D^L_{\min}$), Campbell (2009) model for Q_{ef}, and $\Delta\kappa$ for Treasure Island vertical array site.

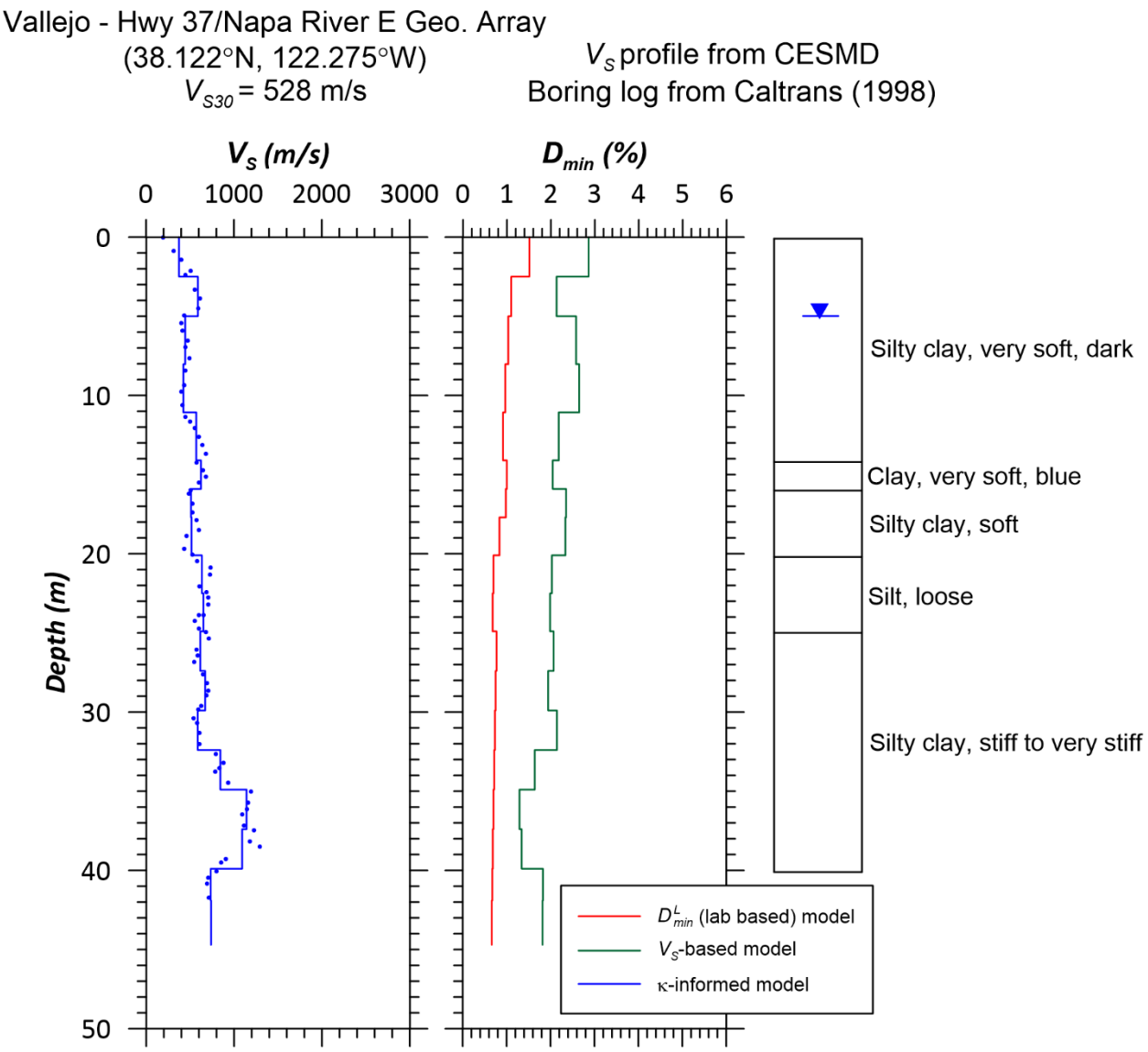

Figure 4.24. V_S profile and D_{min} profiles based on geotechnical models for laboratory damping (D^L_{min}), Campbell (2009) model for Q_{ef}, and $\Delta\kappa$ for Vallejo-Hwy 37/Napa River E. site.

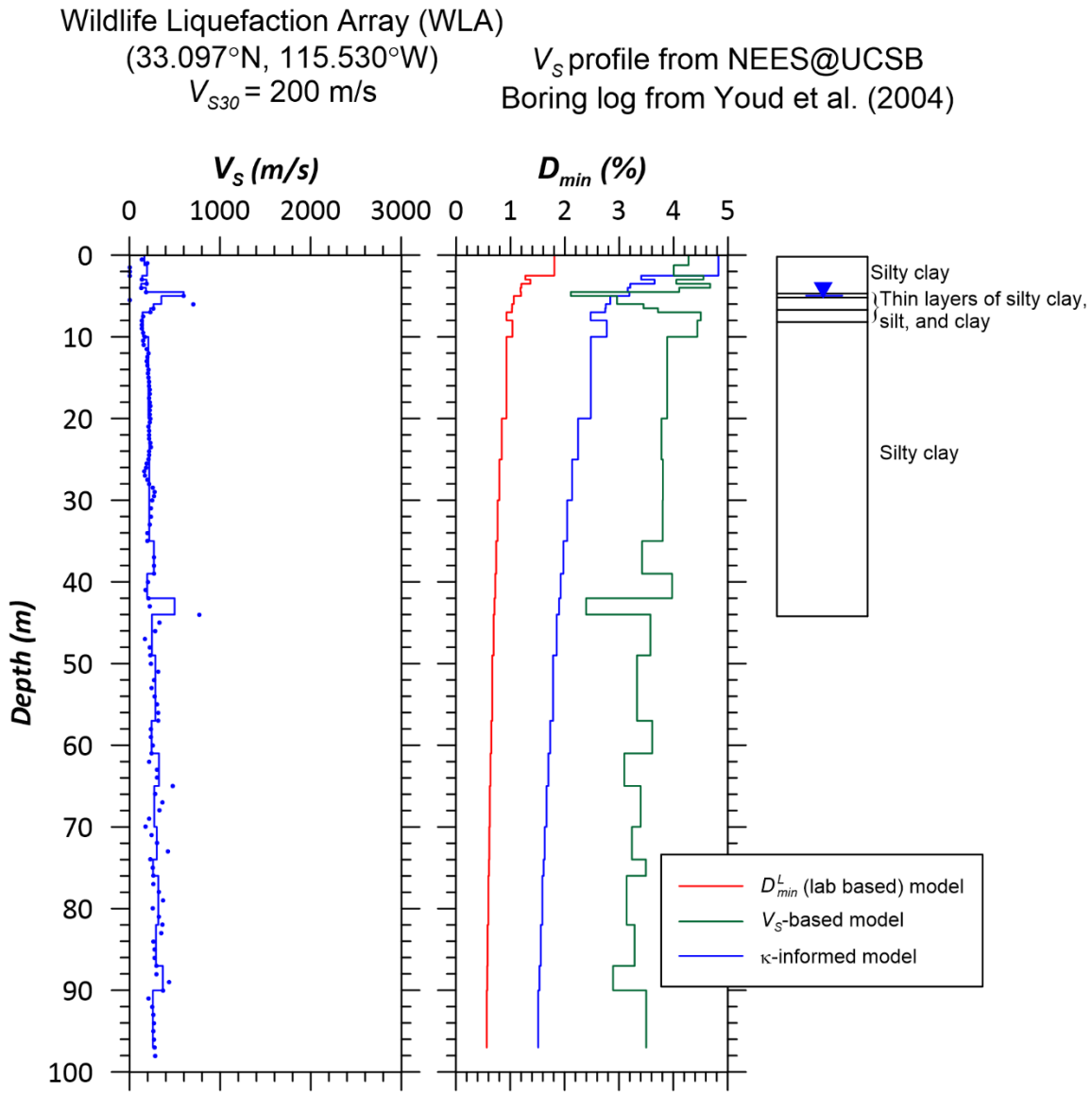

Figure 4.25. V_S profile and D_{min} profiles based on geotechnical models for laboratory damping (D^L_{min}), Campbell (2009) model for Q_{ef}, and $\Delta\kappa$ for Wildlife Liquefaction Array (WLA) site.

Table 4.3. Summary statistics of $\Delta\kappa$ (measured from ETF), $\Delta\kappa$ implied from $D_{\min}^{L}$ profiles, and F_D. for the vertical array sites.

Site	Station NO (CSMIP)	$\overline{\Delta\kappa}$ (sec)	$\Delta\kappa$ implied by $D_{\min}^{L}$ (sec)	F_D
Antioch-San Joaquin S	67266	0.0116	0.00366	3.18
Bay Bridge	58961	0.0085	NA	4.97
Benicia South	68323	0.0044	NA	4.53
Borrego Valley	NA	0.0053	0.00632	0.74
Corona	13186	0.0078	0.00085	9.15
Coronado East	3192	0.0133	0.00415	3.21
Coronado West	3193	0.0063	0.00324	1.95
Crockett-1	68206	0.0016	0.00121	0.94
El Centro-Meloland	1794	0.0013	0.00656	0.22
Eureka	89734	0.0203	0.00456	4.46
Foster City	58968	-0.0033	NA	NA
Garner Valley	NA	0.0136	0.0025	5.43
Hayward-580W	58487	0.0234	NA	8.19
Hayward-San Mateo	58798	0.0330	NA	4.64
Hollister digital	NA	0.0236	0.00429	5.50

Site	Station NO (CSMIP)	$\overline{\Delta\kappa}$ (sec)	$\Delta\kappa$ implied by $D_{\min}^{L}$ (sec)	F_D
La-Cienega	24703	0.0042	0.00325	1.29
Obregon Park	24400	0.0074	0.00212	3.48
San Bernardino	23792	0.0000	0.00139	1.72
Treasure Island	58642	0.0118	0.00684	1.62
Vallejo	68310	-0.0080	0.00136	NA
Wildlife Liquefaction	NA	0.0167	0.00628	2.67

4.3 INFERENCES OF SITE RESPONSE EFFECTS FROM TRANSFER FUNCTIONS

4.3.1 Calculation of Transfer Functions

Empirical transfer functions (ETFs) representing site response between the downhole and surface accelerometers are computed from ratios of Fourier amplitudes as follows:

$$H(f) = \frac{G(f, x_1)}{G(f, x_2)} \tag{4.12}$$

where $H(f)$ is the ETF, $G(f,x_1)$ is the surface FAS and $G(f,x_2)$ is the downhole FAS. ETFs are only used over the usable frequency range based on record processing. The ETF is taken as the geometric-mean of ETFs for the two horizontal components of the recordings (at their as-recorded azimuths) for each site. The results shown subsequently are smoothed through the use of a logarithmic window function proposed by Konno and Ohmachi (1998) with the coefficient for bandwidth frequency (b) equal to 20.

Theoretical transfer functions (TTF) are a direct outcome of linear and equivalent-linear analysis (Section 4.2.1). In other words, the calculation of TTFs does not require analysis of ground motions and their Fourier amplitudes as in Eq. (4.1). When time-domain procedures are used, the ground motions must be calculated, their FAS computed, and then TTF can be taken using Eq. (4.12). It is worth mentioning that what is defined here as the ratio of surface/downhole ground motion amplitudes is a bit different than the definition for *PSA* amplification. Unlike for *PSA* amplification, or transfer functions, I do not convert the downhole motion to equivalent-outcrop, therefore the downhole motion amplitude used for computing the ratio will have the effects of downgoing waves.

4.3.2 Transfer Function Comparisons from KiK-Net Array in Japan

Thompson et al. (2012) studied 100 KiK-net sites in Japan in order to assess the variability in site amplification and the performance of linear 1D GRA. These sites have recorded a large number of surface and downhole recordings. For GRA, they used the program NRATTLE, which is a part of the ground motion simulation program SMSIM (Boore, 2005). NRATTLE performs linear GRA using Thomson–Haskell matrix method. The input parameters for NRATTLE include shear wave velocity (V_S), soil density, and the intrinsic attenuation of shear-waves (Q_S^{-1}) which represents damping. Soil density was estimated from P-wave velocity using the procedures suggested by Boore (2008), and Q_S^{-1} was estimated using a grid-search algorithm to optimize the fit to $H(f)$. Note that by optimizing damping in this manner, Thompson et al. (2012) do not assess the performance of alternative damping models, as described in Section 4.2.3. Moreover, this optimization would not be possible to perform in a forward sense when vertical array recordings from a site are not available.

Thompson et al. (2012) computed ETFs with Eq. (4.11) using available data meeting certain selection requirements. In order to minimize the potential for nonlinear effects, only records having a ground surface PGA < 0.1 g were selected. In total, 3714 records from 1573 earthquakes were considered for the 100 KiK-net sites. The mean and 95% confidence intervals were computed across all selected recordings at a given site, with the example results (for two sites) given in Figure 4.26. TTFs from the GRA are also shown in Figure 4.26.

Figure 4.4 (a) provides an example of poor fit between the ETF and TTF whereas Figure 4.4 (b) shows a good fit. Goodness-of-fit was quantified using Pearson's sample correlation coefficient (r) as a measure of how well the model predictions and the data are correlated.

Parameter r quantifies how well the shapes of the transfer functions align, including the locations and shapes of peaks. Parameter r is insensitive to relative overall levels of amplification, which is better quantified in the next subsection in *PSA* amplifications. Similar to this study, I calculate the Pearson's sample correlation coefficient for i^{th} earthquake and j^{th} analysis (based on damping estimation approach) as follows for a given site:

$$r_{ij} = \frac{\sum\left(\mathrm{ETF}_i(f) - \overline{\mathrm{ETF}_i}\right)\left(\mathrm{TTF}_j(f) - \overline{\mathrm{TTF}_j}\right)}{\sqrt{\sum\left(\mathrm{ETF}_i(f) - \overline{\mathrm{ETF}_i}\right)^2}\sqrt{\sum\left(\mathrm{TTF}_j(f) - \overline{\mathrm{TTF}_j}\right)^2}} \tag{4.13}$$

The summations in Eq. 4.13 are taken over a frequency range with a lower bound f_{min} corresponding to the first peak in the TTF and an upper bound f_{max} that is the minimum of the frequency of the fourth peak of the TTF or 20 Hz. The summation is performed over all frequency points between f_{min} and f_{max}, which are equally spaced in logarithmic units. The mean value of r across all events (r_j) for a given site is denoted $\overline{r}$.

A value of r=0.6 was taken by Thompson et al. as the threshold for good fit. The corresponding r values for the two sites in Figure 4.26 are 0.10 for the poor fit site and 0.79 for the good fit site. Dispersion curves (phase velocity vs. frequency) for the two example sites are shown in Figure 4.26. The results show that there is a large degree of variability in the dispersion curves for the poor fit site and consistency in the dispersion curves for the good fit site. Multiple dispersion curves are only available for two of the 100 sites considered by Thompson et al. (2012). Nonetheless, the limited available data indicate that geologic complexity, as reflected by spatial variability in the Rayleigh wave velocity structure, may correlate to the accuracy of GRA prediction. More complex geologic structure would be expected to produce 3D site effects that are not captured by GRA.

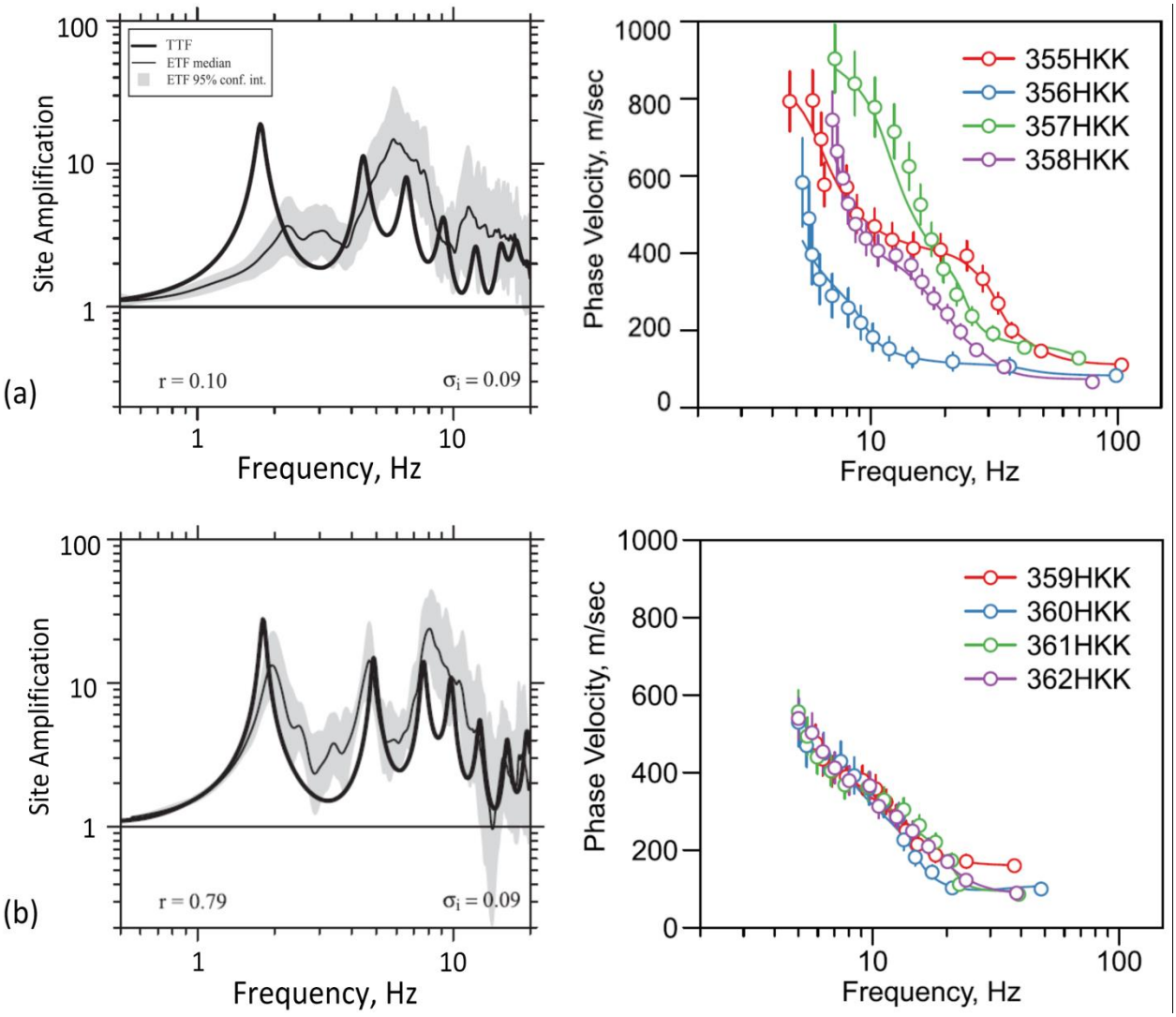

Figure 4.26. Examples of a poor fit (a) and good fit (b) between ETF and TTF at two KiK-net sites along with the dispersion curves from multiple SASW tests for both sites (adapted from Thompson et al., 2012).

Results for the 100 considered sites show that only 18% have a good fit between ETFs and TTFs, indicating 1D GRA fails to provide an accurate estimation of site response for a larger majority of KiK-net sites. Subsequent to Thompson et al. (2012), Kaklamanos et al. (2013) use the same sites to study the bias and variability of 1D GRA, and Kaklamanos et al. (2015) use a subset of six KiK-net sites where a good ETF-TTF fit was obtained to study the issue of when increased levels of sophistication in nonlinear modeling is needed in GRA. They use results from Kaklamanos et al. (2013), and use SHAKE for additional Equivalent-Linear (EL) and DEEPSOIL

and Abaqus (Dassault Systèmes, 2009) for additional Nonlinear (NL) GRA. Using a wide range of weak to strong ground motions, they determine the strain levels at which each model breaks down. They recommend not using linear GRA when strain levels exceed (0.01% to 0.1%).

A second metric considered by Thompson et al. (2012) concerns the inter-event variability of transfer function ordinates, which they computed as a median value of the standard deviations computed across the frequencies within the range to compute *r*. Large values of this standard deviation indicate large event-to-event differences in observed site amplification, suggesting potential complexities from 3D geologic structure. The two sites shown in Figure 4.4 have low levels of variability (0.09); results for all sites and a comparison to California data is presented in the next section.

4.3.3 Transfer Function Comparisons for California Vertical Array Data

Using the data set described in Chapter 3, I compute ETF ordinates for each of the 21 selected California vertical array sites. In this sense our approach is similar to that of Thompson et al. (2012) – I 'cast the net widely' to study site response performance over a wide range of conditions. Unlike several studies conducted since Thompson et al. (2012), I do not screen sites to identify those for which the ETF matches the shape of a TTF; instead I seek to understand how frequently such a match is achieved in relatively weak motion data from California vertical array sites.

Similar to Thompson et al. (2012), I exclude recordings with strong ground shaking (*PGA* at surface instrument > 0.1 g) so as to minimize nonlinear effects. Figure 4.27 shows histograms of *PGA* and *PGV* for the downhole instrument records used in the present work.

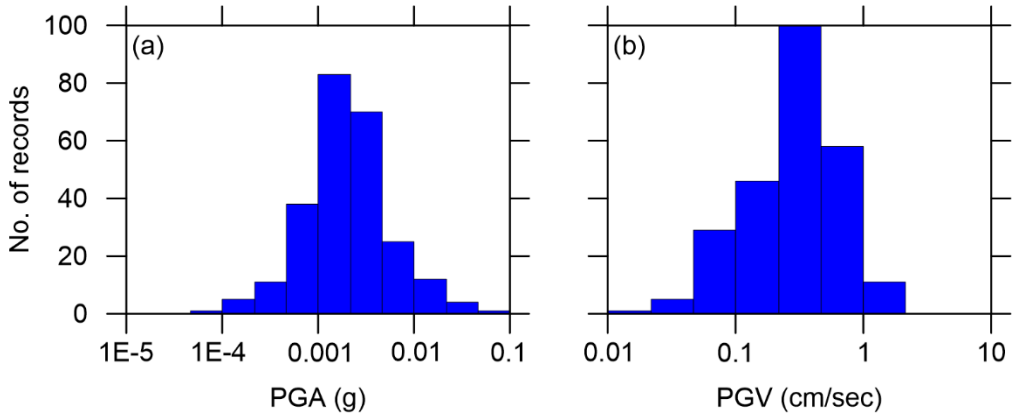

Figure 4.27. Histograms of PGA (a) and PGV (b) for downhole recordings used in this study.

I assume a log-normal distribution for ETF ordinates and compute for each site the median ($\mu_{\ln}$) (equivalent to the exponent of the natural log mean) and the natural log standard deviation of ETF ($\sigma_{\ln}$) at each frequency using all available record pairs. Figure 4.28 shows example ETFs for all record pairs at the San Bernardino and Obregon Park sites along with the median and 95% confidence intervals of ETF. For plotting purposes, I show results over a frequency range between 0.5 and 10 Hz. The all-inclusive usable frequency range is 0.2-28 Hz for San Bernardino site recordings, and 1.4-18 Hz for Obregon Park. Therefore, the range shown focuses attention on frequencies that significantly contribute to *PSA* ordinates. The median ETF and its standard deviation are shown for all sites in plots in the Appendix.

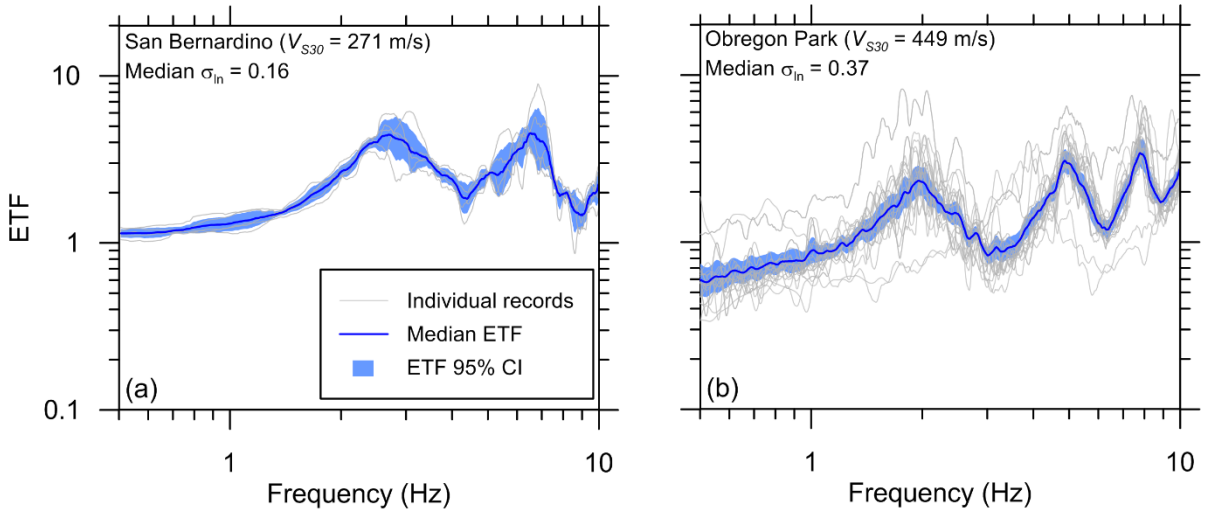

Figure 4.28. Empirical transfer functions plots for (a) San Bernardino site with low ETF variability, and (b) Obregon park with high ETF variability.

Theoretical transfer functions (TTFs) are computed by linear visco-elastic 1D GRA in DEEPSOIL. As the downhole sensor is recording both up-going and down-going waves, we take the boundary condition at the base of the model as rigid (Kwok et al., 2007). The visco-elastic analysis in DEEPSOIL is performed in the frequency domain, and the transfer function predicted by the model is independent of the input motion. Similar to ETFs, the TTFs are smoothed by Konno and Ohmachi (1998) function with b= 20. Input soil properties for the visco-elastic analysis include the V_S profile, layer mass densities (assumed based on soil types and material descriptions), and material damping. I utilize alternate approaches for estimating small-strain soil damping as described in Section 4.2.2-4.2.3 to provide insight and guidance on best practices for selection of small-strain damping (D_{min}). Note that this aspect of our analysis departs from the prior work of Thompson et al. (2012), who back-calculated damping to optimize the ETF-TTF fit.

Figure 4.3729-4.38 shows model-data comparisons by plotting together TTFs and ETFs. Unlike the amplification of *PSA* which is discussed in Section 4.4, transfer functions are able to show multiple modal frequencies for the soil column from both recordings and simulations. The comparison of position of the first several peaks in TEF and TTFs are a good indicator of if there

is a good agreement between the shapes of the transfer functions. In the example of El Centro-Meloland site (Figure 4.37), the simulations are not able to capture the position of any of the visible five peaks seen in ETF plot. This is an indication that 1D GRA is unable to simulate the site response between surface and downhole regardless of damping model. On contrary, for Treasure Island site (Figure 4.35), the position of all six peaks in ETF are captured by GRA, which is an indication that 1D assumption is valid for this site.

In addition to the above qualitative assessments of goodness of fit, it is also useful to consider quantitative metrics. One such metric is the Pearson's sample correlation coefficient *r* (also used by Thompson et al., 2012), which was computed in the manner described in Section 4.3.2. I use the mean value over all recordings at a given site, $\bar{r}$, which is shown in Figure 4.39. Generally, sites with qualitatively good fit between ETF and TTF have values of $\bar{r} > 0.6$ (e.g., Treasure Island site in Figure 4.10) and sites with poor fit have $\bar{r} < 0$ (e.g., El Centro-Meloland site).

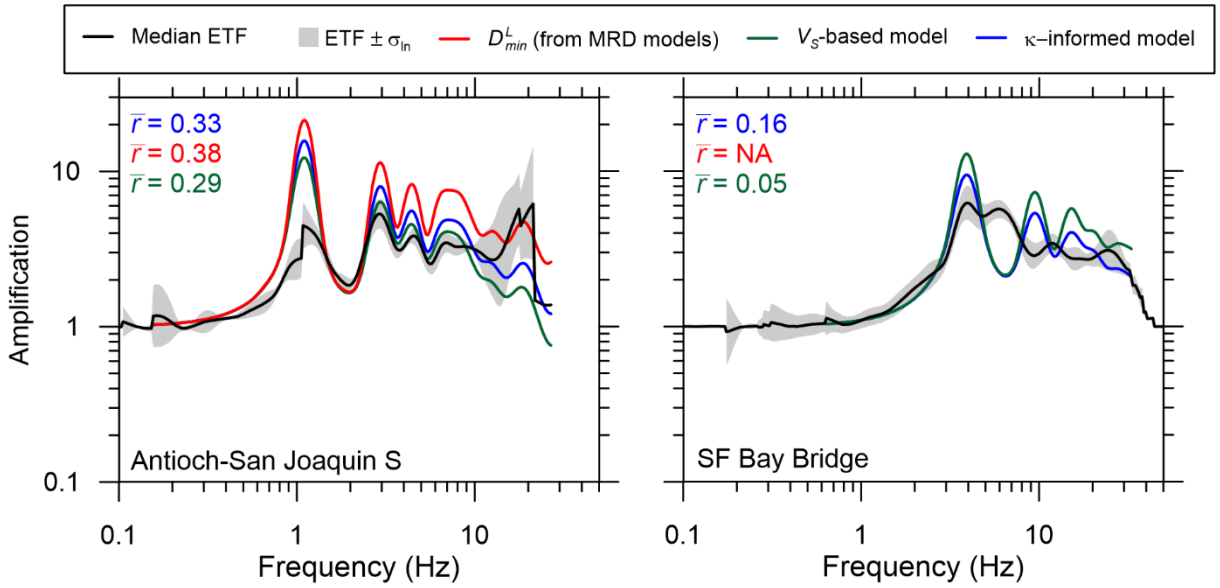

Figure 4.29. Comparison of ETF and TTFs for Antioch-San Joaquin S and San Francisco Bay Bridge. Values of $\bar{r}$ for each damping model are shown in different colors (red: $D^{L}_{\min}$, green: V_S-based, blue: κ-informed).

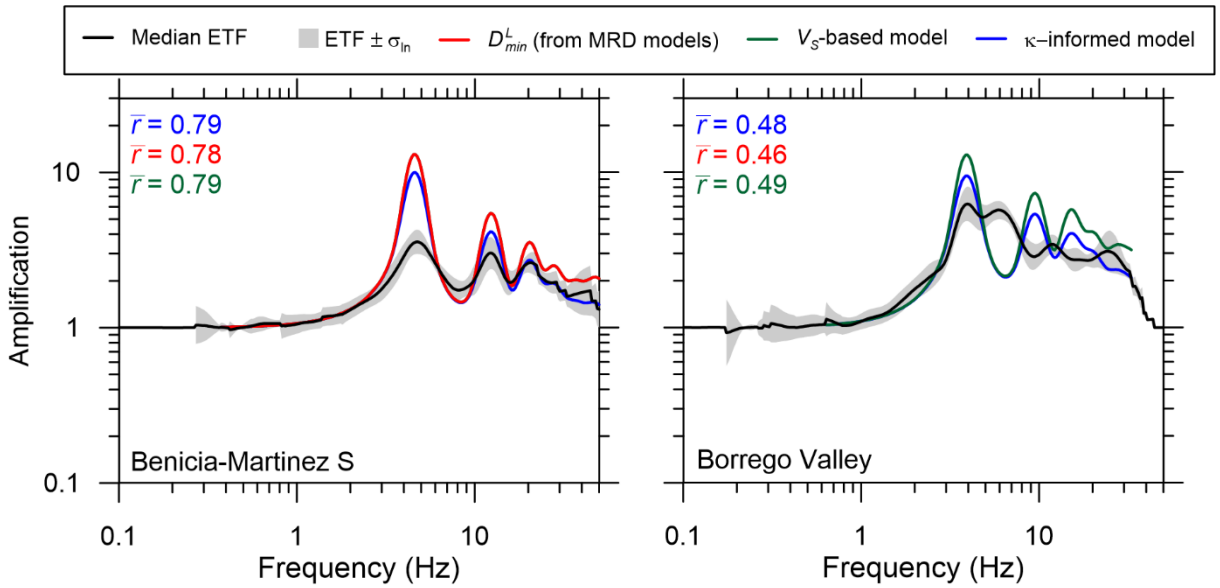

Figure 4.30. Comparison of ETF and TTFs for Benicia-Martinez S and Borrego Valley (BVDA). Values of $\bar{r}$ for each damping model are shown in different colors (red: $D^{L}_{\min}$, green: V_S-based, blue: κ-informed).

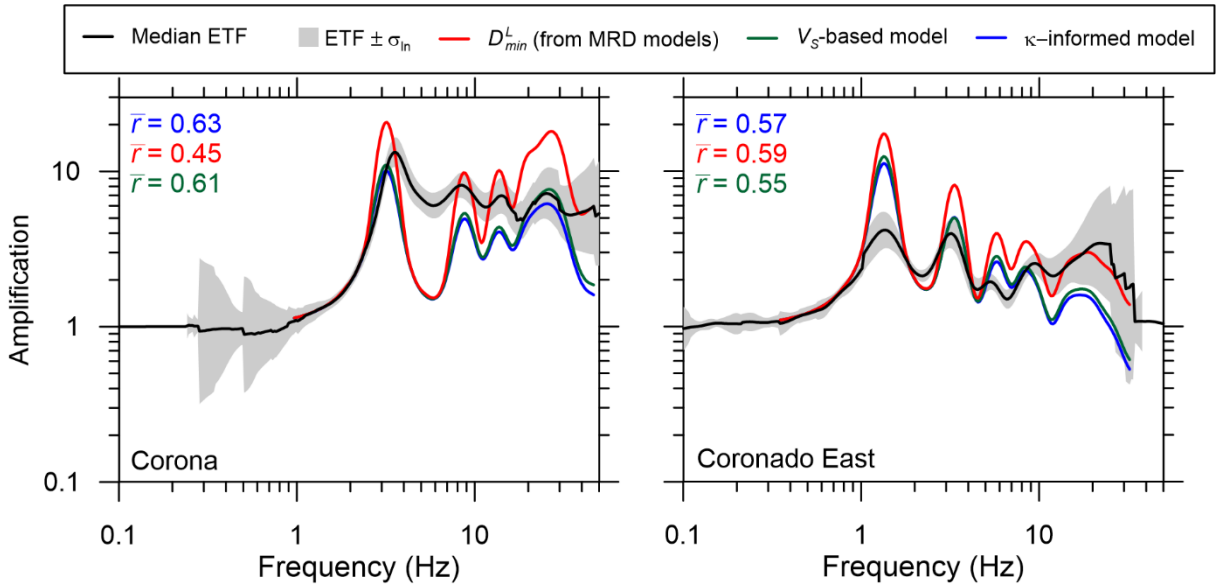

Figure 4.31. Comparison of ETF and TTFs Corona and Coronado East. Values of $\bar{r}$ for each damping model are shown in different colors (red: $D_{\min}^{L}$, green: V_S-based, blue: κ-informed).

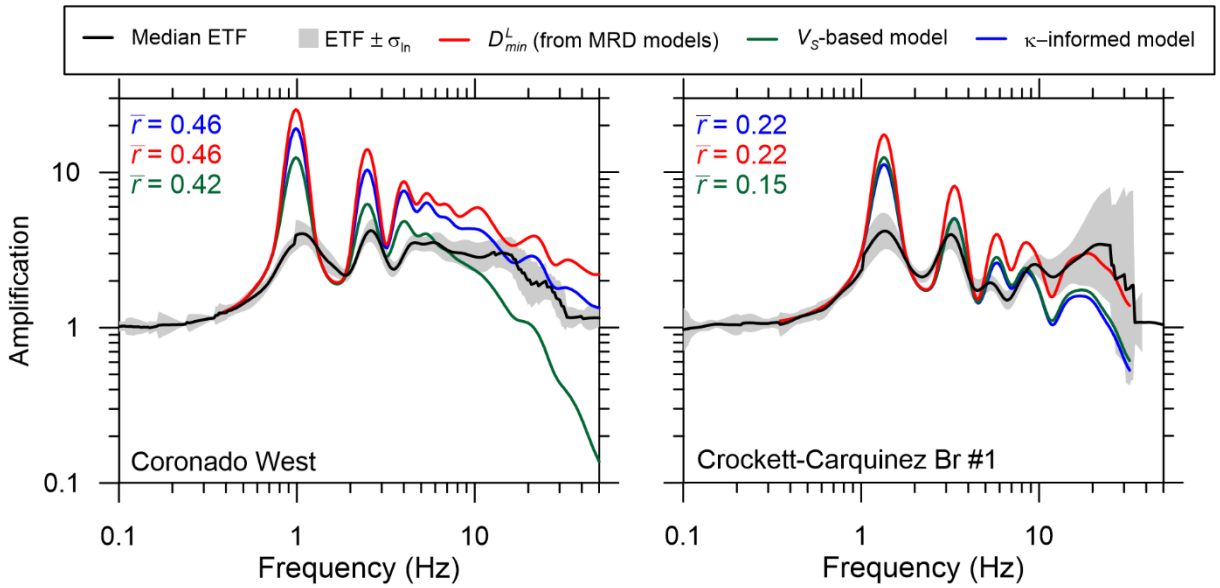

Figure 4.32. Comparison of ETF and TTFs for Coronado West and Crockett-Carquinez Br #1. Values of $\bar{r}$ for each damping model are shown in different colors (red: $D_{\min}^{L}$, green: V_S-based, blue: κ-informed).

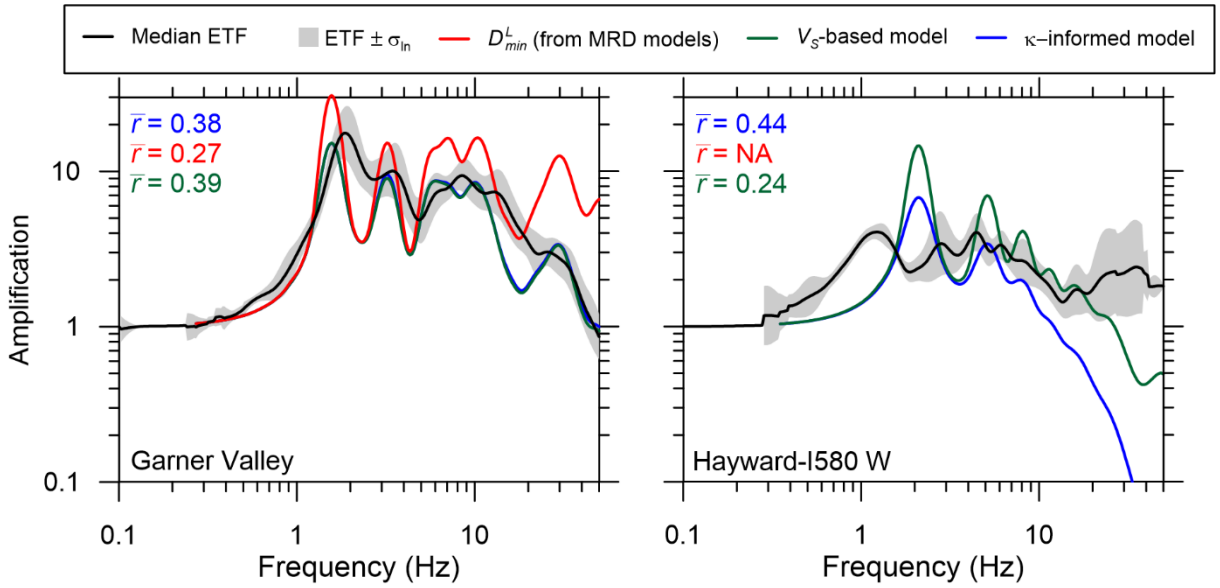

Figure 4.33. Comparison of ETF and TTFs for Garner Valley and Hayward-I580W. Values of $\bar{r}$ for each damping model are shown in different colors (red: $D_{\min}^{L}$, green: V_S-based, blue: κ-informed).

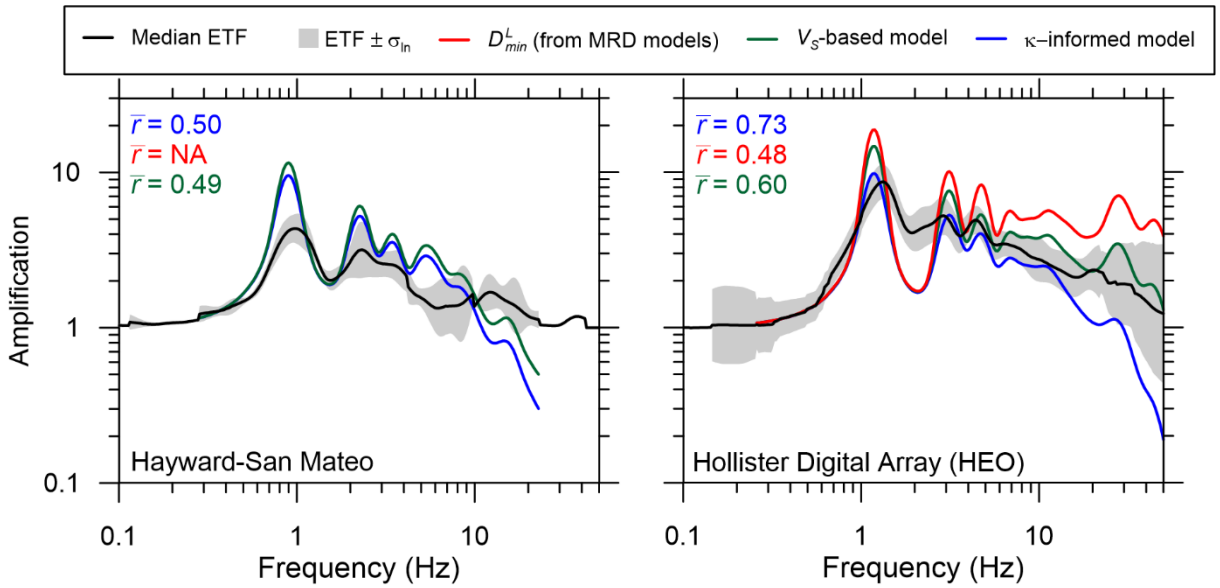

Figure 4.34. Comparison of ETF and TTFs for Hayward-San Mateo and Hollister Digital Array (HEO). Values of $\bar{r}$ for each damping model are shown in different colors (red: $D_{\min}^{L}$, green: V_S-based, blue: κ-informed).

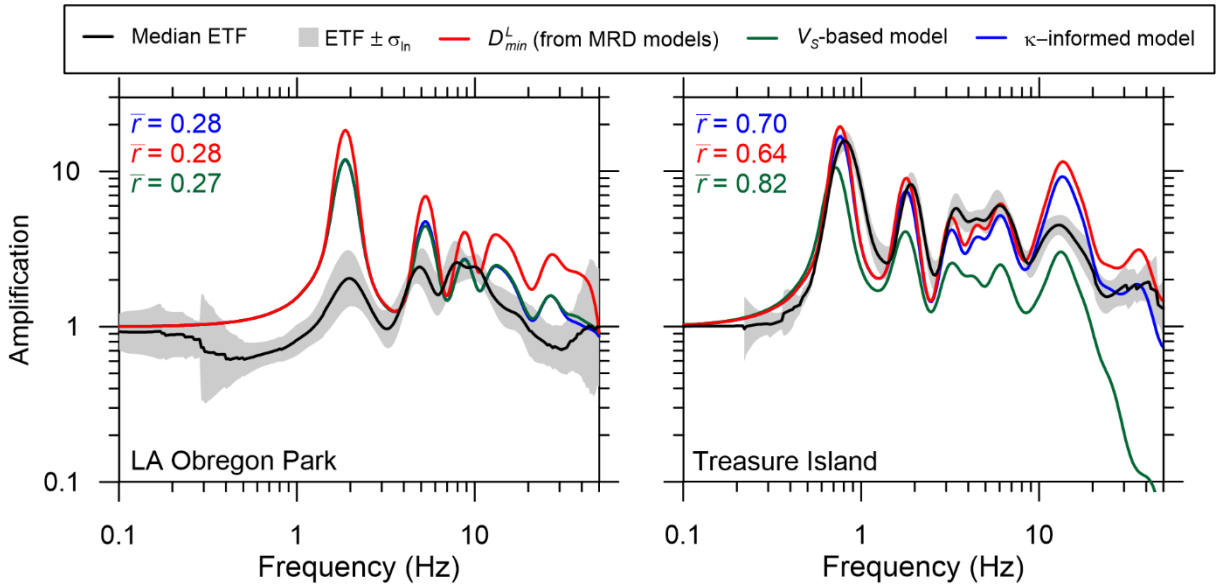

Figure 4.35. Comparison of ETF and TTFs for LA Obregon Park and Treasure Island. Values of $\bar{r}$ for each damping model are shown in different colors (red: $D^{L}_{\min}$, green: V_S-based, blue: κ-informed).

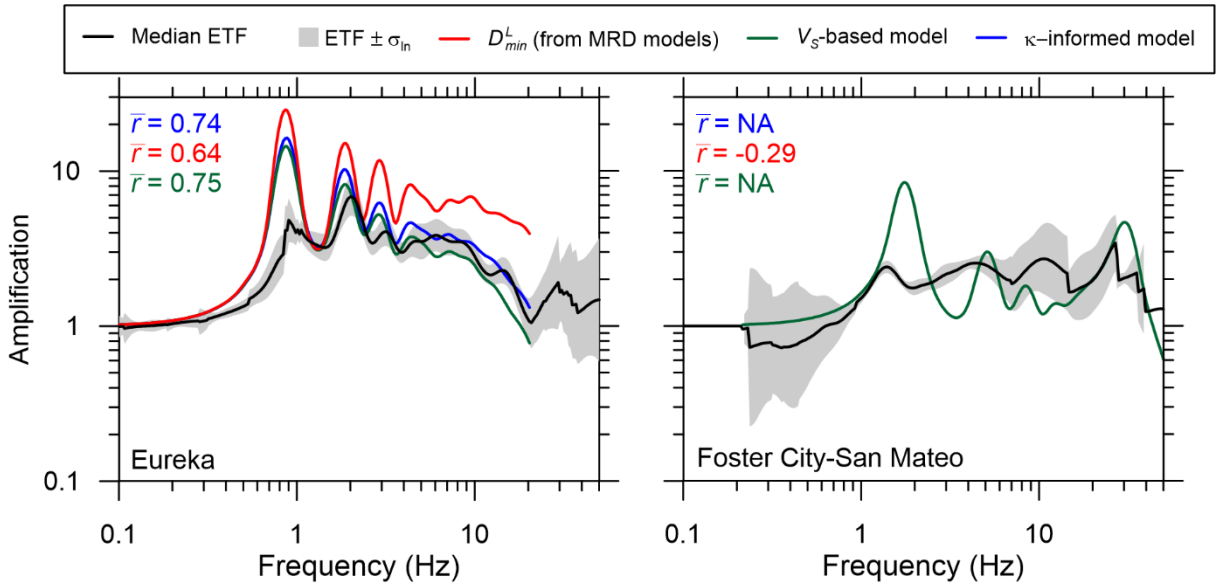

Figure 4.36. Comparison of ETF and TTFs for Eureka and Foster City-San Mateo. Values of $\bar{r}$ for each damping model are shown in different colors (red: $D^{L}_{\min}$, green: V_S-based, blue: κ-informed).

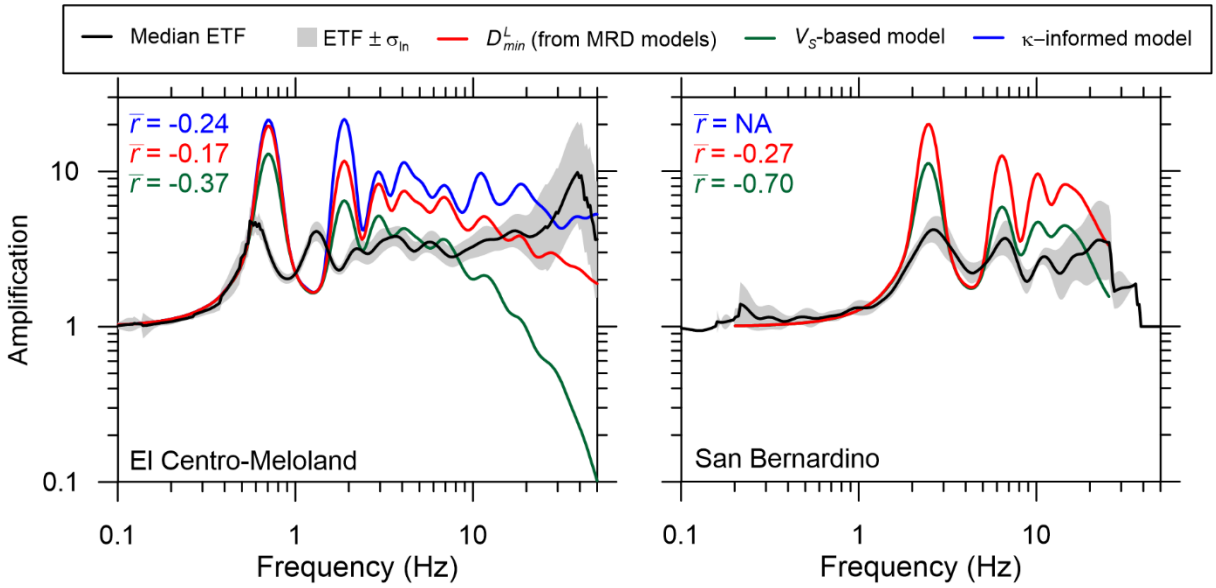

Figure 4.37. Comparison of ETF and TTFs for El Centro-Meloland and Treasure Island. Values of $\bar{r}$ for each damping model are shown in different colors (red: $D^L_{\min}$, green: V_S-based, blue: κ-informed).

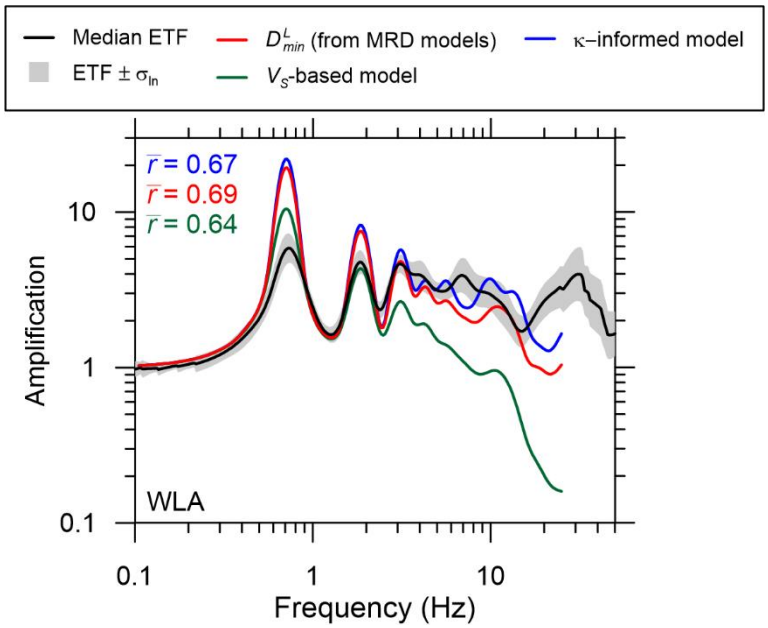

Figure 4.38. Comparison of ETF and TTFs for Wildlife Liquefaction array (WLA). Values of $\bar{r}$ for each damping model are shown in different colors (red: $D^L_{\min}$, green: V_S-based, blue: κ-informed).

Figure 4.37 shows histograms of $\bar{r}$ from the California vertical array sites using the three damping models (geotechnical, V_S-based, κ-informed). Also shown for comparison is the distribution from Thompson et al. (2012) for KiK-net sites, although the optimization of damping performed in that study makes the comparison somewhat 'apples-to-oranges', with Japan sites expected to have higher $\bar{r}$. I see that California sites have higher values of $\bar{r}$ in aggregate, with a higher population median and lower standard deviation. There is also a higher percentage of sites with strong correlation ($\bar{r} > 0.6$) in comparison to their counterparts for the KiK-net arrays in Japan regardless of the damping model. This suggests that the ability of GRAs to match observation is better for the California vertical arrays than for KiK-net sites.

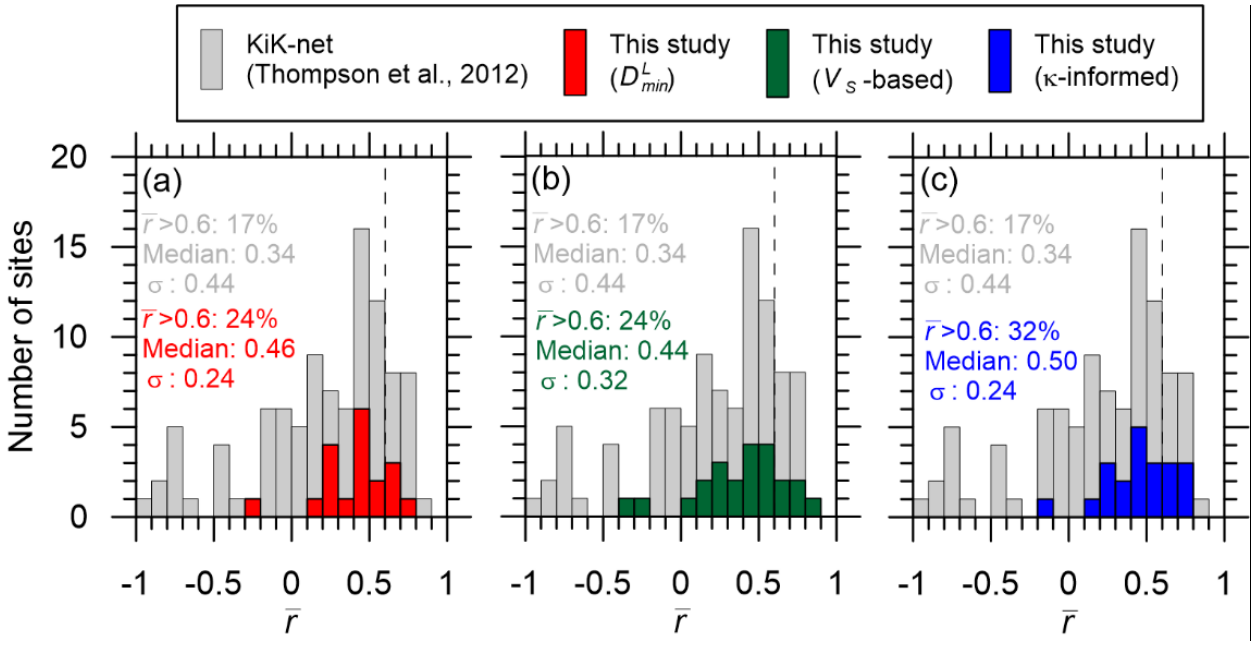

Figure 4.39. Histograms of $\bar{r}$ for California and KiK-net sites as well as their medians and standard deviations. Values and summary statistics of $\bar{r}$ for each damping model are shown in different colors for California sites (red: $D^L_{\min}$, green: V_S-based, blue: κ-informed model).

As described in Section 4.3.2, Thompson et al. (2012) introduced a metric of ETF variability that is useful to consider in combination with $\bar{r}$ because it quantifies event-to-event

variability in observed site response across the vertical array. This metric is computed by first taking the natural log standard deviation of ETF ordinates for each of the frequencies considered in the analysis of $\bar{r}$ (i.e., between the lower and upper bound frequencies $f_{\min}$ and $f_{\max}$). Then the median across those standard deviations is taken, which is denoted σ_{ln}^{M}. Figure 4.40 shows the distribution of σ_{ln}^{M} for the California vertical array sites, with the values reported by Thompson et al. (2012) for the KiK-net sites also shown for comparison (the method of computation is the same in both cases). The inter-event dispersion is notably smaller for the California sites, with only two (10%) exceeding the value of 0.35 considered as 'high dispersion' by Thompson et al. (2012).

The better fit and smaller ETF dispersion encountered for the California sites as compared to the KiK-net sites may result from the former mostly being located within large sedimentary basins and relatively flat areas, whereas the later are often on firmer ground conditions (often weathered rock or thin soil over rock) with uneven ground conditions. The geologic conditions at the KiK-net sites are such that horizontal layering of sediments is less likely to be an acceptable assumption, with the site response being strongly influenced by 2D and 3D effects associated with irregular stratigraphy and (in some cases) topography. The 2D and 3D effects in site response in KiK-net sites has been studied by De Martin et al. (2013) which suggests the period and amplitude of site response peaks are significantly sensitive to 2D and 3D effects due to non-horizontal layering. Another possible factor resulting in a better fit for California sites is the quality of V_S measurements. The vertical arrays in California used in this study have high-resolution suspension logging measurements (with Garner Valley being the only exception), while the KiK-net sites are characterized with lower-resolution downhole measurements.

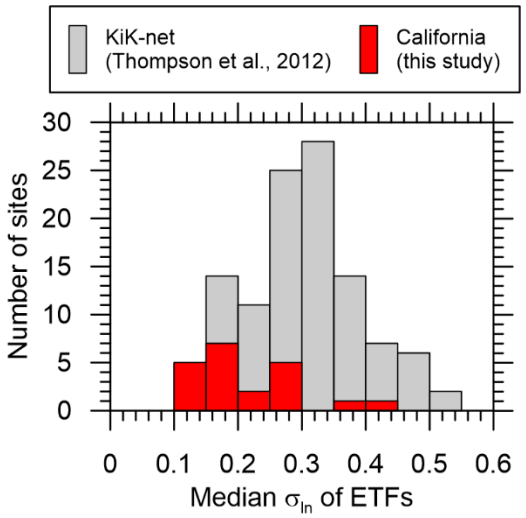

Figure 4.40. Histogram of ETF between-event standard deviation term σ_{ln}^{M} for California and KiK-net vertical array sites.

4.4 ANALYSIS OF *PSA* AMPLIFICATIONS

In this section, I examine features of site amplification for the inventory of California vertical array sites from Chapter 3 in the form of *PSA* amplification. The objective of the analysis presented here is in part complimentary to the analysis of transfer function results, in that I seek insight into GRA model effectiveness for the three considered damping models. However, in addition, I will present an approach that can be used to quantify uncertainty in the prediction of site response as estimated from GRA. This uncertainty quantification is of interest for PSHA in which site terms are taken from the results of GRA, in which case epistemic uncertainties in the site response should be considered using a logic tree framework.

Subsequent sections describe the methodology for statistical analysis of the data to infer bias and uncertainty, present results as derived from the California data, and compare to comparable results obtained previously for KiK-net sites (Kaklamanos et al., 2013).

4.4.1 Residuals Analysis to Quantify Bias and Uncertainty of Site Response Predictions from GRA

Our analysis of epistemic uncertainty is based on comparing observations (in this case, the surface recordings at California vertical array sites) to predictions. I use 5%-damped *PSA* of the recorded and predicted surface ground motions. I use the RotD50 parameter which is the median single-component horizontal ground motion across all non-redundant azimuths (Boore 2010). In order to quantify the misfits between the predictions and recordings, I compute the residuals between the recorded and predicted *PSA* in natural logarithmic space:

$$R_{G,kj} = \ln\left(Z_{kj}^{obs}\right) - \ln\left(Z_{kj}^{pre}\right) \tag{4.14}$$

where $R_{G,kj}$ is the residual for recording j at site k, Z_{kj}^{obs} is the observed intensity measure (generally *PSA* at a certain oscillator period), and Z_{kj}^{pre} is the predicted intensity measure. Quantity Z_{kj}^{pre} has source, path and site attributes; source, path, and site attributes below the level of the input motion are fully captured by the downhole input motion, and only the site response is computed.

4.4.2 Results from California Data

One example of predicted/recorded *PSA* plots and the computed residual is shown in Figure 4.41. Positive residuals indicate underprediction and negative residuals indicate overprediction of the recorded ground motion by GRA. Because the downhole recording is used in the calculation of Z_{kj}^{pre}, any misfit in the prediction of the surface motions is attributed to the misfits in site response.

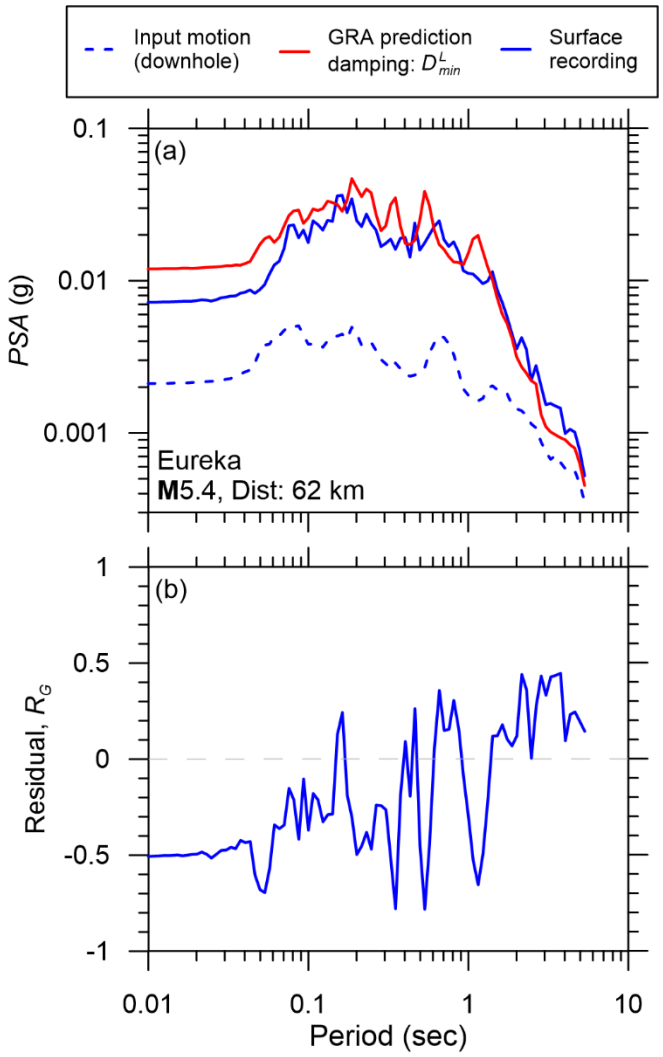

Figure 4.41. An example of (a) response spectrum plots of the downhole motion, surface recorded motion, and surface predicted motion at Eureka (M5.4, epicenteral distance: 62 km); (b) The plot of residuals between observed and predicted ground motions.

Because one objective of our analysis is to assess the performance of alternative small-strain damping models, I sought to identify recordings for which the dynamic soil behavior could, as a first approximation, be represented by layer-specific small-strain shear moduli (G_{max}) and damping (D_{min}). Kaklamanos et al. (2015) recommend that linear, visco-elastic GRA procedures can be used when the maximum shear strain in a soil column, $\gamma_{max} < 0.01$-0.1%. In the selection of recordings used in these analyses, I sought record sets with $\gamma_{max}<0.01\%$, to ensure that soil

nonlinearity is not appreciably affecting the GRA and resulting findings on damping models. In order to exclude strong recordings which are dominated by the effects of soil nonlinearity, I use shear strain index (I_γ) defined by Kim et al. (2016) as the ratio of input motion *PGV* to V_{S30} in order to approximate the maximum shear strain (γ_{max}) in the soil profile. After applying this screening, the data set consists of 250 recordings at 21 stations.

I perform mixed-effects regression with the LME routine in program R (Pinheiro et al., 2013) to partition the residuals into multiple components:

$$R_{G,kj} = c_{G,l} + \eta_{G,S,k} + \varepsilon_{G,kj} \tag{4.15}$$

where $c_{G,l}$ is the overall model bias, $\eta_{G,S,k}$ is the between-site residual (site term) for site *k*, which represents the average deviation from the prediction for an individual site, and $\varepsilon_{G,ij}$ is the within-site residual, which is the remaining misfit after removing the overall bias and the between-site residual. It should be noted that there is no event-to-event variability in the computed residuals because for the predicted motion (Z_{kj}^{pre}), the actual downhole recording has been used as the input motion. The lack of event-to-event variability eliminates any contribution from the variability in source effects (event terms). This makes Eq. (4.15) slightly different from what is customary in the analysis of residuals when utilizing ground motion data only from surface recordings. The term $\eta_{G,S,k}$ is the indicator of how well GRA is predicting site response for site *k*, with large absolute values of $\eta_{G,S}$ indicating poor prediction of site response. Two examples of $\eta_{G,S}$ plots for a site with good fit (La-Cienega) and poor fit (Corona) are shown in Figure 4.13.

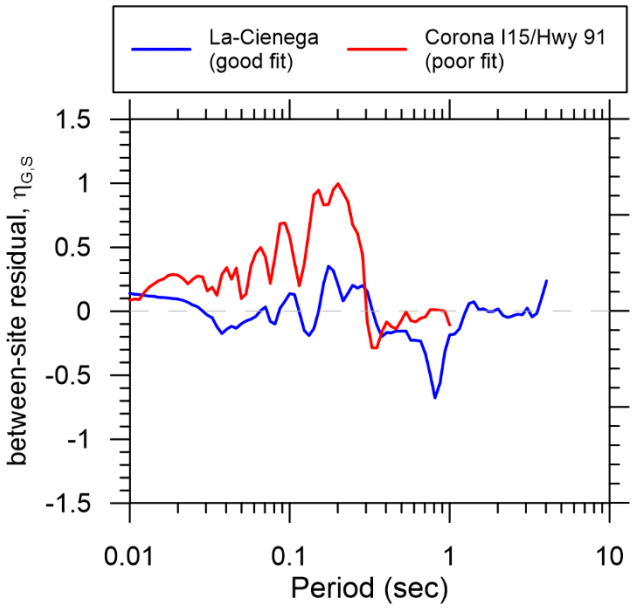

Figure 4.42. Plots of between-site residuals ($\eta_{G,S}$) for La-Cienega with a good fit; and Corona with a poor fit between recordings and predictions. The smaller values of ($\eta_{G,S}$) indicate a better fit.

The overall bias is plotted in Figure 4.43 for the three different damping models used in this study. The c_l for the three damping models have relatively similar trends with period, each having a relatively flat trend with period for T >~0.1 sec and negative residuals (indicating over-prediction) at short periods. The geotechnical model exhibits the least bias for T >~0.1 sec and the largest over-prediction bias at shorter periods. The V_S-based model tends to produce the largest damping, and has bias terms 0.2-0.4 larger than the geotechnical model. The κ-informed model provides intermediate results.

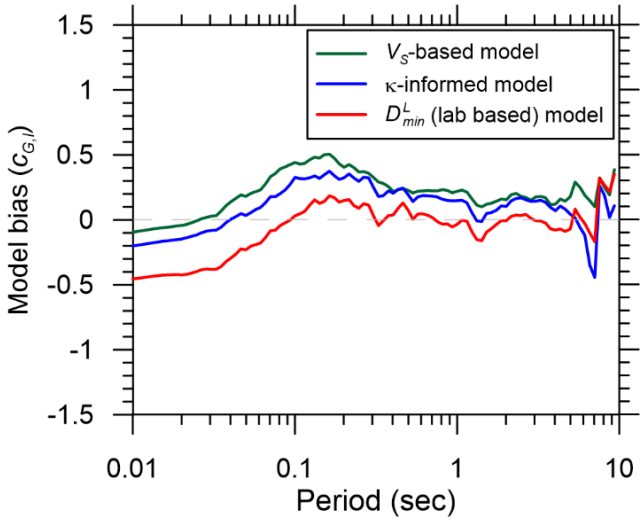

Figure 4.43. The overall bias ($c_{G,l}$) of GRA models in prediction of site response.

Figure 4.44-4.21 show the average total residuals ($c_{G,l}+\eta_{G,S,k}$) for all sites starting from the ones with lowest $R_V=V_{SDH}/V_{S5}$. In these figures, the site-specific bias can be studied for each individual site. I seek to find any trend between the behavior of sites with their characteristics. The figures show that the bias plots have a decrease (valley) near the site period, and do not show any trend with R_V. For example, both Wildlife Liquefaction array ($R_V=1.44$) and Borrego Valley ($R_V=12.22$) have a similar behavior despite very different levels of impedance contrast.

Furthermore, there is no evidence of any significant trend between the behavior of sites with the depth of the array. For example, La Cienega and Borrego Valley are the deepest arrays (depth: 245 and 235 m, respectively), however their behavior is not systematically different from the shallowest arrays, Benicia South and Bay Bridge (depth: 35 and 40 m, respectively) except for the valley near the site period happening at a shorter period (as expected).

Figure 4.44-4.21 also show no significant pattern in the performance of damping models with the properties of the sites (e.g. depth and R_V). The general pattern of overprediction and underprediction with the three damping models are similar to what is reflected in Figure 4.43 with the geotechnical model having the least bias, the V_S-based model being the most biased

(underpredicting) for long periods and the least biased for very short periods, and κ-informed model between the other two. This is the overall trend, and does not happen for all of the sites.

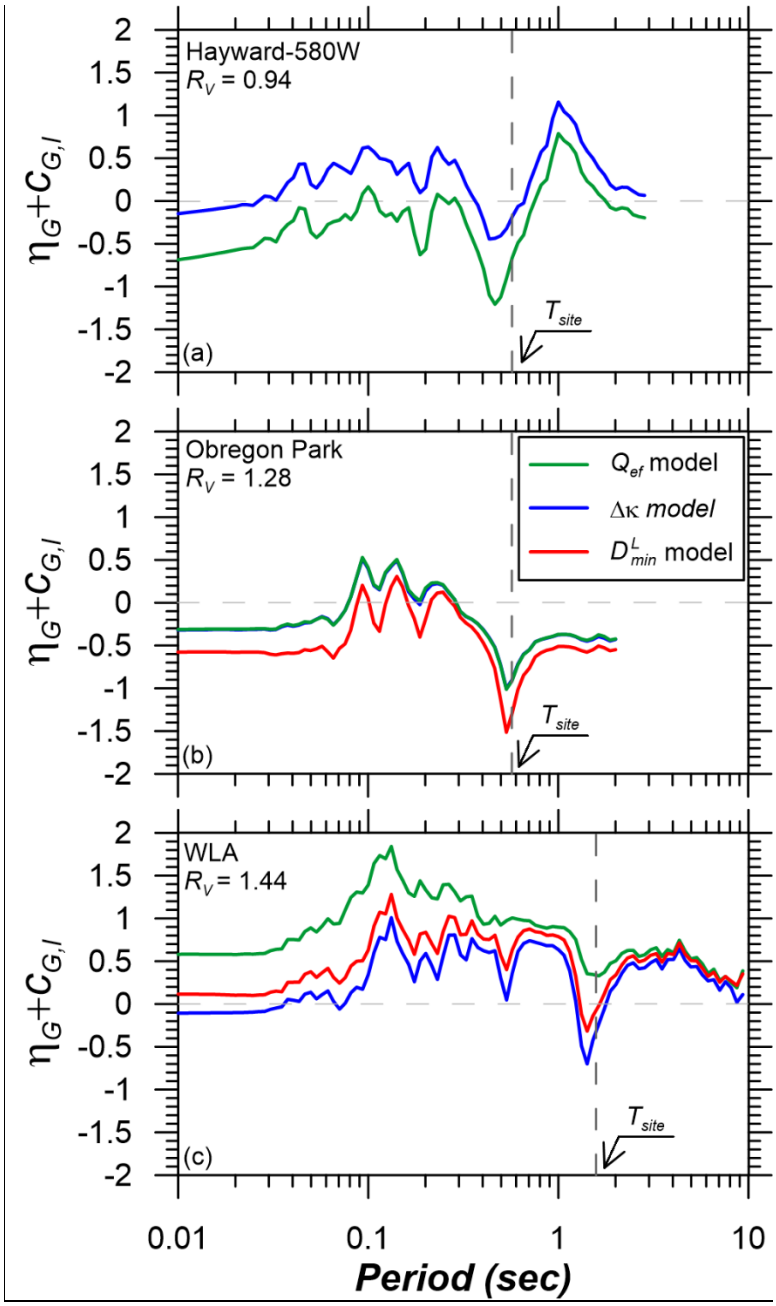

Figure 4.44. Comparison of total residuals (bias+site term) using the three models for damping for sites with different values of R_V: (a) Hayward-580 W, (b) Obregon Park, and (c) Wildlife Liquefaction Array (WLA).

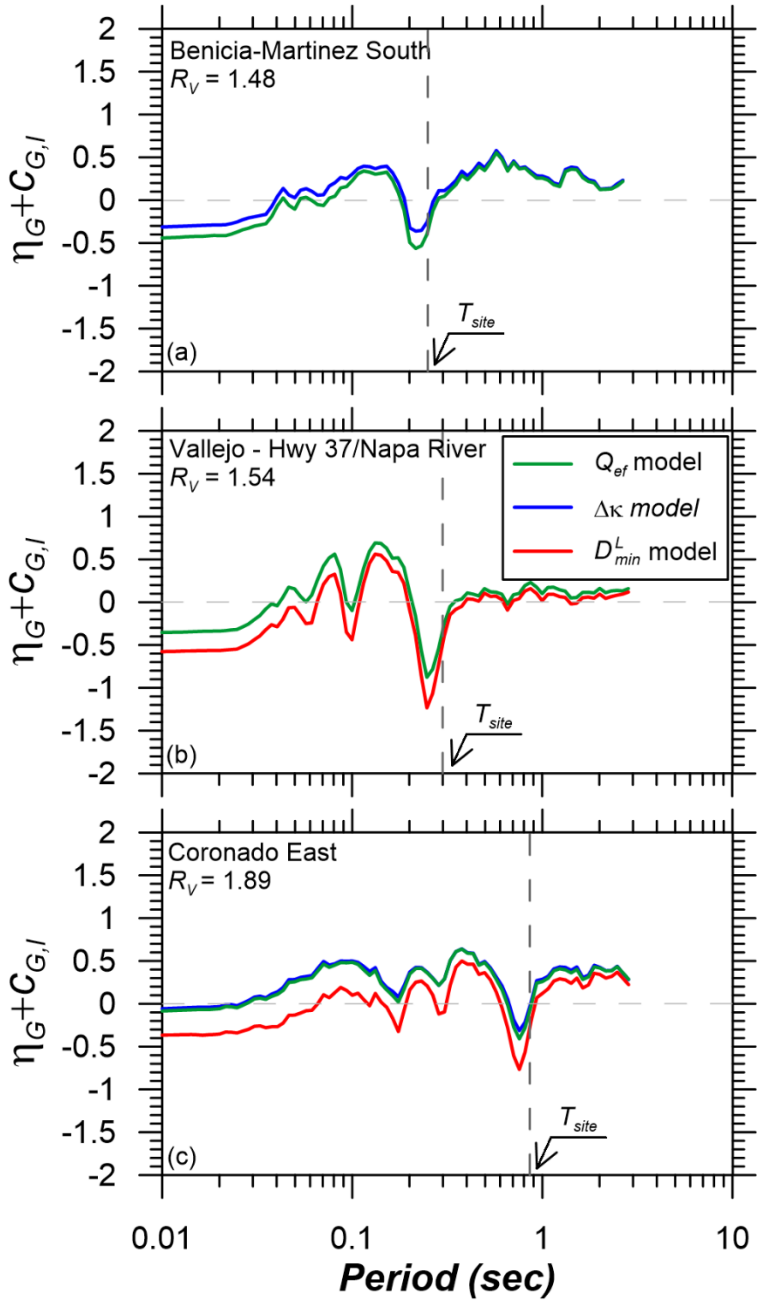

Figure 4.45. Comparison of total residuals (bias+site term) using the three models for damping for sites with different values of R_V: (a) Benicia-Martinez South, (b) Vallejo - Hwy 37/Napa River, and (c) Coronado East.

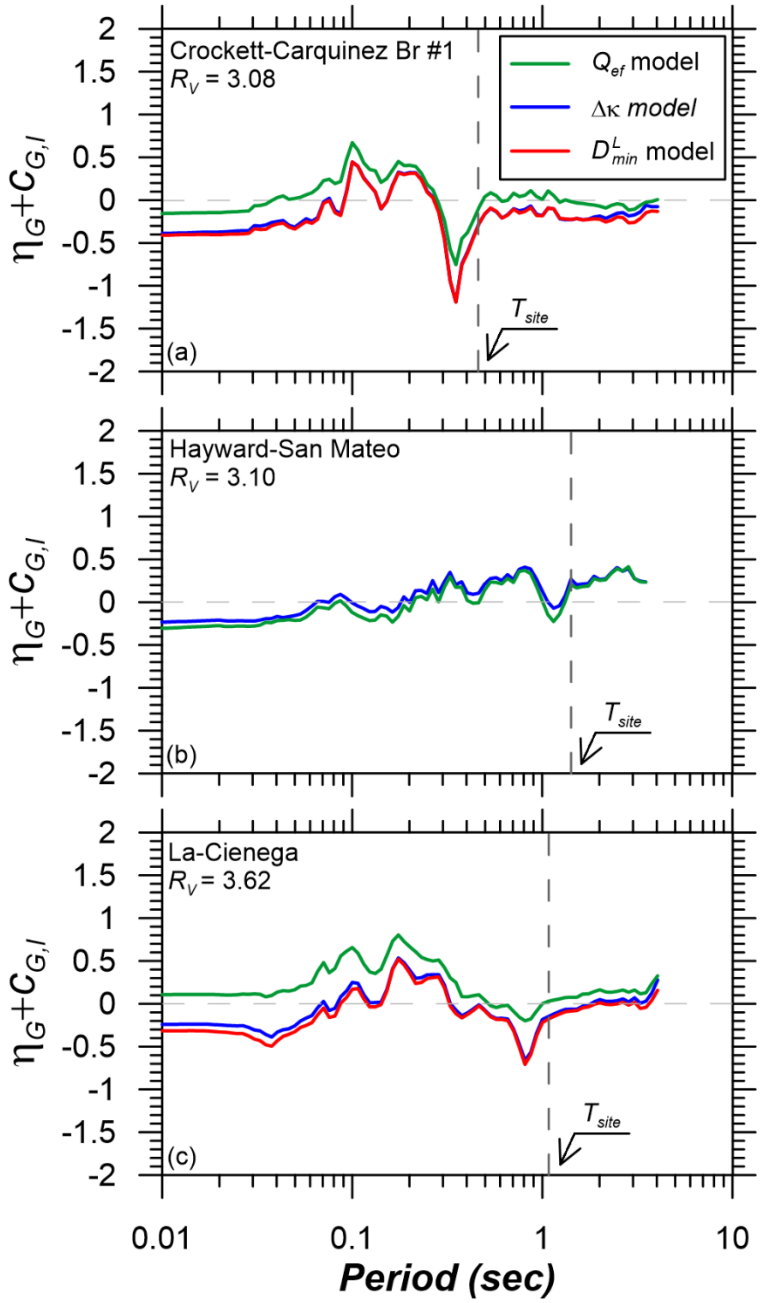

Figure 4.46. Comparison of total residuals (bias+site term) using the three models for damping for sites with different values of R_V: (a) Crockett-Carquinez Br #1, (b) Hayward-San Mateo, and (c) La-Cienega.

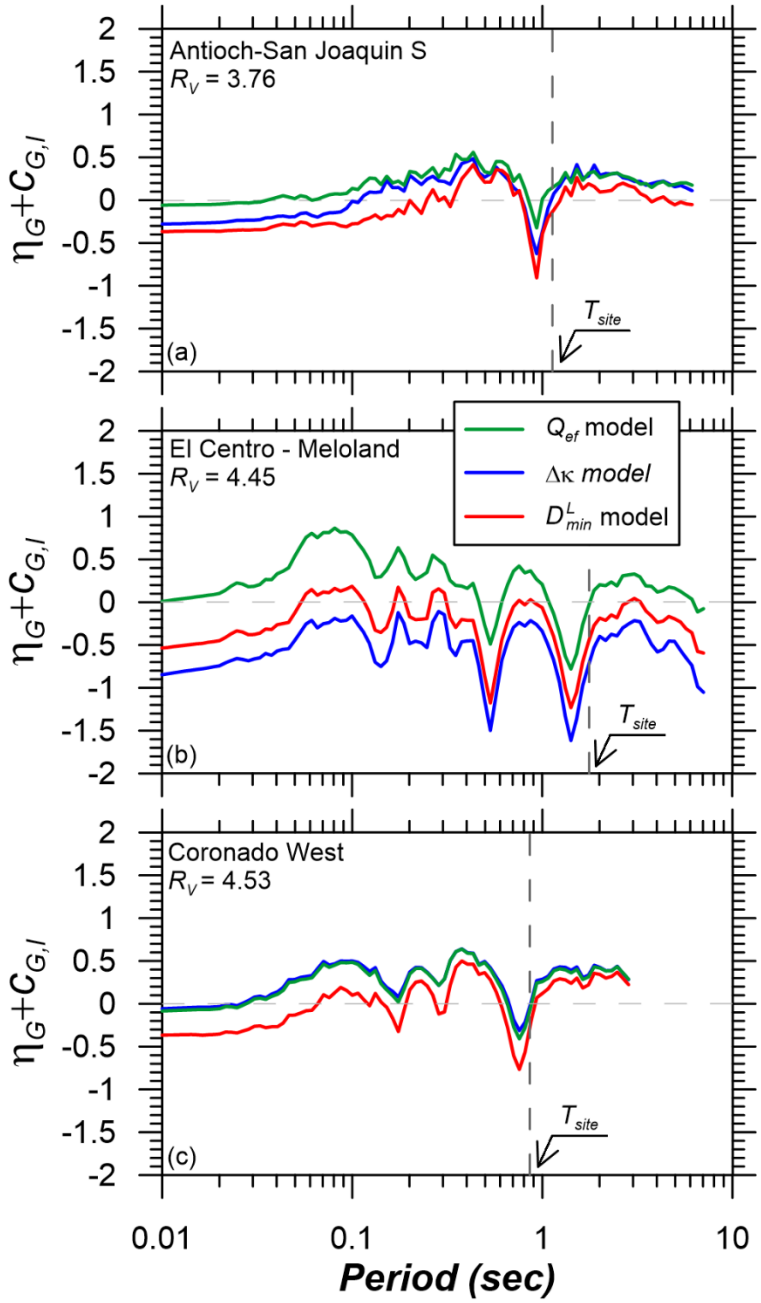

Figure 4.47. Comparison of total residuals (bias+site term) using the three models for damping for sites with different values of R_V: (a) Antioch-San Joaquin S, (b) El Centro - Meloland, and (c) Coronado West.

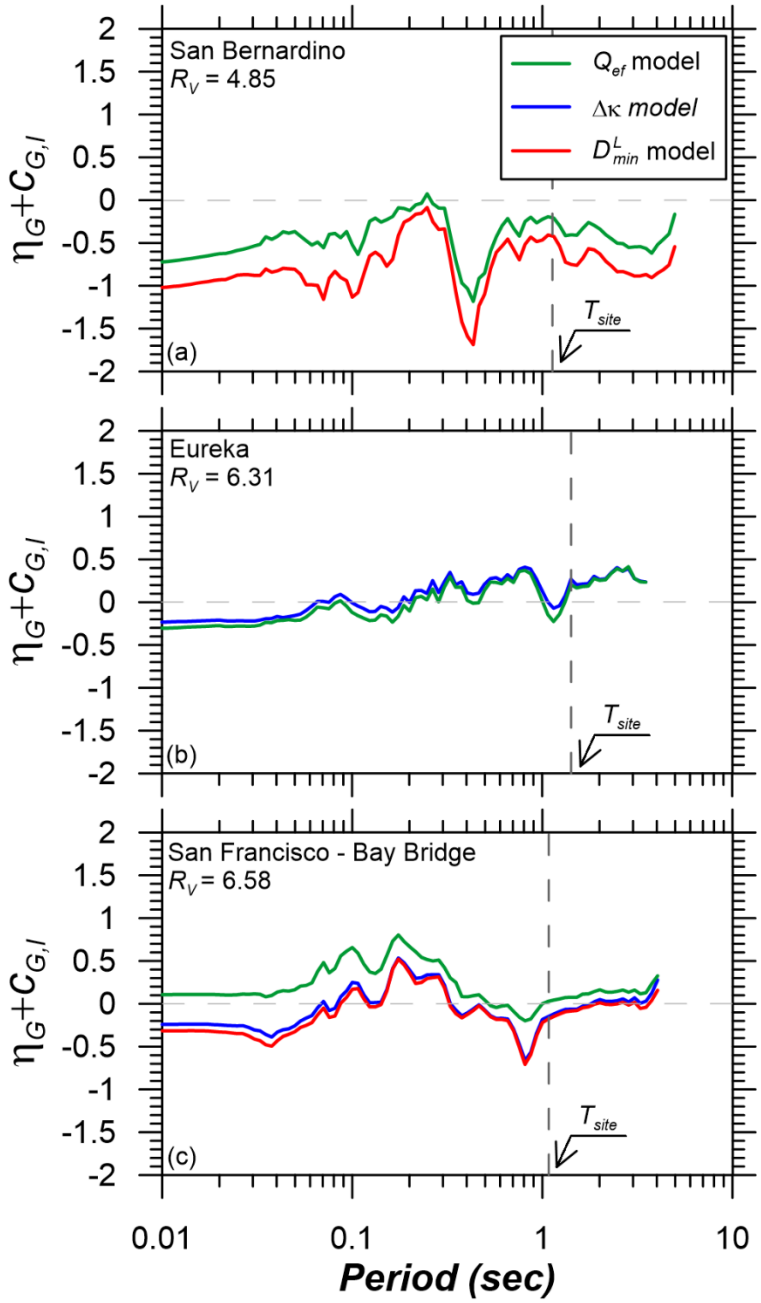

Figure 4.48. Comparison of total residuals (bias+site term) using the three models for damping for sites with different values of R_V: (a) San Bernardino, (b) Eureka, and (c) San Francisco - Bay Bridge.

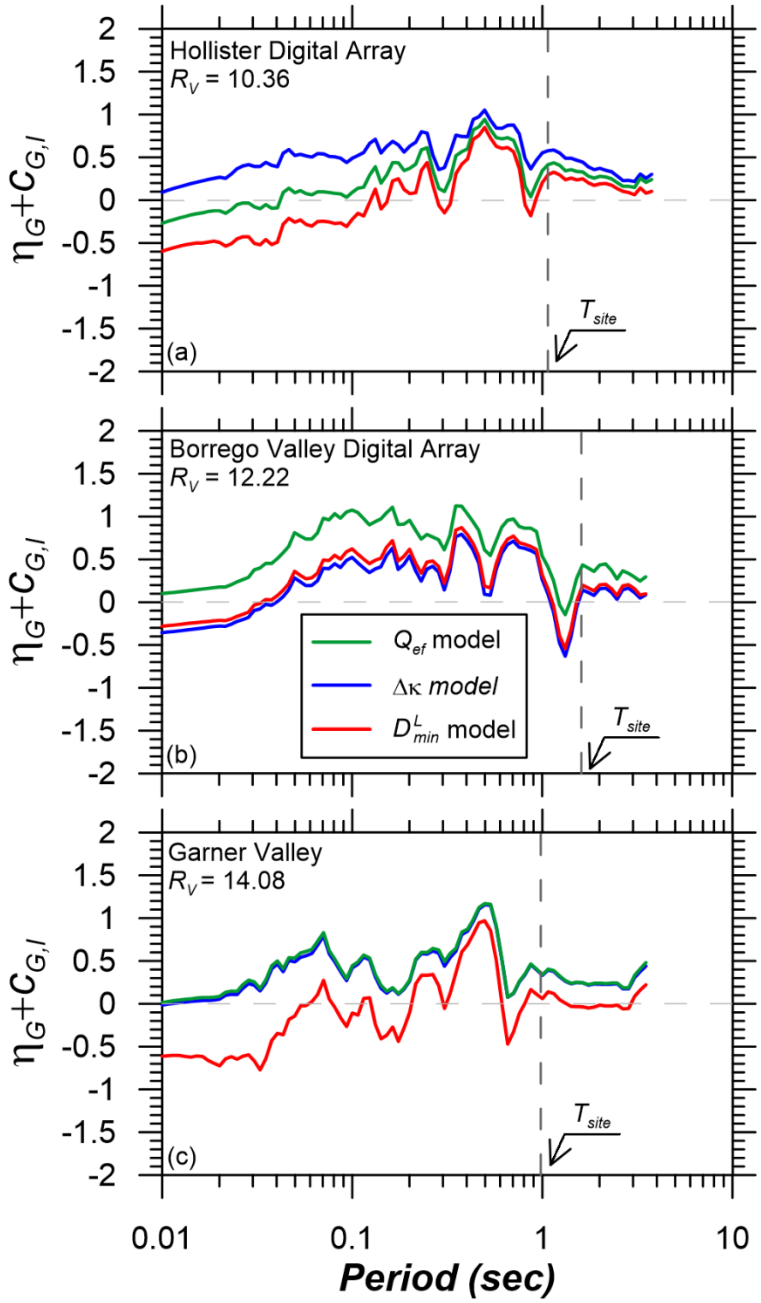

Figure 4.49. Comparison of total residuals (bias+site term) using the three models for damping for sites with different values of R_V: (a) Hollister Digital Array, (b) Borrego Valley Digital Array, and (c) Garner Valley.

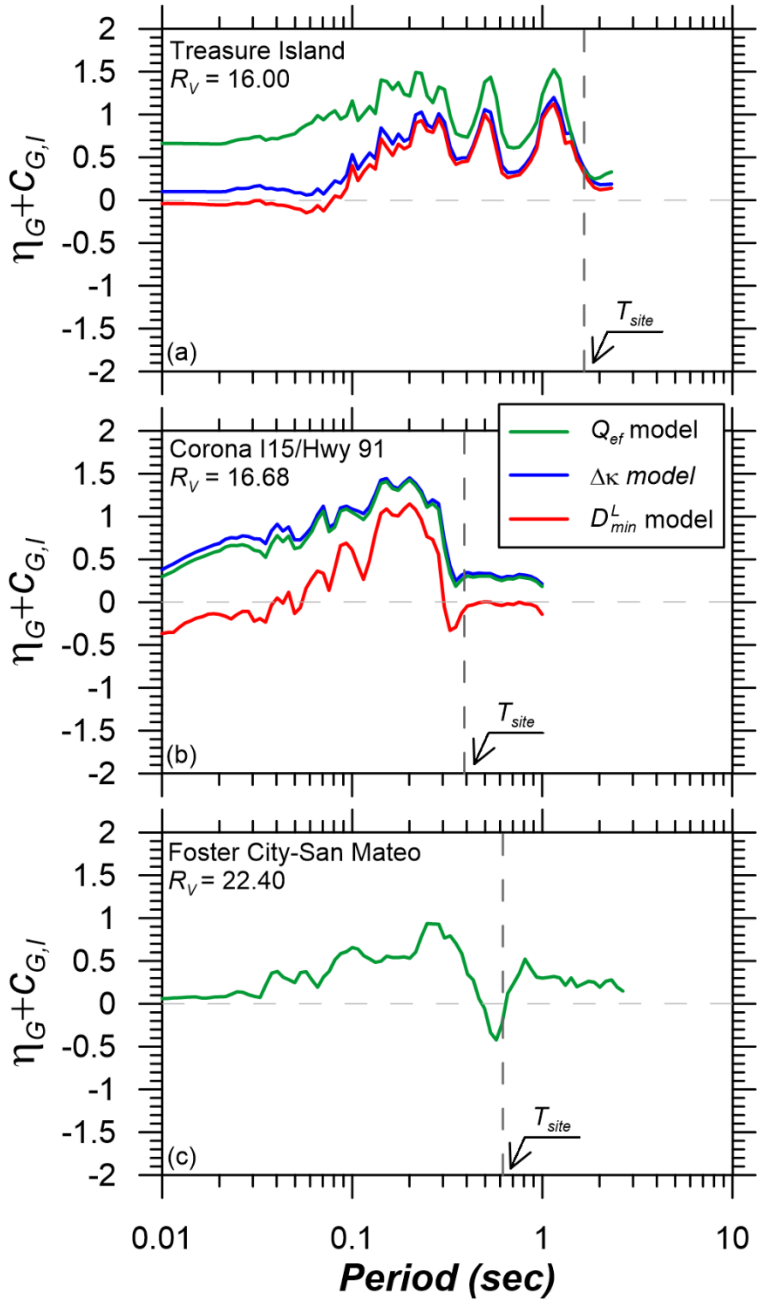

Figure 4.50. Comparison of total residuals (bias+site term) using the three models for damping for sites with different values of R_V: (a) Treasure Island, (b) Corona I15/Hwy 91, and (c) Foster City-San Mateo.

The standard deviations of the residuals are computed as follows:

$$\sigma_Y^2 = \tau_{G,S}^2 + \phi_{\mathrm{G,ln}Y}^2 \tag{4.16}$$

In the equation above, σ_Y, $\tau_{G,S}$, and $\phi_{G,lnY}$ are the standard deviation of $R_{G,kj}$, $\eta_{G,S,k}$, and $\varepsilon_{G,ij}$, respectively. In this study, I am mainly interested in $\tau_{G,S}$ which represents the site-to-site variability of the misfit in the prediction of ground motion using GRA. In other words, the epistemic uncertainty about how well GRA is able to predict the effects of site response is quantified by $\tau_{G,S}$. Figure 4.51 shows the period-dependence of the between-site variability $\tau_{G,S}$ and the within-site variability $\phi_{G,lnY}$. For $\tau_{G,S}$, the results of this study on the sites in California are slightly better for the κ-informed model for periods between 0.1 and 1 sec, showing that relating damping to κ can slightly improve the GRA and reduce the site-to-site variability, however I acknowledge that this difference is not very significant. The comparison to results in Japan is presented in the next section.

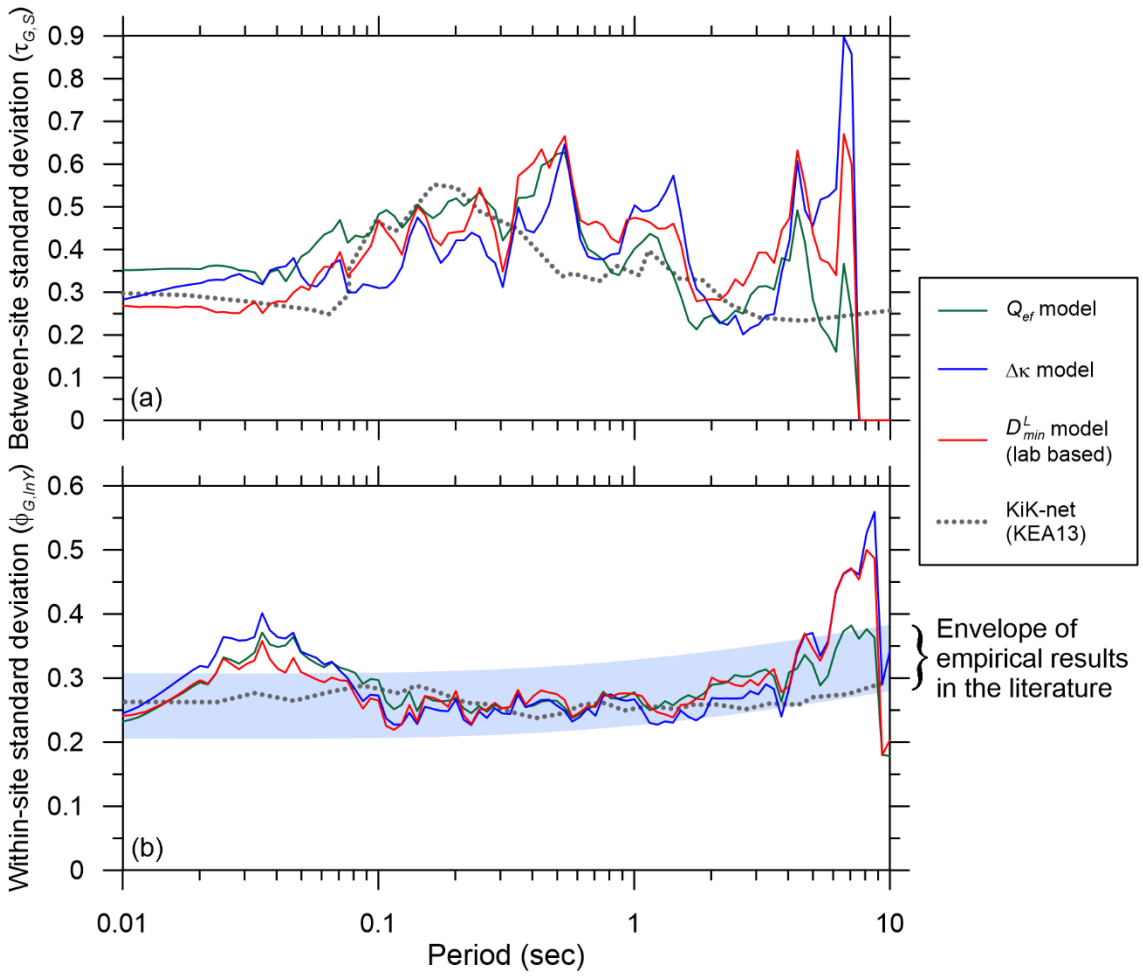

Figure 4.51. Comparison of (a) between-site standard deviation (τ_S), and (b) within-site standard deviation ($\phi_{G,lnY}$) for sites in California and KiK-net sites studied by KEA13 (Kaklamanos et al., 2013).

4.4.3 Comparison to Prior Results

Bias: Our results show the small-strain damping from geotechnical models provides the least bias in estimated site amplification at California vertical array sites for periods longer than 0.1 sec. This is contrary to the findings by previous studies on a small number of vertical array sites by Tsai and Hashash (2009), Elgamal et al. (2001), and Yee et al. (2013). Tsai and Hashash (2009) used vertical array data from the Lotung, Taiwan, (soft silts) and La-Cienega, California, (soft clay) arrays in a neural network based inverse analysis to extract soil properties. Because their analyses were not

constrained by model-based assumptions of soil behavior, they hold the potential to provide insights into in situ soil behavior. However, the approach does have the potential to map-modeling errors unrelated to soil behavior (e.g., lack of 1D response) into inverted soil properties. Shear-wave velocity models were slightly adjusted from data in the "learning" process and stress-strain loops were extracted. Modulus reduction and damping curves were then computed from the loops, which demonstrate stronger nonlinearity than laboratory-based curves (i.e., lower modulus reduction and higher damping). The observation of higher damping is also in agreement with system identification results obtained from Lotung data by Elgamal et al. (2001). In another study, Yee et al. (2013) analyzed vertical array data from the Kashiwazaki, Japan, Service Hall Array site (stiff deep soil) under relatively weak and strong shaking conditions. The weak motion data showed that D_{min} should be increased by 2-5% for GRA results to adequately capture observations. Increasing D_{min} by 2-5% will make the D_{min} estimations very close to the estimations from V_S-based model.

Kaklamanos and Bradley (2016) used recordings from two KiK-net sites, and observed positive (under-prediction) bias in linear GRA with lab-based D_{min}. In order to improve the results, they used a depth-dependent gradient for the V_S profile for eliminating unrealistically large steps in the V_S profiles, and decreased the lab-based D_{min} by 50%. This reduction of geotechnical model damping to achieve fit to data is the opposite of the observation from Tsai and Hashash (2009), Elgamal et al. (2001), and Yee et al. (2013). Given the fact that all of these studies are based on analyzing only one or two sites, it is not surprising that there is not a clear consensus on the issue of D_{min} in the available literature. By considering multiple sites, I anticipate the findings from California vertical arrays will be a valuable addition to the literature.

Variability: I compare our results of $\tau_{G,S}$ and $\phi_{G,lnY}$ with prior studies in the literature in Figure 4.17a and 4.17b, respectively. The only applicable study of which I am aware is Kaklamanos et al. (2013), who used the same KiK-net sites used by Thompson et al. (2012). Similar to Thompson et al. (2012), Kaklamanos et al. (2013) optimize damping for each site and recording, which improves fit to data relative to the application of damping models as in the present application.

The comparable values of $\tau_{G,S}$ shown in Figure 4.51a indicate levels of variability in California comparable to KiK-net sites. Therefore, while I observe no considerable regional dependency in dispersion of residuals when using *PSA* amplifications, I recognize the potential for countering trends: (1) the KiK-net site-to-site dispersion is likely reduced by the damping optimization, at least for high frequencies, and (2) the KiK-net dispersion would otherwise be expected to be higher than in California due to the relatively poor fit of 1D models to the observations.

In Figure 4.51b, the $\phi_{G,lnY}$ plot from California is slightly higher than $\phi_{G,lnY}$ for KiK-net sites, but interestingly, I see the California results fitting inside the approximate range for ϕ_{lnY} recommended in Chapter 2. The results of these studies on ϕ_{lnY} have a flat trend with period, and are remarkably consistent despite the differences in their methods of analysis and their databases.

4.5 SUMMARY OF THE RESULTS AND RECOMMENDATIONS

In this study, I utilized a database of recordings from vertical array sites in California in order to study the performance of 1D GRA in predicting site response effects between the downhole and surface instruments. The performance of the 1D assumption was studied by computing theoretical and empirical transfer functions, and a goodness of fit parameter (r) was

used as an indicator of how well the shapes of theoretical and empirical site response transfer functions are matching. The shape of the transfer functions are mainly controlled by the position of the peaks, and a good match (r>0.6) indicates the 1D model is able to predict the frequencies of different resonance modes. I also quantified the dispersion in empirical transfer functions with the assumption of a log-normal distribution for the transfer function. The goodness of fit parameter (r) and the median standard deviation (σ_{ln}) of the transfer functions from California vertical array sites were compared to the similar results from Thompson et al. (2012) study on KiK-net sites. I observed a better goodness of fit and less dispersion for California sites, which indicates better predictability of site response transfer functions. However, it is worth mentioning that the goodness of fit for a vertical array does not necessarily indicate that 1D GRA would perform well for predicting the surface ground motion at a site. In fact, the ability of vertical arrays for validation of 1D GRA is limited by their depth if the array does not go deep enough to reach a stiff bedrock representing "reference" conditions. For example, the high value of the goodness of fit parameter ($\overline{r}$) for WLA site is an indicator of good performance of 1D GRA for predicting site response between the surface and the downhole sensor which is 100 m deep. However, the site is located in a large basin which is several kilometers deep, and the downhole sensor is located in a soil layer with V_S=257 m/s. In this case, the effects of the deep basin on surface waves and the amplification of long period ground motions are expected, but the amplification would affect the motions both at the surface and the downhole, therefore the amplification of long periods cannot be observed using the recordings from the vertical array. In other words, 1D GRA can work well for site response between surface and downhole, but it may not work as accurately for site response between the deep bedrock and the surface if the downhole sensor does not reach the bedrock depth. Therefore, caution needs to be taken when using 1D GRA for deep basin sites as discussed in

Chapter 2. Another example of a deep basin site (LA La Cienega) is shown in Figure 4.52. In this case, the measurements are compared to the estimation from SCEC Community velocity model version 4 (See Small et al., 2017). The SCEC model estimations go much deeper, and reach more competent materials which are located far below the downhole sensor (Note that depth is shown in logarithmic space). As such, we do not expect the vertical array to capture the global site response modal frequencies.

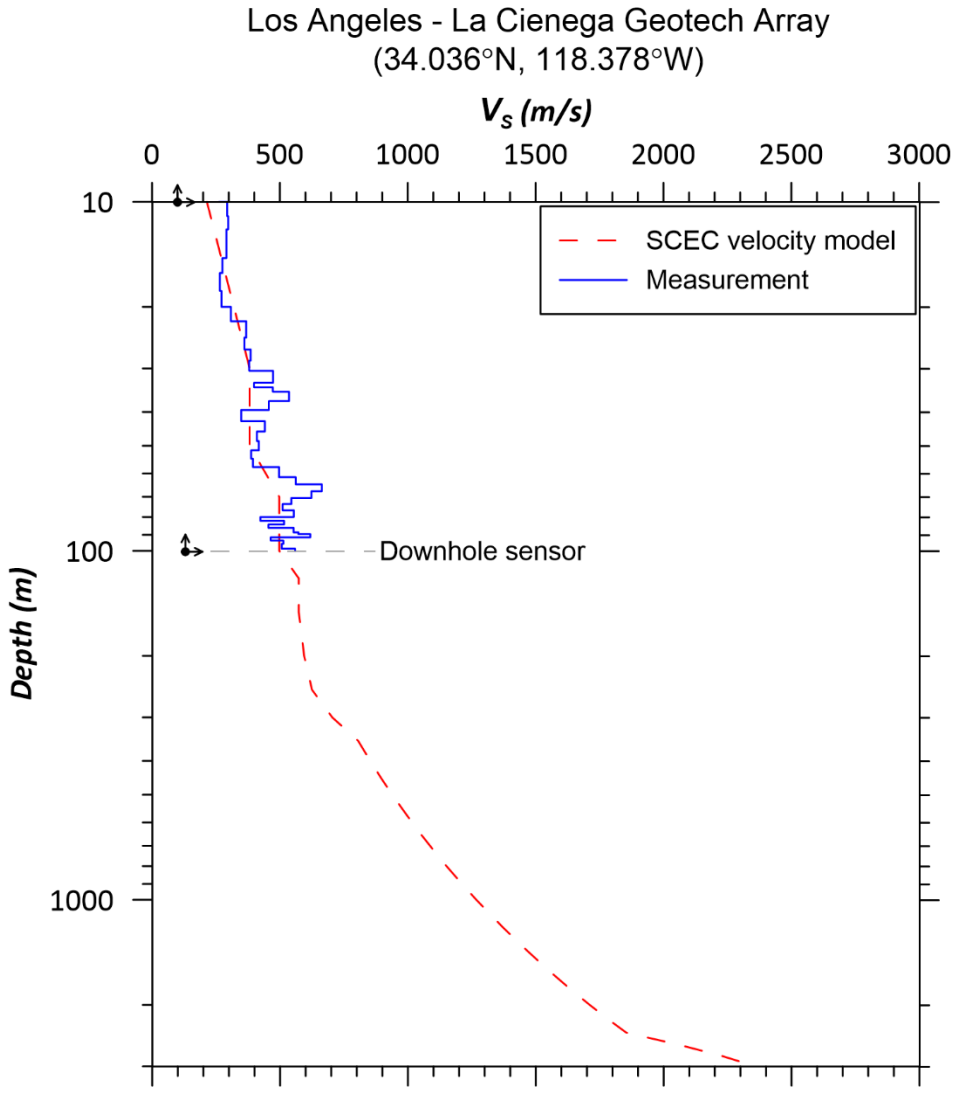

Figure 4.52. Shear wave velocity measurements for LA La Cienega site and comparison to the prediction by SCEC velocity model (Magistrale et al., 2000)

We also quantified the bias and dispersion of 1D GRA predictions of *PSA* amplifications with three different models for small-strain damping. I used bias to compare the effectiveness of the three models for estimating in-situ small strain damping. For most of the period range (T >~0.1 sec) the lab-based damping provides an unbiased estimate of site response, and the V_S-based model is unbiased for very short periods (T <~0.02 sec), and the bias from GRA with κ-informed damping falling between the two other damping models. The lab-based and V_S-based model are completely empirical based on geotechnical parameters and V_S respectively. In the κ-informed model, the actual recordings at the site have been used as input parameters which makes the κ-informed model site-specific, and the site-specific nature of the κ-informed model leads to a slight decrease in site-to-site variability ($\eta_{G,S}$). This indicates a potential predictive power in κ for estimation of in-situ D_{min} in 1D GRA.

I compared the between-site and within site standard deviations of *PSA* amplification residuals for California sites to the results from KiK-net sites in Japan (Kaklamanos et al., 2013), and compare within site standard deviations to the empirical range recommended in Chapter 2. Unlike the results from transfer functions, the results indicate no significant regional dependency of dispersion for *PSA* amplification.

5 A physically Parametrized Model for Significant Duration in Active Crustal Regions

5.1 INTRODUCTION

We develop prediction equations for metrics describing the duration of strong ground motion using a global database for active crustal regions recently developed for the Next Generation Attenuation NGA-West2 project (Ancheta et al., 2014). I utilize functions in which source and path duration are additive (in arithmetic units, i.e., units of sec), consistent with prior work by Abrahamson and Silva (1996) and the second author (Kempton and Stewart, 2006 – hereafter KS06). The present work is, for the most part, an update of KS06 using the much larger NGA-West2 data set, which allows for broadening of the moment magnitude (**M**) and rupture distance (R_{rup}) ranges for which the equations are applicable, as well as some adjustments of the equations themselves to capture features of the data.

Prediction equations related to duration parameters published since KS06 include Bommer et al. (2009), Lee and Green (2014), Bora et al. (2014), and Boore and Thompson (2014). None of these studies utilize the large NGA-West2 data set to provide prediction equations for the significant duration parameters most often used for engineering applications. In particular, Bommer et al. (2009) utilize the older and smaller NGA-West1 data set (Chiou et al., 2008); Lee and Green (2014) focused principally on duration parameters for stable continental regions, but

perform comparative analysis using a small subset of active crustal region data compiled in 2001 (McGuire et al., 2001); Bora et al. (2014) utilize a European data set (Akkar et al., 2014) to develop predictive models for durations computed to optimize the fit of a stochastic ground motion simulation procedure to pseudo spectral accelerations computed from recordings (i.e., the durations are not measured directly from time series); and Boore and Thompson (2014) utilize the NGA-West2 data set, but focus solely on the path term (they do not present source or site terms). After our model was developed, Du and Wang (2016) also developed a model based on NGA-West2 database which expanded the usable magnitude range to **M**3-7.9 (similar to our model). Du and Wang (2016) has a different functional form in comparison to our model as discussed below.

A distinguishing feature of our model relative to other recent duration GMMs (Bommer et al., 2009; Lee and Green, 2014; Bora et al., 2014; and Du and Wang, 2016) is that I take the source and path contributions to duration as additive in arithmetic units (i.e., sec) and the source term is parameterized in physical terms. Other models take source, path, and site terms as additive in natural log units, which is multiplicative in arithmetic units. Source terms are typically linear functions of **M**. I hypothesize that path durations would be better represented as additive to those for source, based on the physics of the problem. In particular, path durations arise in part from the "spreading" of wave arrivals in time due to their different seismic velocities, a process that would be expected to produce path durations that scale approximately with site-to-source distance and to be essentially independent of source duration. I acknowledge that wave scattering provides another physical mechanism that contributes to path duration, and this mechanism is not unambiguously additive to source duration. Ultimately, the selected path function must have compatibility with the data, which I found to support an additive path duration function (described further in the *Path Model* section).

Subsequent sections of this chapter present the prediction equations and regression coefficients. This is followed by descriptions of the manner by which the coefficients were developed, and a review of model performance in terms of residuals analysis and comparisons to prior results in the literature.

The findings in this chapter have been published in a journal article by Afshari and Stewart (2016).

5.2 DATA SELECTION

I utilize the NGA-West2 database described by Ancheta et al. (2014). The version of the flatfile that I used in our analysis is dated 29 August 2013 and contains 21,539 pairs of duration parameters for two as-recorded horizontal components. Metadata accompanying each recording that is used in our work includes moment magnitude (**M**), rupture distance (R_{rup}), focal mechanism (based on T- and P-axis plunge angles; Boore et al., 2013), and the V_{S30} site parameter (time-averaged shear wave velocity in upper 30 m of recording site). Some sites also include the depth to the 1.0 km/s shear wave isosurface (z_1).

I initially adopted the data screening protocols of Boore et al. (2014) (hereafter BSSA14), some important aspects of which include requiring availability of magnitude, distance, and site metadata, using only data from active crustal regions, excluding records from large structures, and screening of data at large distance as a function of magnitude and instrument type (Figure 1 of BSSA14). I consider ground motions from Class 1 (CL1: mainshocks) and Class 2 (CL2: aftershocks) events (Wooddell and Abrahamson, 2014), using only events having at least four recordings. I exclude any records flagged as questionable by manual inspection by Ancheta et al.

(2014); specifically, I require that the "Spectra Quality Flag" under Column JK in the flatfile equals 0. This screening reduced the size of the data set to 11,284 duration pairs.

Records were further screened to remove accelerograms judged to be noise-dominated for a sufficient portion of the record length that much of the energy accumulation is unrelated to seismic wave arrivals. This was a non-trivial process that required considerable data analysis and judgement. To illustrate the issue, Figure 5.1(a) shows a record that is noise-dominated in the sense that the normal sequence of wave arrivals is obscured in the accelerogram and high-frequency energy is persistent throughout the recording. Conversely, the record in Figure 5.1(b) has clearly evident p- and s-wave arrivals and the frequency content changes across the signal duration. Both records pass screening criteria for GMMs predicting peak accelerations, velocities, and pseudo-spectral accelerations (such as BSSA14) because spectral ordinates are reliable over some frequency range, whereas I posit that the record in Figure 5.1(a) should not be selected for duration GMM development.

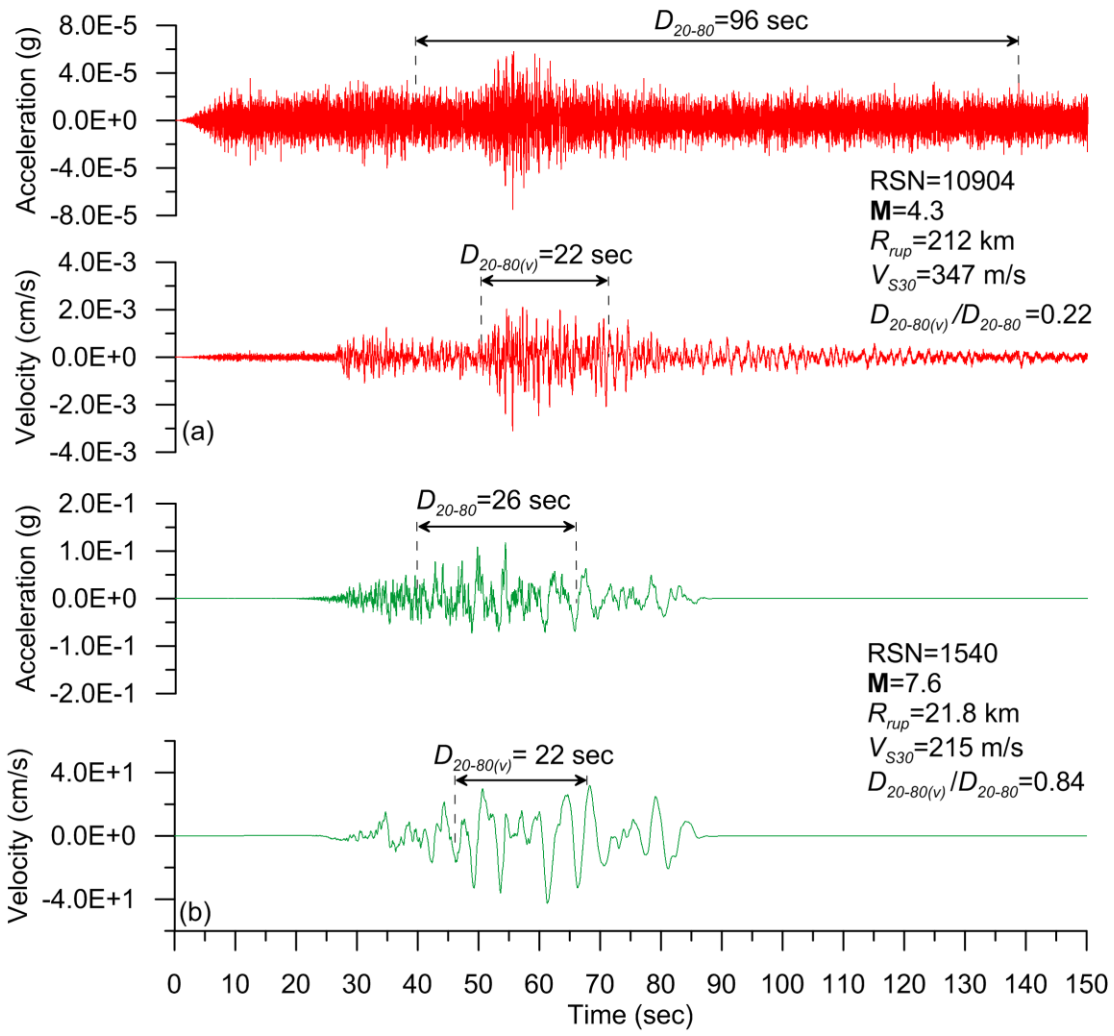

Figure 5.1. Examples of (a) low-amplitude record with duration parameters affected by noise (small value of $D_{20\text{-}80(v)}$ / $D_{20\text{-}80}$); (b) usable record with duration measures judged as reliable.

The reason for excluding records such as that in Figure 5.1(a) is the duration measured from the accelerogram is unreasonably large, reflecting signal noise. While these problems are often obvious from visual inspection, I sought to develop a relatively automated procedure given the large number of records in the NGA-West2 database. A feature I found to often be characteristic of the condition in Figure 5.1(a) is that durations measured from velocity time series are much shorter than those from accelerograms [the calculation of significant duration for velocity time series mimics that for acceleration, but with velocity substituted for acceleration in Eq. (1.5) (similar to Trifunac and Brady, 1975); result is denoted $D_{20\text{-}80(v)}$]. For screening purposes I flag

records with $D_{20\text{-}80(v)} / D_{20\text{-}80} < 0.65$ for visual inspection, and exclude records which appear to be noisy.

Following application of the above criteria, the data set consists of 22,390 individual-component duration values (11,195 pairs) for each duration parameter. I combine significant durations from the two as-recorded horizontal components to produce 11,195 geometric mean values. Figure 5.2 shows in red the data distribution in moment magnitude - rupture distance space as well as the subset of data also used by KS06 in blue. Data points shown in grey are those from the NGA-West2 database that did not pass BSSA14 screening criteria, while those in black were excluded by the duration ratio criteria and visual inspection.

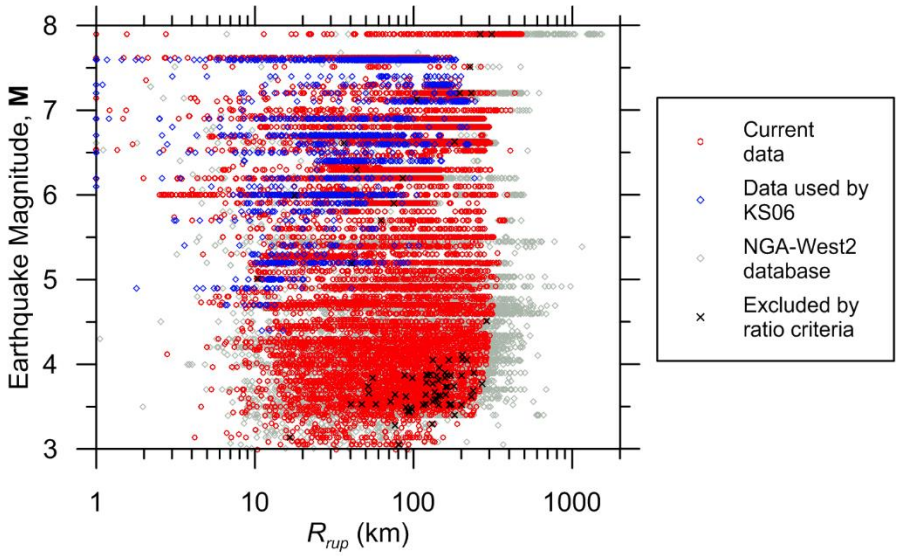

Figure 5.2. Magnitude and distance distribution of data used in the current work and KS06 (records with R_{rup} < 1 km are shown at 1 km). Data points in black were excluded based on the proposed duration ratio criteria and visual inspection.

5.3 THE EQUATIONS

I formulated equations in consideration of the physical factors described in the *Introduction* as well as subjective interpretation of nonparametric plots of data such as in Figure 5.3. Those plots

show the magnitude- and distance-dependence of duration for strike-slip earthquakes. The data are adjusted to a uniform site condition of V_{S30} = 760 m/s, using the site model described below (these corrections are small). Important features of the data that are evident from these plots include: the data are insensitive to changes in **M** for **M** < ~6, with modest increases at larger magnitudes; duration increases substantially with distance (i.e., the path duration) – when plotted on log-log axes, the path duration increases with distance in a nonlinear manner, generally becoming progressively steeper with increasing R_{rup} (this feature is consistent with the notion of path and source durations being additive in arithmetic units, whereas multiplicative models would be linear when plotted in log-log space as in Figure 5.3); the aforementioned trends with **M** and R_{rup} are consistently observed for the three considered duration parameters; and data dispersion decreases with increasing **M** and is smaller for $D_{5\text{-}95}$ than for $D_{5\text{-}75}$ or $D_{20\text{-}80}$.

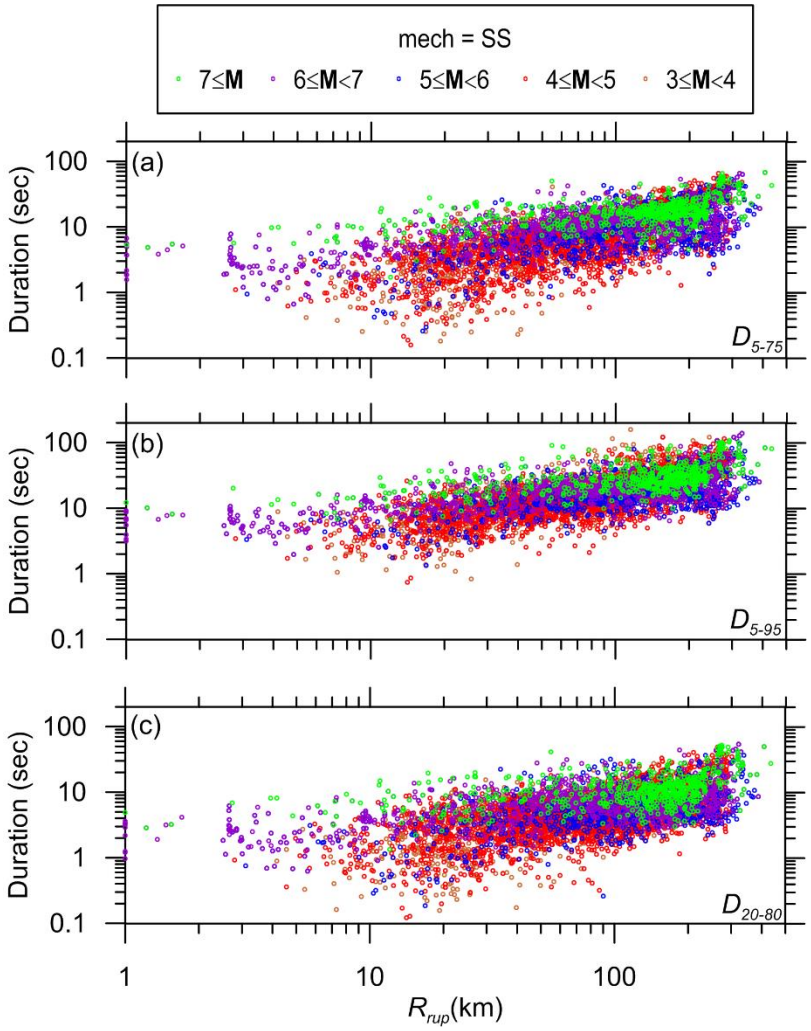

Figure 5.3. Variation with rupture distance of duration parameters for strike-slip earthquakes binned by M. **Records with R_{rup} < 1 km are shown at 1 km.**

I predict ground motion duration using the following expression:

$$\ln D = \ln\left(F_E\left(\mathbf{M}, mech\right) + F_P\left(R_{rup}\right)\right) + F_S\left(V_{S30}, \delta z_1\right) + \varepsilon_n \sigma\left(\mathbf{M}\right) \tag{5.1}$$

where ln$D$ is the natural log of significant duration; F_E and F_P are functions for source ("event") and path durations, respectively, expressed in units of sec; F_S is a site term that is additive in natural log units (hence multiplicative with the source and path durations); ε_n is the standard normal variate representing the fractional number of standard deviations of a single predicted value of ln$D$ away from the mean (e.g., ε_n= -1.5 is 1.5 standard deviations smaller than the mean); and

σ is the total standard deviation of the model. Although not shown here for brevity, the data were found to be log-normally distributed at confidence levels > 95% (using the Pearson chi-square normality test; Pearson, 1900) when de-trended in the form of residuals.

Source duration is taken as the inverse of the corner frequency (f_c) in the Fourier Amplitude Spectrum (Hanks and McGuire, 1981):

$$F_E = \begin{matrix} 1/f_0 & \mathbf{M} > \mathbf{M}_1 \\ b_0(mech) & \mathbf{M} \le \mathbf{M}_1 \end{matrix} \tag{5.2}$$

The use of a constant duration (b_0) at small magnitudes ($\mathbf{M} \le \mathbf{M}_1$) is motivated by the lack of **M**-dependence in the data for small magnitudes, as shown in Figure 5.3. Corner frequency is related to seismic moment and stress drop as (Brune, 1970, 1971):

$$f_0 = 4.9 \cdot 10^6 \beta \left(\Delta\sigma / M_0\right)^{1/3} \tag{5.3}$$

where β is the shear wave velocity at the source (taken as 3.2 km/s), $\Delta\sigma$ is stress parameter in bars (following KS06, I interpret $\Delta\sigma$ as an index parameter loosely related to stress drop for model-building purposes), and M_0 is the seismic moment in dyne-cm, which is computed as (Hanks and Kanamori, 1979):

$$M_0 = 10^{1.5\mathbf{M}+16.05} \tag{5.4}$$

Stress index parameter $\Delta\sigma$ as used here is intended to capture source duration characteristics only, and as such, should not be confused with terms such as *stress drop* or *stress parameter* used elsewhere in studies of ground motion amplitude (e.g. Atkinson and Beresnev, 1997; Boore, 2003). I relate $\Delta\sigma$ to **M** using two connected line segments:

$$\Delta\sigma = \begin{cases} \exp\left[b_1(mech) + b_2\left(\mathbf{M} - \mathbf{M}^*\right)\right] & \mathbf{M} \le \mathbf{M}_2 \\ \exp\left[b_1(mech) + b_2\left(\mathbf{M}_2 - \mathbf{M}^*\right) + b_3\left(\mathbf{M} - \mathbf{M}_2\right)\right] & \mathbf{M} > \mathbf{M}_2 \end{cases} \tag{5.5}$$

where b_1, b_2, b_3, and $\mathbf{M}_2$ are model parameters and $\mathbf{M}^*$ is a reference magnitude (taken as 6).

Path duration is linearly dependent on distance R_{rup}, but with different slopes for three R_{rup} intervals with changing slopes at R_1 and R_2:

$$F_P = \begin{cases} c_1 R_{rup} & R_{rup} \le R_1 \\ c_1 R_1 + \left(c_2\right)\left(R_{rup} - R_1\right) & R_1 < R_{rup} \le R_2 \\ c_1 R_1 + \left(c_2\right)\left(R_2 - R_1\right) + \left(c_3\right)\left(R_{rup} - R_2\right) & R_{rup} > R_2 \end{cases} \tag{5.6}$$

where c_1 to c_3, R_1 and R_2 are model parameters. Site term F_S is taken as:

$$F_S = \begin{cases} c_4 \ln\left(\dfrac{V_{S30}}{V_{ref}}\right) + F_{\delta z_1} & V_{S30} \le V_1 \\ c_4 \ln\left(\dfrac{V_1}{V_{ref}}\right) + F_{\delta z_1} & V_{S30} > V_1 \end{cases} \tag{5.7}$$

$$F_{\delta z_1} = \begin{cases} c_5 \delta z_1 & \delta z_1 \le \delta z_{1,ref} \\ c_5 \delta z_{1,ref} & \delta z_1 > \delta z_{1,ref} \end{cases} \tag{5.8}$$

Parameters c_4, c_5, V_{ref}, V_1, and $\delta z_{1,ref}$ are model parameters set by regression or by visual inspection of the data. The model produces scaling with V_{S30} only for $V_{S30} \le V_1$. The basin depth term $F_{\delta z_1}$ captures the effects of depth to bedrock which is dependent on sediment depth differential δz_1. The scaling is present for δz_1 smaller than the upper limit $\delta z_{1,ref}$. According to BSSA14, δz_1 is calculated as the difference between the depth to shear wave velocity of 1000 m/s for the site (z_1), and a median depth μ_{z1} conditional on V_{S30}:

$$\delta z_1 = z_1 - \mu_{z1}(V_{S30}) \tag{5.9}$$

Depth z_1 is best obtained from a site-specific V_S profile that penetrates the 1000 m/s shear-wave horizon. Lacking that information, z_1 can be estimated using basin models in the literature, which are currently available for Japan and urban portions of California (links and references given in Seyhan et al., 2014) as well as Seattle (Frankel et al., 2007) and Taipei, Taiwan (Wang et al., 2014). Median depth μ_{z1} conditional on V_{S30} can be computed for California and Japan as:

$$\text{California: } \ln(\mu_{z1}) = \frac{-7.15}{4}\ln\left(\frac{V_{S30}^4 + 570.94^4}{1360^4 + 570.94^4}\right) - \ln(1000) \tag{5.10}$$

$$\text{Japan: } \ln(\mu_{z1}) = \frac{-5.23}{2}\ln\left(\frac{V_{S30}^2 + 412.39^2}{1360^2 + 412.39^2}\right) - \ln(1000) \tag{5.11}$$

where μ_{z1} is in units of km and V_{S30} is in units of m/sec. Models for μ_{z1} are not currently available outside of California and Japan; such applications should use a default value of $\delta z_1 = 0$.

The total standard deviation σ is partitioned into components representing between- and within-event standard deviations (τ and ϕ, respectively):

$$\sigma(\mathbf{M}) = \sqrt{\tau^2(\mathbf{M}) + \phi^2(\mathbf{M})} \tag{5.12}$$

The **M**-dependent component standard deviations are given by:

$$\tau(\mathbf{M}) = \begin{cases} \tau_1 & \mathbf{M} < 6.5 \\ \tau_1 + (\tau_2 - \tau_1)\left(\dfrac{\mathbf{M} - 6.5}{7 - 6.5}\right) & 6.5 \le \mathbf{M} < 7 \\ \tau_2 & \mathbf{M} \ge 7 \end{cases} \tag{5.13}$$

$$\phi(\mathbf{M}) = \begin{cases} \phi_1 & \mathbf{M} < 5.5 \\ \phi_1 + (\phi_2 - \phi_1)\left(\dfrac{\mathbf{M} - 5.5}{5.75 - 5.5}\right) & 5.5 \le \mathbf{M} < 5.75 \\ \phi_2 & \mathbf{M} \ge 5.75 \end{cases} \tag{5.14}$$

where parameters τ_1, τ_2, ϕ_1, and ϕ_2 are estimated based on values of **M**-dependent τ and ϕ. Model coefficients are given in Tables 5.1 – 5.3.

Table 5.1. List of parameters used for source model (N: normal, R: reverse, SS: strike-slip)

	$\mathbf{M}_1$	$\mathbf{M}_2$	$\mathbf{M}^*$	b_0 (sec)	b_1	b_2	b_3
$D_{5\text{-}75}$	5.35	7.15	6	1.555 (N) 0.7806 (R) 1.279 (SS) 1.280 (Unknown)	4.992 (N) 7.061 (R) 5.578 (SS) 5.576 (Unknown)	0.9011	-1.684
$D_{5\text{-}95}$	5.2	7.4	6	2.541 (N) 1.612 (R) 2.302 (SS) 2.182 (Unknown)	3.170 (N) 4.536 (R) 3.467 (SS) 3.628 (Unknown)	0.9443	-3.911
$D_{20\text{-}80}$	5.2	7.4	6	1.413 (N) 0.7754 (R) 0.8833 (SS) 0.8851 (Unknown)	4.778 (N) 6.579 (R) 6.188 (SS) 6.182 (Unknown)	0.7414	-3.164

Table 5.2. List of parameters used for the path model and site terms

	c_1 (sec/km)	c_2 (sec/km)	c_3 (sec/km)	c_4	c_5 (1/km)	R_1 (km)	R_2 (km)	V_1 (m/s)	V_{ref} (m/s)	$\delta z_{1,ref}$ (m)
$D_{5\text{-}75}$	0.1159	0.1065	0.0682	-0.2246	0.0006	10	50	600	368.2	200
$D_{5\text{-}95}$	0.3165	0.2539	0.0932	-0.3183	0.0006	10	50	600	369.9	200
$D_{20\text{-}80}$	0.0646	0.0865	0.0373	-0.4237	0.0005	10	50	600	369.6	200

Table 5.3. List of parameters used for standard deviation components

	τ_1	τ_2	ϕ_1	ϕ_2
$D_{5\text{-}75}$	0.28	0.25	0.54	0.41
$D_{5\text{-}95}$	0.25	0.19	0.43	0.35
$D_{20\text{-}80}$	0.30	0.19	0.56	0.45

5.4 MODEL DEVELOPMENT

Our GMMs were developed in a phased process in which certain model elements were held constant (e.g. path and site) while one was regressed against the data (e.g., source). The subsequent phase would then hold the just-established model element fixed while regressing another component. Phasing of this sort was required because a single mixed-effects regression with the full function would not converge. I describe the specific implementation of this approach for the source, path, and site terms in the following sections.

5.4.1 primary source model: M-scaling

The source model consists of constant term b_0 for $\mathbf{M} < \mathbf{M}_1$ and **M**-dependent terms at larger magnitudes. Per Eqs. (5.2)–(5.4), a source model in which duration is constant with respect to **M** requires linear scaling of $\Delta\sigma$ with **M** at a slope of $b_2 = b_3 = 3.45$. This slope is shown in Figure 5.4 with a dashed blue line. The steep increase of $\Delta\sigma$ with **M** shown by this line is required to keep f_0 high and duration low as **M** increases.

I regress the duration data to investigate the variation of $\Delta\sigma$ with **M**, expecting slower scaling of $\Delta\sigma$ than required for the constant duration model. In the first phase of this regression, I adopted the function in Eqs. (5.1)–(5.5) but with no site term ($F_S = 0$), path coefficient c_1 in Eq. (5.6) set from KS06 (c_2 and c_3 were taken as zero for this preliminary analysis), and $\Delta\sigma$ as a free parameter. I evaluated source duration for each individual earthquake using mixed-effects analysis

performed with the LME routine in program R (Pinheiro et al., 2013). The estimated source duration is then converted to $\Delta\sigma$ using Eqs. (5.2)–(5.3), with results similar to those shown by the discrete symbols in Figure 5.4. Using this same process, I also evaluate median values of $\Delta\sigma$ for events within bins 0.5 magnitude units in width using mixed effects procedures (marked as 'binned medians' in Figure 5.4).

The discrete data points and binned medians shown in Figure 5.4 were derived following several phases of analysis in which source and path terms were incrementally adjusted (details below). The plotted points reflect the $\Delta\sigma$ values that are derived when the final recommended path and site terms are considered in the derivation of the event-specific stress drop indices $\Delta\sigma$. The results in Figure 5.4 are for the $D_{20\text{-}80}$ duration parameter – similar results for the other duration parameters are given in the Electronic Supplement.

Source durations for some earthquakes do not appear in Figure 5.4 – this occurs when source durations (obtained from the subtraction of path durations from observations) are negative, in which case $\Delta\sigma$ is undefined for that event. In contrast, the binned median values of $\Delta\sigma$ are computed using all events within the bin, including those producing a negative source duration. This can cause the binned median values of $\Delta\sigma$ in Figure 5.4 to not plot near the center of the data (this occurs near $\mathbf{M}_1$ for $D_{20\text{-}80}$ and $D_{5\text{-}95}$).

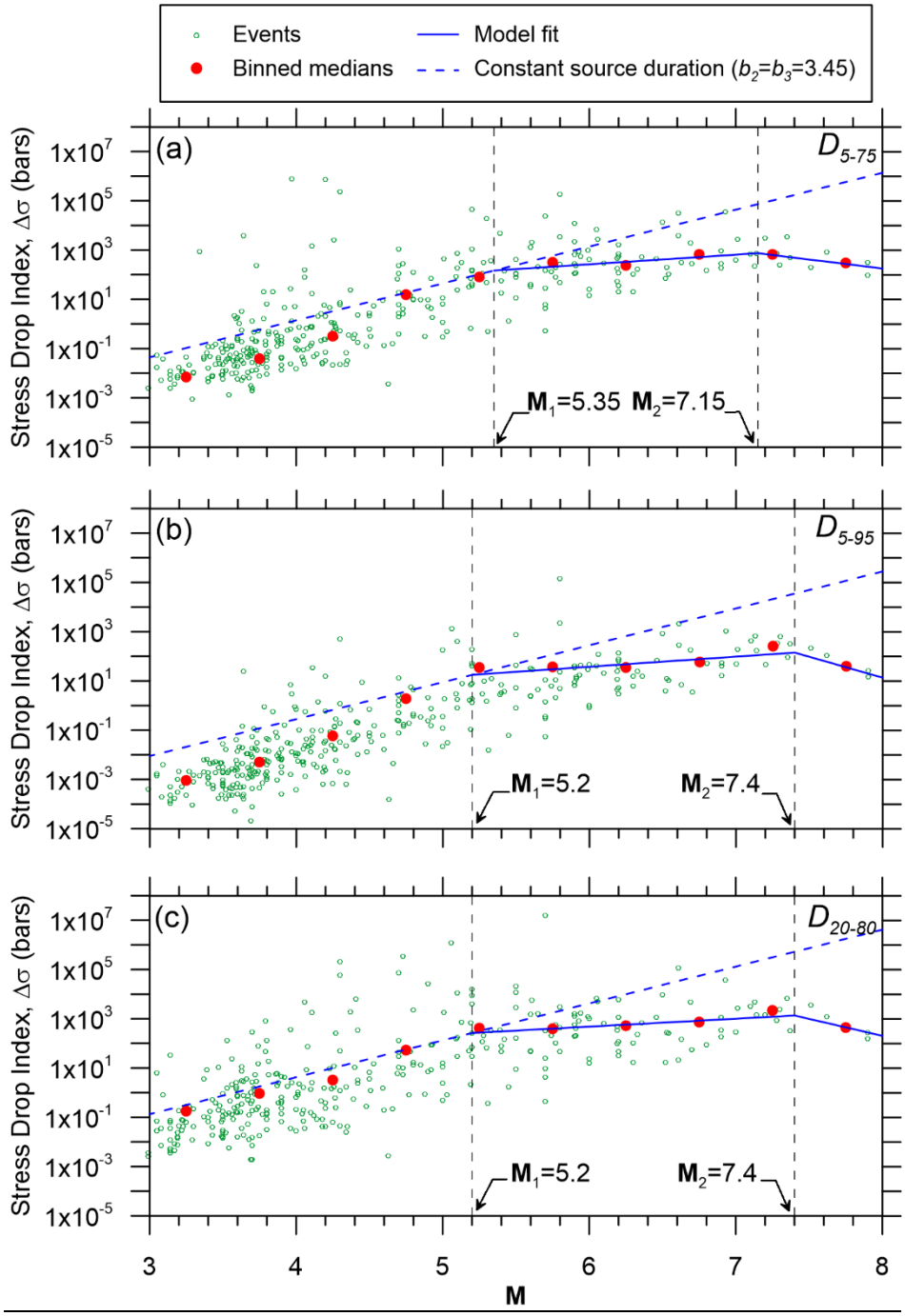

Figure 5.4. Stress drop index values calculated for each event for $D_{5\text{-}75}$ (a), $D_{5\text{-}95}$ (b), and $D_{20\text{-}80}$ (c) as well as the binned medians and fitted function (mechanism-independent).

The trends of the results in Figure 5.4 indicate that $\Delta\sigma$ increases with **M** at progressively slower rates as **M** increases across the considered range of **M**=3–8. I parsed the full range into

three intervals bounded by $\mathbf{M}_1$ (at about 5–5.5) and $\mathbf{M}_2$ (at about 7–7.5). For $\mathbf{M} < \mathbf{M}_1$, $\Delta\sigma$ increases with **M** at approximately the rate required for **M**-independent source duration for $D_{20\text{-}80}$, (Figure 5.4c) and at even faster rates for other duration parameters (Figure 5.4a and b). I consider this feature of the computed stress drop indices to be influenced by difficulties in properly separating path from source durations for small **M** events, where source durations are small and noise effects in the data are large. Nonetheless, the data in Figure 5.4 support the **M**-independent model represented by coefficient b_0 in Eq. (5.2), which is the source duration at $\mathbf{M} = \mathbf{M}_1$ in units of seconds. As such, our model can be used to provide duration predictions for $\mathbf{M} < \mathbf{M}_1$, albeit with a higher degree of epistemic uncertainty than at higher magnitudes. I recognize that this **M**-independent duration feature of the low-magnitude data requires the stress drop term to exhibit stronger magnitude-dependence than has been observed previously for amplitude-related ground motion intensity measures (Allmann and Shearer, 2007 and 2009). This presumably occurs because source attributes affecting low-frequency ground motions (i.e., near corner frequency f_0) are not perfectly correlated with those controlling duration, at least with respect to their relative magnitude-dependencies. I accept these differences in $\Delta\sigma$ trends because our objective is to capture features of duration data. This underscores our previous remark that $\Delta\sigma$ is a stress index and should not be confused with other stress parameters in the literature used for prediction of ground motion amplitude.

For $\mathbf{M} > \mathbf{M}_1$, $\Delta\sigma$ increases with **M** at a slower rate that required for a constant duration model, indicating that source duration increases with **M** as expected. For the two largest events in the NGA-West2 data set (**M** 7.9 Denali, Alaska and **M** 7.9 Wenchuan, China), $\Delta\sigma$ is markedly lower than suggested by a trend line established at lower magnitudes. I considered ignoring these features and simply extending the linear relation between $\Delta\sigma$ and **M** beyond $\mathbf{M}_2$. However, such

an approach produces severe distortion of residuals at large magnitudes, and so we elected to capture this feature of the data in our model. I acknowledge that other modelers may make different decisions in this regard, and as such, that model performance at large magnitudes ($\mathbf{M} > \mathbf{M}_1$) is subject to larger epistemic uncertainty than at lower **M**. I considered alternate functions to capture this feature of the data (bi-linear with second line being flat, parabolic), but after much trial and error settled upon the tri-linear model shown in Figure 5.4 that allows $\Delta\sigma$ to have a negative slope set by data at large magnitudes ($\mathbf{M} > \mathbf{M}_2$). The model fit shown in Figure 5.4 for $\mathbf{M} > \mathbf{M}_1$ is based on a simple least-squares linear regression through the binned medians to set coefficients b_1–b_3. Attempts to set these coefficients through alternative procedures (linear mixed effects regression and least-squares linear regression through event-specific $\Delta\sigma$ values) produced poorer fits to the data than the adopted approach.

Focal mechanism affects the low-**M** duration (b_0) and the apparent stress drop scaling term b_1. I initially estimated those parameters as overall averages set by regression without consideration of mechanism. Those values are given in Table 5.1 with the mechanism marked as 'unknown'. The adjustments for focal mechanism were then set following establishment of path scaling through residuals analysis, as described further in the *Secondary Effects* section below. Results of those analyses are reflected in the mechanism-dependent b_0 and b_1 coefficients in Table 5.1 and are illustrated in Figure 5.5. Normal fault earthquakes have the largest source durations for a given **M** and reverse mechanisms the smallest, with strike-slip being intermediate. Also shown in Figure 5.5 are event-specific source durations compatible with their associated stress drop indices (from Figure 5.4).

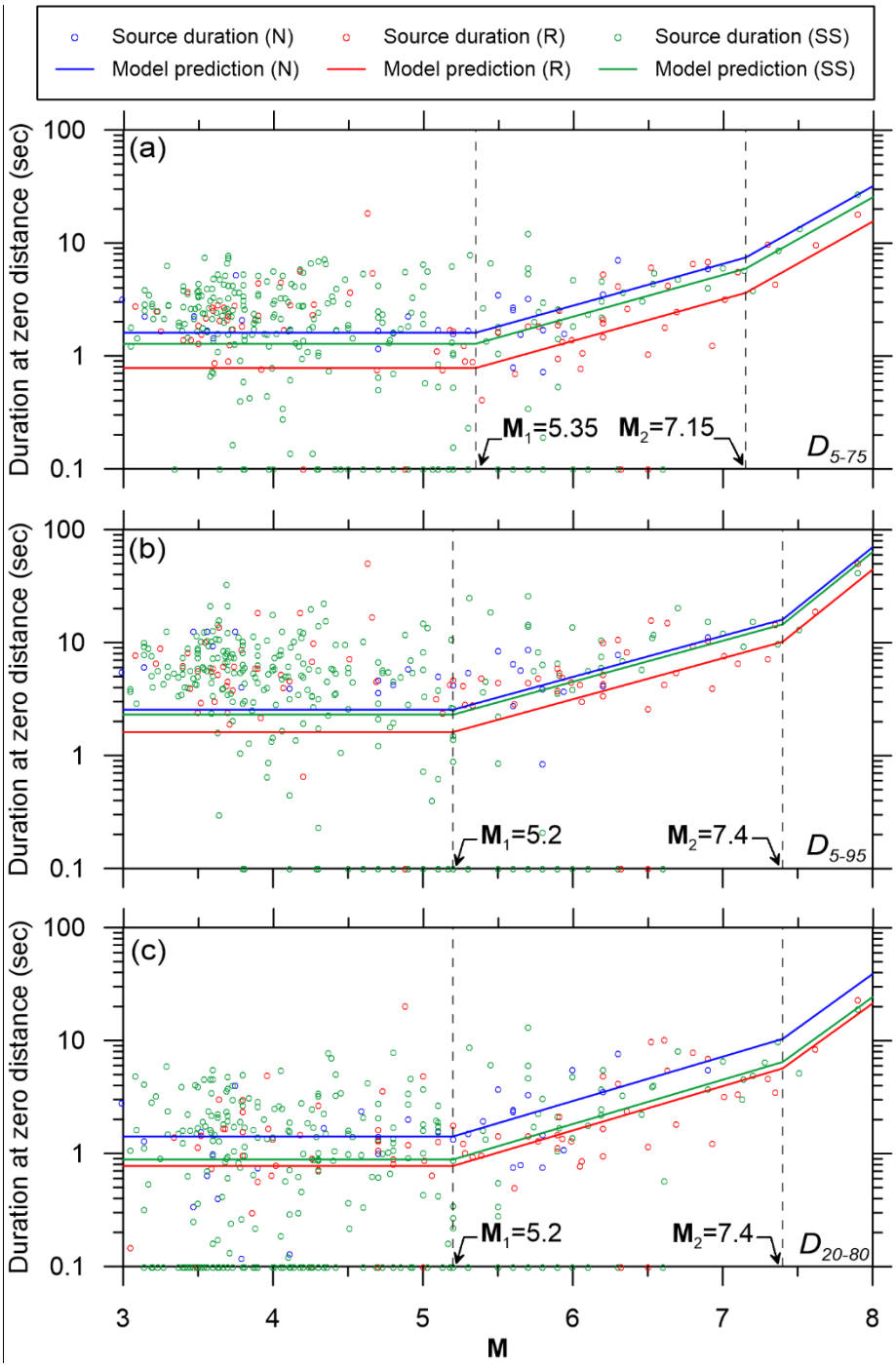

Figure 5.5. Average source durations for $D_{5\text{-}75}$ (a), $D_{5\text{-}95}$ (b), and $D_{20\text{-}80}$ (c) by event type, evaluated from stress drop index per Eq. (5.2) and (5.3). Source durations smaller than 0.1 sec are plotted at 0.1 sec.

Because of the aforementioned difficulties in separating source and path durations for low magnitude data (i.e., for events with $\mathbf{M} < \mathbf{M_1}$), work on other model components (other than

primary magnitude-scaling) utilized data with $\mathbf{M} \geq \mathbf{M_1}$. This smaller subset of data consists of 5903 recordings from 107 earthquakes for $D_{5\text{-}75}$, and 6089 recordings from 114 earthquakes for $D_{5\text{-}95}$ and $D_{20\text{-}80}$. The applicability of path and site models developed on this basis for lower magnitudes is verified subsequently through residuals analysis.

5.4.2 path model

The path model consists of distance scaling coefficients c_1 to c_3, which differentiate path scaling rates for three distance ranges: $R_{rup} \leq R_1$, $R_1 < R_{rup} \leq R_2$, and $R_{rup} > R_2$. As indicated in the *Introduction*, our path term is additive with source duration, which is different from most recent duration GMMs but consistent with KS06 and BT14. KS06 used a simple linear path scaling function, whereas BT14 use a multi-linear function with slope breaks at 7, 45, 125, 175, and 270 km.

As described in the previous section, our first iteration in developing the source model regressed for parameters b_1-b_3 with path terms fixed at the values from KS06. In order to guide our selection of a path function, I then sought to 'turn off' the path model and identify misfits of the data relative to a path-removed model with adjustments for event-specific data/model misfits. This was done by first computing residuals between data and model:

$$R_{ij} = \ln D_{ij} - \mu_{ij}\left(\mathbf{M}, R_{rup}\right) \tag{5.15}$$

where μ_{ij} is the GMM mean in natural log units for recording j in event i. Those residuals were then partitioned into between- and within-event components as follows using mixed-effects analysis as implemented in the LME command in program R (Pinheiro et al., 2013):

$$R_{ij} = c_k + \eta_i + \varepsilon_{ij} \tag{5.16}$$

In this approach, c_k is the overall model bias (nearly zero since residuals are being computed for the same data used in model development), η_i is the between-event residual (event term) for earthquake *i*, which represents the degree to which an individual event is high or low relative to the average, and ε_{ij} is the within-event residuals for recording *j* in event *i*.

Armed with η_i values, I then computed record-specific path duration against an approximately bias-removed source model as follows:

$$F_{P,ij} = D_{ij} - \exp\left[\mu_{ij}^{0}\left(\mathbf{M}, R_{rup} = 0\right) + \eta_i\right] \tag{5.17}$$

where the superscript '0' on μ_{ij}^{0} is to indicate that the duration prediction has the path term removed (equivalent to setting $R_{rup} = 0$). I plot in Figure 5.6 the quantity $F_{P,ij}$ (in units of sec) against R_{rup} for the $D_{20\text{-}80}$ duration parameter. I found this form for the plots to be useful in guiding selection of a path duration function. The data points shown in Figure 5.6 are derived from the final model, following multiple iterations whereby in each iteration the path model is modified, and those modified path models are used to re-derive the source model. Through this process the trends of the path terms were relatively consistent from iteration-to-iteration. Moreover, whereas initial stages of this analysis did not consider site effects in the derivation of $F_{P,ij}$, in the final iteration site effects were included in the analysis of μ_{ij}^{0} in Eq. (5.17).

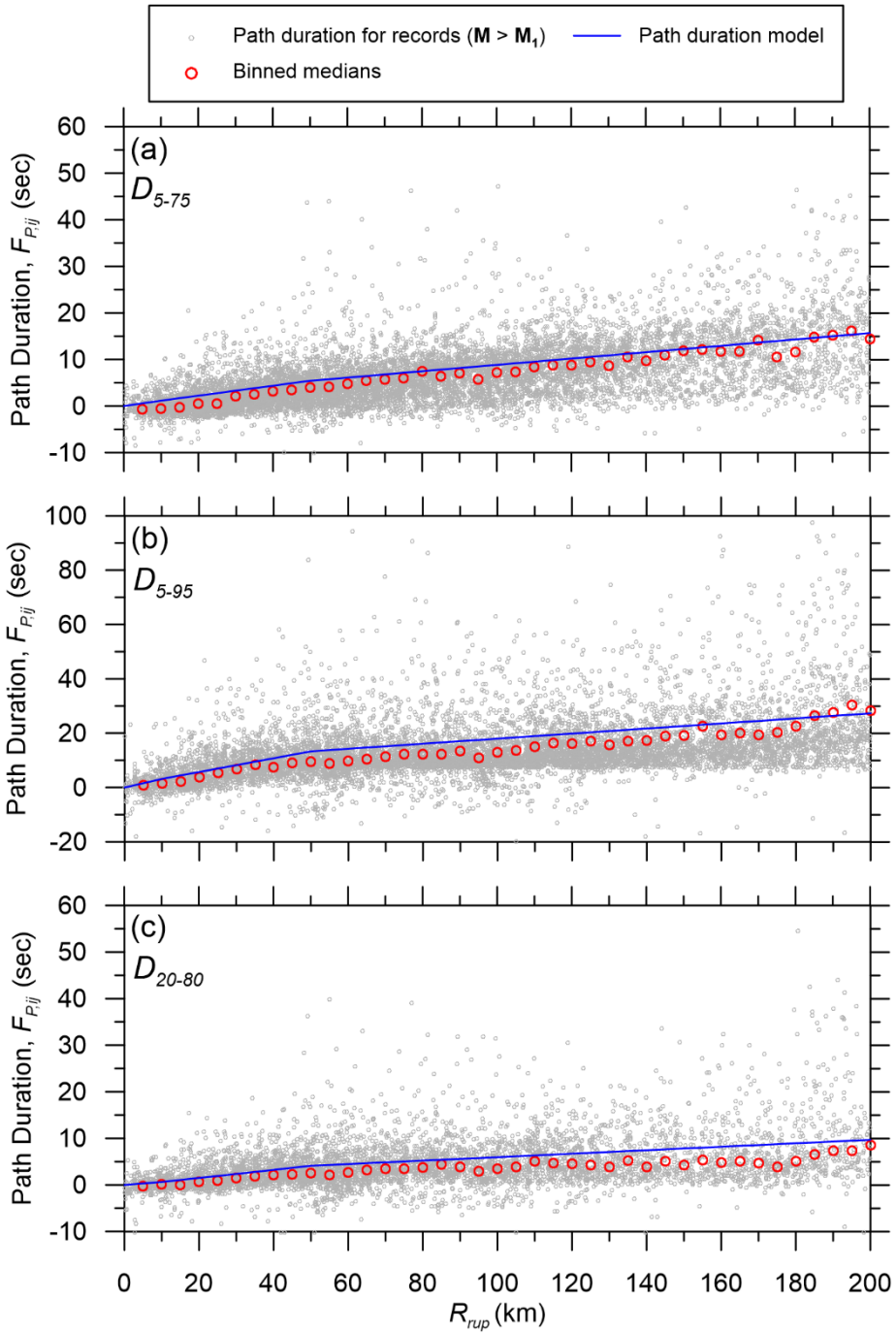

Figure 5.6. Path durations calculated for $D_{5\text{-}75}$ (a), $D_{5\text{-}95}$ (b), and $D_{20\text{-}80}$ (c); path duration points calculated for records with M>M$_1$ after subtracting the source duration and the effects of event-to-event variability (η_i). Binned medians also shown along with model fit.

Figure 5.6 shows individual path durations for **M**>**M**$_1$ along with median values within equally spaced distance bins. The most clearly evident data trends in Figure 5.6 are relatively linear

above and below a transition distance of 50 km, with faster path scaling at closer distances. When the data was fit in this manner, I encountered misfit for $R_{rup} < 10$ km, so a second break in the path term was introduced at 10 km. Coefficients for the resulting tri-linear distribution were derived from nonlinear least squares regression as part of the iterative model derivation [the use of least squares in this case is compatible with the principles of mixed effects regression, because random effects (event terms) have been removed from each data point]. The resulting fits to data are shown in Figure 5.6. The model fit is slightly higher than the binned medians because model coefficients are set to fit the mean of the data. Figure 5.7 shows that path durations are ordered as $D_{20\text{-}80} < D_{5\text{-}75} < D_{5\text{-}95}$ (total durations typically order as $D_{20\text{-}80} \sim D_{5\text{-}75} < D_{5\text{-}95}$; Figure 5.7 shows model fits only).

I queried the path durations for possible **M**-dependency. When the path durations are separated into distinct **M** bins, F-tests (Cook and Weisberg, 1999) do not show the results to be significantly distinct. The finding that path durations are not significantly different over the wide **M** range in the data set indicates that an additive path function is preferred to a multiplicative function, which would necessarily couple path duration with magnitude. I note that BT14 also recommend an **M**-independent path duration.

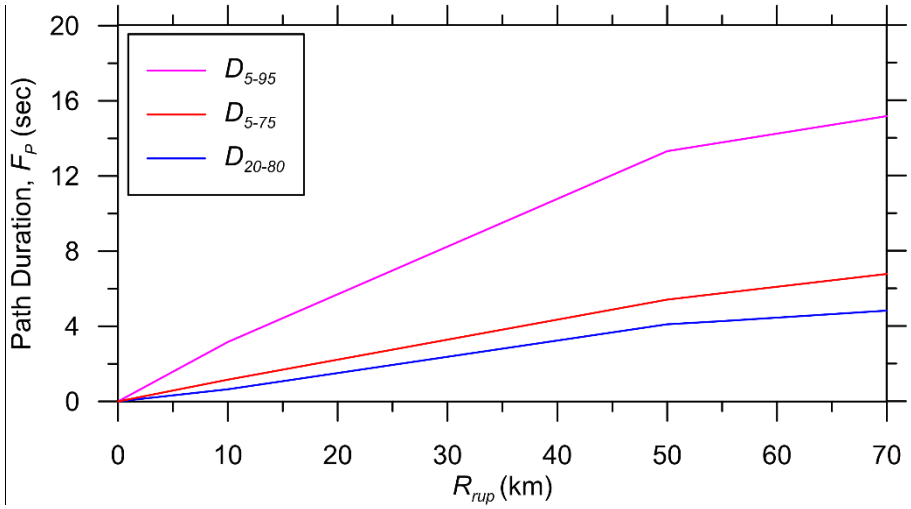

Figure 5.7. Mean path durations predicted for the three duration measures.

5.4.3 Primary Site model: V_{S30}-scaling

Our model development process reached stable and consistent results for the source and path models by performing multiple iterations in which these model components were successively regressed using the function in Eq. (5.1) with the site term F_S set to zero. I then examined site effects using mixed effects residuals analysis (Eq. 15-16) with records from events with $\mathbf{M}>\mathbf{M}_1$. I investigated V_{S30}-scaling by plotting within-event residuals (ε_{ij} from Eq. 5.16) against V_{S30} as shown in Figure 5.8. The figure shows individual data points, binned means, and the fit line as described further below.

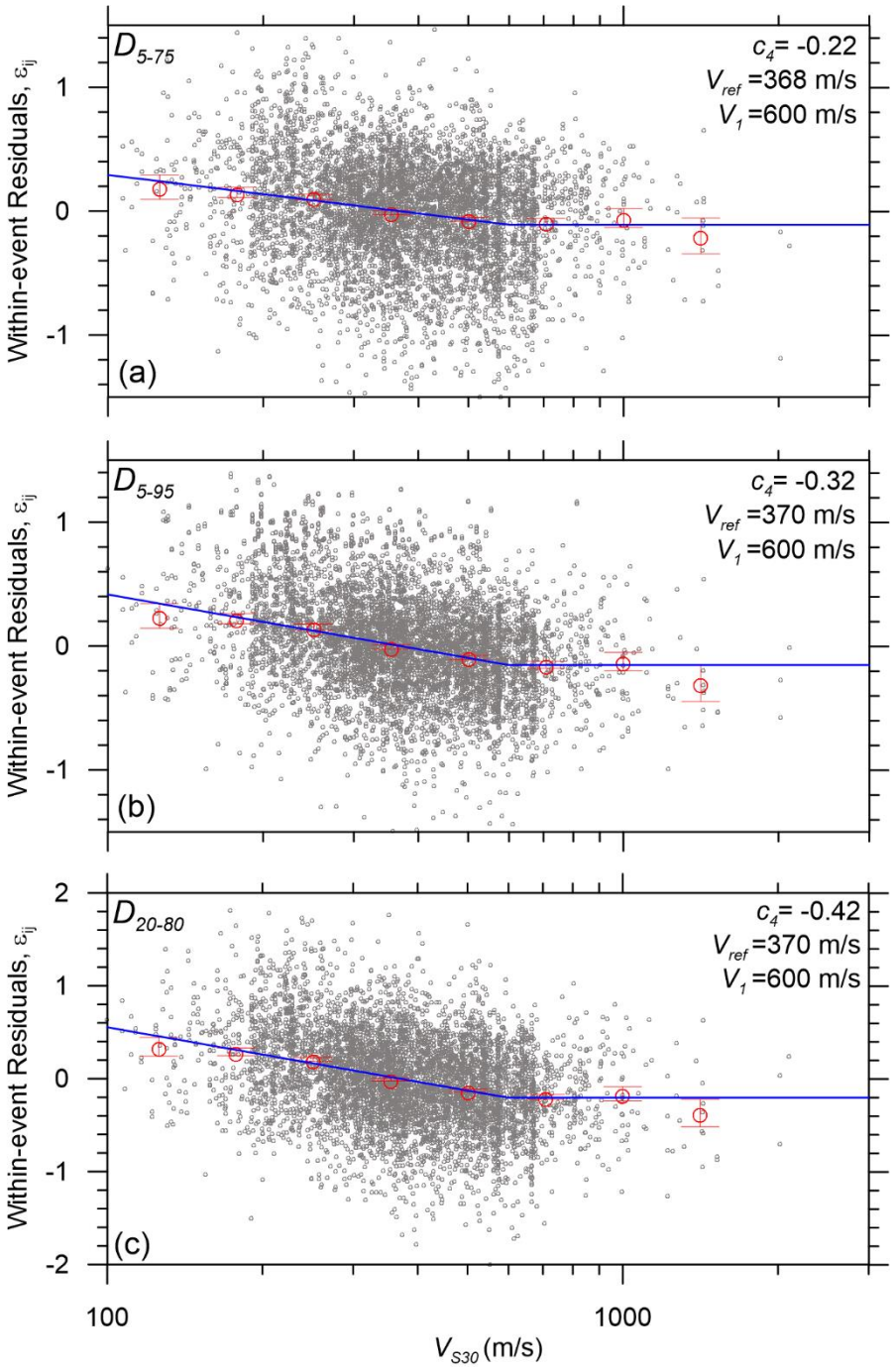

Figure 5.8. V_{S30}-dependence of within-event residuals of model in which site term F_S in Eq. (5.1) is set to zero for $D_{5\text{-}75}$ (a), $D_{5\text{-}95}$ (b), and $D_{20\text{-}80}$ (c). Individual data points are shown for records with M>M_1 along with binned means, their 95% confidence intervals, and the final fit. The final model uses the slope (c_4) and limiting velocity (V_1) marked in the figure.

I find the binned means of residuals to decrease essentially linearly with V_{S30} up to a limiting value (V_1) of 600 m/s. The slopes are modest, being approximately -0.22, -0.32, and -0.42 for $D_{5\text{-}75}$, $D_{5\text{-}95}$, $D_{20\text{-}80}$, respectively. For comparison, V_{S30}-gradients for PGA and PGV are approximately -0.6 and -0.84, respectively (Seyhan and Stewart, 2014). The trends shown in Figure 5.8 motivated selection of the V_{S30}-scaling function in Eq. (5.7). The regression results are indicated in Table 5.2.

Final coefficients for the site model were obtained using an iterative process in which the fit through the binned means is added to the site term from previous step until reaching a flat trend in ε_{ij} against V_{S30} at the final iteration. Once the site model had been established in this manner, site corrections were applied in the development of the final source and path durations and related regressions, with the results presented in prior sections.

5.4.4 Secondary effects

Once the primary **M**-scaling function (using the mechanism-independent b_0 and b_1 values), path function, and V_{S30}-scaling had been established, I investigated additional effects related to focal mechanism, event type, and basin depth through mixed-effects residuals analysis carried out using Eqs. (5.15)-(5.16).

The effects of focal mechanism are investigated by binning event terms η_i by event type for $\mathbf{M}>\mathbf{M}_1$, as shown in Figure 5.9 along with binned means. Relative to a mechanism-independent model, I find strike-slip earthquakes to be effectively unbiased (unsurprising as they dominate the data set) and normal- and reverse-slip events to have positive and negative bias, respectively. These trends for duration are opposite to those for high-frequency pseudo-spectral accelerations (high amplitudes are associated with short durations and vice-versa), which is consistent with prior work

showing negative correlation between these ground motion intensity measures (Bradley, 2011). The mean values for the respective bins guided the mechanism-specific b_0 and b_1 values in Table 5.1.

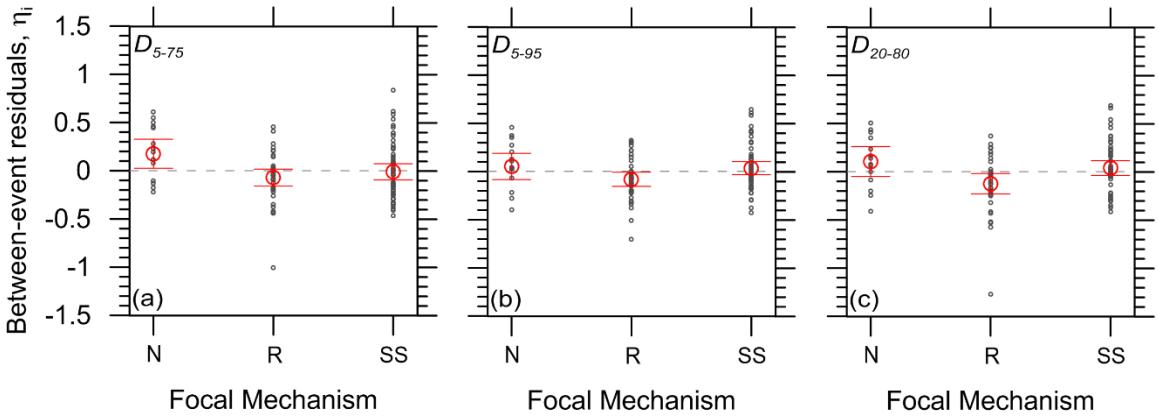

Figure 5.9. Between-event residuals binned by focal mechanism for records with M>M_1 along with binned means and their 95% confidence intervals indicating the systematic biases for different focal mechanisms. Results shown for all three investigated duration parameters.

In Figure 5.11(a, c, and e), I show event terms for CL1 and CL2 event types against **M**. The regions contributing the majority of the CL2 data are China and California. The CL2 events from China are generally in the range **M** ~ 4.5-6 and have negative event terms. Similar trends for Chinese CL2 events, but with positive event terms, were found by Boore et al. (2013) for some amplitude-related intensity measures. While casual inspection of Figure 5.11(a, c, and e) suggests the presence of **M** ranges with significant bias of CL2 events relative to CL1 events, an evaluation of this type fails to account for several key features of the data: (1) of the 104 CL2 events, 49 are from a single event (Wenchuan) and 14 are single CL2 events trailing a mainshock CL1 event. Hence, the data sampling (in terms of numbers of CL2 events following the parent CL1 events) is highly non-uniform.

As was done for amplitude by BSSA14 and Boore et al. (2013), we consider the differences between CL2 events and the parent CL1 event to be a more robust means by which to assess the effects of event type, because it accounts for possible correlations between parent and child event terms. I consider CL1 events with 3 or more child CL2 events. For each pairing, I compute ($\Delta\eta = \bar{\eta}_{C2} - \eta_{C1}$), where $\bar{\eta}_{C2}$ is the mean of the CL2 event terms and η_{C1} is the event term for the parent CL1 event. Figure 5.10(b, d, and f) shows the resulting values of $\Delta\eta$ as a function of **M** for the CL1 event. I see no significant trend in the results, nor any particular bias. Accordingly, I conclude that the GMMs, which were developed using both CL1 and CL2 events, can be considered applicable to both.

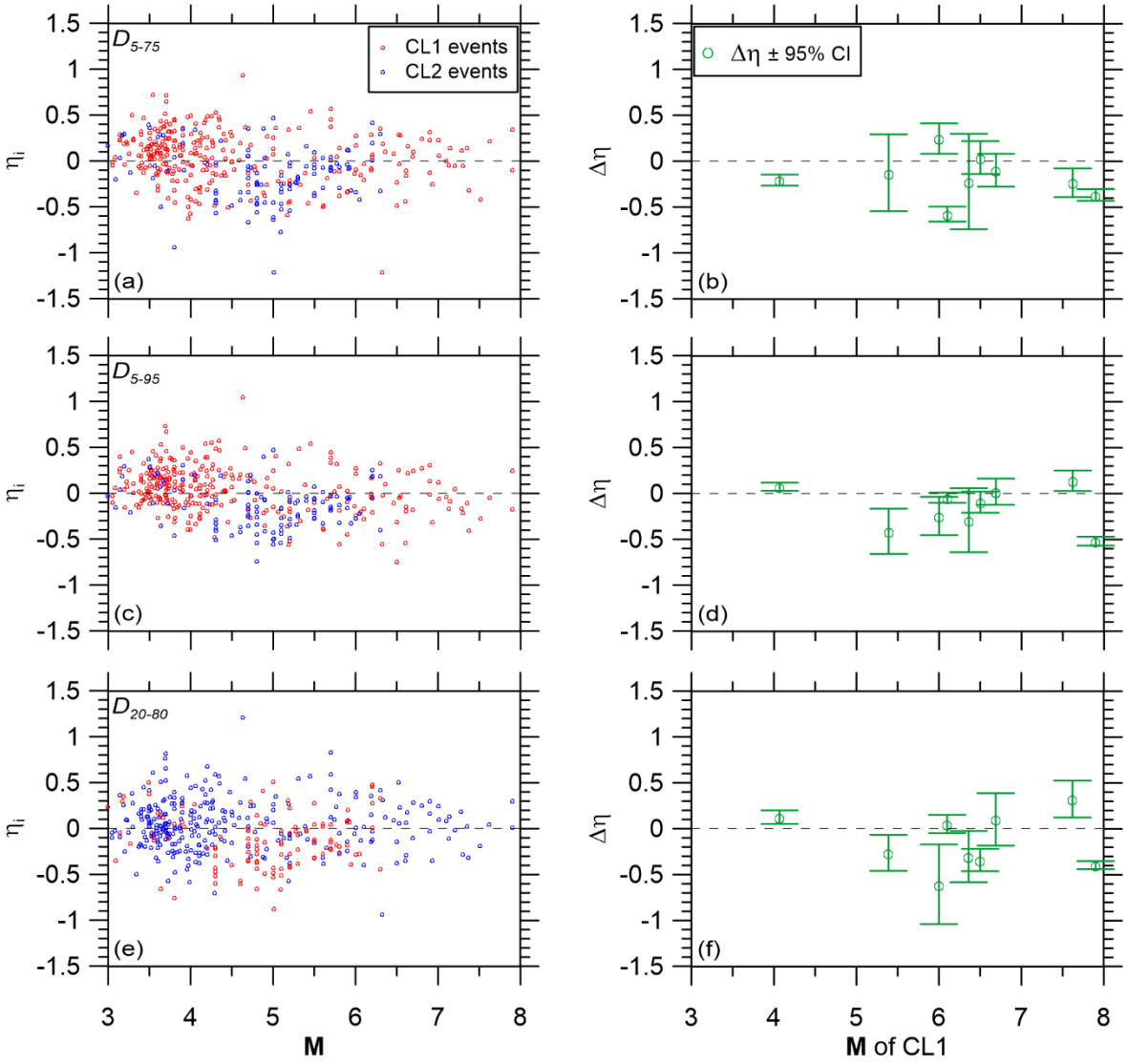

Figure 5.10. Between-event residuals plotted against M for CL1 and CL2 events for $D_{5\text{-}75}$ (a), $D_{5\text{-}95}$ (c), and $D_{20\text{-}80}$ (e); and differential event terms ($\Delta\eta$) plotted against the magnitude of their parent event along with 95% confidence intervals for $D_{5\text{-}75}$ (b), $D_{5\text{-}95}$ (d), and $D_{20\text{-}80}$ (f).

As shown in Figure 5.11, the effects of basin depth were investigated by plotting within-event residuals for $\mathbf{M}>\mathbf{M}_1$ against basin depth differential δz_1 for the subset of the data where this parameter is available. I find no scaling with δz_1 for $\delta z_1 > 200$ m; note this does not imply no dependence of duration on depth in this range, but merely indicates that information on basin depth does not carry predictive power beyond the default basin depths associated with V_{S30}.

For $\delta z_1 <$ ~ 200m, residuals increase with δz_1 in a statistically significant manner (based on non-overlapping confidence intervals of binned means at the limits of the range). A two-segment linear function was fit through the binned means to establish the coefficients in Eq. (5.8).

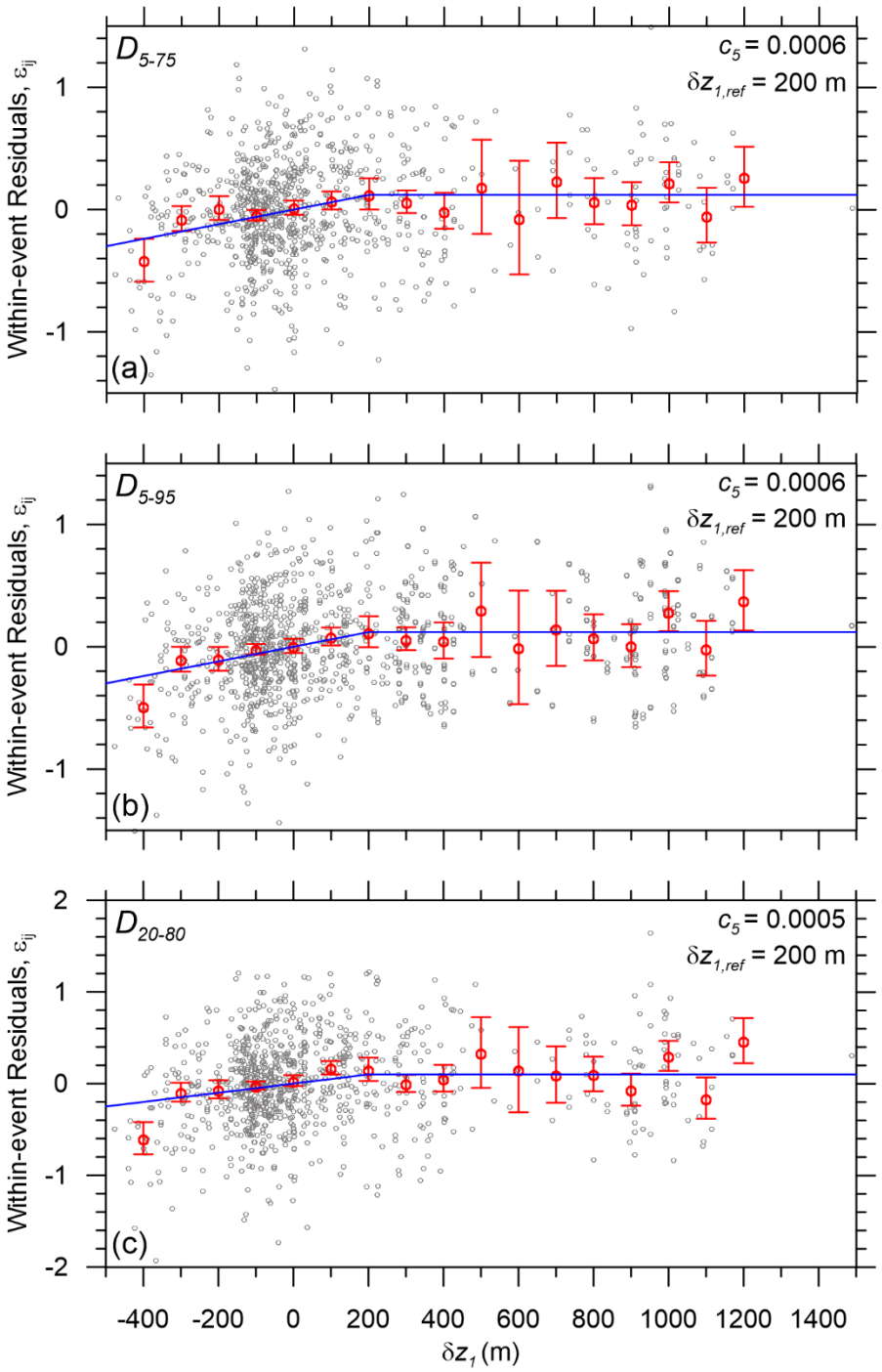

Figure 5.11. Variation of within-event residuals with basin depth differential δz_1 for $D_{5\text{-}75}$ (a), $D_{5\text{-}95}$ (b), and $D_{20\text{-}80}$ (c) using records with M>M_1. The plotted residuals were derived without using a basin depth term in the site model.

5.5 MODEL PERFORMANCE

5.5.1 residuals

The performance of the final model, following the many adjustments and iterations described in the prior sections, is tested by mixed-effects residuals analysis (Eqs. 5.15 and 5.16). These residuals analyses are performed both for the subset of data with $\mathbf{M}>\mathbf{M_1}$ (encompassing most engineering applications) and for the full data set including smaller magnitudes.

For the $\mathbf{M}>\mathbf{M_1}$ data, overall model bias term c_k is 0.0099, -0.0002, and 0.0393 for parameters $D_{5\text{-}75}$, $D_{5\text{-}95}$, and $D_{20\text{-}80}$, respectively. These are considered acceptably small. Plots of between-event residuals (η_i) and within-event residuals (ε_{ij}) against relevant independent variables are shown in Figures 5.12-5.14. Performance of the source model is judged by plots of η_i versus **M** and by binned means within focal mechanism groups. As shown in Figures 5.12-5.14, these trends are flat for $\mathbf{M} > \mathbf{M}_1$. Performance of the path and site models is judged from trends of ε_{ij} against rupture distance R_{rup} and V_{S30}, respectively. The trends are flat, suggesting these effects are properly captured in the model. The data for $R_{rup} < \sim 3$ km are sparse, so I have less confidence in the robustness of the trends in this range. Although not shown in Figures 5.12-5.14, there are also no trends with δz_1.

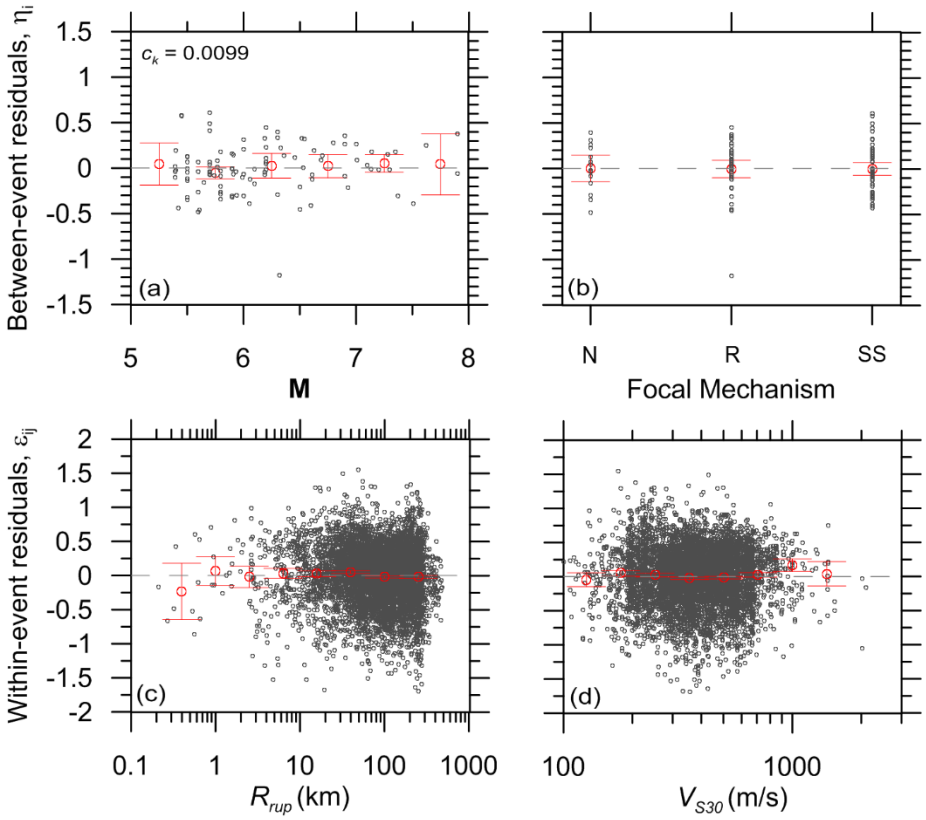

Figure 5.12. Plots of between-event and within-event residuals for $D_{5\text{-}75}$ along with their binned means and 95% confidence intervals showing their trends with (a) magnitude, (b) focal mechanism, (c) distance, and (d) V_{S30}.

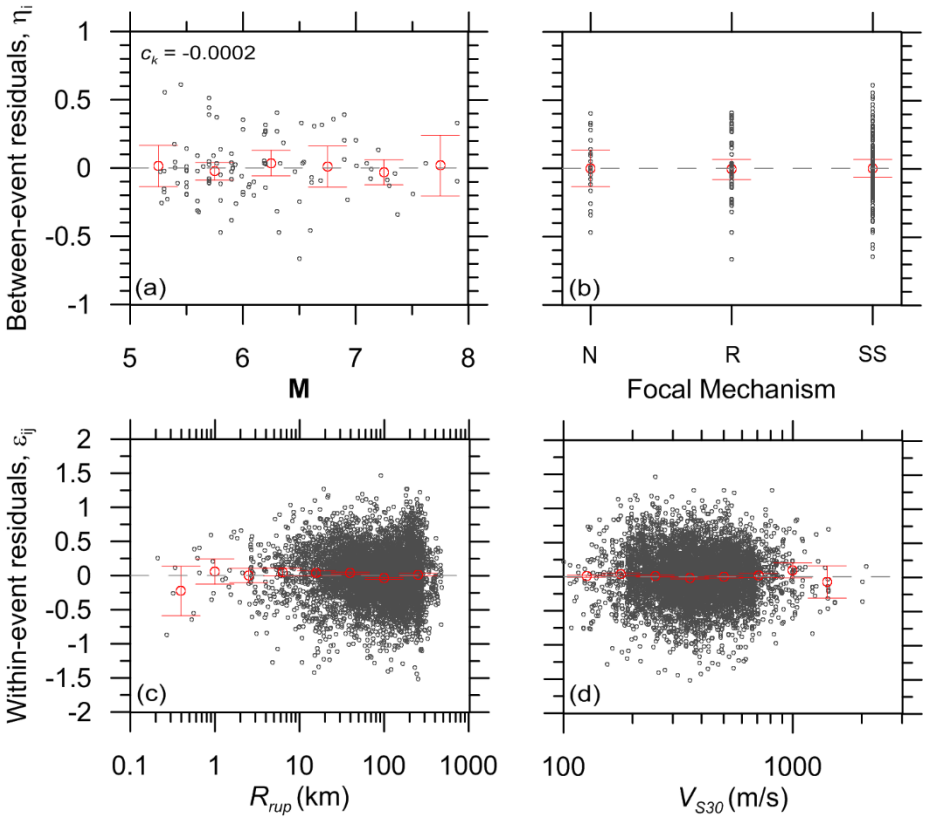

Figure 5.13. Plots of between-event and within-event residuals for $D_{5\text{-}95}$ along with their binned means and 95% confidence intervals showing their trends with (a) magnitude, (b) focal mechanism, (c) distance, and (d) V_{S30}.

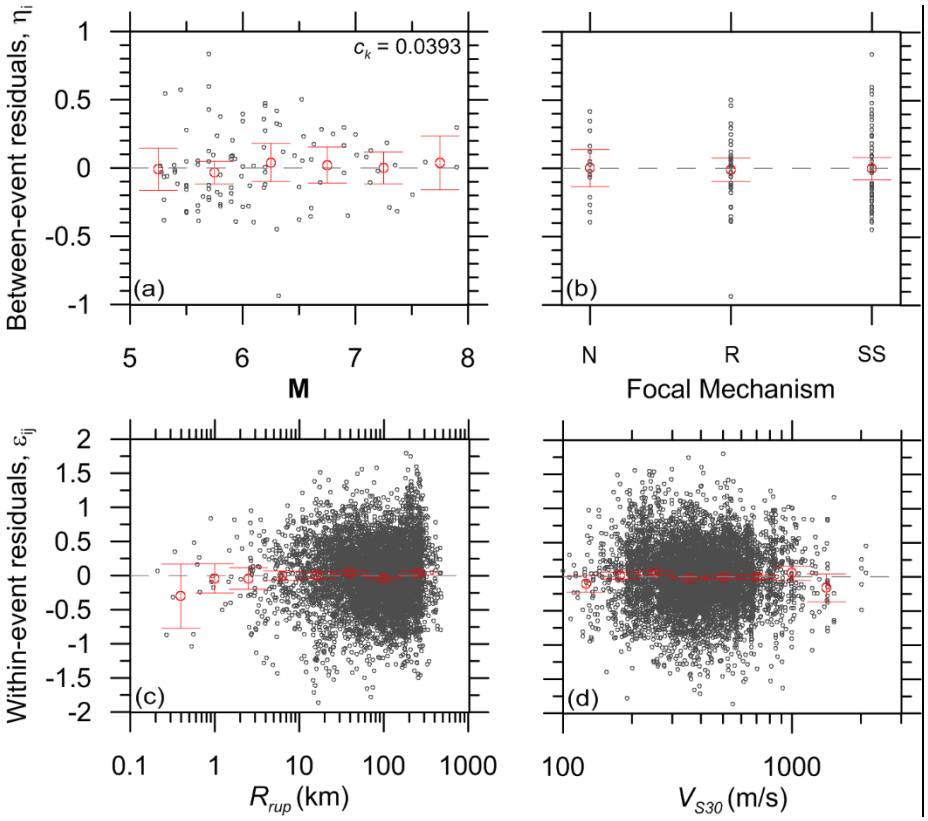

Figure 5.14. Plots of between-event and within-event residuals for $D_{20\text{-}80}$ along with their binned means and 95% confidence intervals showing their trends with (a) magnitude, (b) focal mechanism, (c) distance, and (d) V_{S30}.

Residuals analyses were also performed for the full data set. The model exhibits some bias relative to this data, which I illustrate by plotting the sum $c_k + \eta_i$ against **M** in Figure 5.15(a, c, and e). The bias occurs for **M** < $\mathbf{M_1}$ events, being negative near **M**5 and positive for **M** < ~4.5. I consider these source duration trends from the data to be unrealistic and to reflect aforementioned difficulties in separating source and path effects at small magnitudes. For this reason, I did not attempt to model these features, instead adopting a relatively simple **M**-independent source duration for **M** < $\mathbf{M_1}$. Figure 5.15(b, d, and f) shows trends of ε_{ij} with distance for the **M** < $\mathbf{M_1}$ data only. The binned means of these residuals retain a nearly flat trend with distance, with the

95% confidence interval for most bins encompassing zero. This indicates that the path durations derived for larger magnitude data remain applicable for $\mathbf{M < M_1}$.

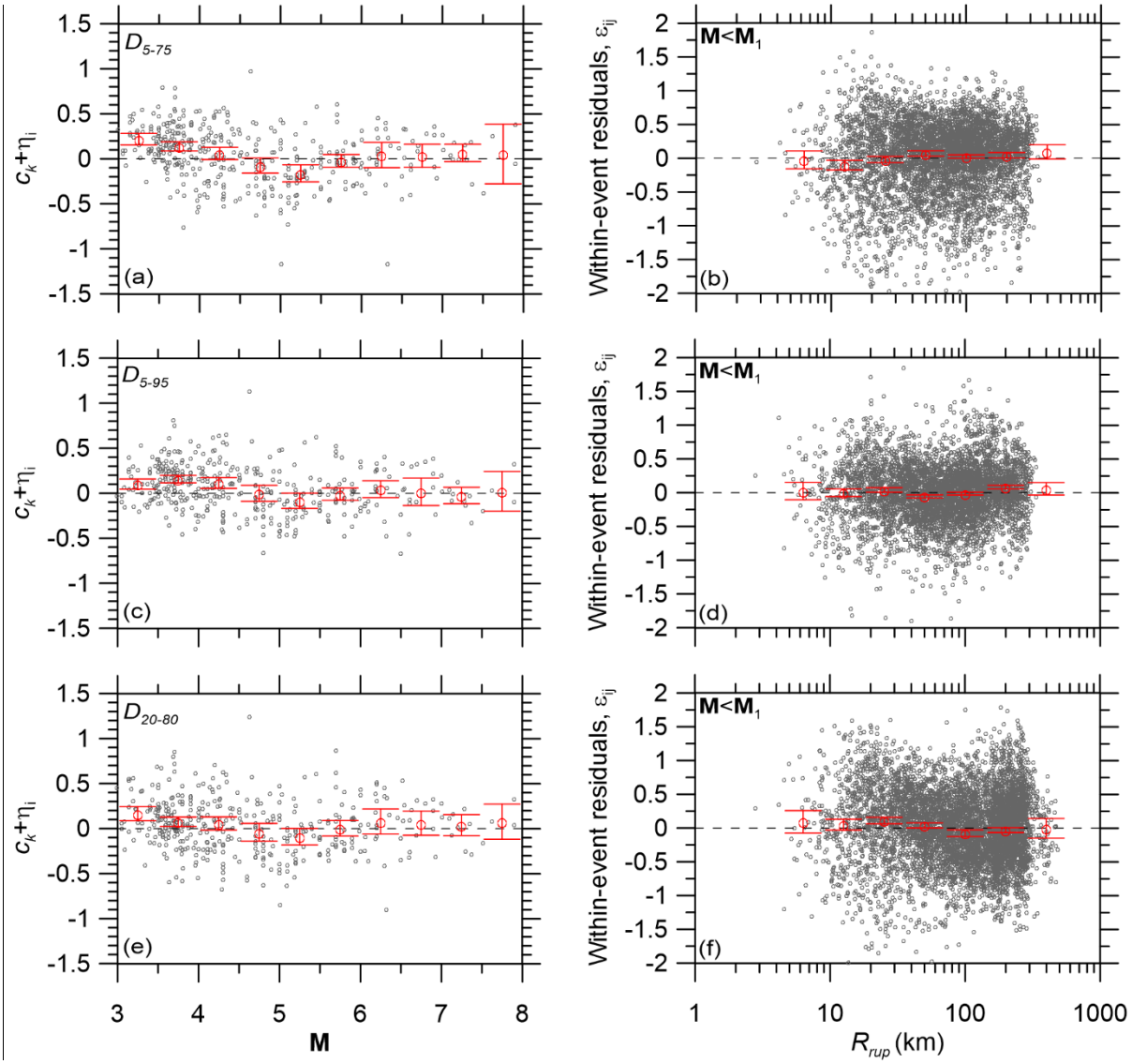

Figure 5.15. Plots of between-event residuals for $D_{5\text{-}75}$ (a), $D_{5\text{-}95}$ (c), and $D_{20\text{-}80}$ (e) across the full M range; and within-event residuals for $D_{5\text{-}75}$ (b), $D_{5\text{-}95}$ (d), and $D_{20\text{-}80}$ (f) showing trend with rupture distance, using data for $M < M_1$ only along with their binned means and 95% confidence intervals.

5.5.2 Standard Deviation

The standard deviation model has two components: between-event standard deviation (τ) and within-event standard deviation (ϕ). Figures 5.16-5.18 shows binned values of both τ and ϕ with **M** and ϕ with R_{rup}. These standard deviations were derived using the full data set (including **M** < $\mathbf{M_1}$ events). Key features from these plots are that the ϕ term is larger, and that while both terms are **M**-dependent, the sensitivity to **M** is greater for ϕ than for τ. Given the magnitude dependence of ϕ, the trends of ϕ vs R_{rup} were evaluated using data from events with **M** > 5.75, as shown in Figures 5.16-5.18(c). Unlike with amplitude parameters (Boore et al., 2014), standard deviation ϕ has no clear dependence on R_{rup}. I capture the **M**-dependence of τ and ϕ by computing standard deviations within relatively broad **M** bins (defined per Eqs. 5.13-5.14). I considered many possible limiting magnitudes for the upper bound of the low-**M** bin and the lower bound of the high-**M** bin. The bounding magnitudes reflected in Eqs. (5.13-5.14) reflect limits beyond which systematic changes in these standard deviations were observed from these analyses. I use a simple linear interpolation between the limiting magnitudes, as shown in Figures 5.15-5.18.

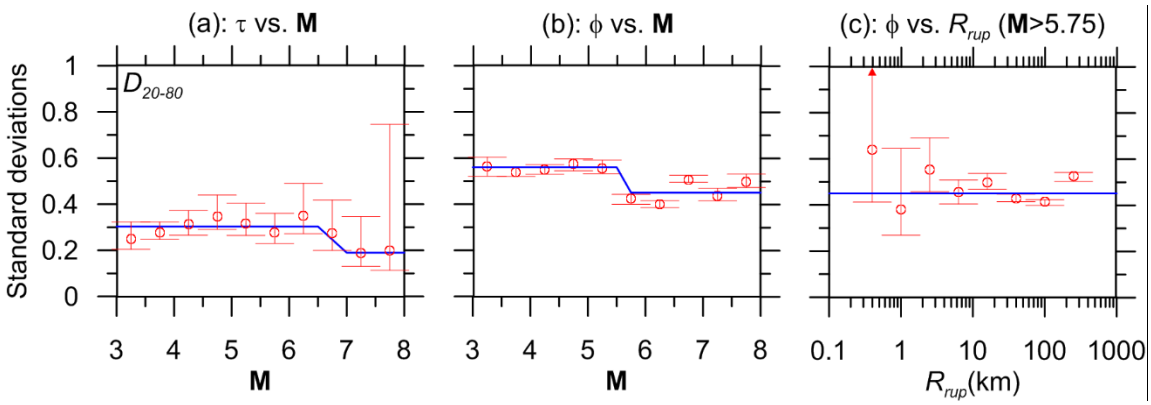

Figure 5.16. Binned standard deviation terms for D_{20-80} plotted against independent variables along with standard deviation models per Eqs. (5.13)-(5.14): (a) between-event standard deviation τ vs. magnitude, (b) within-event standard deviation ϕ vs. magnitude, and (c) ϕ vs. distance for M > 5.75 data. Confidence intervals for binned standard deviations are assumed to follow the chi distribution, which is not symmetric.

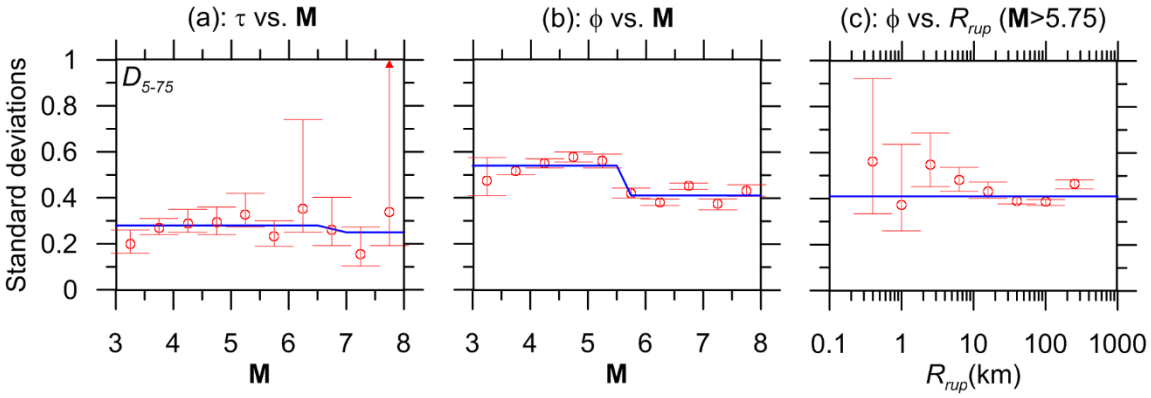

Figure 5.17. Binned standard deviation terms for D_{5-75} plotted against independent variables along with standard deviation models per Eqs. (5.13)-(5.14): (a) between-event standard deviation τ vs. magnitude, (b) within-event standard deviation ϕ vs. magnitude, and (c) ϕ vs. distance for M > 5.75 data. Confidence intervals for binned standard deviations are assumed to follow the chi distribution, which is not symmetric.

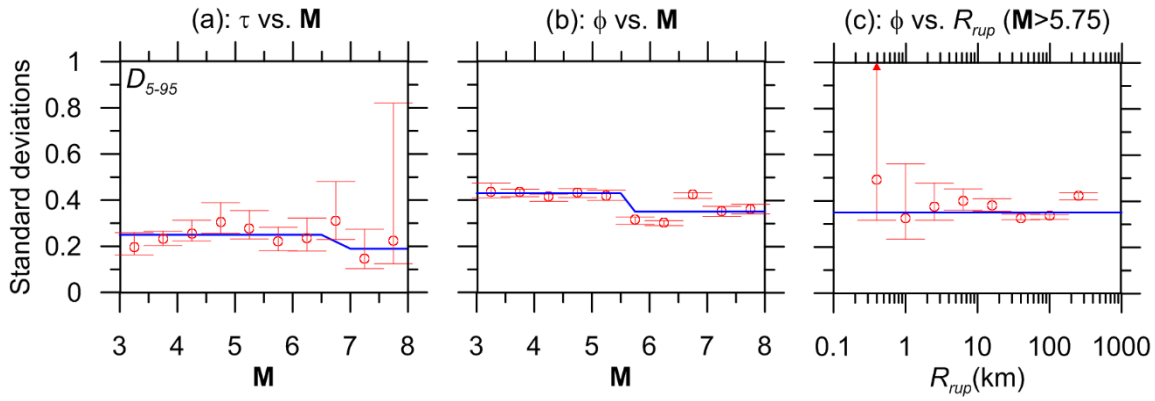

Figure 5.18. Binned standard deviation terms for D_{5-95} plotted against independent variables along with standard deviation models per Eqs. (5.13)-(5.14): (a) between-event standard deviation τ vs. magnitude, (b) within-event standard deviation ϕ vs. magnitude, and (c) ϕ vs. distance for M > 5.75 data. Confidence intervals for binned standard deviations are assumed to follow the chi distribution, which is not symmetric.

5.6 COMPARISON TO OTHER MODELS

I compare the present model to the other recent duration GMMs referenced in the *Introduction*. Separate comparisons are made for source, path, and total durations and I comment on epistemic uncertainties as inferred from these comparisons.

5.6.1 Source duration

Source durations are computed from the GMMs using zero distance, a reference site condition of V_{S30}=760 m/s, and a strike-slip focal mechanism. Resulting trends of median D_{5-75} and D_{5-95} source durations with **M** are shown in Figure 5.19.

For D_{5-75}, all source models except Du and Wang (2016) model have an exponential form resulting in linear trends in semi-logarithmic space (as plotted, KS06 appears as slightly nonlinear due to an additive site term that is non-zero for V_{S30}=760 m/s). Our model also has an exponential form for source duration, but the tri-linear function for $\Delta\sigma$ introduces slope changes at $\mathbf{M}_1$ and $\mathbf{M}_2$. the gradient of the two NGA-Ist2 models expressing the scaling of source duration with **M** for

$\mathbf{M}_1$<**M**< $\mathbf{M}_2$ is somewhat flatter than older models. I note here that the prior models generally did not use data from the two **M**7.9 events in the NGA-West2 data set (exception is Bommer et al. 2009, who used the NGA-West1 data set, which included the 2004 Alaska earthquake recordings), hence the two new models are presumably better constrained at large magnitude. Results for $D_{5\text{-}95}$ are similar, except that Lee and Green (2014) use a nonlinear-exponential source function that produces a nonlinear trend in semi-logarithmic space (Figure 5.19). That nonlinear trend flattens at small **M**, approaching the constant source duration term employed in our model for **M** < $\mathbf{M}_1$.

Bearing in mind that the ordinate axis has a logarithmic scale, the ratio of upper/lower bound median models near the middle of the data range (around **M** 6) is approximately a factor of 1.5 for $D_{5\text{-}75}$ and two for $D_{5\text{-}95}$. This level of epistemic uncertainty almost certainly increases considerably beyond the approximate limits of the older models, namely for **M** < 4-5 and **M** > ~7.5. For both $D_{5\text{-}75}$ and $D_{5\text{-}95}$, our model and Du and Wang (2016) model deviate in their trends with **M** from extrapolations of older models in the literature for small magnitudes. I have introduced the flat trend while Du and Wang (2016) model still has a small **M**-scaling for small magnitudes. For **M** > ~7.5, the Du and Wang (2016) model does not reflect a sharp change in magnitude scaling. This shows a difference in **M**-scaling in the two models despite the fact that they are based on the same database. The difference is due to the fact that I have chosen to introduce a sharp change in **M**-scaling in order to better capture the long duration of the two **M**7.9 events (Denali and Wenchuan), while Du and Wang (2016) decided not to change **M**-scaling because of these two specific events. The difference between **M**-scaling between the two models as discussed above, must be noted, and reflected in the epistemic uncertainty of prediction of very small or very large magnitude events.

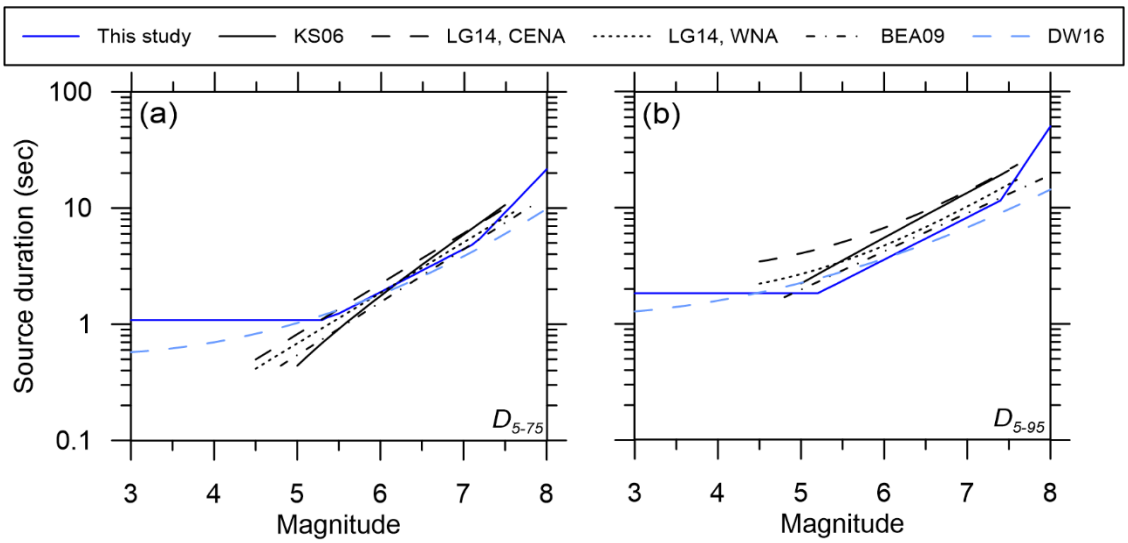

Figure 5.19. Comparison of the prediction by different models for zero distance and reference site condition (V_{S30}=760 m/s) for (a) $D_{5\text{-}75}$ and (b) $D_{5\text{-}95}$. CENA=central and eastern north America; WNA=western north America; KS06=Kempton and Stewart (2006); LG14=Lee and Green (2014); BEA09=Bommer et al. (2009); DW16=Du and Wang (2016).

5.6.2 path duration

Our path duration term is additive, and as such can only be compared to similarly formatted additive path duration models in the literature (KS06; BT14). As shown in Figure 5.20, the path durations for different models have general similarity, although KS06 use a single slope and BT14 use a multi-linear model with somewhat different trends than those found here (i.e., flatter between 40 and 120 km).

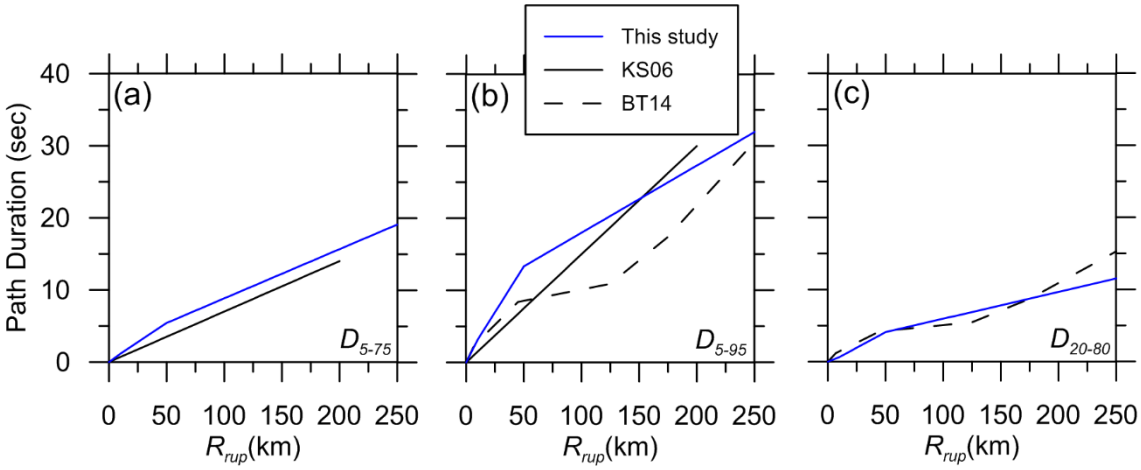

Figure 5.20. Comparison of path duration predicted by different models

5.6.3 Total duration

We compare in Figure 5.21 total median durations predicted by our model with those for other duration GMMs. I include each of the GMMs discussed in the *Introduction* with the exception of Bora et al. (2014), which is not for significant duration. The source durations (at R_{rup} = 0) exhibit model-to-model variability (largest/smallest) of about a factor of 1.5 for $\mathbf{M} \geq 6.25$, which grows to a factor of more than two at a distance of 200 km.

The results in Figure 5.17 provide a more complete picture of model-to-model variability inclusive of path duration, because the use of total duration allows models with multiplicative path duration functions to be included. The variability is somewhat higher than is reflected in Figure 5.20, which is driven in part by the LG14 CENA model (which often provides upper bounds at large magnitudes) and the BEA09 model. The BEA09 model has a much flatter trend with distance at large magnitudes, which results from their use of an **M**-dependent path term in which path scaling decreases with **M**. For **M**5, there is a notable difference between our model and DW16 model in their trends with distance. Similar to what was observed for the source durations, this difference is a result of different assumptions in developing the two models. I suspect that the weak recordings having a small magnitude and large distance can be affected by noise, so I introduced methodologies to address the issue, and introduced a flat trend with **M** for small magnitudes, while this approach was not taken in developing DW16 model.

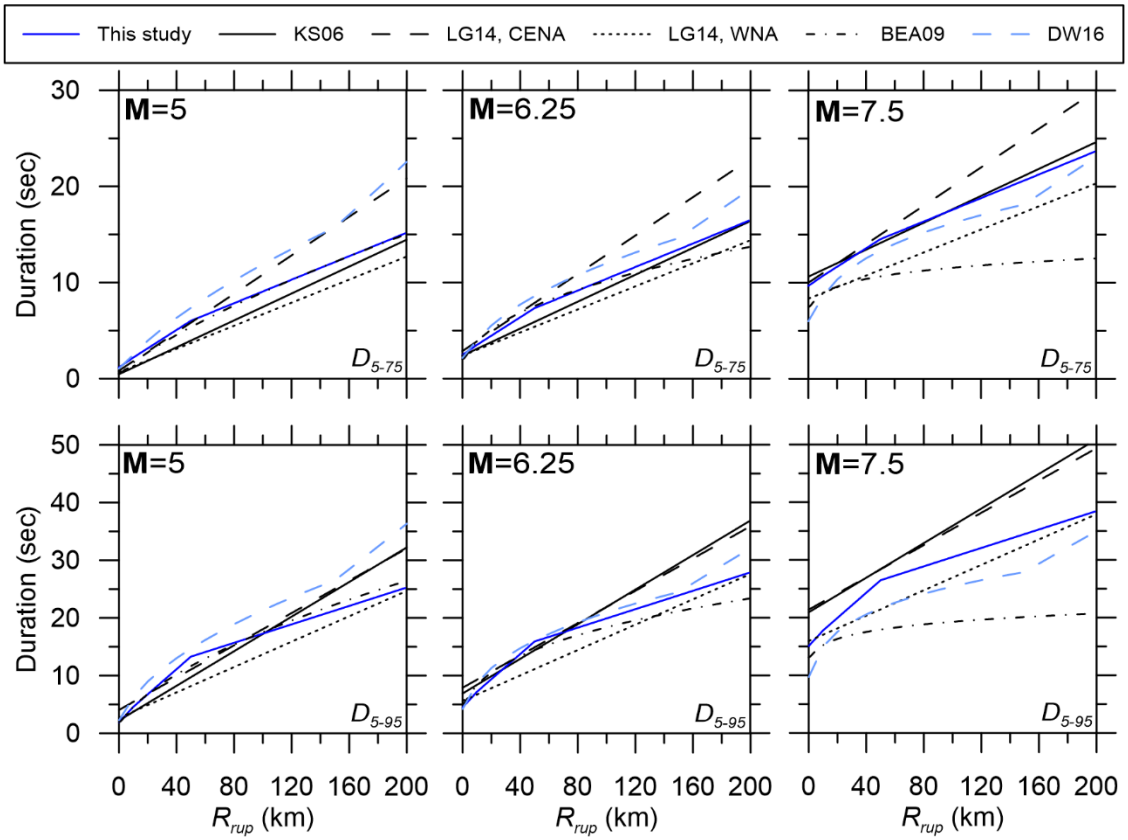

Figure 5.21. Comparisons of median durations predicted by other models for a reference site condition (V_{S30}=760 m/s) and the duration parameters of D_{5-75} and D_{5-95}.

5.7 CONCLUSIONS

I present GMMs for three significant duration parameters derived from the NGA-West2 database. The new relations are a significant improvement over KS06 and other recent duration GMMs because of the size of the database and associated improvements in the reliability of the models.

Our GMMs are intended for application in tectonically active crustal regions. I recommend the following limits for the predictor variables used in our GMMs:

- Strike-slip and reverse-slip earthquakes, **M** = 3 to 8.0. As discussed in the text, epistemic uncertainties are relatively large below **M** 5 (due to difficulties in separating source and path durations) and above **M** 7.5 (due to only two events).
- Normal-slip earthquakes, **M** = 3 to 7
- Distance, R_{rup} = 0 to 300 km
- Time-averaged shear wave velocities of V_{S30} = 150 to 1500 m/s
- Basin depth, z_1 = 0 to 3.0 km
- CL1 (mainshock) or CL2 (aftershock) event types

These limits are subjective estimates based on the distributions of the recordings used to develop the equations. Unlike KS06, I have not considered near-fault effects (such as pulse-like ground motions) in our formulation of the duration model. This was done in large part because of the lack of consensus from the NGA-West2 project on optimal parameterizations of near-fault effects. I expect these effects to be considered in future work.

6 Validation of Duration Parameters from SCEC Broadband Platform Simulated Ground Motions

6.1 INTRODUCTION

The Southern California Earthquake Center (SCEC) has developed a broadband platform (BBP) that hosts five finite source simulation methods, with the intention of developing those methods to a degree that they can be considered suitable for engineering application. Achieving this level of acceptance requires validation of the motions produced by the simulation routines, which has been undertaken through a coordinated program involving different validation approaches considering different ground motion intensity measures. The validation studies can be divided into two groups: (1) studies which compare the intensity measures from the simulation to the ones from recorded data or empirical models, and (2) studies that validate simulated motions indirectly by comparing computed structural responses for the cases of excitation from simulations vs. recorded ground motions.

An example of the first type of validation is Goulet et al. (2015), who investigated the suitability of predicted pseudo-spectral accelerations as estimated from 1D simulation models (i.e., Green's functions used in the simulations assumed a laterally constant site condition). This evaluation was completed by Dreger et al. (2015) using SCEC BBP version 14.3 simulation methods denoted EXSIM, GP, SDSU, and UCSB (Atkinson and Assatourians, 2015; Graves and

Pitarka, 2010 and 2015; Olsen and Takedatsu, 2015; and Crempien and Archuleta, 2015 respectively). Based on comparisons of the simulations to recorded pseudo-spectral accelerations (PSAs) from specific earthquakes and trends from semi-empirical ground motion models, and focusing on median trends only (i.e., not considering dispersion), Dreger et al. (2015) found that these simulations can "provide acceptable estimates of median PSA from 0.01 to 3 s oscillator period within the validation magnitude range (**M** 5.4-7.2)". Burks and Baker (2014) proposed a list of checks beyond PSA that can be considered as part of validation exercises including the correlations of spectral acceleration across periods, ratio of maximum-to-median component spectral accelerations, and ratios of inelastic-to-elastic spectral displacements for single degree-of-freedom oscillators. Rezaeian et al. (2015) conducted a validation study based on the evolution of intensity and frequency content of ground motions. Duration was used as a validation parameter by Hartzell et al. (1999), who considered duration along with Fourier amplitude and response spectra to validate simulations of 1994 Northridge earthquake ground motions using the 13 simulation techniques. Examples of the second type of validation have typically examined the response of nonlinear, multi-degree of freedom structural systems (Galasso et al., 2013; Zhong and Zareian, 2016).

This study fits into the first group –comparisons of intensity measures (in this case, duration) from simulations to those from a semi-empirical GMM. I acknowledge that validation solely on the basis of duration provides an inadequate basis for judging the suitability of a particular set of simulations for engineering practice because the amplitude and frequency-content of ground motion are more important features controlling structural response. As such, the present work is intended to supplement the prior work of Goulet et al. (2015) and Dreger et al. (2015),

which did not consider duration, as a part of a broader 'validation gauntlet' being undertaken by SCEC (*http://collaborate.scec.org/gmsv/Main_Page*).

I utilize the significant duration metric (Trifunac and Brady, 1975), which is defined from the time variation of normalized Arias intensity (I_A). I consider significant duration parameters for time intervals between 5-75%, 5-95%, and 20-80% of normalized I_A, which are denoted $D_{5\text{-}75}$, $D_{5\text{-}95}$, and $D_{20\text{-}80}$, respectively. Various significant duration parameters have been found to have predictive power for a number of engineering applications, including structural collapse capacity (Hancock and Bommer, 2007; Raghunandan and Liel, 2013; Chandramohan et al., 2016), landslide displacement (Bray and Rathje, 1998), and response of concrete dams (Zhang et al., 2013). Both $D_{5\text{-}95}$ and $D_{5\text{-}75}$ have been considered in these applications. Boore and Thompson (2014) used $D_{20\text{-}80}$ for predicting path effects on duration, anticipating that it would better represent the time window of shear-wave arrivals, and was less affected by noise effects. To our knowledge there are no uniformly agreed upon (and published) criteria for judging one significant duration parameter against another in terms of its usefulness in engineering application. Rather, the use of these parameters has been rather ad hoc, with the primary factor driving the choice of $D_{5\text{-}75}$ vs. $D_{5\text{-}95}$ being whether the analyst is mostly interested in the shear-wave portion of records (in which case they typically pick $D_{5\text{-}75}$) vs. the combination of shear waves and some amount of surface waves/coda ($D_{5\text{-}95}$).

I compare duration predictions from simulation methods to trends from observation as reflected by a the GMM discussed in Chapter 5 (Afshari and Stewart, 2016 – hereafter AS16). I use version 15.3 simulated ground motions for this validation study, as obtained from SCEC servers in December 2015. Version 15.3 is the most recent version available as of this writing. I

am unaware of other validation exercises performed specifically with this version of the simulation codes.

The AS16 GMM for the significant duration of ground motions was derived using the NGA-West2 database for active crustal regions (Ancheta et al., 2014). The model consists of equations for the effects of magnitude (**M**), rupture distance (R_{rup}), and time-weighted average shear wave velocity in upper 30 m of the site (V_{S30}) on the mean and standard deviation (between- and within-event components) of $D_{5\text{-}75}$, $D_{5\text{-}95}$, and $D_{20\text{-}80}$. The model is also able to capture the effects of focal mechanism and depth to the 1.0 km/s shear wave velocity isosurface (z_1). The AS16 GMM is developed as an update of the prior work by Kempton and Stewart (2006) which was developed using a smaller database. Both of these GMMs have functional forms adapted from an earlier GMM by Abrahamson and Silva (1996). Other available GMMs for duration include Bommer et al. (2009), which is based on NGA-West1 database for active crustal regions (Chiou et al., 2008); Lee and Green (2014) for stable continental regions; and Bora et al. (2014), which is based on a European data set (Akkar et al., 2014).

The AS16 GMMs were used for the present validation because they were developed using the largest and most recent database for active crustal regions. Significantly, each of the validation events considered in the following section contributed data to the flatfile used in the development of AS16.

The findings in this chapter have been published in a journal article by Afshari and Stewart (2016).

6.2 VALIDATION OF SIMULATED GROUND MOTIONS

We consider simulated ground motions as computed for five events loosely associated with previous California earthquakes (1986 **M**6.1 North Palm Springs (NPS), 1987 **M**6.0 Whittier, 1989 **M**6.9 Loma Prieta, 1992 **M**7.3 Landers, and 1994 **M**6.7 Northridge). Figure 6.1 shows the epicenter locations. The SCEC BBP has ground motions for 50 realizations of each event. All simulations were performed for a 1D crustal model with surface site condition with time-averaged shear wave velocity V_{S30} = 863 m/s. Additional details regarding the source and path conditions considered in the simulations are given by Goulet et al. (2015). I consider all 50 realizations for each event and examine trends in the simulated motions to evaluate distance scaling, **M** scaling, and dispersion of the simulated motions. Those ground motion features are, in turn, compared to the corresponding trends observed empirically as represented by the AS16 GMMs.

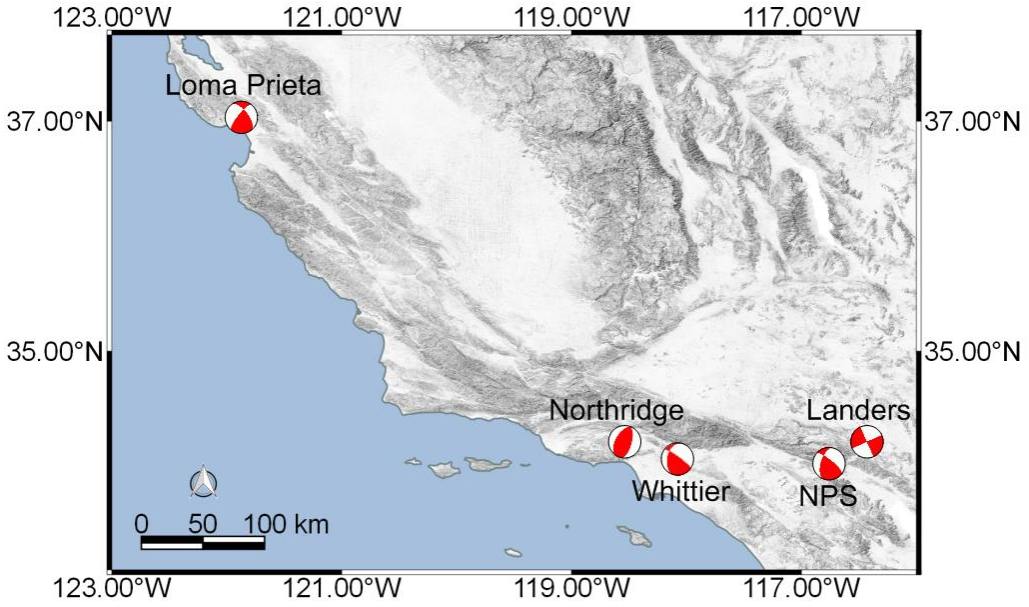

Figure 6.1. Location of epicenters for the five simulated events (1986 M6.1 NPS, 1987 M6.0 Whittier, 1989 M6.9 Loma Prieta, 1992 M7.3 Landers, and 1994 M6.7 Northridge).

Figures 6.2-6.7 show the simulated ground motion durations from EXSIM, GP, SDSU and UCSB plotted against R_{rup} along with GMM predictions for $D_{5\text{-}75}$, $D_{5\text{-}95}$, and $D_{20\text{-}80}$. The GMMs are represented by event-term adjusted medians and medians ± one within-event standard deviations (ϕ) in the plots. The event terms used for the adjustment are based on the recorded data for the five events, and hence are unrelated to the simulations. The rationale for including the event term adjustment is that a particular event may have non-mean centered data arising from its source attributes that I cannot expect the GMM to capture, but which should be captured by the finite fault and slip models used in the simulations. Hence, making this adjustment to the GMM provides for a more 'apples-to-apples' comparison of GMM and simulations.

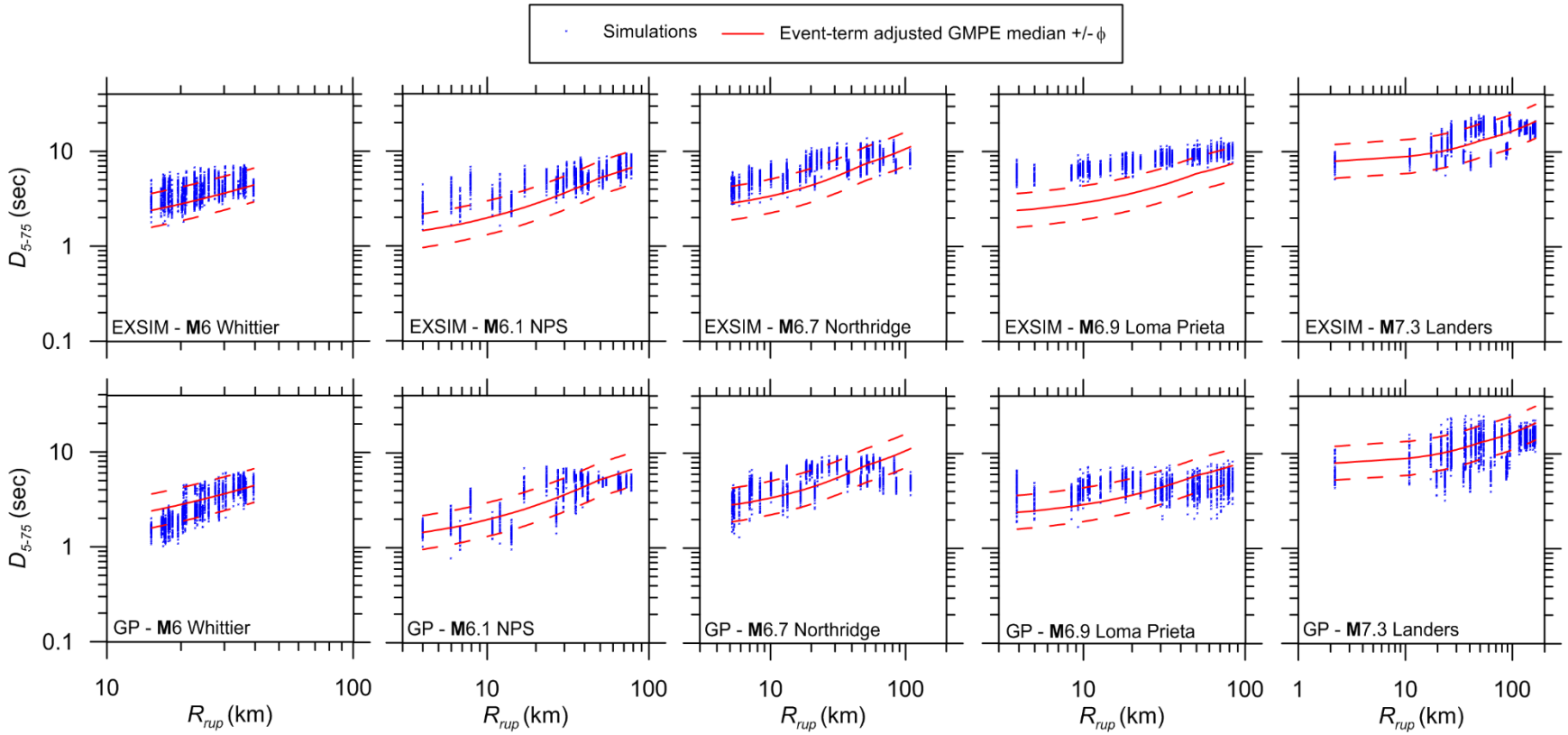

Figure 6.2. Variation with distance of simulated ground motion duration $D_{5\text{-}75}$ for five events (Whittier, NPS, Loma Prieta, Northridge, and Landers) from finite fault methods (EXSM and GP) and event-term adjusted prediction from GMM. GMM was exercised for the site condition used in the simulations, which is V_{S30} = 863 m/s.

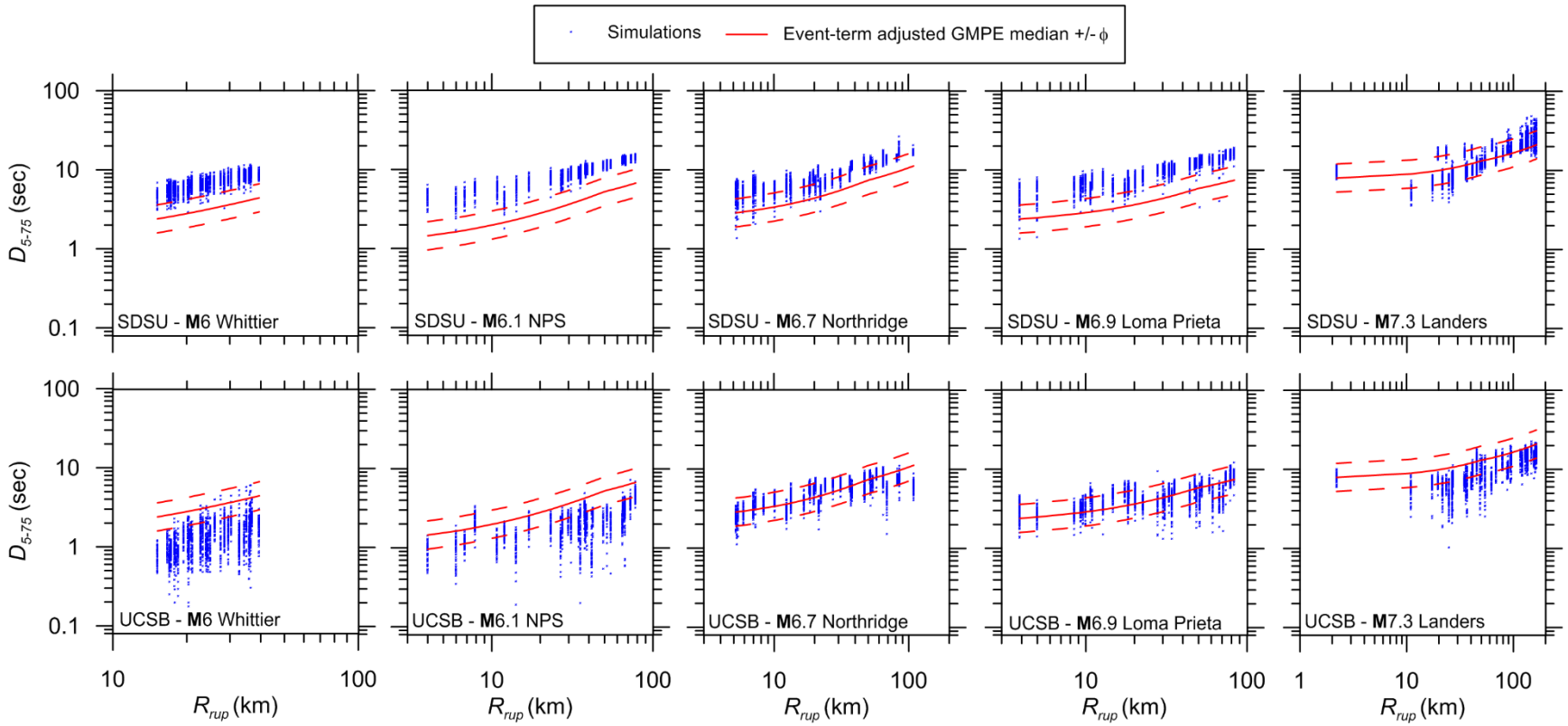

Figure 6.3. Variation with distance of simulated ground motion duration D_{5-75} for five events (Whittier, NPS, Loma Prieta, Northridge, and Landers) from finite fault methods (SDSU and UCSB) and event-term adjusted prediction from GMM. GMM was exercised for the site condition used in the simulations, which is V_{S30} = 863 m/s.

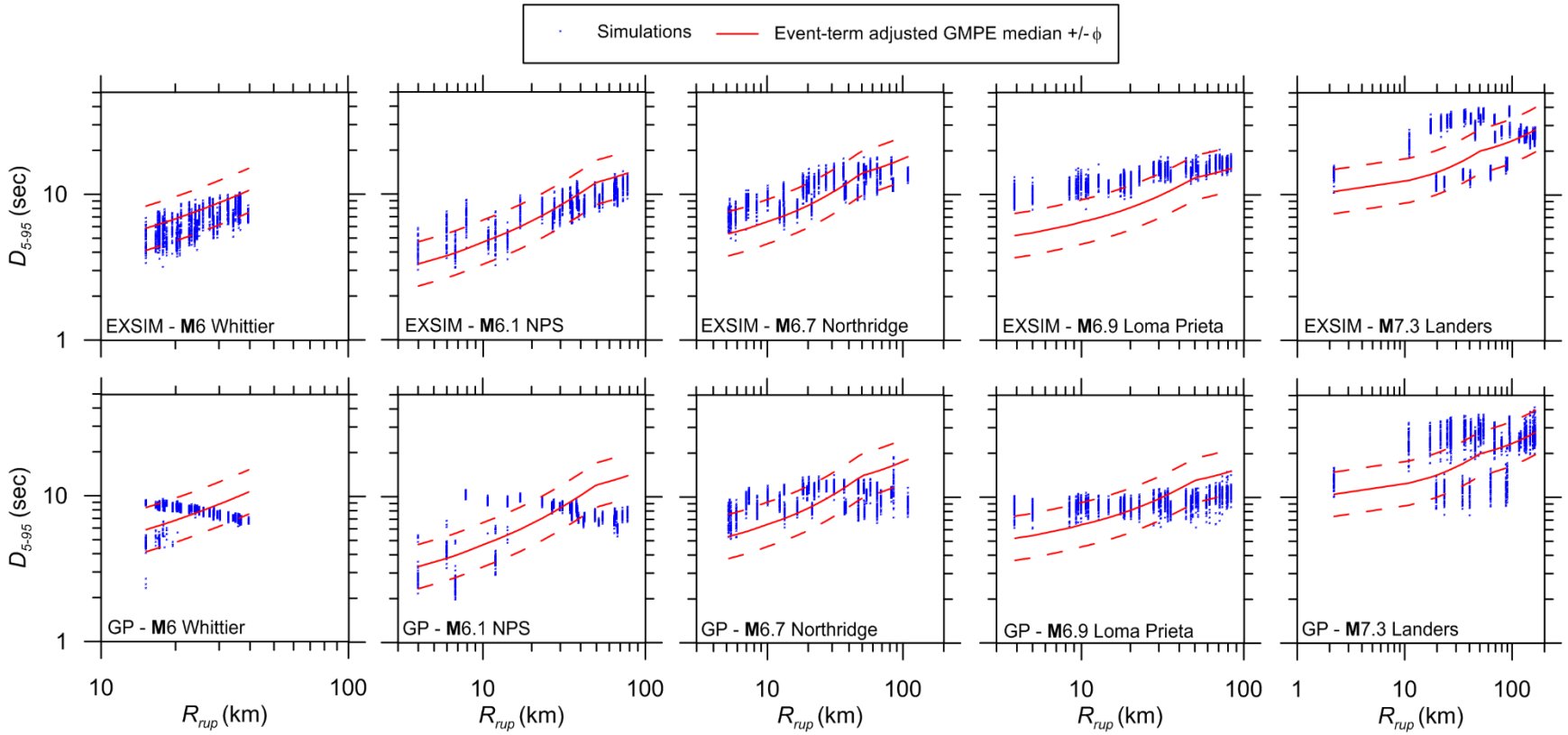

Figure 6.4. Variation with distance of simulated ground motion duration $D_{5\text{-}95}$ for five events (Whittier, NPS, Loma Prieta, Northridge, and Landers) from finite fault methods (EXSM and GP) and event-term adjusted prediction from GMM. GMM was exercised for the site condition used in the simulations, which is V_{S30} = 863 m/s.

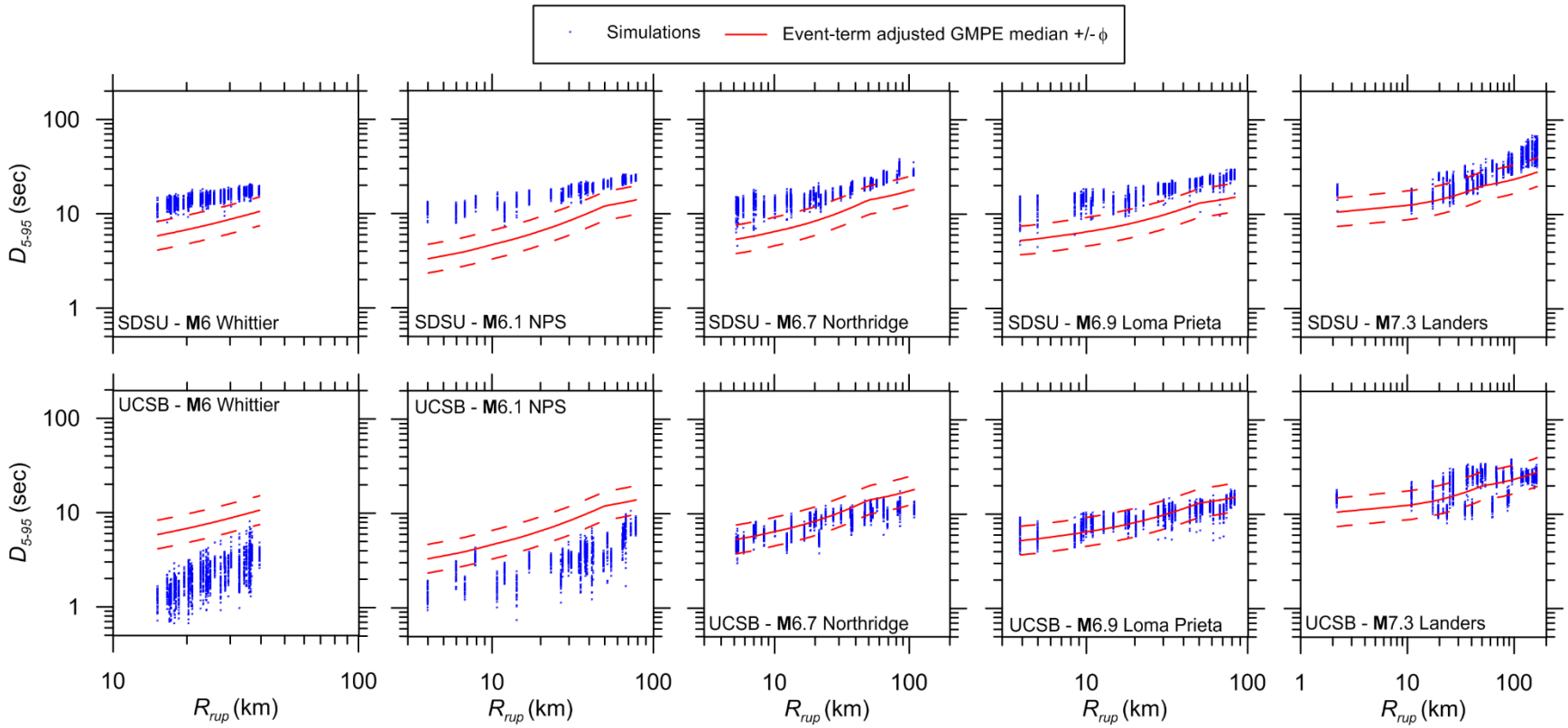

Figure 6.5. Variation with distance of simulated ground motion duration $D_{5\text{-}95}$ for five events (Whittier, NPS, Loma Prieta, Northridge, and Landers) from finite fault methods (SDSU and UCSB) and event-term adjusted prediction from GMM. GMM was exercised for the site condition used in the simulations, which is V_{S30} = 863 m/s.

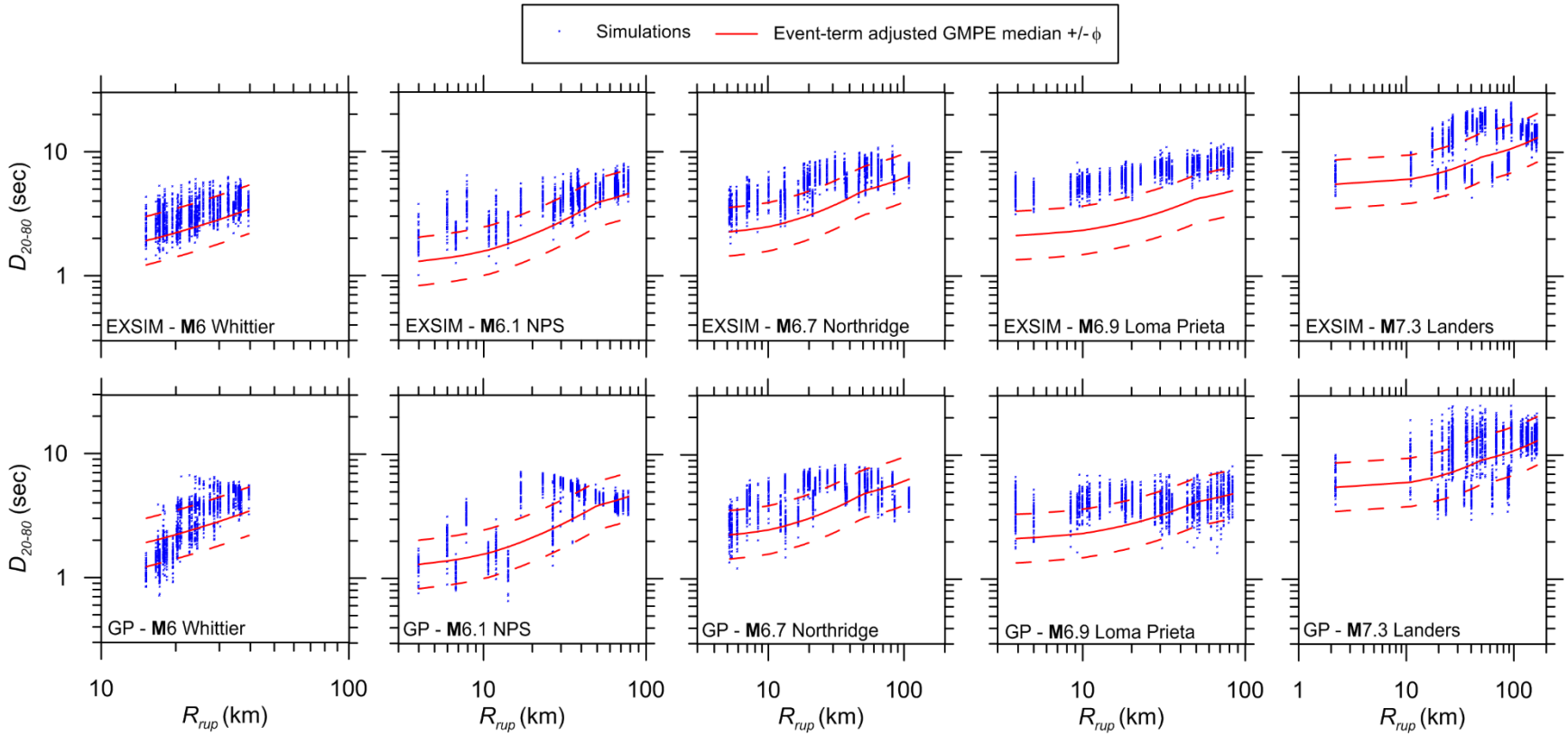

Figure 6.6. Variation with distance of simulated ground motion duration $D_{20\text{-}80}$ for five events (Whittier, NPS, Loma Prieta, Northridge, and Landers) from finite fault methods (EXSM and GP) and event-term adjusted prediction from GMM. GMM was exercised for the site condition used in the simulations, which is V_{S30} = 863 m/s.

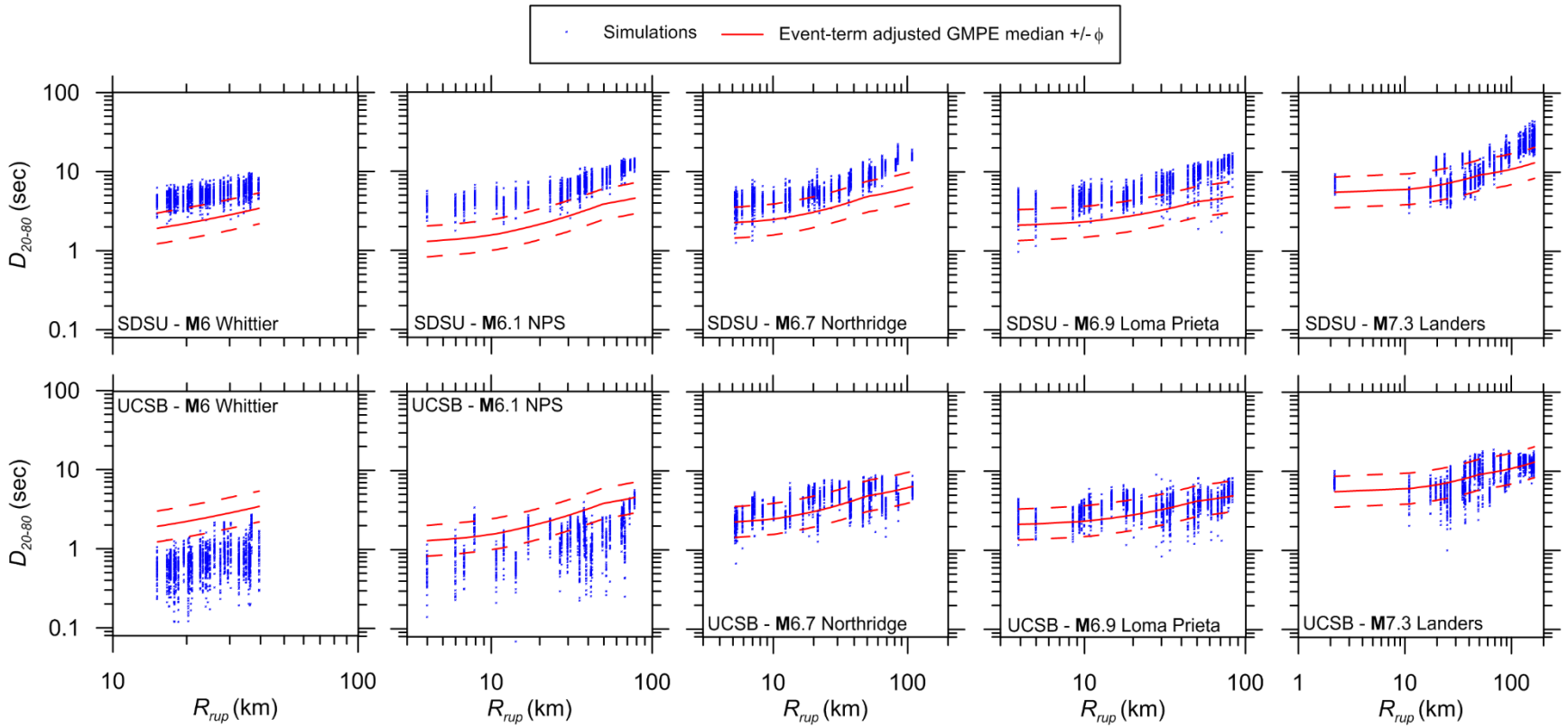

Figure 6.7. Variation with distance of simulated ground motion duration $D_{20\text{-}80}$ for five events (Whittier, NPS, Loma Prieta, Northridge, and Landers) from finite fault methods (SDSU and UCSB) and event-term adjusted prediction from GMM. GMM was exercised for the site condition used in the simulations, which is V_{S30} = 863 m/s

The event-specific results in Figures 6.2-6.7 illustrate how the path effects produced by the simulations compare to those in the GMMs. In most cases the durations of simulated motions increase with R_{rup} at approximately the same rate as provided by the GMMs, although there are some exceptions. In particular, GP durations decrease with increasing distance in several cases, especially for R_{rup} > 10-20 km (Whittier, North Palm Springs, Northridge) and the simulations have a small slope or flat trend with R_{rup} for Loma Prieta (except the SDSU and UCSB methods).

Formal evaluation of the simulated data entails analysis of residuals between the simulations and GMMs. Residuals are computed as:

$$R_{ij}^{sim} = \ln D_{ij}^{sim} - \mu_{ij} \tag{2.1}$$

where D_{ij}^{sim} is the geometric mean duration from pairs of horizontal-component simulated ground motions at site *j* from event *i*, and μ_{ij} is the corresponding GMM mean in natural log units. EXSIM motions are generated only for a single arbitrary horizontal orientation, hence a single-component definition of D_{ij}^{sim} was used in that case. The superscript 'sim' is used here and elsewhere to emphasize that the residuals are computed from simulations, and not from recorded data (as is more customary in GMM development). Residuals can then be partitioned into between- and within-event components through mixed effects regression using the *nlme* command in R (Pinheiro et al., 2013) as:

$$R_{ij}^{sim} = c^{sim} + \eta_i^{sim} + \varepsilon_{ij}^{sim} \tag{2.2}$$

where c^{sim} is the model bias, η_i^{sim} is the between-event residual (event term) for simulated event *i*, and ε_{ij}^{sim} is the within-event residual for simulated motion *j* in event *i*. It should be noted that

residuals in this context take on a different meaning than what is customary for analysis of ground motion recordings (natural log of data minus model). In the analysis of recordings, positive residuals indicate an underprediction bias by the GMM, whereas in the present case positive residuals indicate an overprediction bias of the simulations.

Figure 6.8 shows the model bias (c^{sim}) for each of the simulation methods. The results show that the EXSIM and SDSU simulations are generally biased towards overprediction, UCSB underpredicts, and GP is nearly unbiased. The over- and underpredictions from SDSU and UCSB simulations, respectively, are on the order of 0.5 in natural log units. To put this level of bias in context, it is useful to consider what has been observed previously for these same simulation methods and events using PSA intensity measures. Dreger et al. (2015) computed a combined goodness-of-fit (CGOF) metric that represents the absolute value of PSA bias for each simulation method and event. As such, CGOF has a similar meaning to the absolute value of c^{sim} in the present work. Dreger et al. (2015) found CGOF for the five considered events to generally be in the range 0.3-0.7. Hence, the biases of the SDSU and UCSB methods are within the ranges that have been observed in past simulation validations.

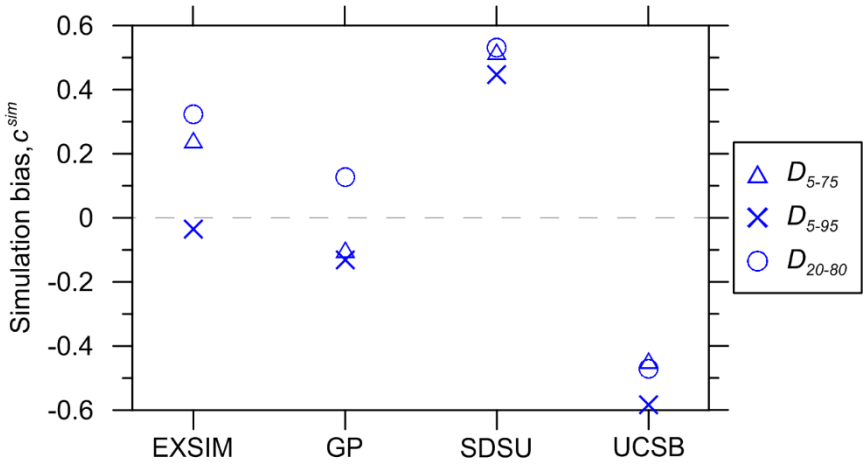

Figure 6.8. Model bias (c^{sim}) for EXSIM, GP, SDSU, and UCSB methods as defined by mean misfit of simulated data for 50 realizations each of five events relative to AS16 GMM.

I compute the mean of 50 event terms derived from mixed effects analysis for each of the considered earthquakes (denoted $\bar{\eta}^{sim}$). In Figures 6.9-6.11 I plot $\bar{\eta}^{sim}$ for the five earthquakes against **M** using $D_{5\text{-}75}$, $D_{5\text{-}95}$, and $D_{20\text{-}80}$ durations. These results are of interest to assess **M**-scaling in the simulations vs. what is captured in the GMM. The event term trends are generally flat for GP, indicating similar scaling. Upward trends are found for EXSIM and UCSB, indicating a more rapid increase of duration with **M** than given by the GMM, whereas a negative trend is found for SDSU. Also shown in Figures 6.9-6.11 is the corresponding event terms for the five earthquakes from data denoted as η_i (these were derived during GMM development). These event terms exhibit a flat trend, which would be expected over the full range of events considered in GMM development, but is coincidental in the present case. The flatness of the trend for these five events indicates that their **M**-trend is consistent with the global average. Accordingly, the aforementioned trends in $\bar{\eta}^{sim}$ arise from features of the simulations themselves, and do not appear to be a by-product of the selected earthquakes.

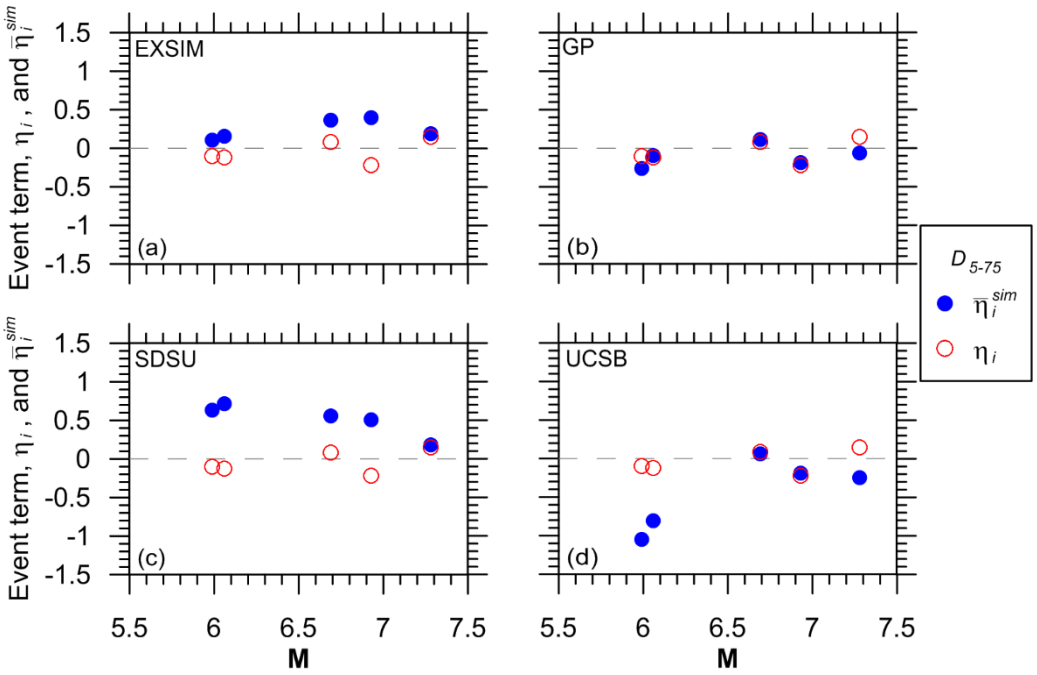

Figure 6.9. Mean of simulation event terms ($\bar{\eta}^{sim}$) and event terms from data for $D_{5\text{-}75}$ plotted vs. M for (a) EXSIM, (b) GP, (c) SDSU, (d) UCSB.`

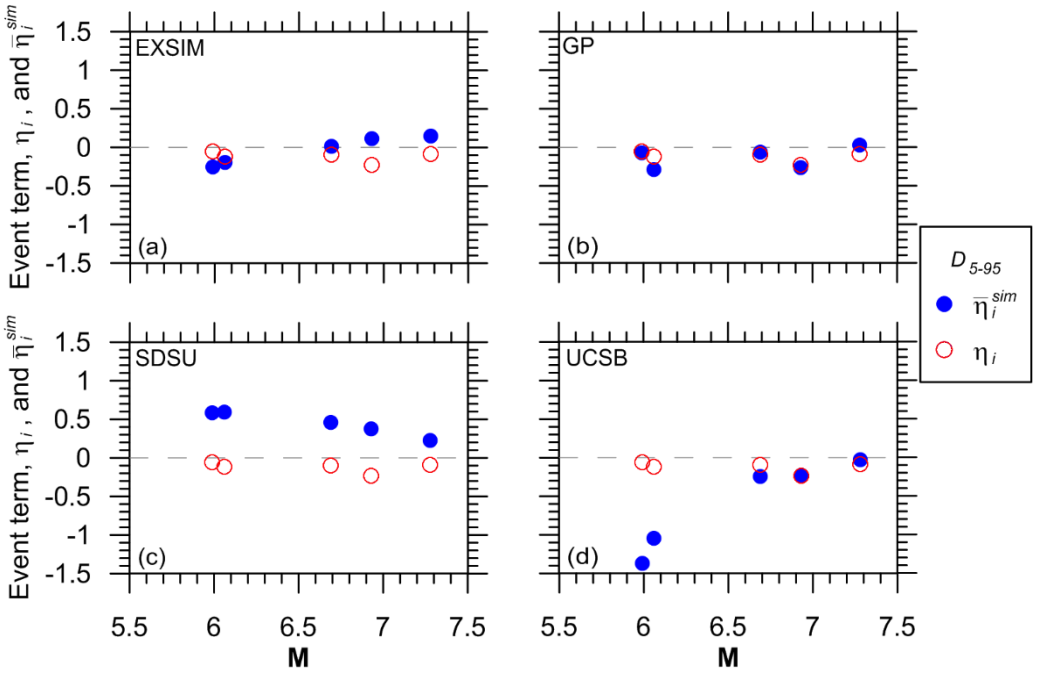

Figure 6.10. Mean of simulation event terms ($\bar{\eta}^{sim}$) and event terms from data for $D_{5\text{-}95}$ plotted vs. M **for (a) EXSIM, (b) GP, (c) SDSU, (d) UCSB.**

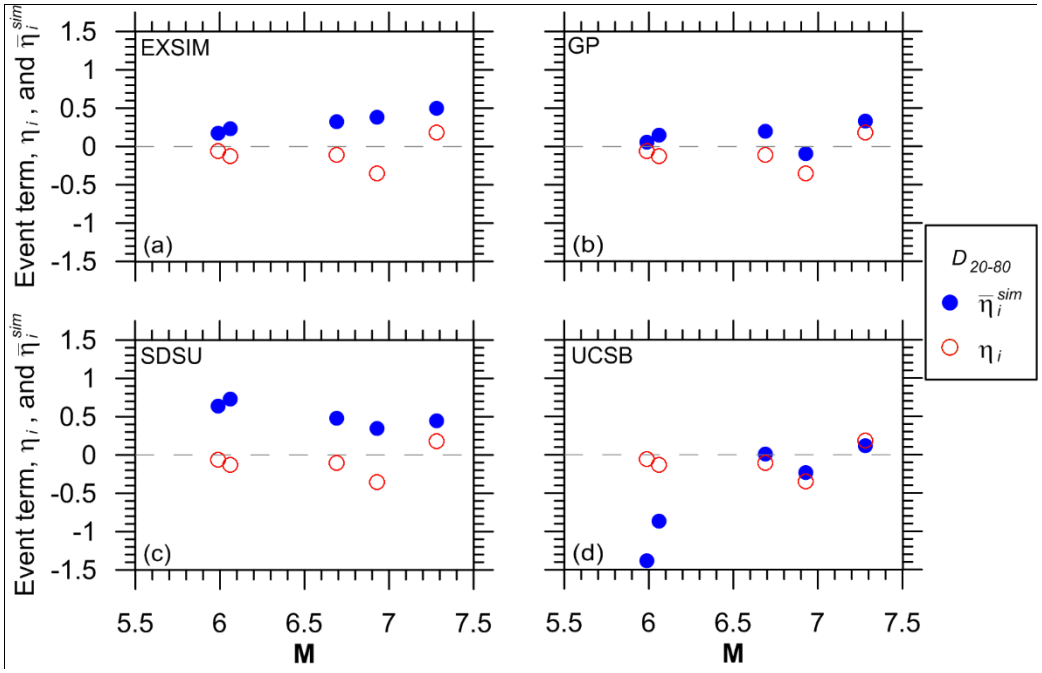

Figure 6.11. Mean of simulation event terms ($\bar{\eta}^{sim}$) and event terms from data for D_{20-80} plotted vs. M for (a) EXSIM, (b) GP, (c) SDSU, (d) UCSB.

Figure 6.12 shows within-event standard deviations from simulations (i.e., standard deviations of ε_{ij}^{sim}) for the five considered earthquakes along with values from the AS16 GMMs. The simulation dispersions are generally significantly lower than those derived empirically, with only UCSB being close to the GMM results at small magnitudes. These relatively low dispersions are consistent with previous findings for PSA (e.g., Star et al. 2011). Interestingly, the variations of dispersion among duration parameters observed in the GMMs (order of increasing dispersion: $D_{5\text{-}95} < D_{5\text{-}75} < D_{20\text{-}80}$) is preserved in the simulations.

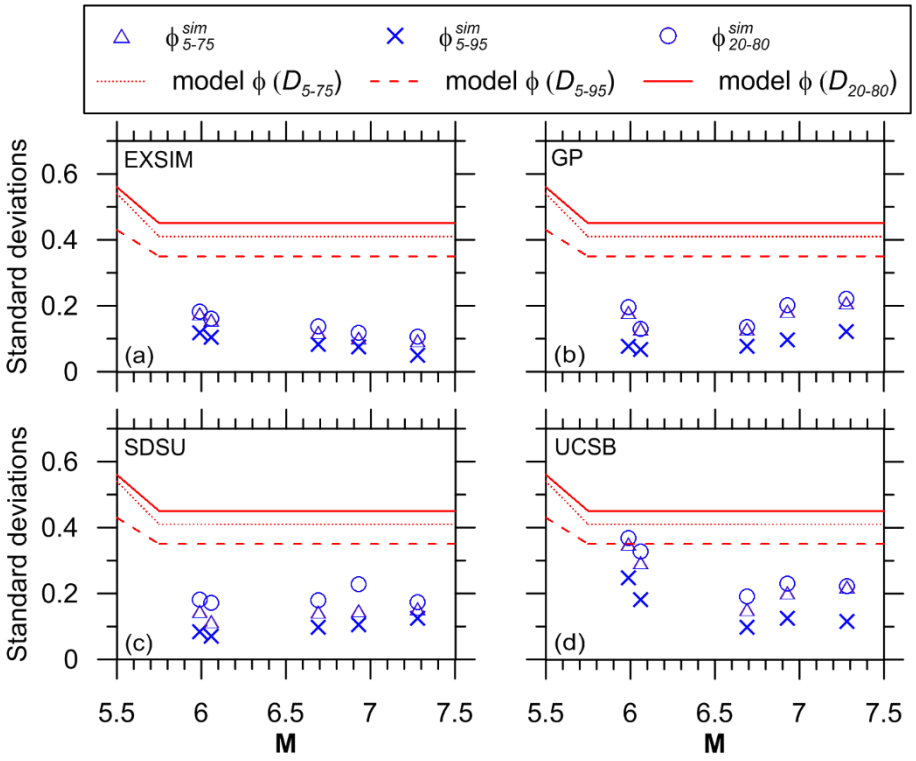

Figure 6.12. Average standard deviation of simulation residuals computed using simulated durations and the GMM for (a) EXSIM, (b) GP, (c) SDSU, (d) UCSB. The standard deviations are plotted against M **as well as within-event standard deviation (ϕ) predicted by the GMM.**

Based on these results, I find that most of the simulation methods recommended by Dreger et al. (2015) for PSA have shortcomings for duration. Specifically, for median ground motion predictions, I am concerned with the large overall bias of the SDSU and UCSB methods, distance scaling problems in the GP method, and **M**-scaling problems in the EXSIM, SDSU, and UCSB methods. These problems suggest some issues in the source and path models that warrant further consideration and which may affect other intensity measures as well. Of the simulation methods considered, GP has the best overall performance with respect to observed median durations as reflected by the GMMs. With regard to dispersion, the general underestimation for durations and other parameters is problematic for seismic hazard or risk applications.

6.3 CONCLUSIONS

In this study, we use recently-developed GMMs to validate the durations of SCEC BBP simulated ground motions. This work is part of a broader validation gauntlet organized by SCEC that includes checks of PSA similar to those described here (Goulet et al. 2015; Dreger et al. 2015) and many additional checks of differences between simulated and recorded ground motions (details in *http://collaborate.scec.org/gmsv/Main_Page*). Relative to several sets of simulated ground motions, the GMMs produce durations that generally have different medians, larger dispersions, and in some cases different scaling with **M** and distance. Accordingly, although several simulation methods have recently been recommended for use to estimate PSA, their use for applications involving duration-sensitive geotechnical or structural systems should be undertaken with caution. Considering the fact that the current BBP simulations are based on wave propagation through a 1D crustal model, the future use of 2D and 3D models similar to CyberShake (Graves et al., 2010) may provide improved results.

7 Summary and Conclusions

7.1 SCOPE

In this dissertation, two matters were studied: site response and duration of ground motion. For the first part, I developed a framework for how to evaluate non-ergodic site response using available recordings at a site, simulations from ground response analysis, or a combination of both. I studied a methodology for quantifying uncertainties in ground motion prediction, and compiled the available literature on the variability of site response. I showed the variability in ground motion prediction can be reduced as the result of reducing the uncertainty in site response. I used probabilistic seismic hazard analysis for three example sites to show the effect of reduced uncertainty in site response leads to reduction in hazard for long return periods.

In another part of the dissertation concerning site response, I compiled a dataset from vertical array sites in California in order to perform a validation study on 1D ground response analysis (GRA). The validation study was performed using site response transfer functions and amplification of Pseudo-Spectral Accelerations (*PSA*). The goodness of fit in transfer functions are used to validate the assumption of one-dimensional soil columns under vertically propagating shear waves, and *PSA* amplifications are used for studying misfits and quantifying uncertainty in GRA. I studied three approaches for damping namely (1) Using geotechnical models for laboratory-based damping; (2) Using an empirical model to estimate damping from shear wave velocity; and (3) Estimating damping from spectral decay parameter (κ). I used mixed effects

analysis of residuals to quantify the uncertainty in the predictions by 1D GRA. The results of this study are compared to a similar study on vertical array sites in Japan.

In the part of this dissertation concerning duration of ground motion, I developed a ground motion model by utilizing NGA-West2 database for active crustal regions. The model is an update to an older model (Kempton and Stewart, 2006), and has a similar functional form. The functional form of this model is intended to be consistent with the physics of the problem as discussed in Chapter 5. I developed a methodology to exclude weak recordings which are affected by noise, and used it in addition to record selection criteria from Boore et al. (2013) to select recording for developing the model. The developed ground motion model was used for validating the magnitude- and path-scaling, as well as dispersion in simulated ground motions from SCEC Broadband Platform.

7.2 RESULTS

In Chapter 2, I show how non-ergodic site response analysis has the benefit of increasing accuracy and decreasing uncertainty in site response in comparison with using ergodic models for site response. In the three example sites, I show how 1D GRA fails to capture the amplification of long period ground motions (potentially 2D and 3D effects of basin effects and surface waves) in deep basin sites (LA Obregon Park and El Centro #7), while GRA provides a much better prediction of site response in the shallow site example (APEEL #2). I also show analyzing recordings at the site (if available) is the best way of evaluating linear site response. Finally, the three example PSHA results show the sensitivity of hazard levels to uncertainty in the predictions. The examples show the reduction in uncertainty due to non-ergodic analysis leads to a considerable reduction in hazard for long return periods.

In Chapter 3, I discuss and summarize the vertical array dataset which was used in Chapter 4 for a validation study of GRA. Analysis of site response transfer functions for California vertical arrays suggest better fit between the data and predictions in comparison to a similar study by Thompson et al. (2012) on KiK-net vertical array sites in Japan. Analysis of the residuals of *PSA* predictions allow for quantifying bias and dispersion in predictions. The results of *PSA* predictions show for the most part of the period range (0.01-10 sec) the geotechnical models for small-strain damping have the least bias, and the V_S-based model is the most biased (mostly positive bias). The results also show site-to-site variability in California sites is similar to site-to-site variability in KiK-net sites which suggests a lack of regional dependency in site-to-site variability. Also, the within-site variability of site response in California vertical arrays is consistent with the other studies in the literature as summarized in Chapter 2.

In Chapter 5, ground motion model for duration is presented, which is developed using the recent NGA-West2 database. The model is used for validation of SCEC Broadband Platform simulations in Chapter 6. The results of the validation study show the simulations generally underpredict the variability in the duration of simulated ground motions, and the medians are often different between our model and the simulations.

7.3 FUTURE WORK

There are a number of aspects of the topics studied in this dissertation that can be improved in a future research project. The potential areas of improvement are as follows:

- In Chapter 3, we provided the methodology for evaluating and implementing non-ergodic site response. I included only three examples because I relied on NGA-West2 database for sites and the available recordings. Compiling richer datasets (potentially for dense areas

such as Los Angeles or San Francisco Bay Area) will allow for evaluating many more examples of non-ergodic site response which will allow for better conclusions on the comparison between different approaches for non-ergodic site response analysis (In this case GRA and using recordings). Potential conclusions can be made on the effects of geology, region, or other parameters on the performance of different methods.

- The correlations between the residuals at surface and downhole (within-event *Z*-*X* correlation coefficient), $\rho_{\ln Z,\ln X}$ can be evaluated by a model. The model can be developed based on a large enough vertical array dataset (potentially KiK-net). The predictive parameters for the model can be site parameters (e.g., V_{S30}, V_S at downhole, z_1, array depth, etc.).
- For studying site response in California vertical arrays, gathering more data will allow for performing analysis of residuals in order to evaluate between-event and within-event residuals. This task was not possible in this study due to the limited size of the dataset. Evaluation of within-event residuals at surface and downhole will allow for evaluating $\rho_{\ln Z,\ln X}$ for California, and studying the possibility of any regional dependency in $\rho_{\ln Z,\ln X}$.
- Regarding the duration of ground motions, the ground motion model can potentially be improved by incorporating the near-fault effects such as rupture directivity. Near fault effects were not taken into account in this study.

8 Appendix: Output plots of site response in vertical arrays

In this appendix, the results of site response transfer function and *PSA* amplification for all 21 vertical array sites using the three damping models are shown. The figures show the empirical and theoretical transfer functions, Empirical and theoretical *PSA* amplifications as well as their standard deviations. The amplification residuals are also shown. The following figures are the output of a program in MATLAB which is developed as a part of this research.

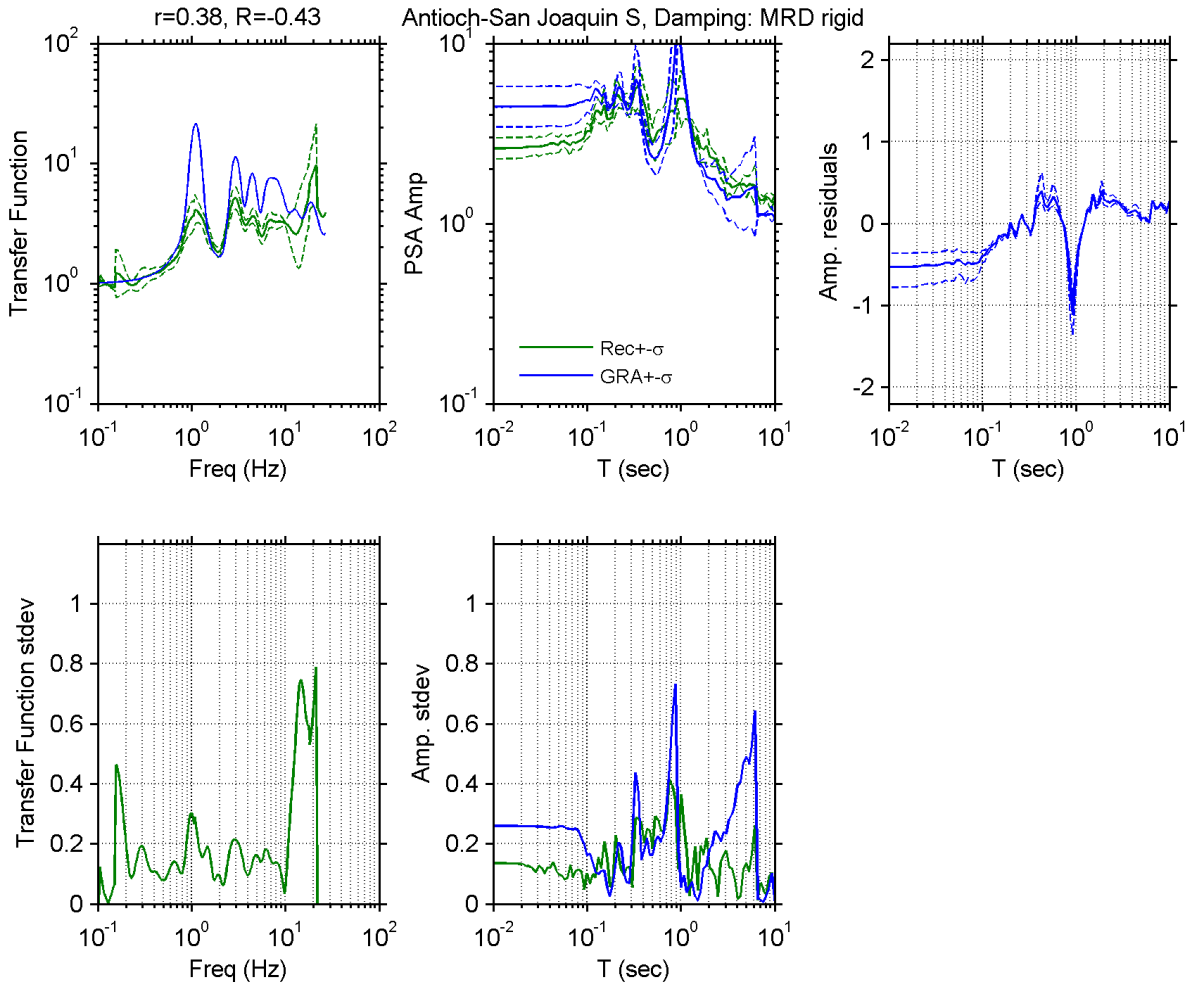

Figure A 1. Observed and simulated site response for Antioch-San Joaquin S site with $D_{\min}^{L}$ model for damping; Top left: Theoretical and median ± standard deviation of empirical transfer functions, Top middle: observed and predicted median ± standard deviation of *PS*A amplification, Top right: median ± standard deviation of *PS*A amplification residuals, Bottom left: standard deviation of empirical transfer functions, Bottom middle: standard deviation of observed and predicted *PS*A amplification residuals.

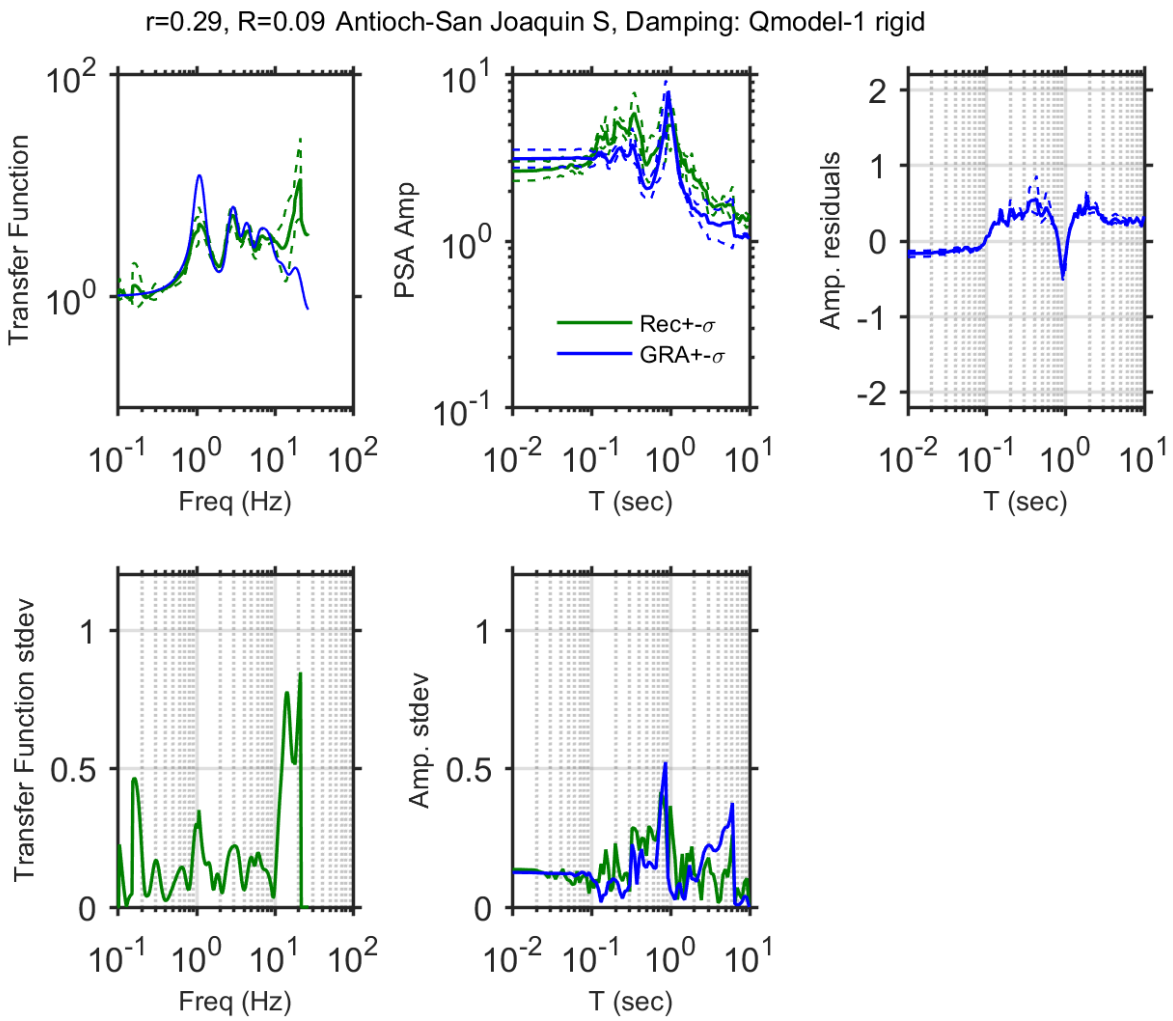

Figure A 2. Observed and simulated site response for Antioch-San Joaquin S site with V_S-based model for damping; Top left: Theoretical and median ± standard deviation of empirical transfer functions, Top middle: observed and predicted median ± standard deviation of *PS*A amplification, Top right: median ± standard deviation of *PS*A amplification residuals, Bottom left: standard deviation of empirical transfer functions, Bottom middle: standard deviation of observed and predicted *PS*A amplification residuals.

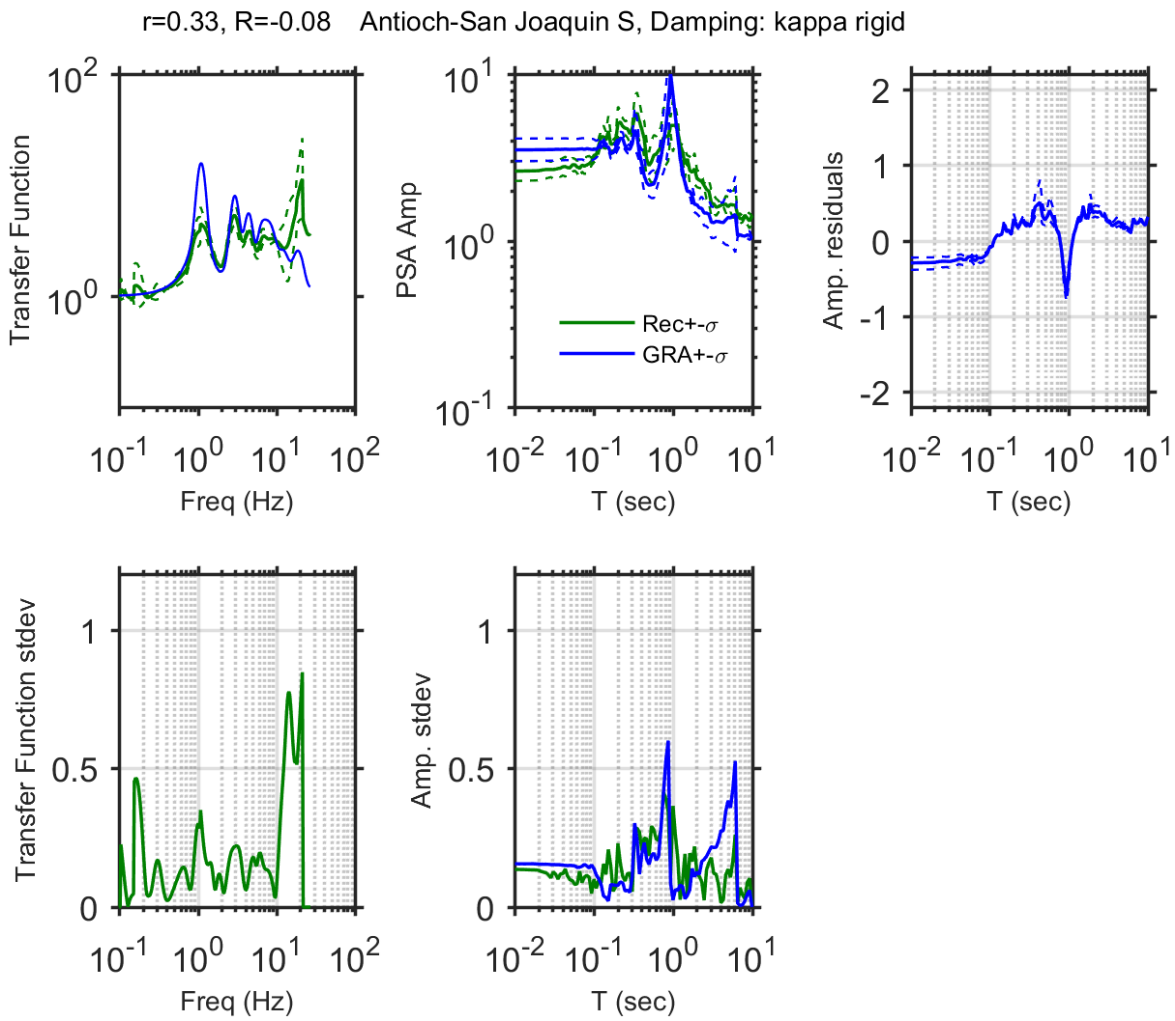

Figure A 3. Observed and simulated site response for Antioch-San Joaquin S site with κ-informed model for damping; Top left: Theoretical and median ± standard deviation of empirical transfer functions, Top middle: observed and predicted median ± standard deviation of *PS*A amplification, Top right: median ± standard deviation of *PS*A amplification residuals, Bottom left: standard deviation of empirical transfer functions, Bottom middle: standard deviation of observed and predicted *PS*A amplification residuals.

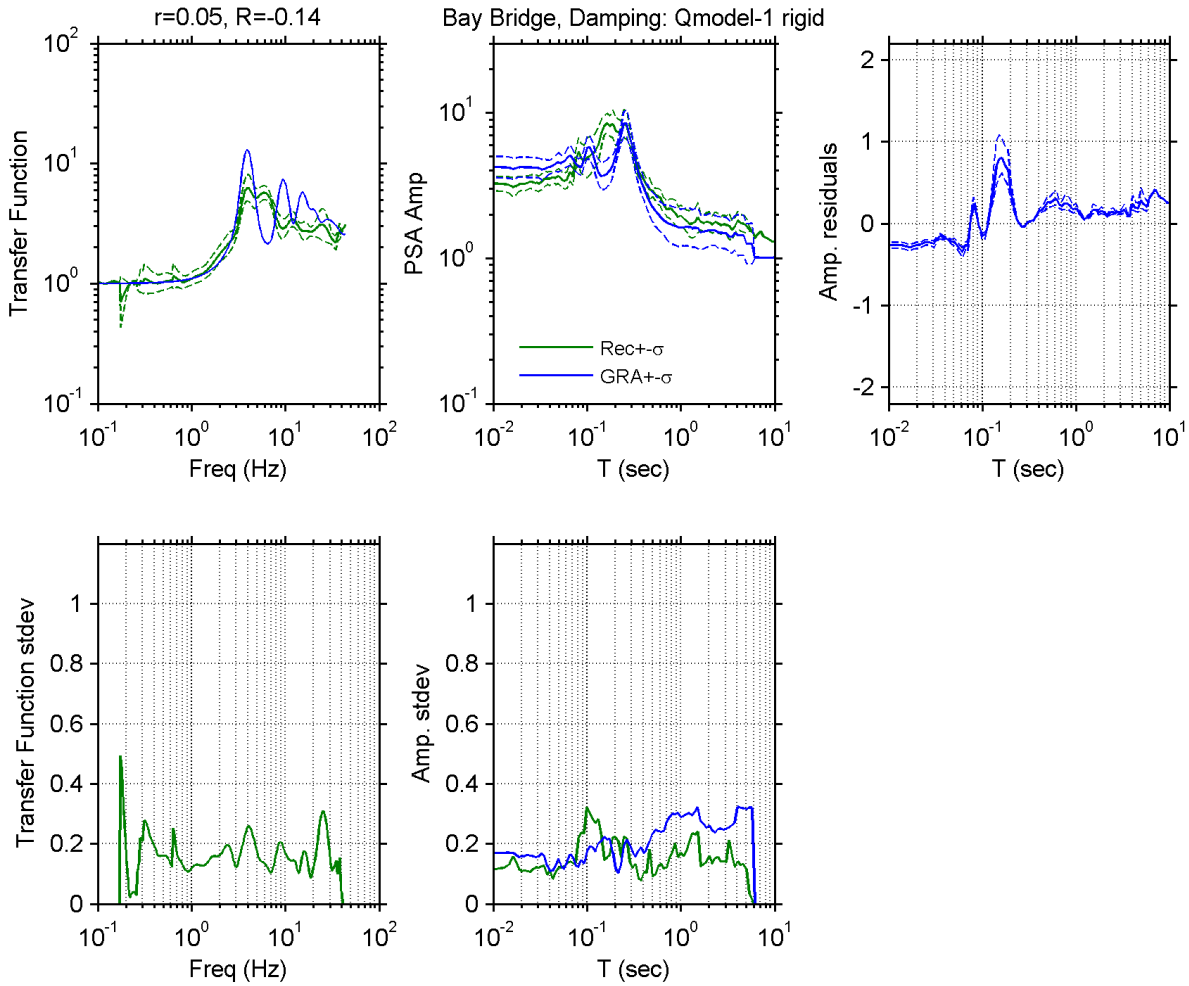

Figure A 4. Observed and simulated site response for San Francisco Bay Bridge site with V_S-based model for damping; Top left: Theoretical and median ± standard deviation of empirical transfer functions, Top middle: observed and predicted median ± standard deviation of *PS*A amplification, Top right: median ± standard deviation of *PS*A amplification residuals, Bottom left: standard deviation of empirical transfer functions, Bottom middle: standard deviation of observed and predicted *PS*A amplification residuals.

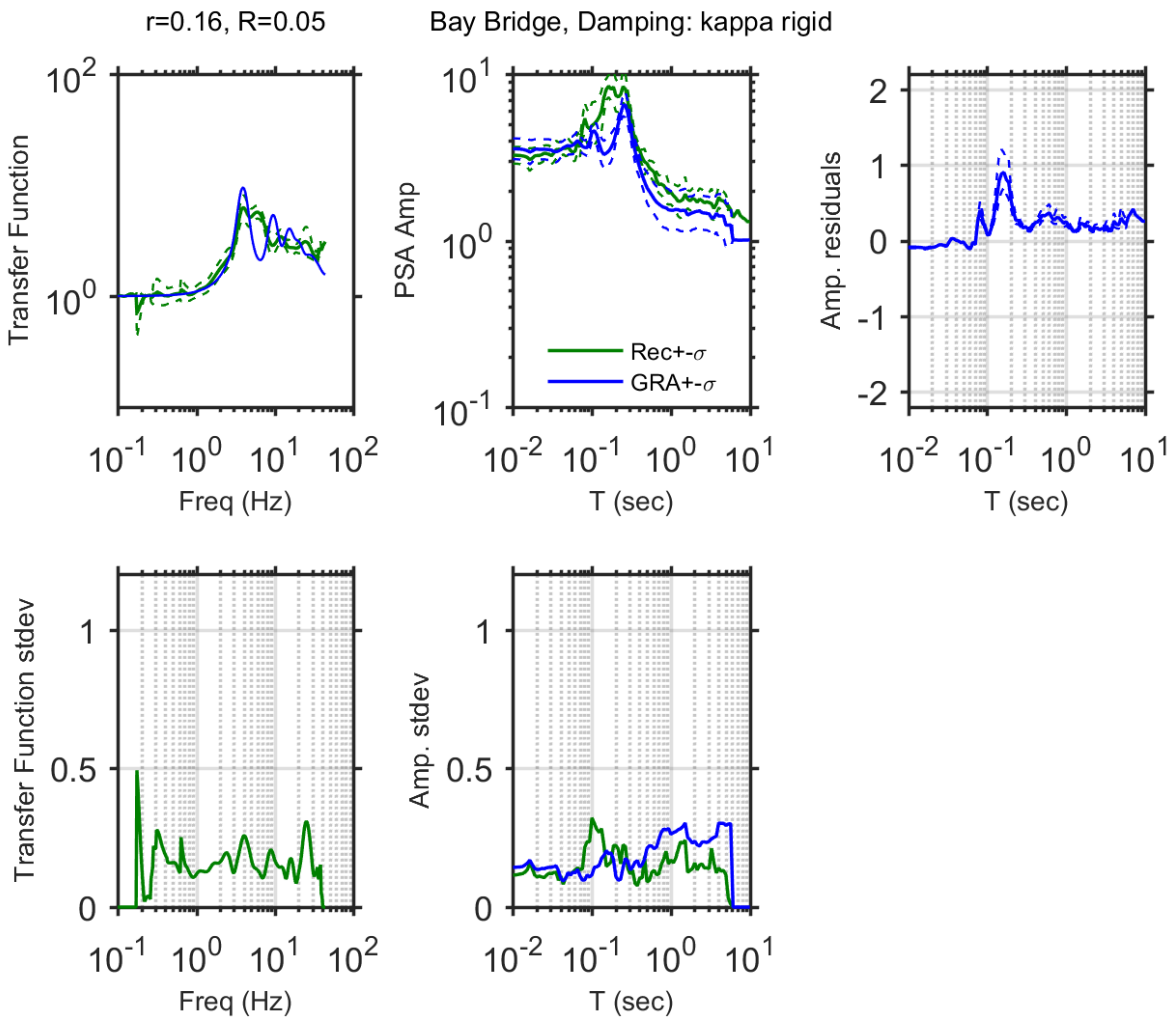

Figure A 5. Observed and simulated site response for San Francisco Bay Bridge site with κ-informed model for damping; Top left: Theoretical and median ± standard deviation of empirical transfer functions, Top middle: observed and predicted median ± standard deviation of *PS*A amplification, Top right: median ± standard deviation of *PS*A amplification residuals, Bottom left: standard deviation of empirical transfer functions, Bottom middle: standard deviation of observed and predicted *PS*A amplification residuals.

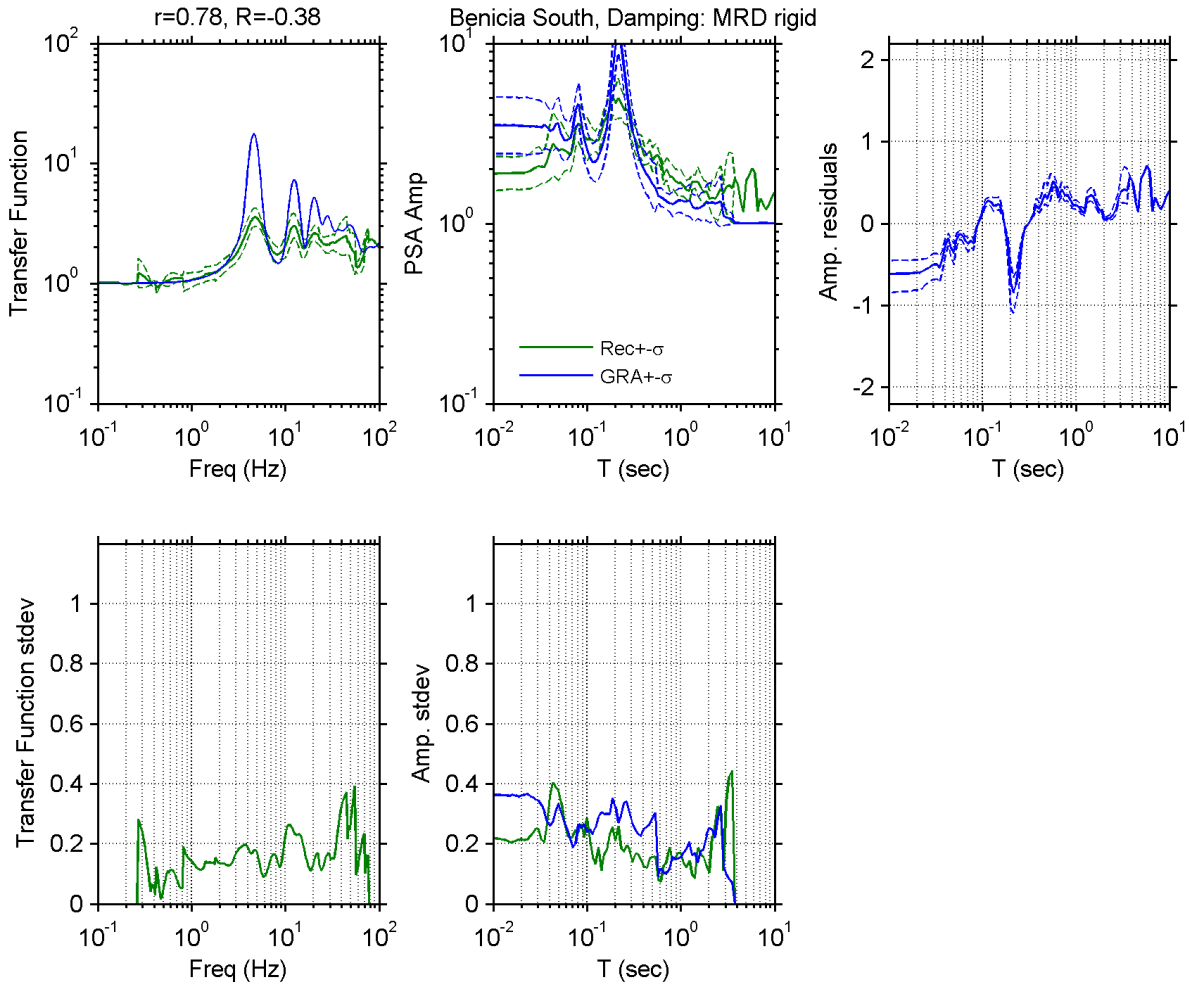

Figure A 6. Observed and simulated site response for Benicia-Martinez S site with $D_{\min}^{L}$ model for damping; Top left: Theoretical and median ± standard deviation of empirical transfer functions, Top middle: observed and predicted median ± standard deviation of *PS*A amplification, Top right: median ± standard deviation of *PS*A amplification residuals, Bottom left: standard deviation of empirical transfer functions, Bottom middle: standard deviation of observed and predicted *PS*A amplification residuals.

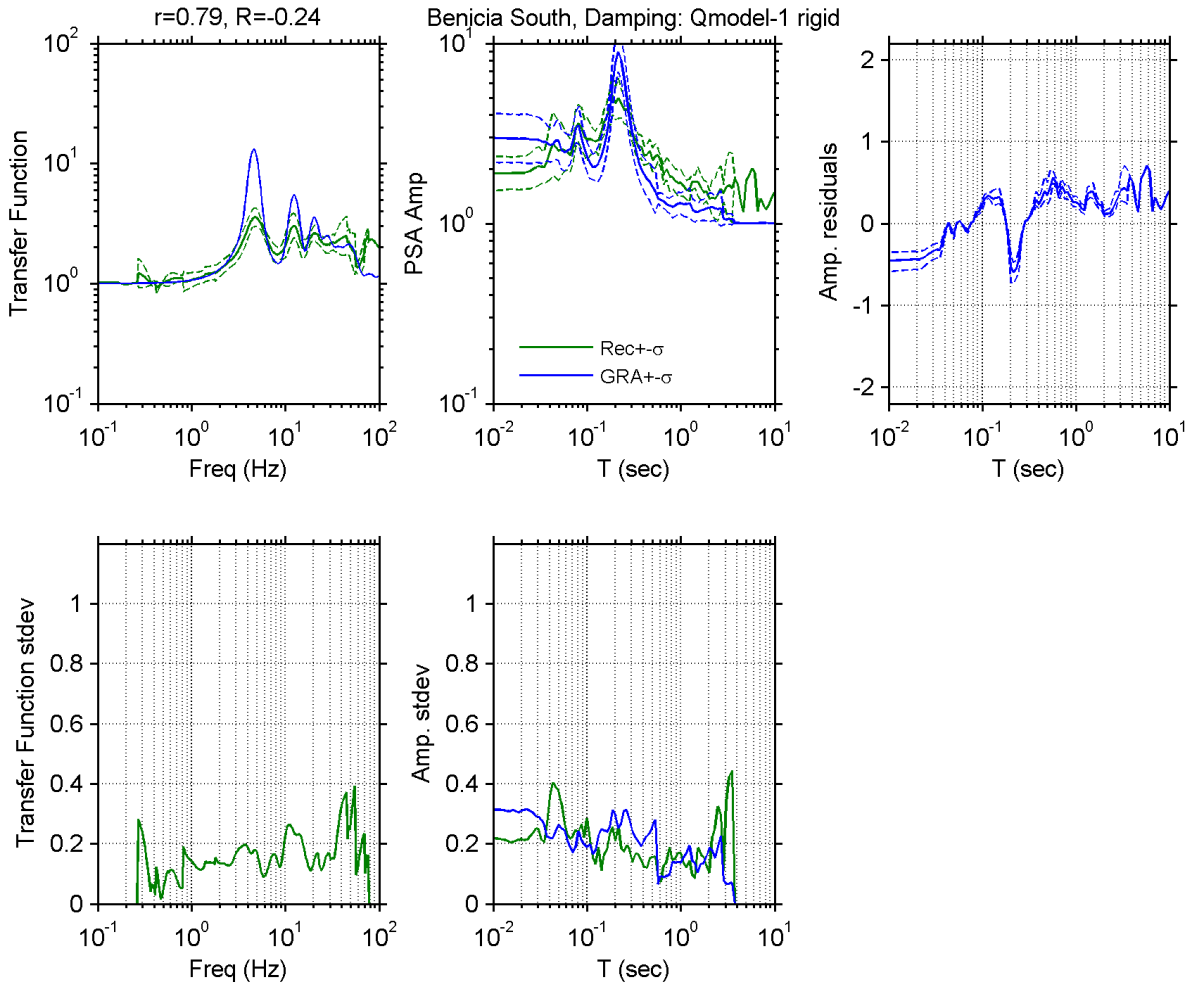

Figure A 7. Observed and simulated site response for Benicia-Martinez S site with V_S-based model for damping; Top left: Theoretical and median ± standard deviation of empirical transfer functions, Top middle: observed and predicted median ± standard deviation of *PSA* amplification, Top right: median ± standard deviation of *PSA* amplification residuals, Bottom left: standard deviation of empirical transfer functions, Bottom middle: standard deviation of observed and predicted *PSA* amplification residuals.

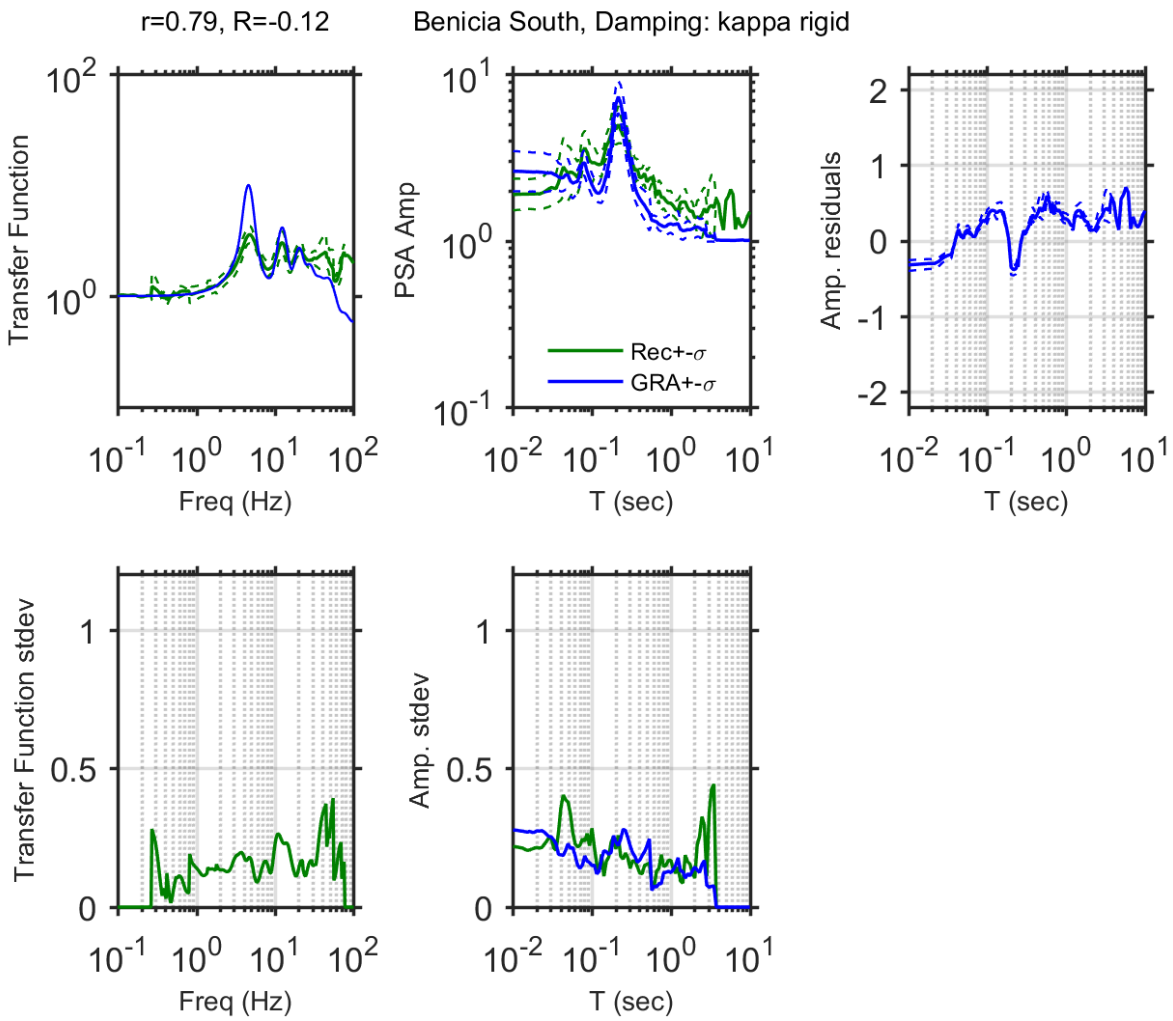

Figure A 8. Observed and simulated site response for Benicia-Martinez S site with κ-informed model for damping; Top left: Theoretical and median ± standard deviation of empirical transfer functions, Top middle: observed and predicted median ± standard deviation of *PS*A amplification, Top right: median ± standard deviation of *PS*A amplification residuals, Bottom left: standard deviation of empirical transfer functions, Bottom middle: standard deviation of observed and predicted *PS*A amplification residuals.

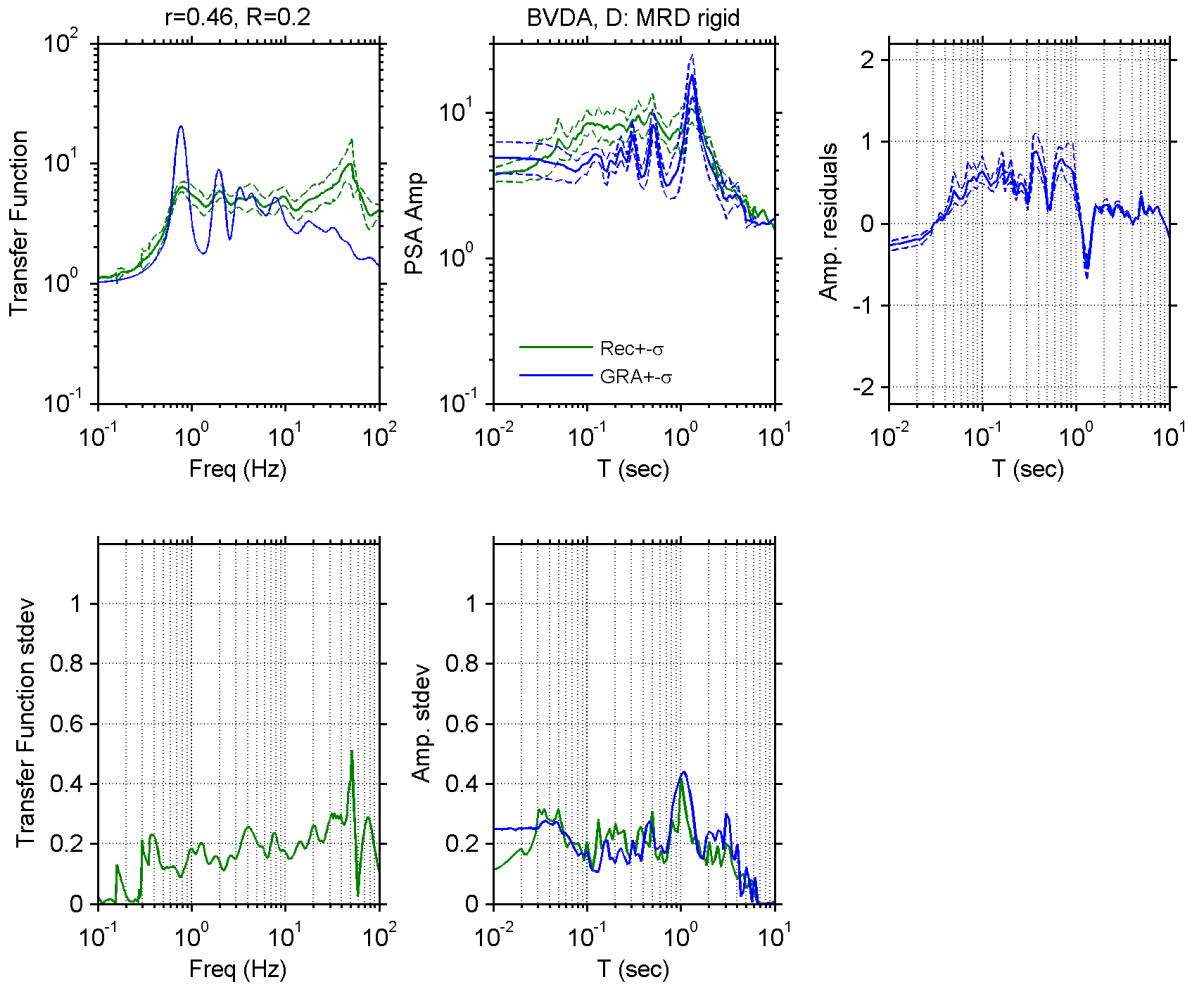

Figure A 9. Observed and simulated site response for Borrego Valley site with $D_{\min}^{L}$ model for damping; Top left: Theoretical and median ± standard deviation of empirical transfer functions, Top middle: observed and predicted median ± standard deviation of *PSA* amplification, Top right: median ± standard deviation of *PSA* amplification residuals, Bottom left: standard deviation of empirical transfer functions, Bottom middle: standard deviation of observed and predicted *PSA* amplification residuals.

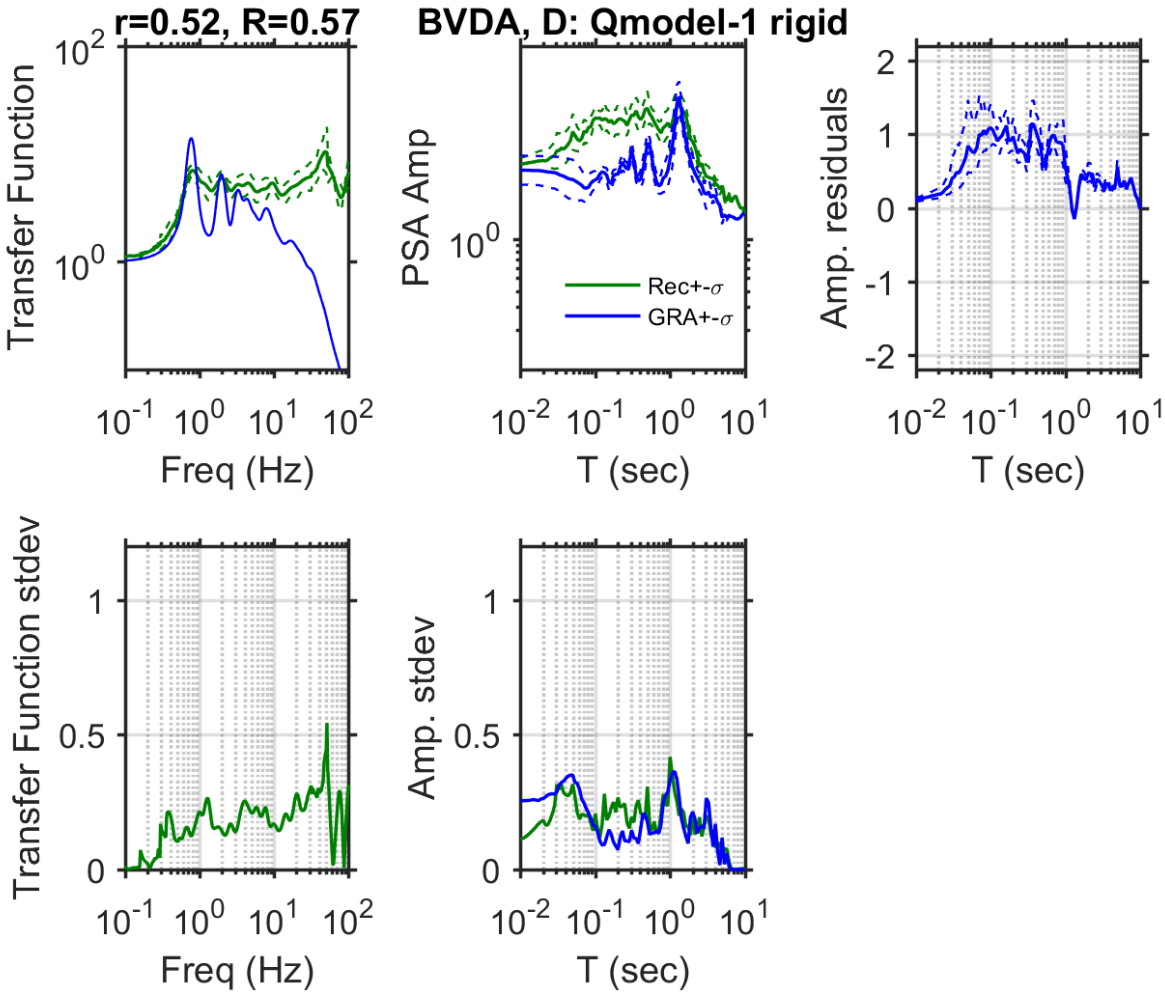

Figure A 10. Observed and simulated site response for Borrego Valley site with V_S-based model for damping; Top left: Theoretical and median ± standard deviation of empirical transfer functions, Top middle: observed and predicted median ± standard deviation of *PS*A amplification, Top right: median ± standard deviation of *PS*A amplification residuals, Bottom left: standard deviation of empirical transfer functions, Bottom middle: standard deviation of observed and predicted *PS*A amplification residuals.

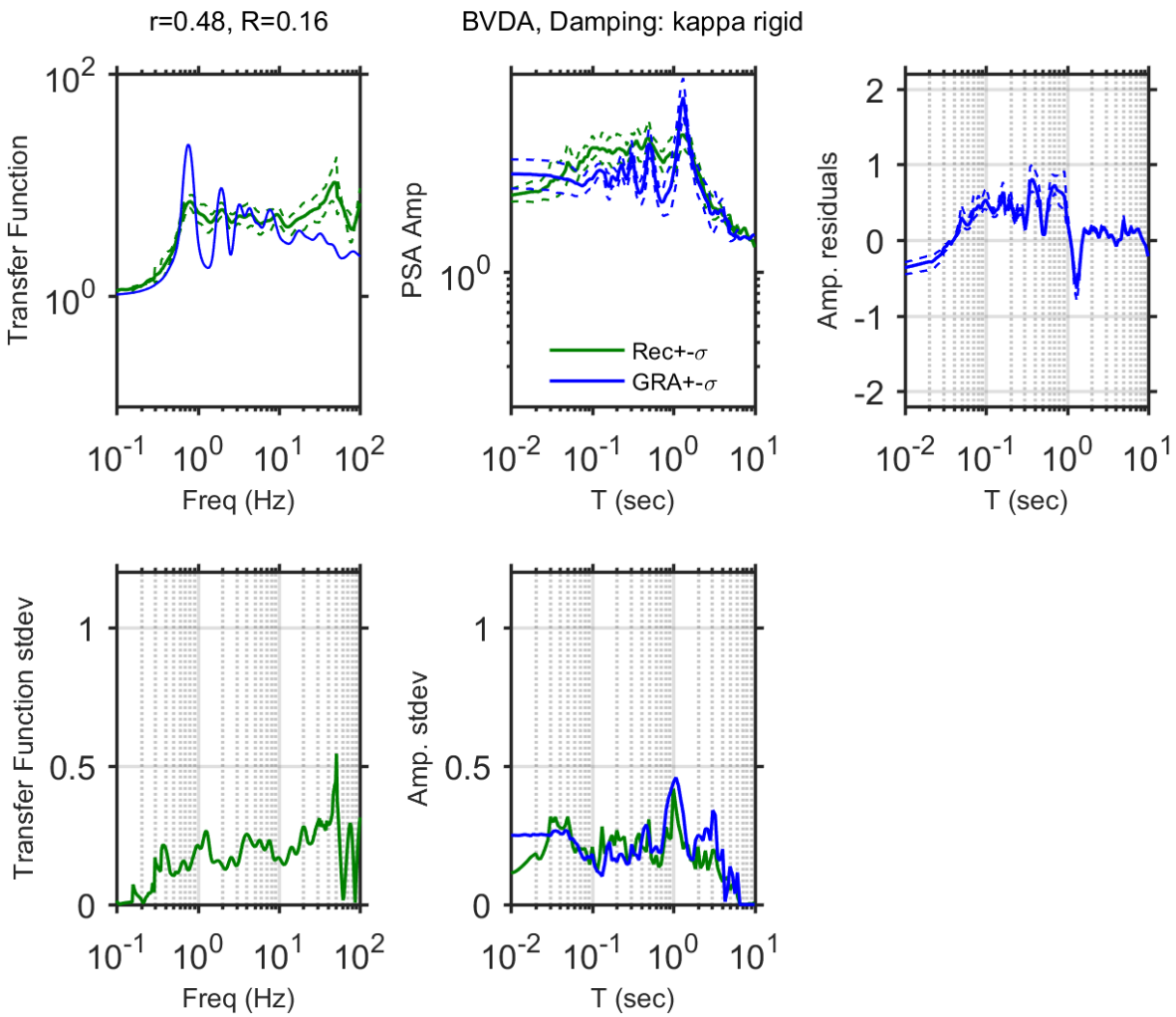

Figure A 11. Observed and simulated site response for Borrego Valley site with κ-informed model for damping; Top left: Theoretical and median ± standard deviation of empirical transfer functions, Top middle: observed and predicted median ± standard deviation of *PS*A amplification, Top right: median ± standard deviation of *PS*A amplification residuals, Bottom left: standard deviation of empirical transfer functions, Bottom middle: standard deviation of observed and predicted *PS*A amplification residuals.

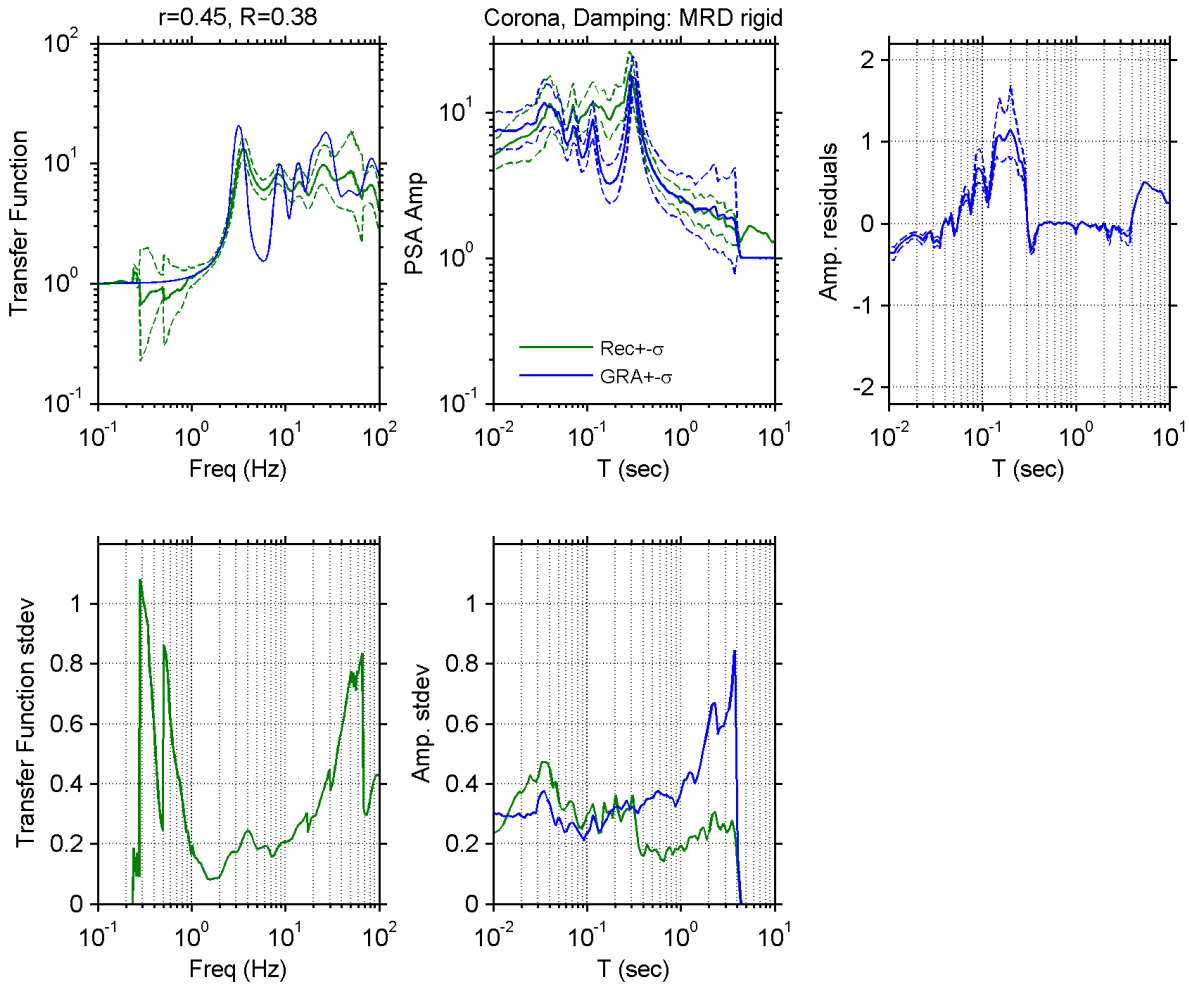

Figure A 12. Observed and simulated site response for Corona-I15/Hwy 91 site with $D^{L}_{\min}$ model for damping; Top left: Theoretical and median ± standard deviation of empirical transfer functions, Top middle: observed and predicted median ± standard deviation of *PS*A amplification, Top right: median ± standard deviation of *PS*A amplification residuals, Bottom left: standard deviation of empirical transfer functions, Bottom middle: standard deviation of observed and predicted *PS*A amplification residuals.

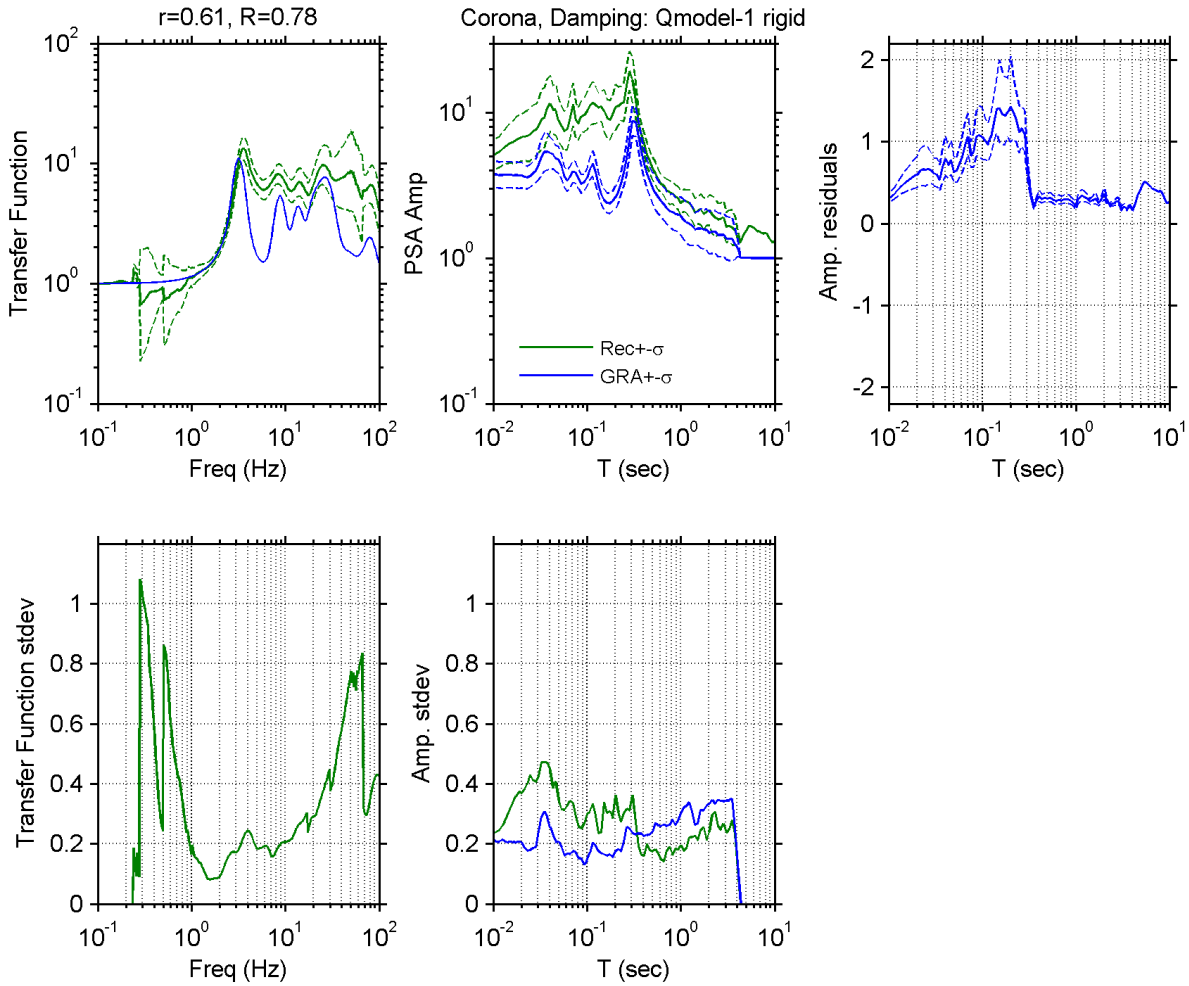

Figure A 13. Observed and simulated site response for Corona-I15/Hwy 91 site with V_S-based model for damping; Top left: Theoretical and median ± standard deviation of empirical transfer functions, Top middle: observed and predicted median ± standard deviation of *PS*A amplification, Top right: median ± standard deviation of *PS*A amplification residuals, Bottom left: standard deviation of empirical transfer functions, Bottom middle: standard deviation of observed and predicted *PS*A amplification residuals.

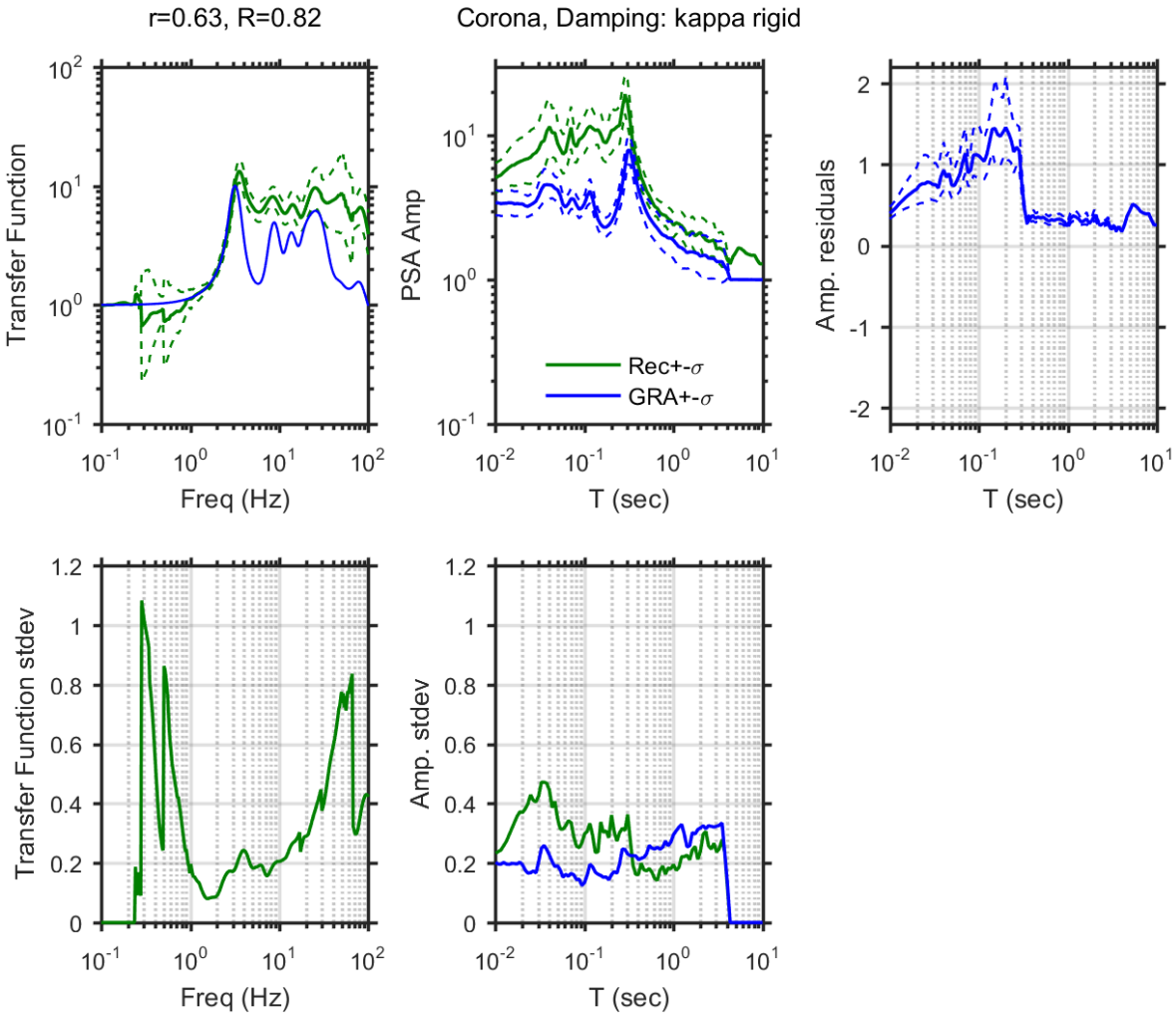

Figure A 14. Observed and simulated site response for Corona-I15/Hwy 91 site with κ-informed model for damping; Top left: Theoretical and median ± standard deviation of empirical transfer functions, Top middle: observed and predicted median ± standard deviation of *PS*A amplification, Top right: median ± standard deviation of *PS*A amplification residuals, Bottom left: standard deviation of empirical transfer functions, Bottom middle: standard deviation of observed and predicted *PS*A amplification residuals.

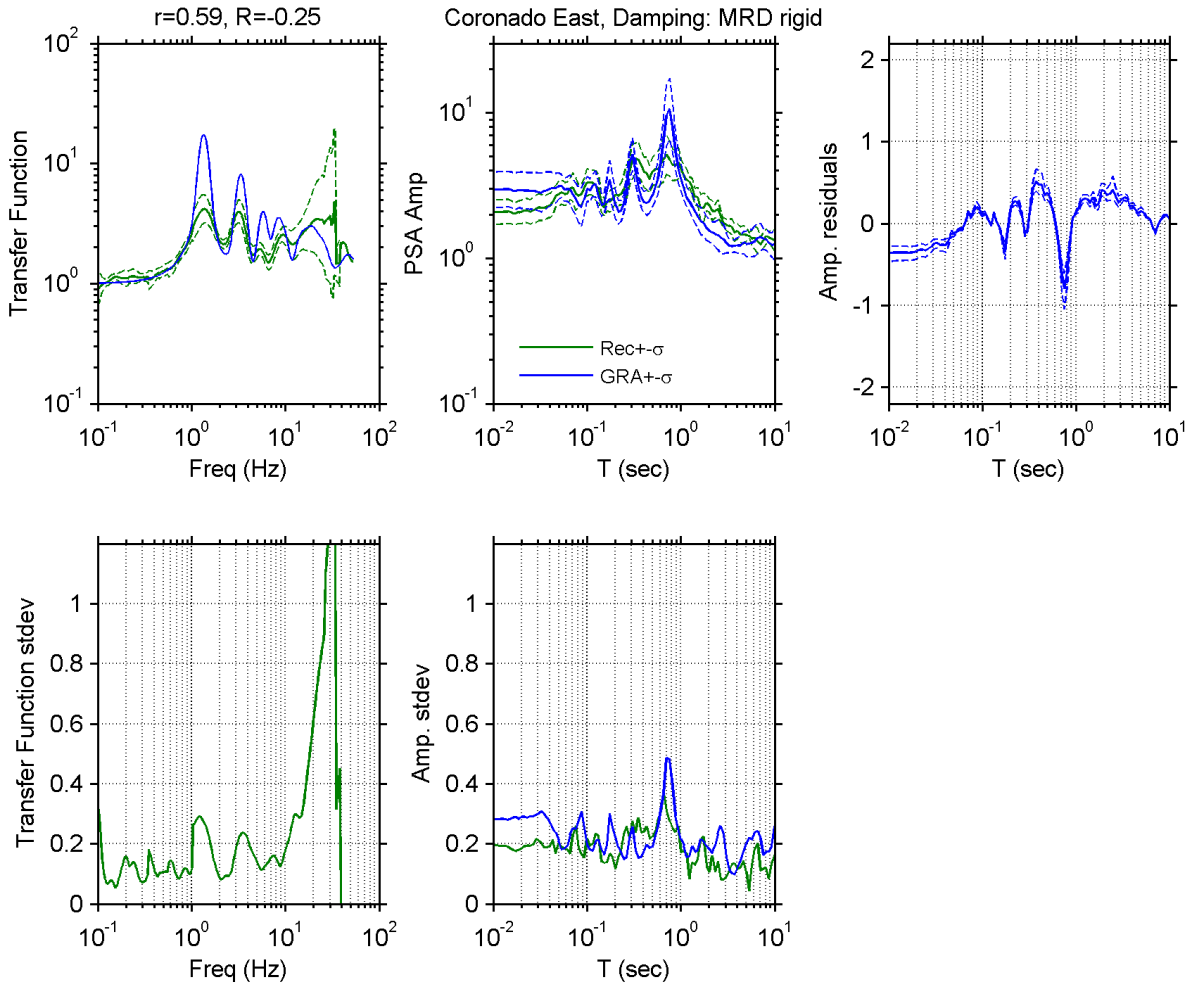

Figure A 15. Observed and simulated site response for Corona-I15/Hwy 91 site with $D_{\min}^{L}$ model for damping; Top left: Theoretical and median ± standard deviation of empirical transfer functions, Top middle: observed and predicted median ± standard deviation of *PS*A amplification, Top right: median ± standard deviation of *PS*A amplification residuals, Bottom left: standard deviation of empirical transfer functions, Bottom middle: standard deviation of observed and predicted *PS*A amplification residuals.

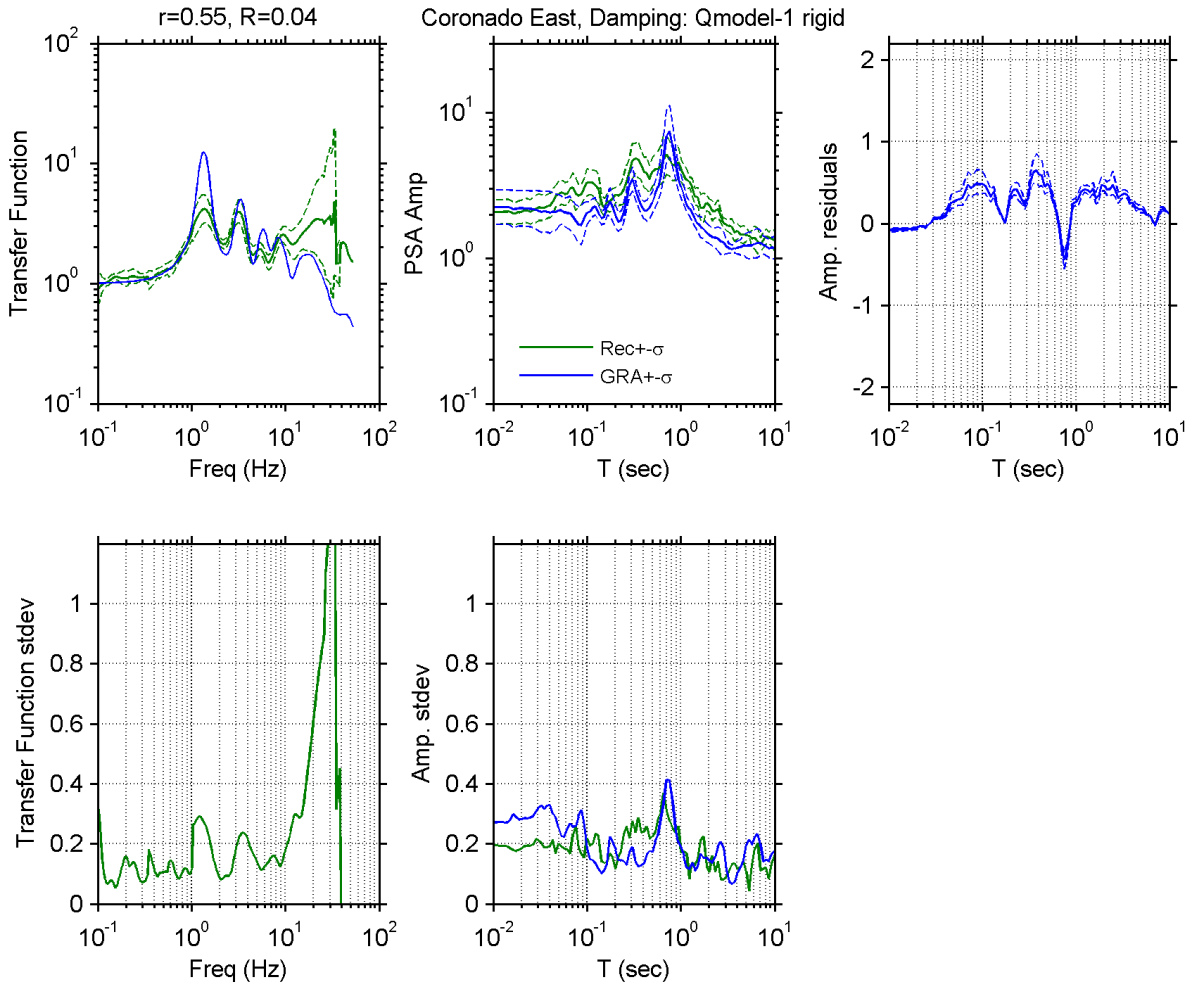

Figure A 16. Observed and simulated site response for Corona-I15/Hwy 91 site with V_S-based model for damping; Top left: Theoretical and median ± standard deviation of empirical transfer functions, Top middle: observed and predicted median ± standard deviation of *PS*A amplification, Top right: median ± standard deviation of *PS*A amplification residuals, Bottom left: standard deviation of empirical transfer functions, Bottom middle: standard deviation of observed and predicted *PS*A amplification residuals.

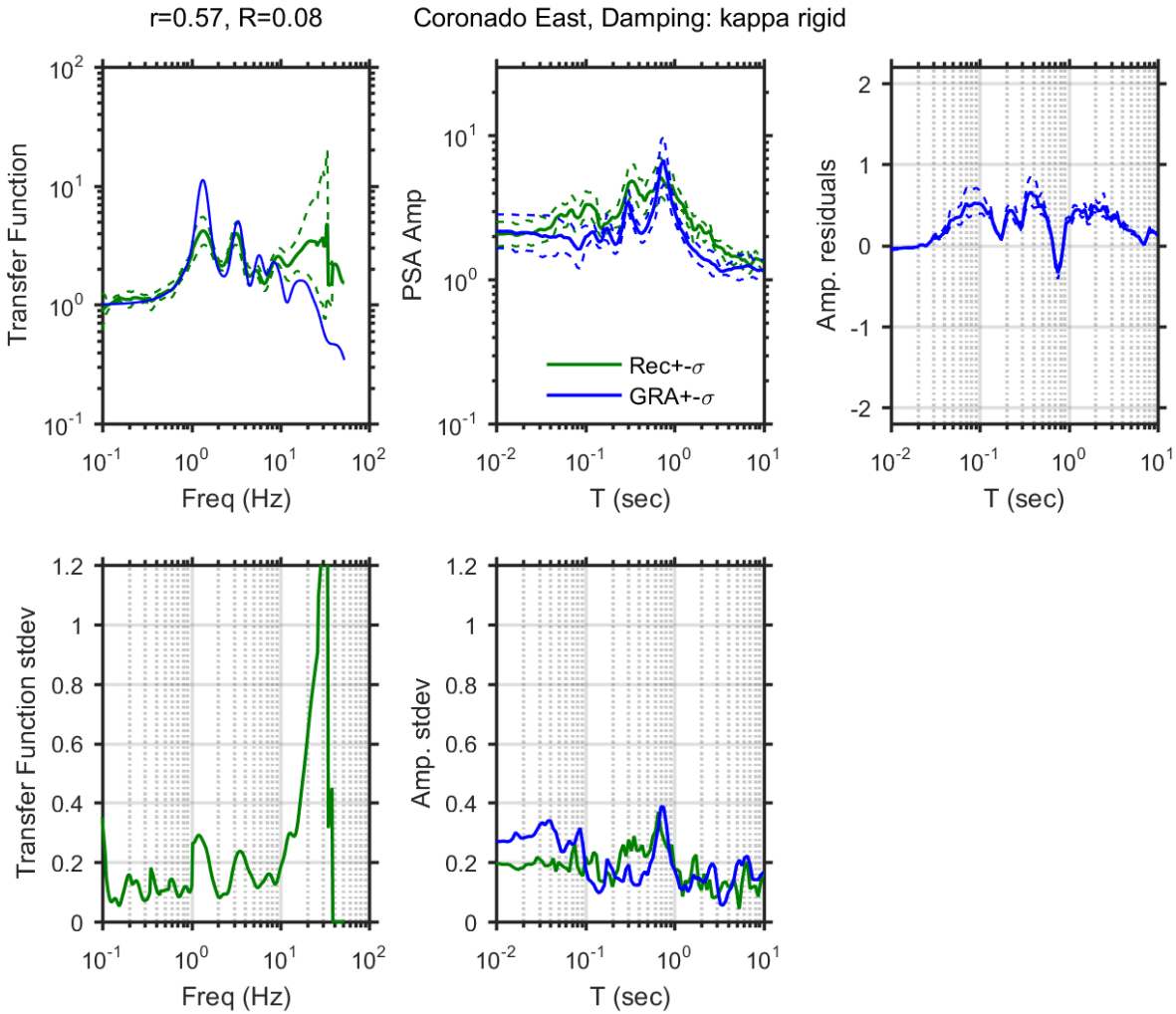

Figure A 17. Observed and simulated site response for Corona-I15/Hwy 91 site with κ-informed model for damping; Top left: Theoretical and median ± standard deviation of empirical transfer functions, Top middle: observed and predicted median ± standard deviation of *PS*A amplification, Top right: median ± standard deviation of *PS*A amplification residuals, Bottom left: standard deviation of empirical transfer functions, Bottom middle: standard deviation of observed and predicted *PS*A amplification residuals.

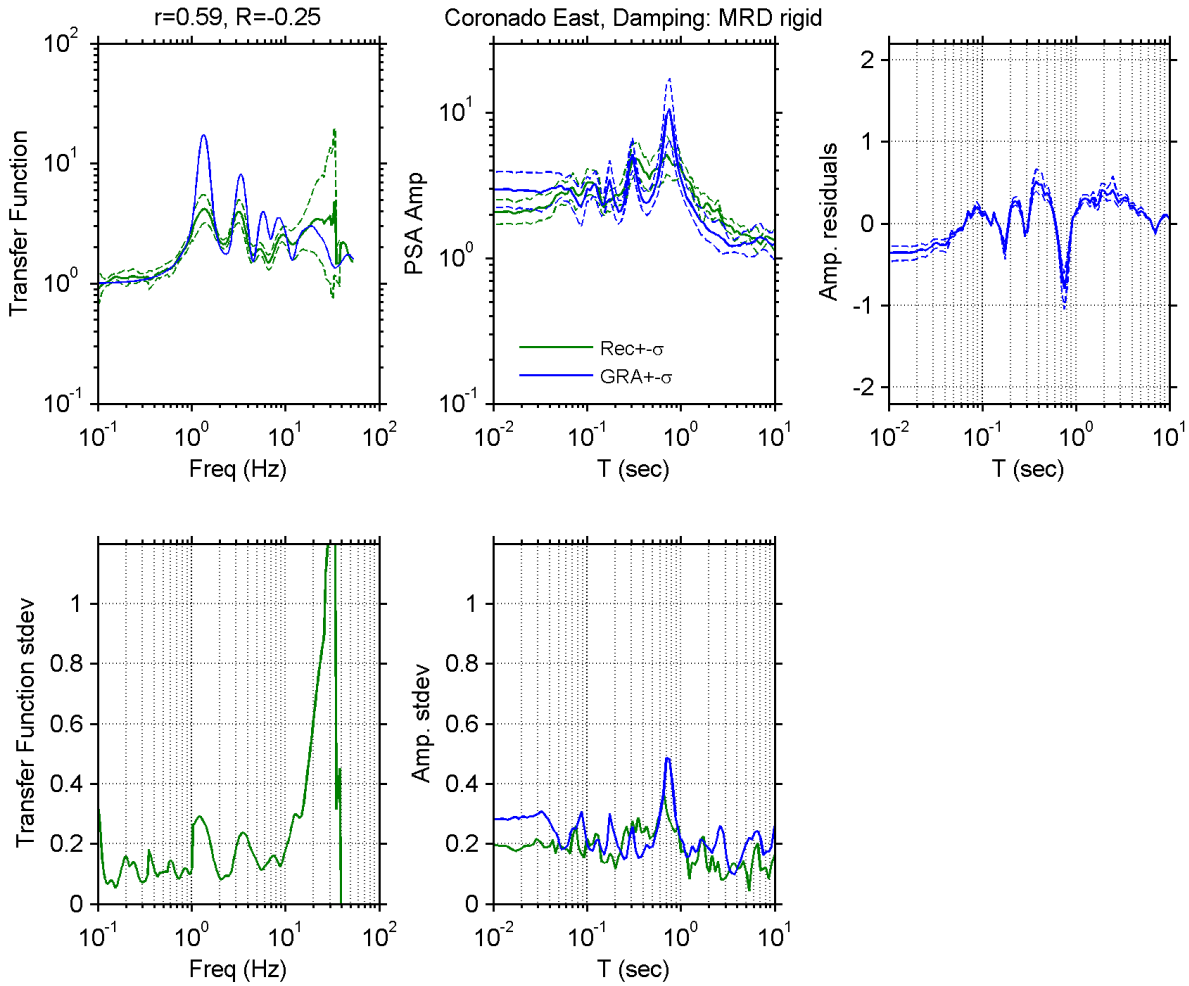

Figure A 18. Observed and simulated site response for Coronado East site with $D_{\min}^{L}$ model for damping; Top left: Theoretical and median ± standard deviation of empirical transfer functions, Top middle: observed and predicted median ± standard deviation of *PS*A amplification, Top right: median ± standard deviation of *PS*A amplification residuals, Bottom left: standard deviation of empirical transfer functions, Bottom middle: standard deviation of observed and predicted *PS*A amplification residuals.

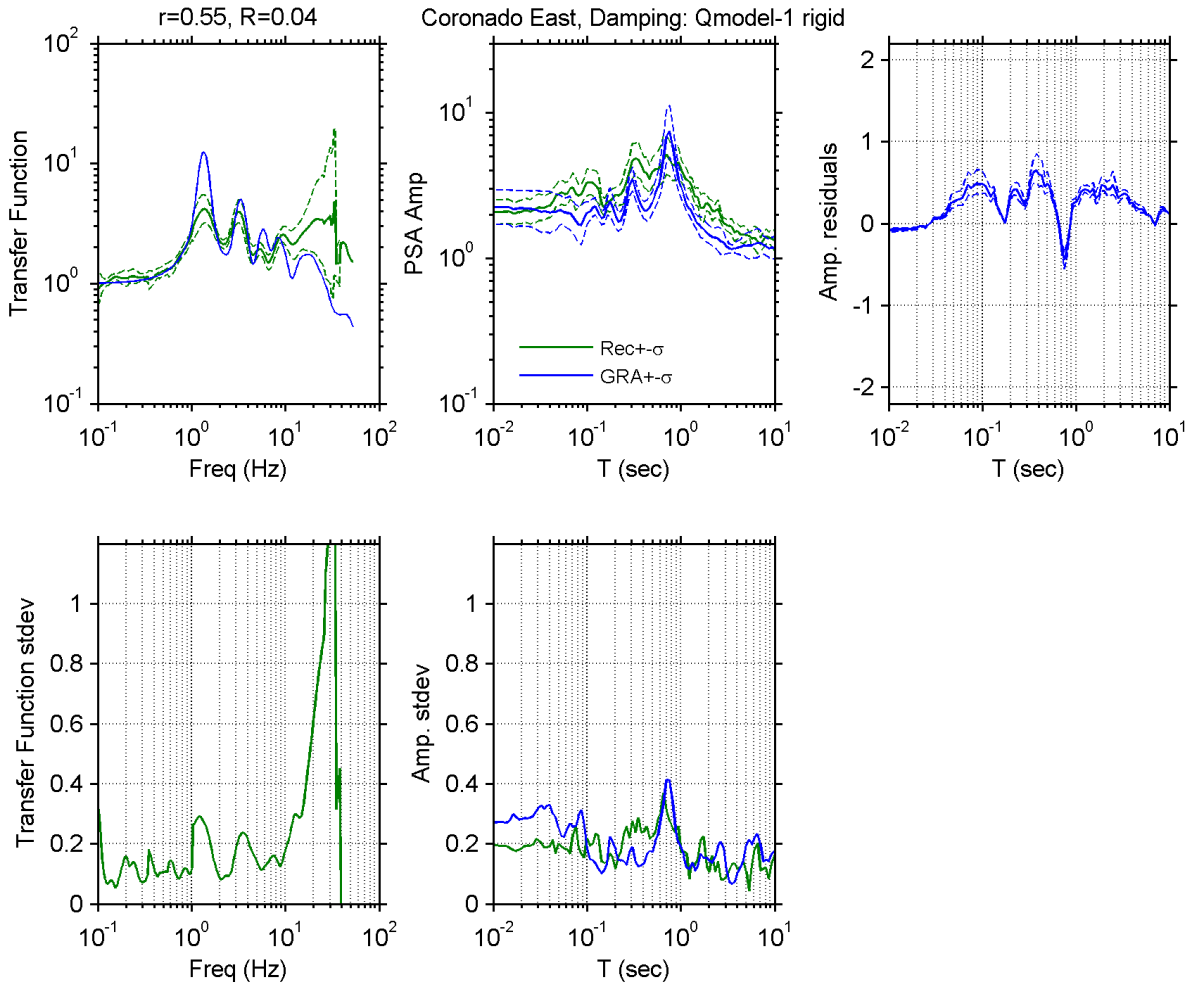

Figure A 19. Observed and simulated site response for Coronado East site with V_S-based model for damping; Top left: Theoretical and median ± standard deviation of empirical transfer functions, Top middle: observed and predicted median ± standard deviation of *PS*A amplification, Top right: median ± standard deviation of *PS*A amplification residuals, Bottom left: standard deviation of empirical transfer functions, Bottom middle: standard deviation of observed and predicted *PS*A amplification residuals.

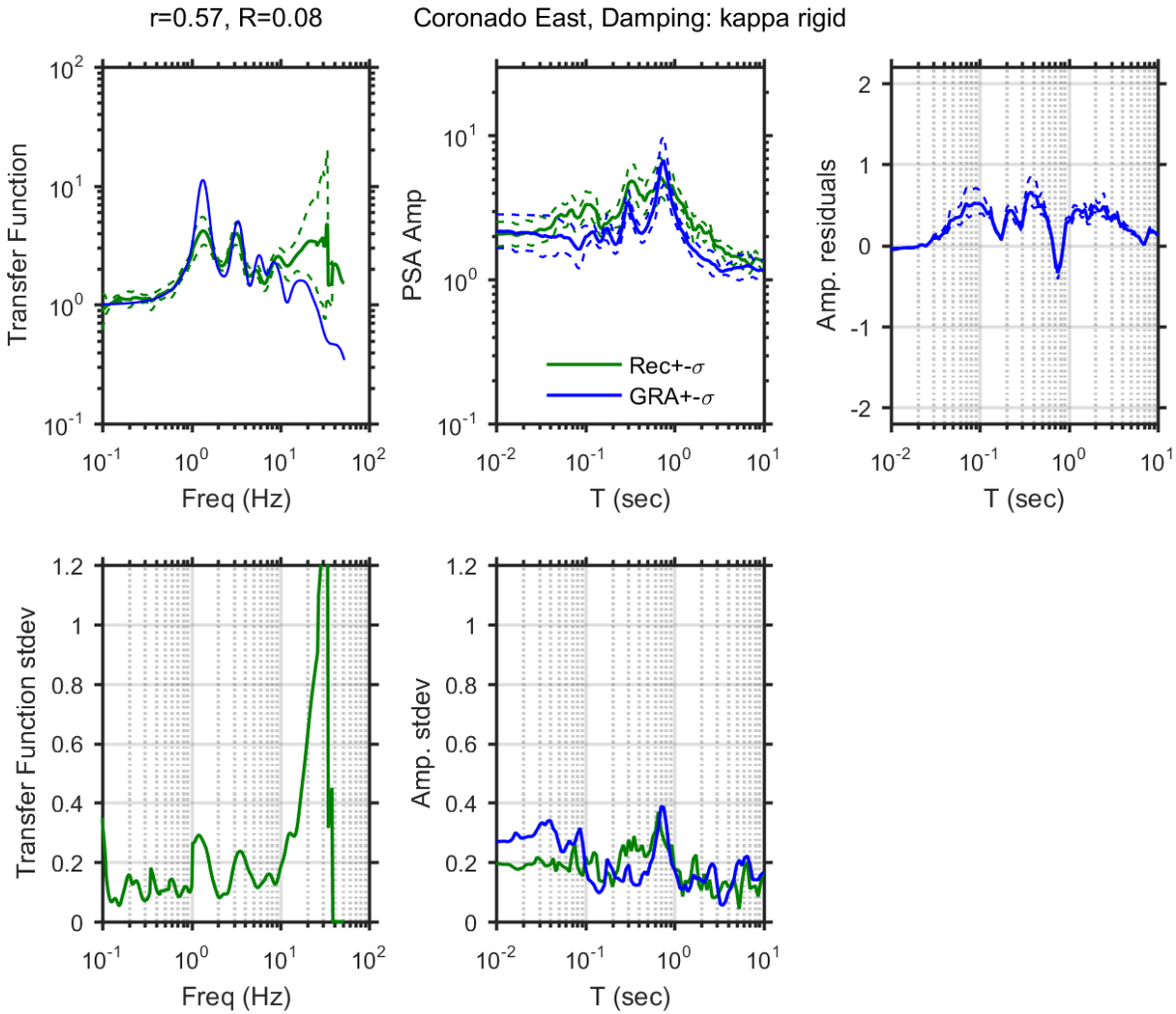

Figure A 20. Observed and simulated site response for Coronado East site with κ-informed model for damping; Top left: Theoretical and median ± standard deviation of empirical transfer functions, Top middle: observed and predicted median ± standard deviation of *PS*A amplification, Top right: median ± standard deviation of *PS*A amplification residuals, Bottom left: standard deviation of empirical transfer functions, Bottom middle: standard deviation of observed and predicted *PS*A amplification residuals.

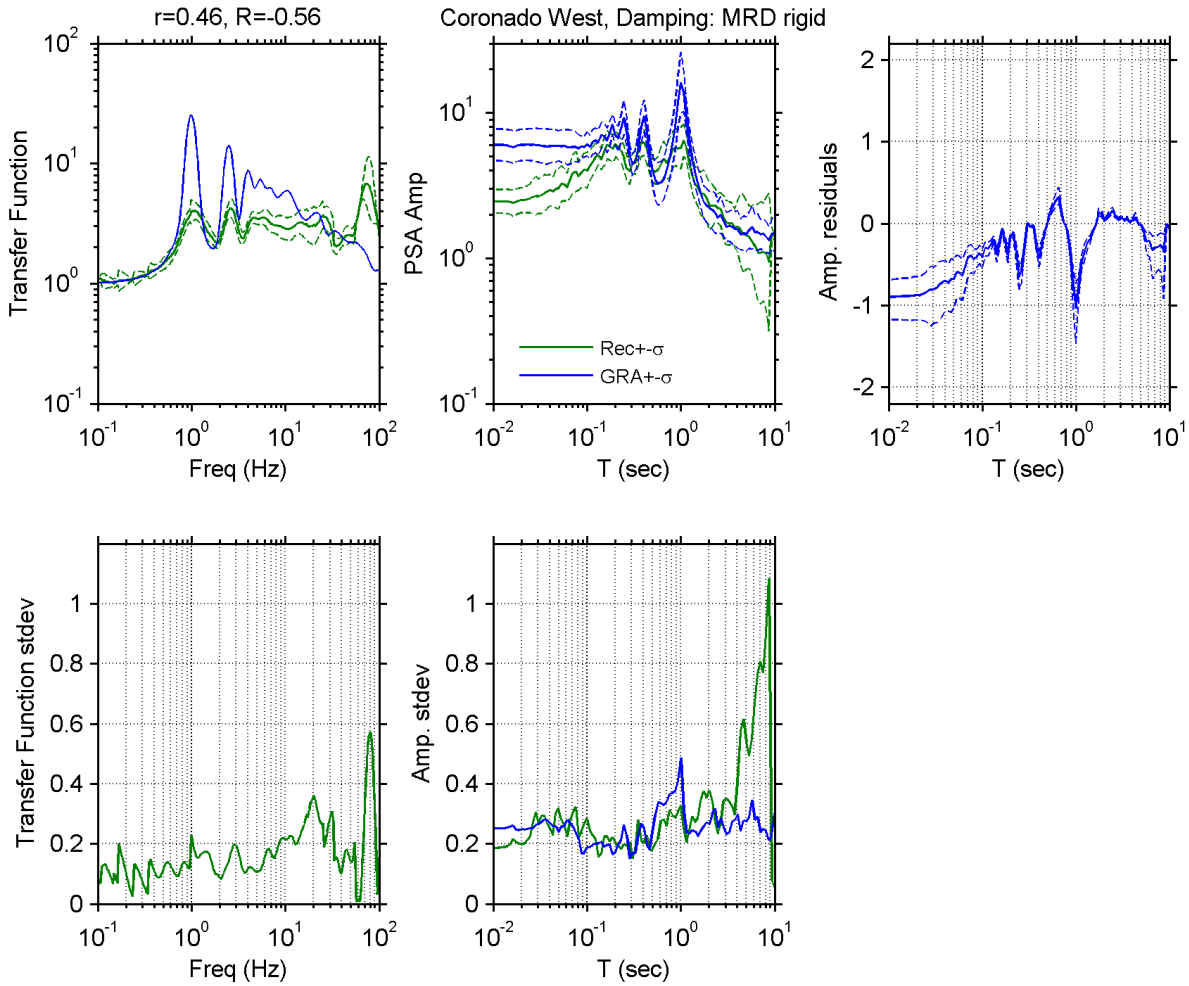

Figure A 21. Observed and simulated site response for Coronado West site with $D_{\min}^{L}$ model for damping; Top left: Theoretical and median ± standard deviation of empirical transfer functions, Top middle: observed and predicted median ± standard deviation of *PS*A amplification, Top right: median ± standard deviation of *PS*A amplification residuals, Bottom left: standard deviation of empirical transfer functions, Bottom middle: standard deviation of observed and predicted *PS*A amplification residuals.

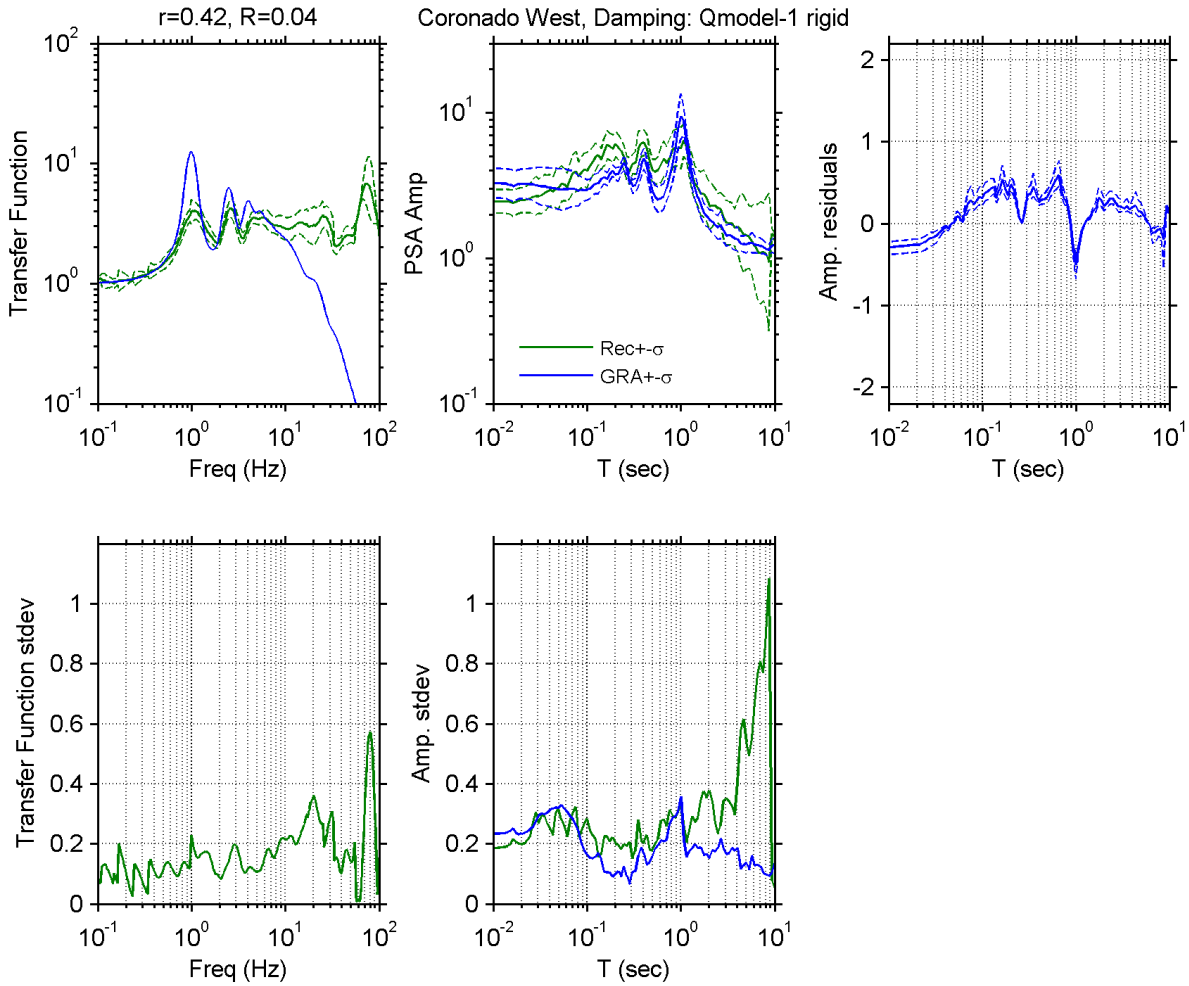

Figure A 22. Observed and simulated site response for Coronado West site with V_S-based model for damping; Top left: Theoretical and median ± standard deviation of empirical transfer functions, Top middle: observed and predicted median ± standard deviation of *PS*A amplification, Top right: median ± standard deviation of *PS*A amplification residuals, Bottom left: standard deviation of empirical transfer functions, Bottom middle: standard deviation of observed and predicted *PS*A amplification residuals.

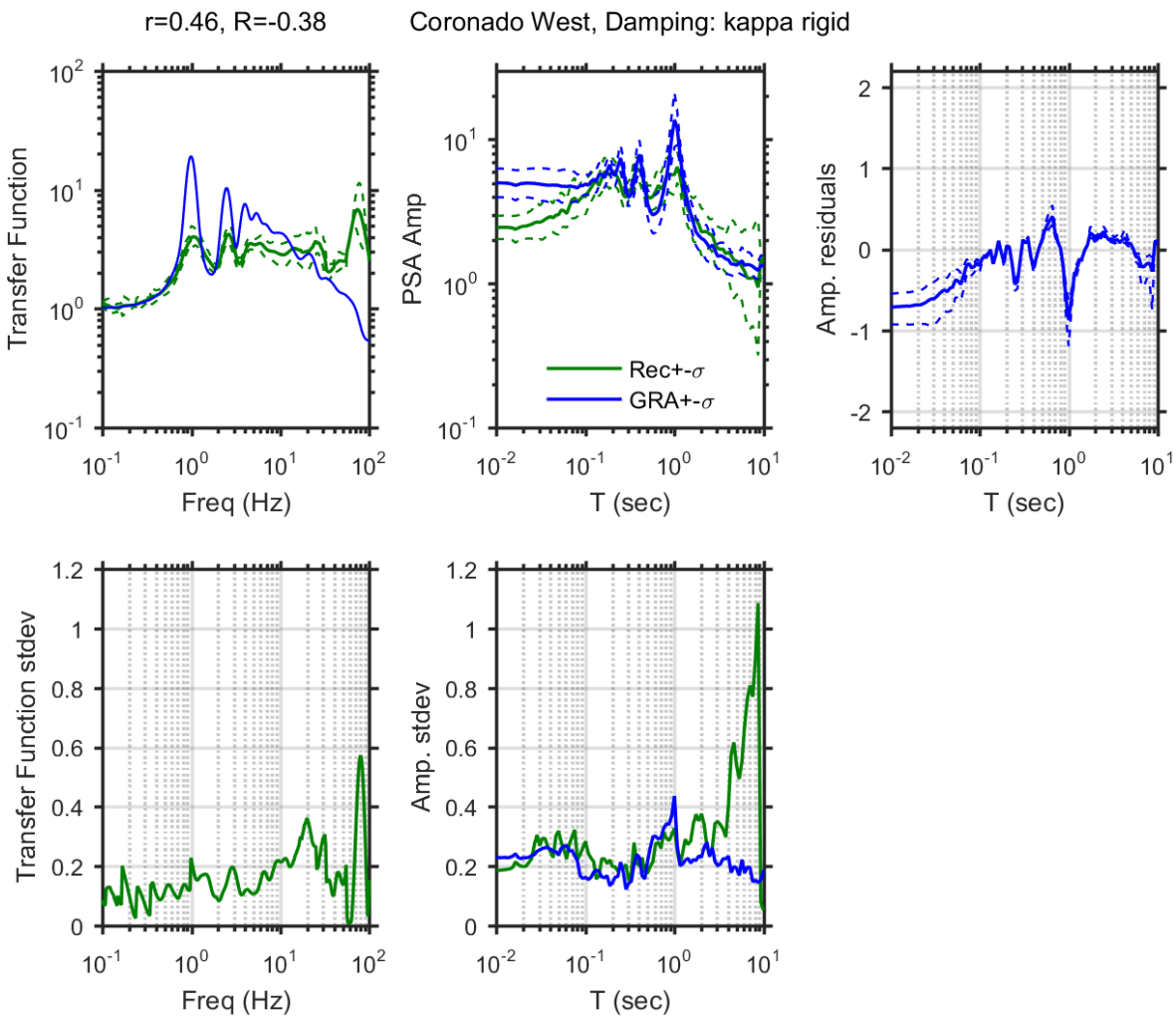

Figure A 23. Observed and simulated site response for Coronado West site with κ-informed model for damping; Top left: Theoretical and median ± standard deviation of empirical transfer functions, Top middle: observed and predicted median ± standard deviation of *PS*A amplification, Top right: median ± standard deviation of *PS*A amplification residuals, Bottom left: standard deviation of empirical transfer functions, Bottom middle: standard deviation of observed and predicted *PS*A amplification residuals.

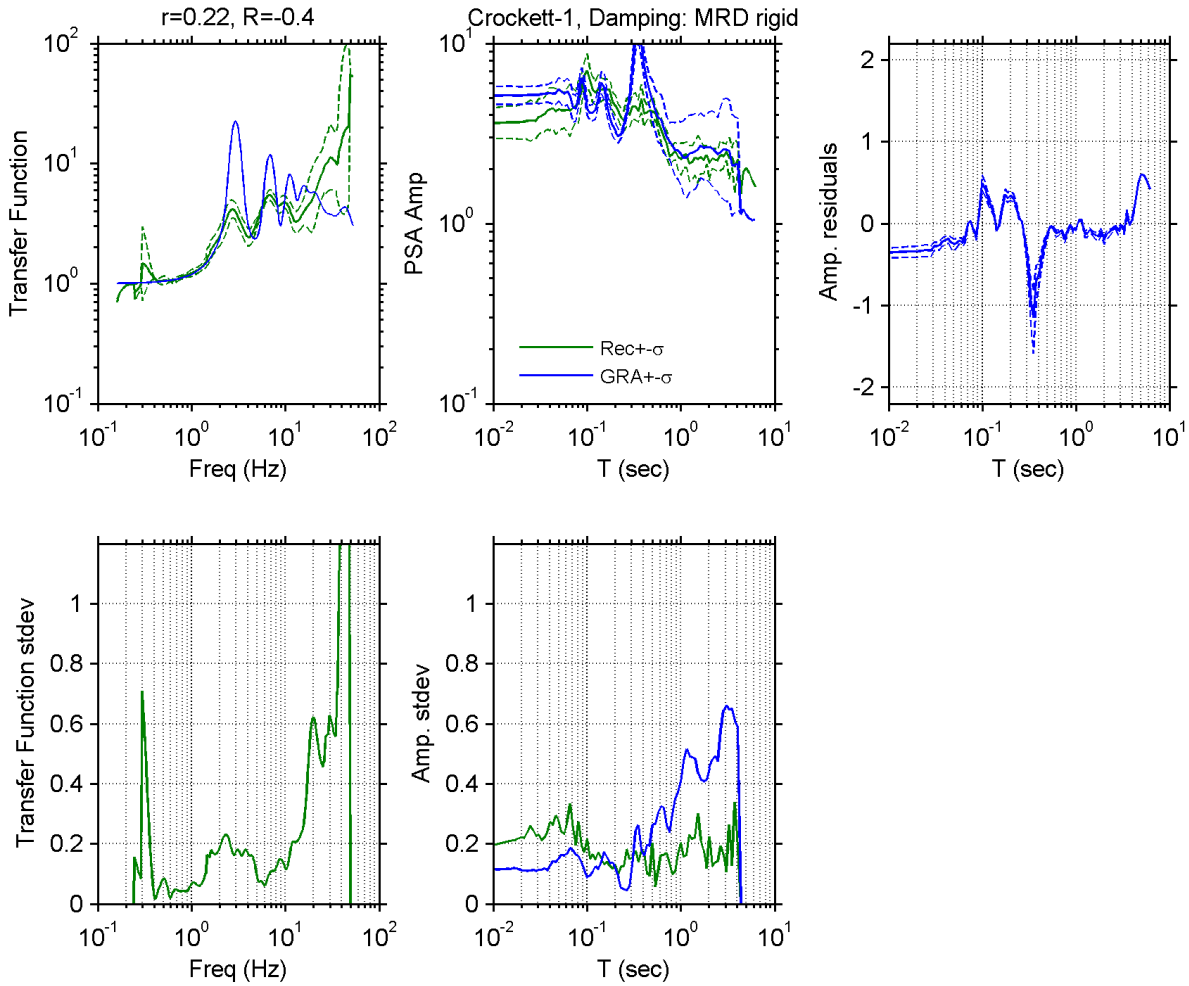

Figure A 24. Observed and simulated site response for Crockett-Carquinez Br #1 site with $D_{\min}^{L}$ model for damping; Top left: Theoretical and median ± standard deviation of empirical transfer functions, Top middle: observed and predicted median ± standard deviation of *PS*A amplification, Top right: median ± standard deviation of *PS*A amplification residuals, Bottom left: standard deviation of empirical transfer functions, Bottom middle: standard deviation of observed and predicted *PS*A amplification residuals.

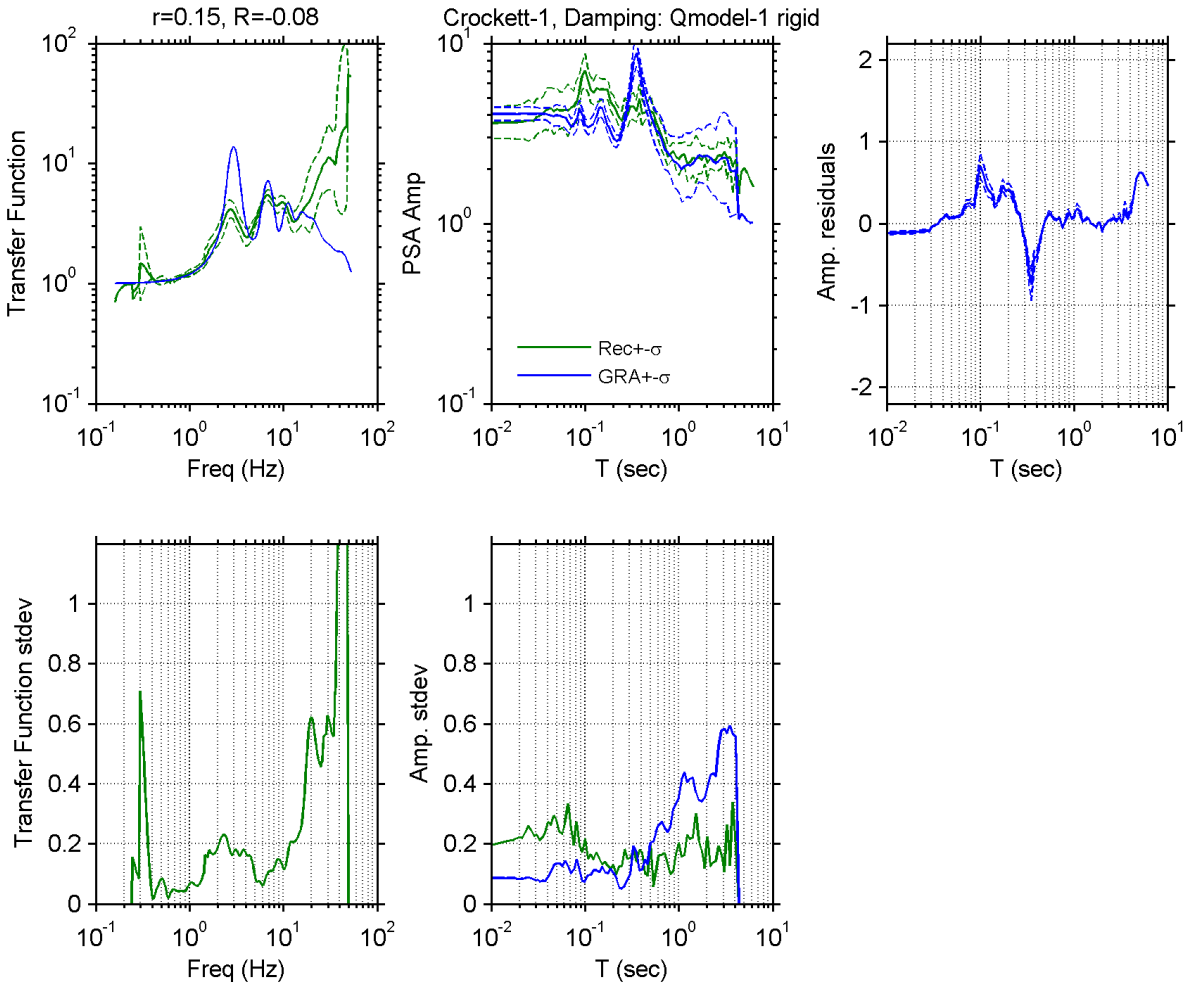

Figure A 25. Observed and simulated site response for Crockett-Carquinez Br #1 site with V_S-based model for damping; Top left: Theoretical and median ± standard deviation of empirical transfer functions, Top middle: observed and predicted median ± standard deviation of *PS*A amplification, Top right: median ± standard deviation of *PS*A amplification residuals, Bottom left: standard deviation of empirical transfer functions, Bottom middle: standard deviation of observed and predicted *PS*A amplification residuals.

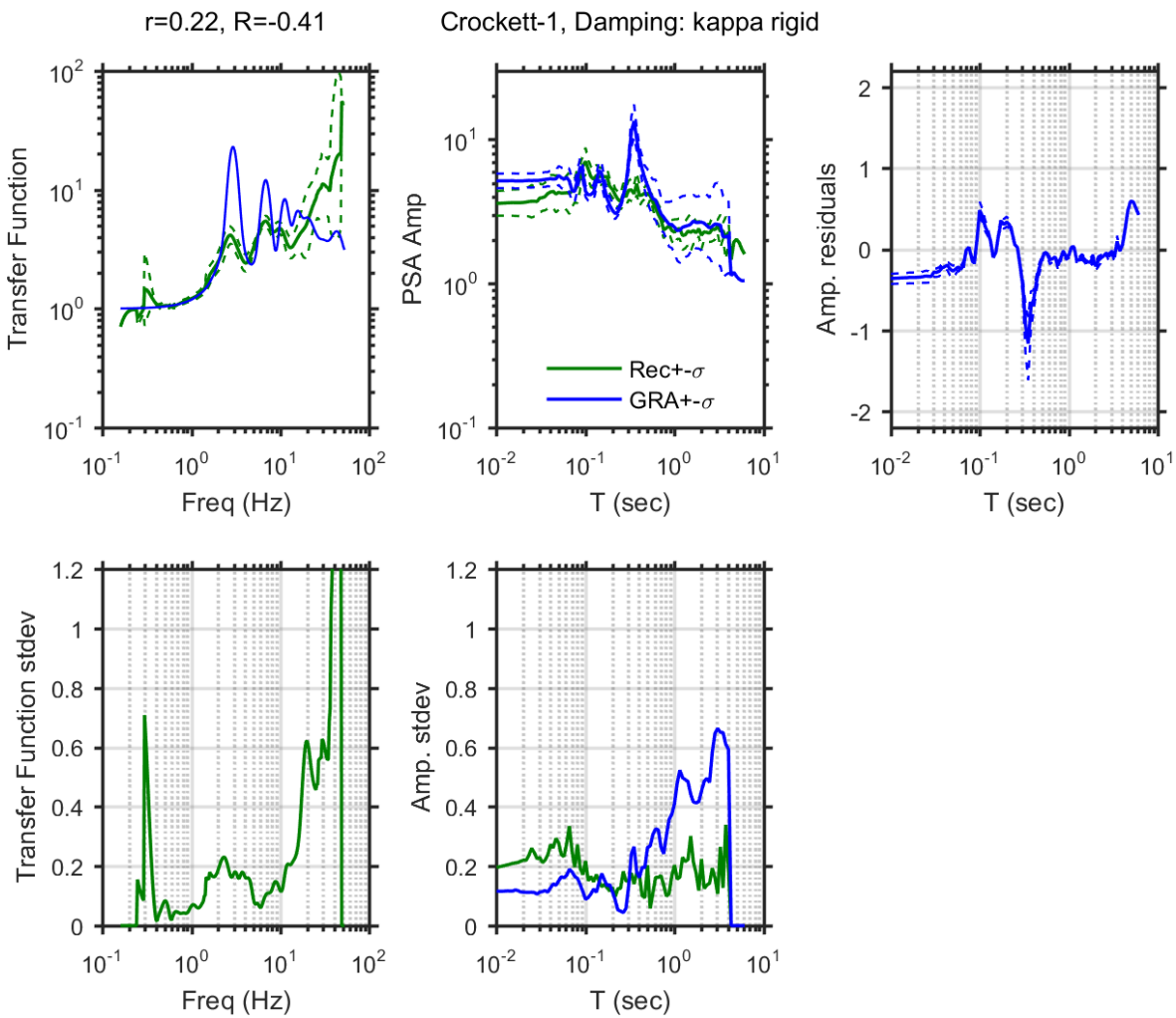

Figure A 26. Observed and simulated site response for Crockett-Carquinez Br #1 site with κ-informed model for damping; Top left: Theoretical and median ± standard deviation of empirical transfer functions, Top middle: observed and predicted median ± standard deviation of *PS*A amplification, Top right: median ± standard deviation of *PS*A amplification residuals, Bottom left: standard deviation of empirical transfer functions, Bottom middle: standard deviation of observed and predicted *PS*A amplification residuals.

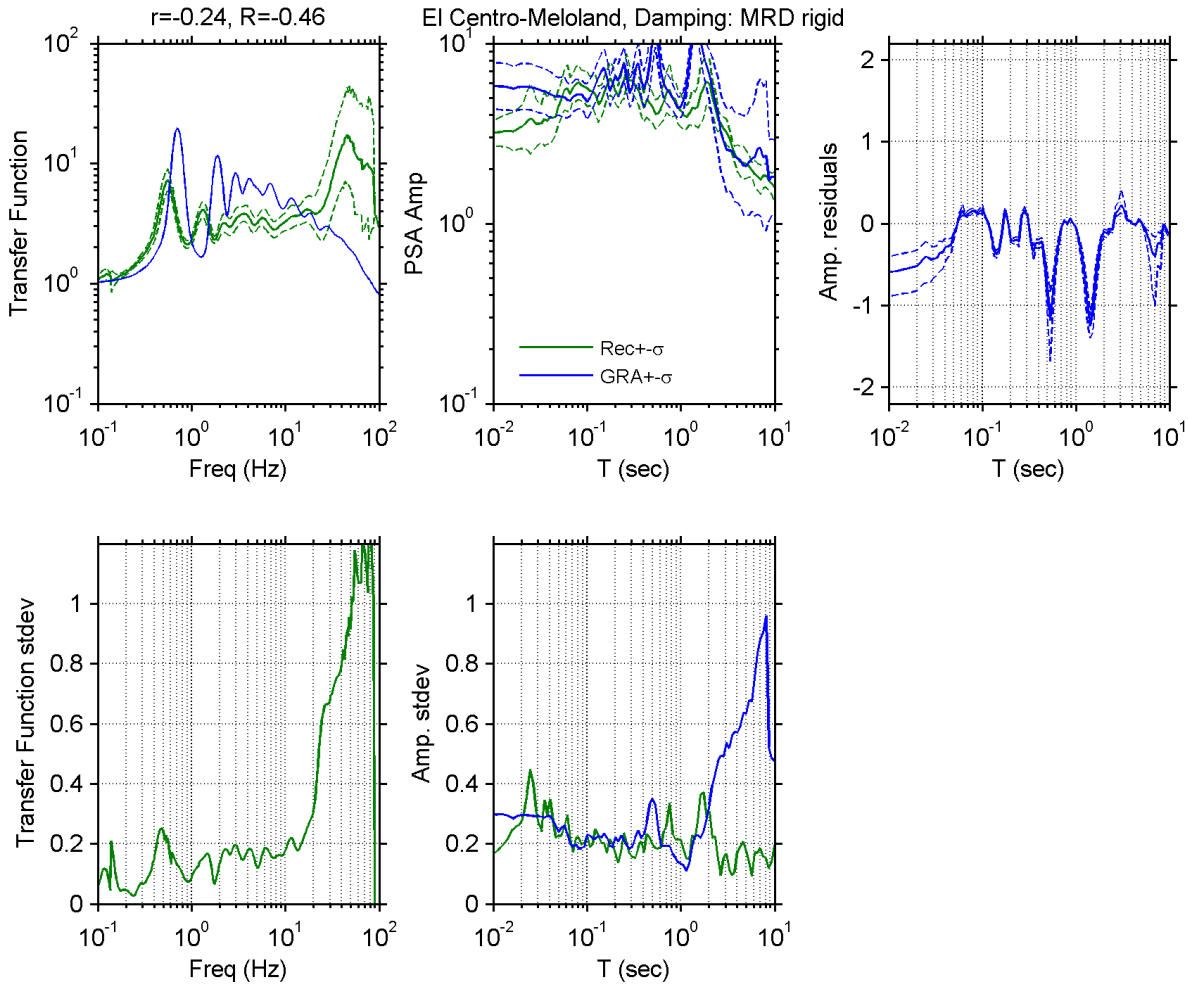

Figure A 27. Observed and simulated site response for El Centro-Meloland site with $D_{\min}^{L}$ model for damping; Top left: Theoretical and median ± standard deviation of empirical transfer functions, Top middle: observed and predicted median ± standard deviation of *PS*A amplification, Top right: median ± standard deviation of *PS*A amplification residuals, Bottom left: standard deviation of empirical transfer functions, Bottom middle: standard deviation of observed and predicted *PS*A amplification residuals.

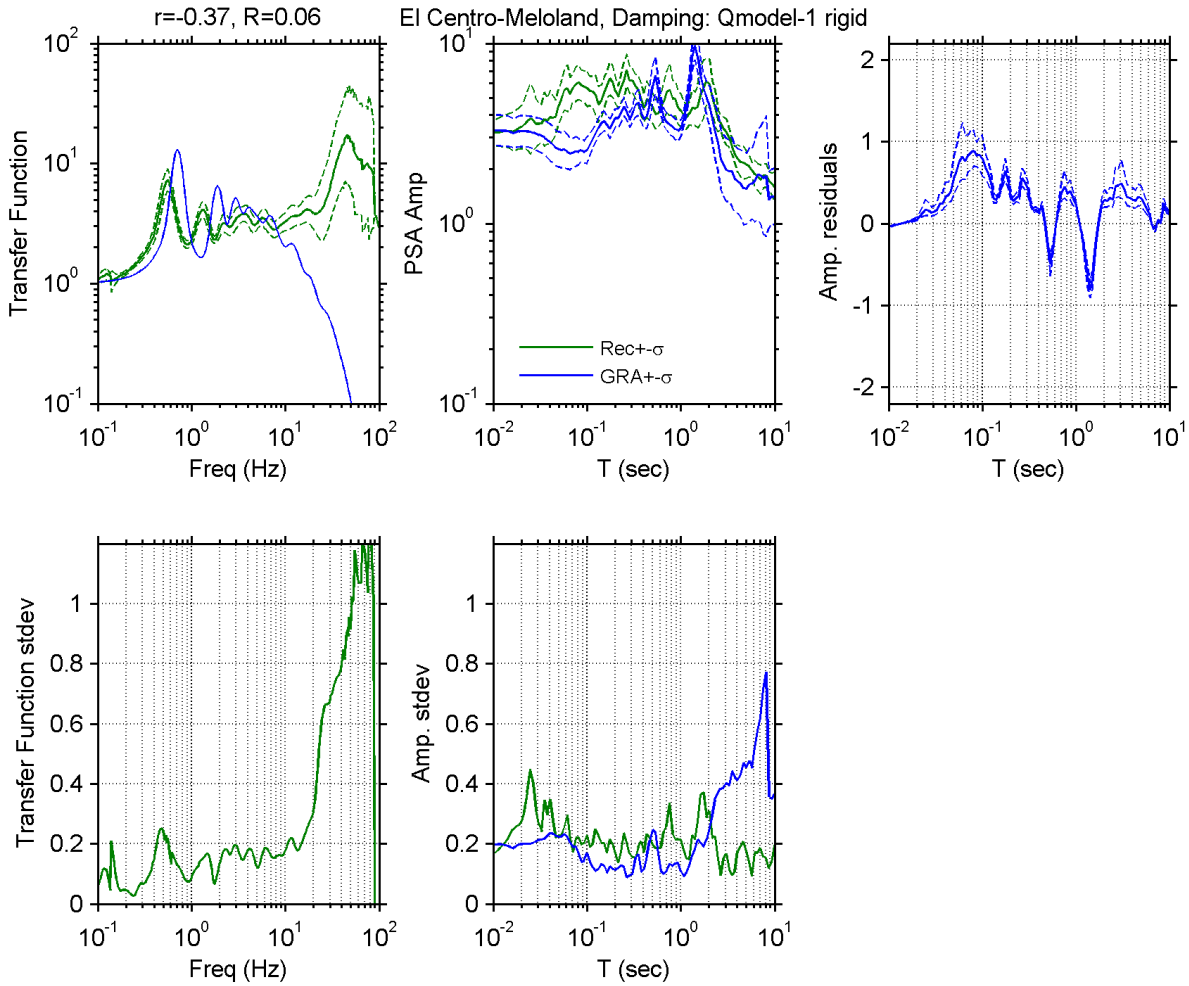

Figure A 28. Observed and simulated site response for El Centro-Meloland site with V_S-based model for damping; Top left: Theoretical and median ± standard deviation of empirical transfer functions, Top middle: observed and predicted median ± standard deviation of *PS*A amplification, Top right: median ± standard deviation of *PS*A amplification residuals, Bottom left: standard deviation of empirical transfer functions, Bottom middle: standard deviation of observed and predicted *PS*A amplification residuals.

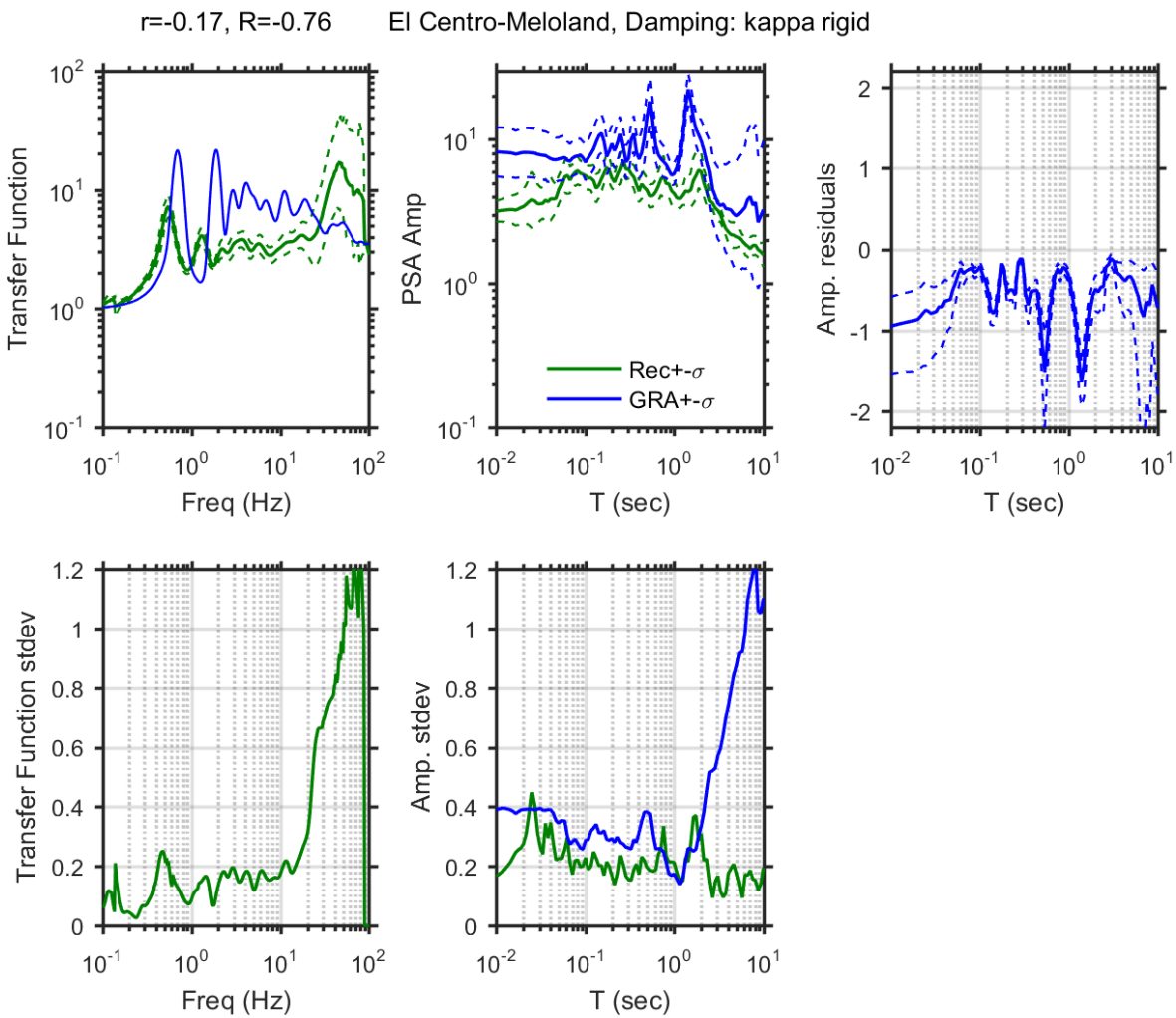

Figure A 29. Observed and simulated site response for El Centro-Meloland site with κ-informed model for damping; Top left: Theoretical and median ± standard deviation of empirical transfer functions, Top middle: observed and predicted median ± standard deviation of *PS*A amplification, Top right: median ± standard deviation of *PS*A amplification residuals, Bottom left: standard deviation of empirical transfer functions, Bottom middle: standard deviation of observed and predicted *PS*A amplification residuals.

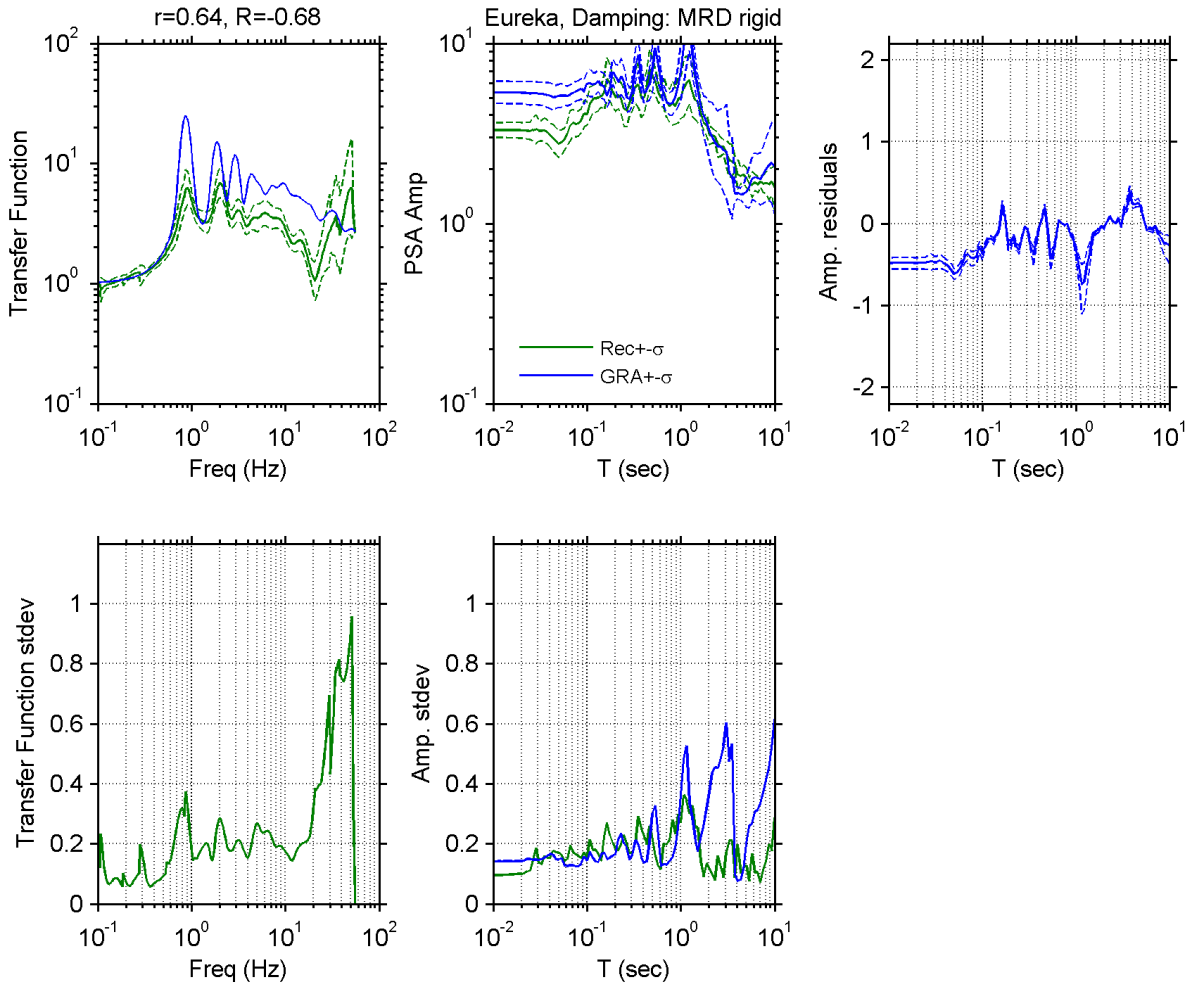

Figure A 30. Observed and simulated site response for Eureka site with $D_{\min}^{L}$ model for damping; Top left: Theoretical and median ± standard deviation of empirical transfer functions, Top middle: observed and predicted median ± standard deviation of *PS*A amplification, Top right: median ± standard deviation of *PS*A amplification residuals, Bottom left: standard deviation of empirical transfer functions, Bottom middle: standard deviation of observed and predicted *PS*A amplification residuals.

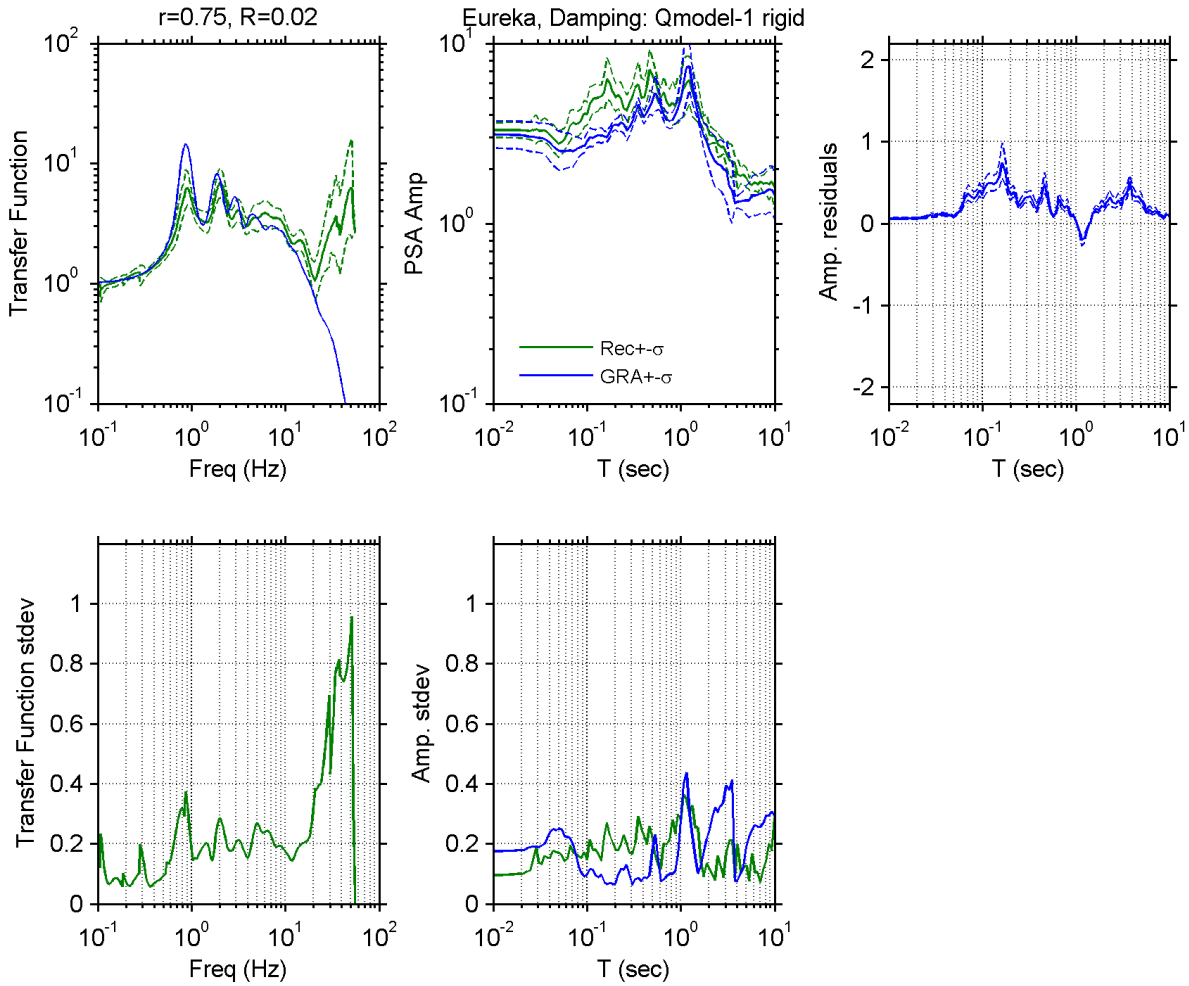

Figure A 31. Observed and simulated site response for Eureka site with V_S-based model for damping; Top left: Theoretical and median ± standard deviation of empirical transfer functions, Top middle: observed and predicted median ± standard deviation of *PS*A amplification, Top right: median ± standard deviation of *PS*A amplification residuals, Bottom left: standard deviation of empirical transfer functions, Bottom middle: standard deviation of observed and predicted *PS*A amplification residuals.

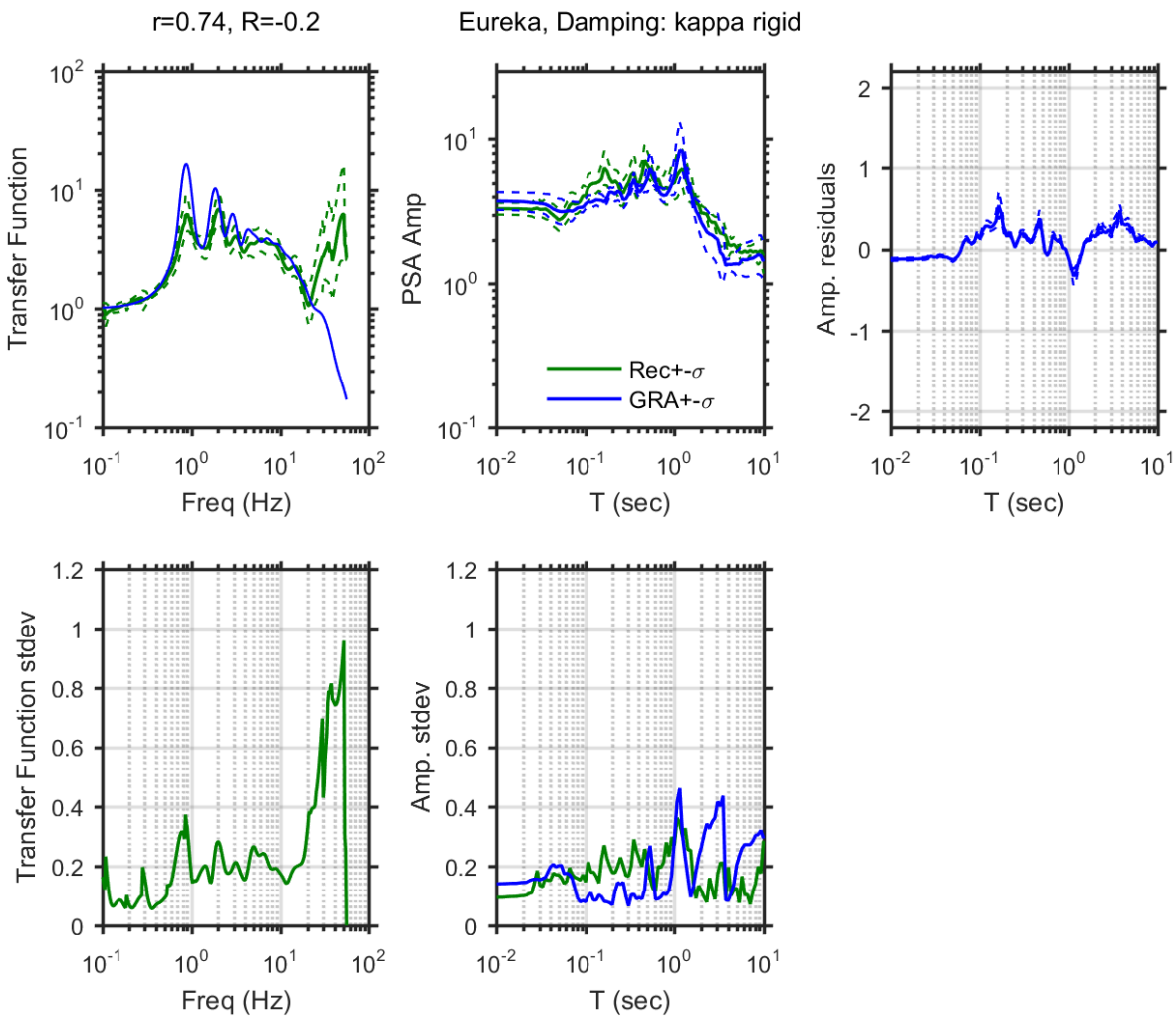

Figure A 32. Observed and simulated site response for Eureka site with κ-informed model for damping; Top left: Theoretical and median ± standard deviation of empirical transfer functions, Top middle: observed and predicted median ± standard deviation of *PS*A amplification, Top right: median ± standard deviation of *PS*A amplification residuals, Bottom left: standard deviation of empirical transfer functions, Bottom middle: standard deviation of observed and predicted *PS*A amplification residuals.

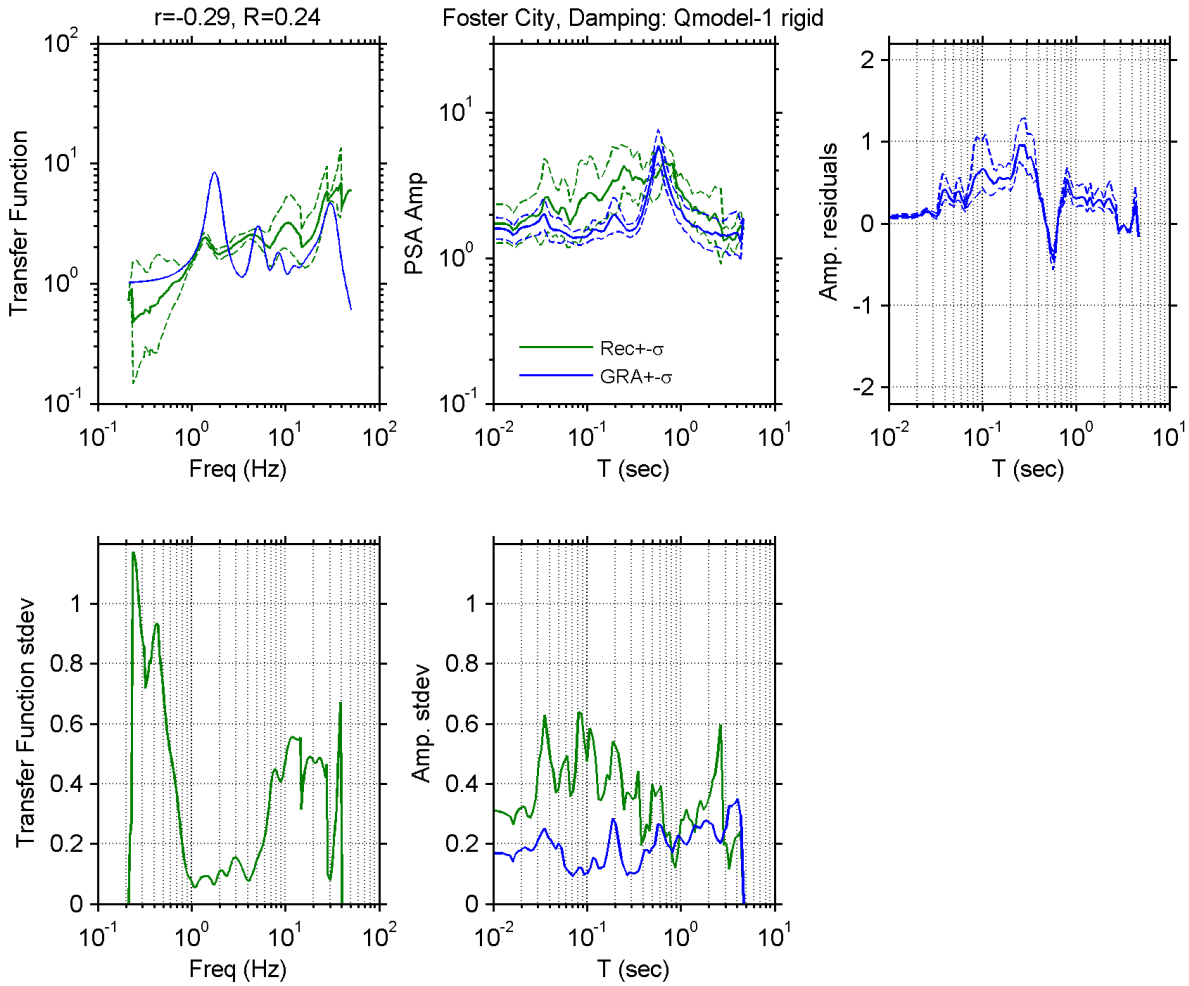

Figure A 33. Observed and simulated site response for Foster City-San Mateo site with V_S-based model for damping; Top left: Theoretical and median ± standard deviation of empirical transfer functions, Top middle: observed and predicted median ± standard deviation of *PS*A amplification, Top right: median ± standard deviation of *PS*A amplification residuals, Bottom left: standard deviation of empirical transfer functions, Bottom middle: standard deviation of observed and predicted *PS*A amplification residuals.

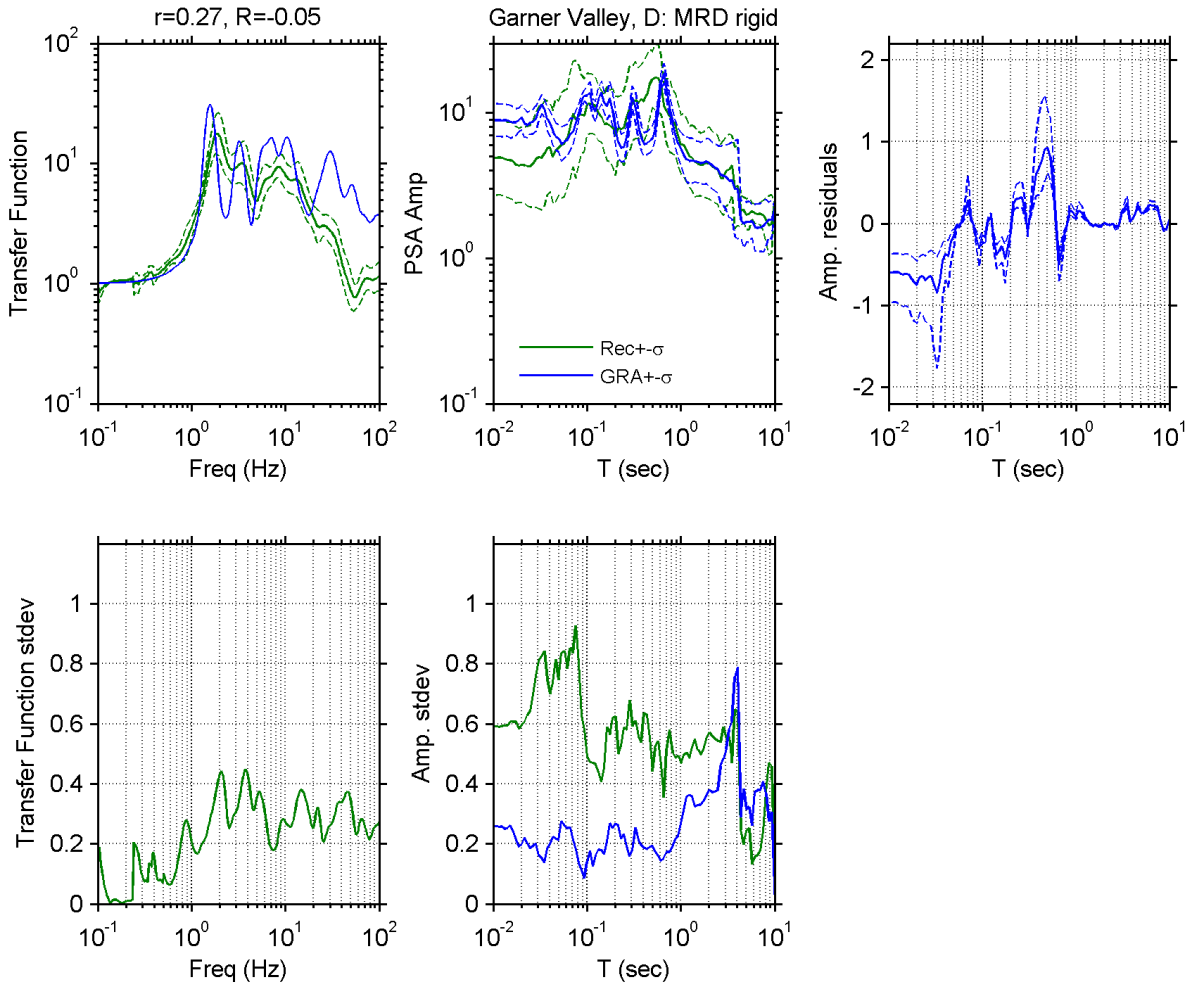

Figure A 34. Observed and simulated site response for Garner Valley site with $D_{\min}^{L}$ model for damping; Top left: Theoretical and median ± standard deviation of empirical transfer functions, Top middle: observed and predicted median ± standard deviation of *PS*A amplification, Top right: median ± standard deviation of *PS*A amplification residuals, Bottom left: standard deviation of empirical transfer functions, Bottom middle: standard deviation of observed and predicted *PS*A amplification residuals.

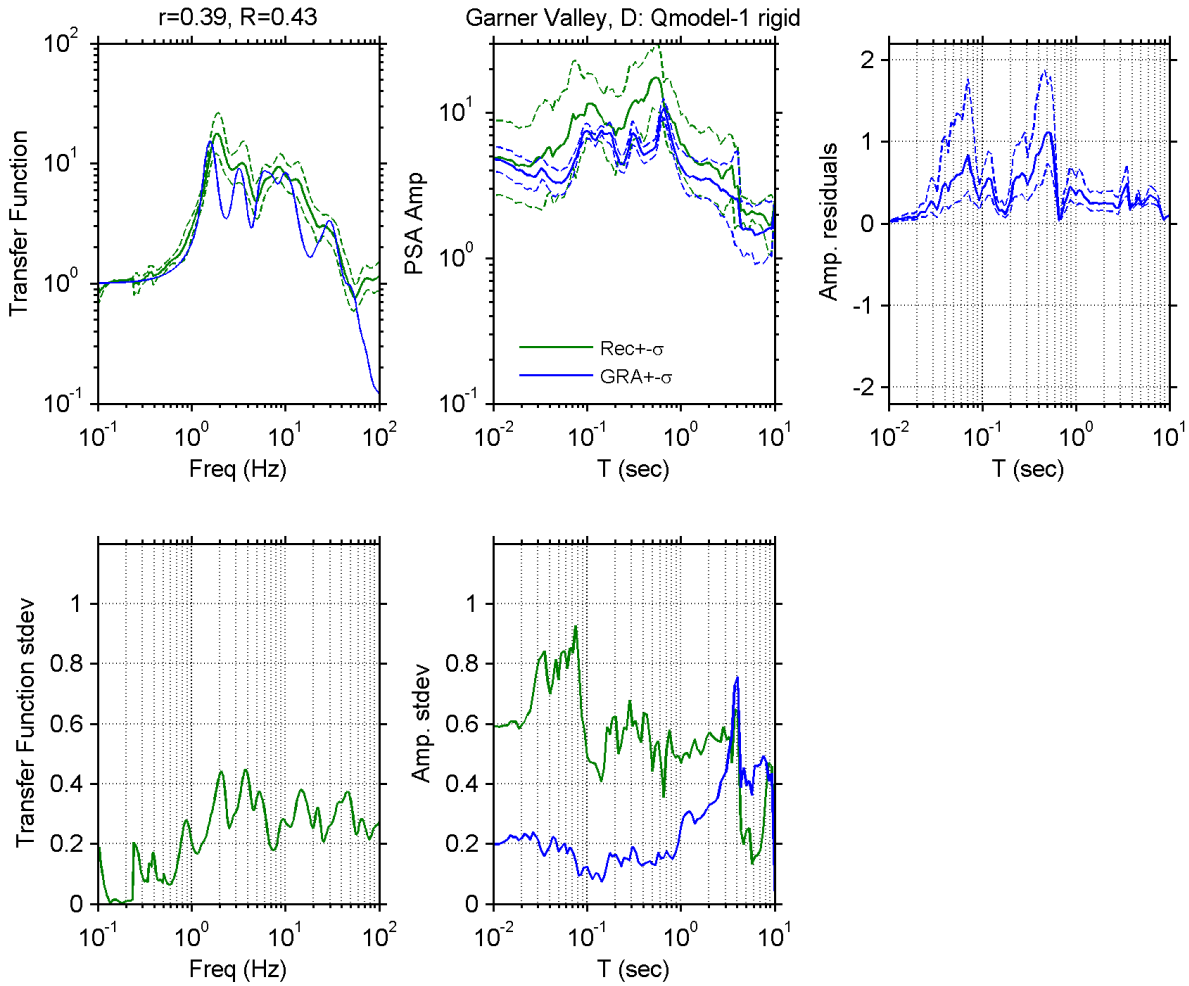

Figure A 35. Observed and simulated site response for Garner Valley site with V_S-based model for damping; Top left: Theoretical and median ± standard deviation of empirical transfer functions, Top middle: observed and predicted median ± standard deviation of *PS*A amplification, Top right: median ± standard deviation of *PS*A amplification residuals, Bottom left: standard deviation of empirical transfer functions, Bottom middle: standard deviation of observed and predicted *PS*A amplification residuals.

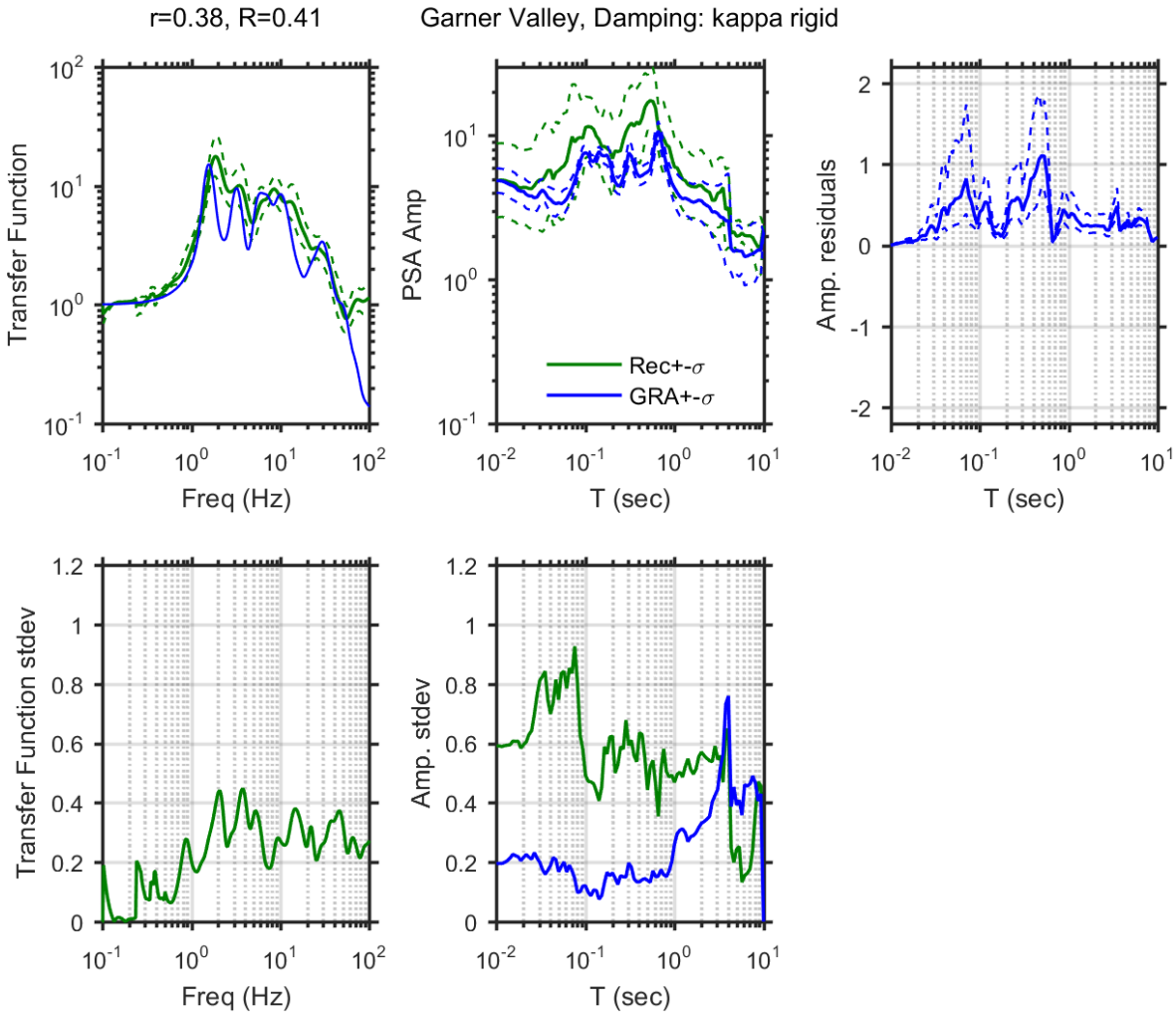

Figure A 36. Observed and simulated site response for Garner Valley site with κ-informed model for damping; Top left: Theoretical and median ± standard deviation of empirical transfer functions, Top middle: observed and predicted median ± standard deviation of *PS*A amplification, Top right: median ± standard deviation of *PS*A amplification residuals, Bottom left: standard deviation of empirical transfer functions, Bottom middle: standard deviation of observed and predicted *PS*A amplification residuals.

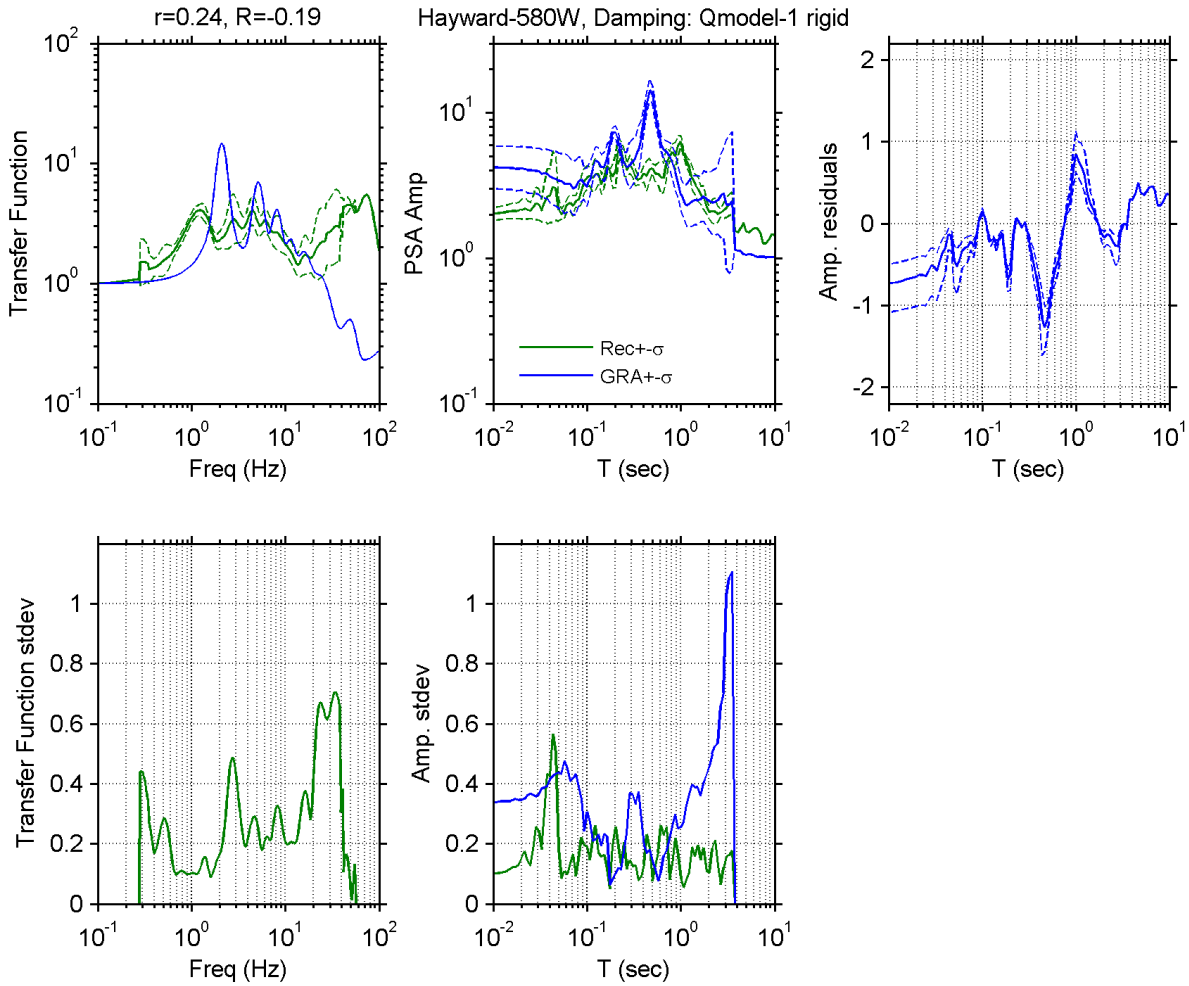

Figure A 37. Observed and simulated site response for Hayward - I580/238 West site with V_S-based model for damping; Top left: Theoretical and median ± standard deviation of empirical transfer functions, Top middle: observed and predicted median ± standard deviation of *PS*A amplification, Top right: median ± standard deviation of *PS*A amplification residuals, Bottom left: standard deviation of empirical transfer functions, Bottom middle: standard deviation of observed and predicted *PS*A amplification residuals.

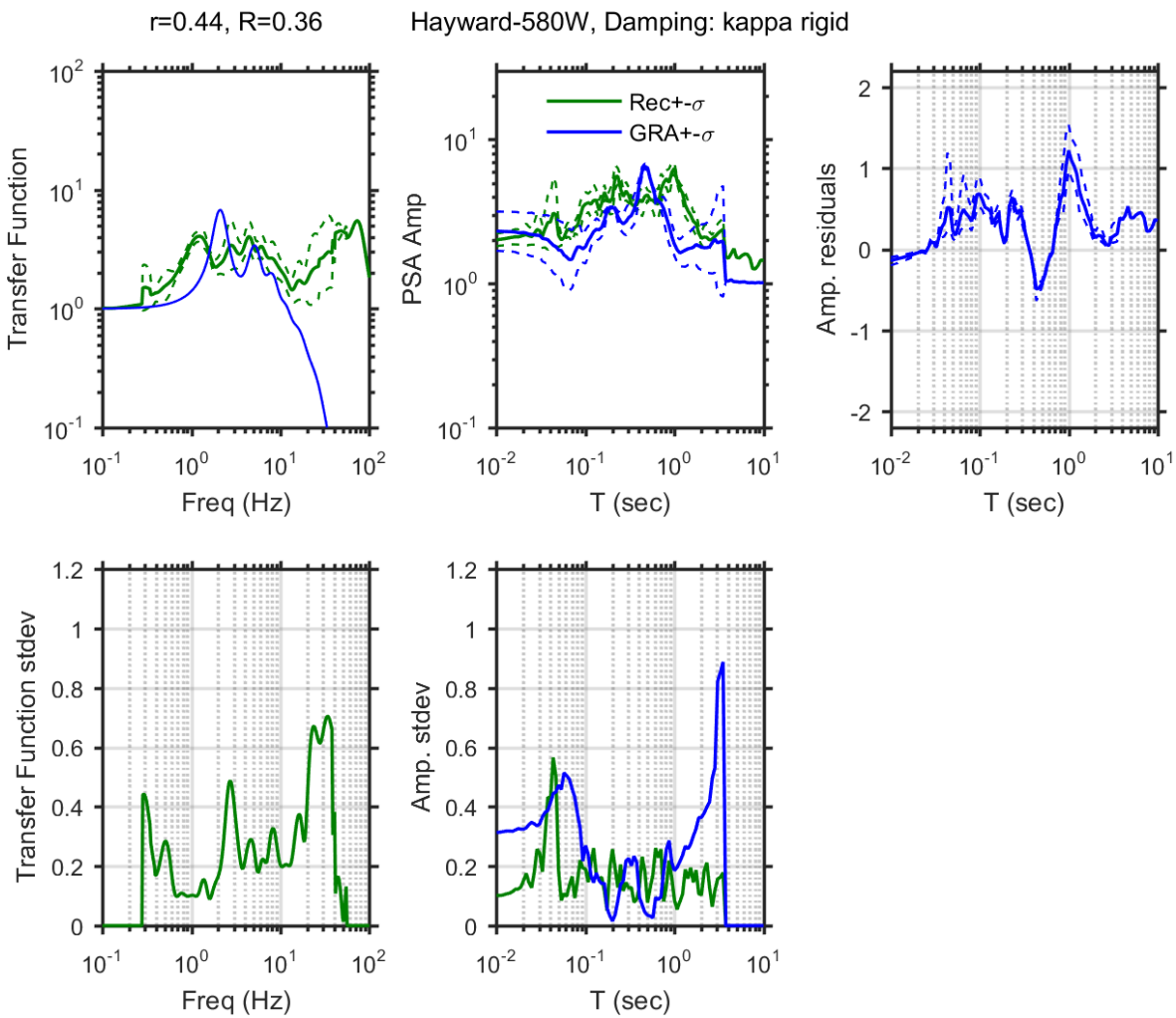

Figure A 38. Observed and simulated site response for Hayward - I580/238 West site with κ-informed model for damping; Top left: Theoretical and median ± standard deviation of empirical transfer functions, Top middle: observed and predicted median ± standard deviation of *PS*A amplification, Top right: median ± standard deviation of *PS*A amplification residuals, Bottom left: standard deviation of empirical transfer functions, Bottom middle: standard deviation of observed and predicted *PS*A amplification residuals.

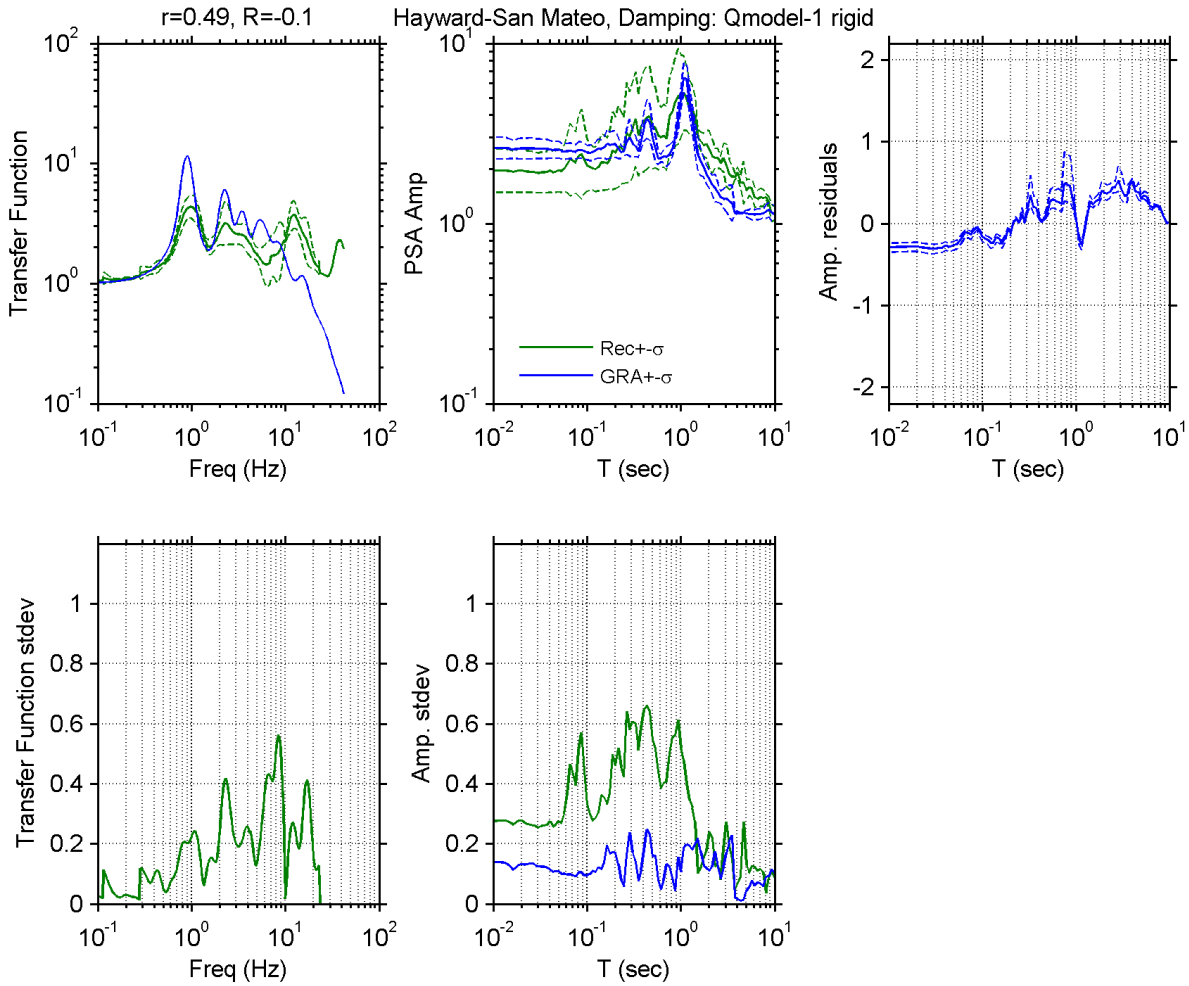

Figure A 39. Observed and simulated site response for Hayward - San Mateo Br site with V_S-based model for damping; Top left: Theoretical and median ± standard deviation of empirical transfer functions, Top middle: observed and predicted median ± standard deviation of *PS*A amplification, Top right: median ± standard deviation of *PS*A amplification residuals, Bottom left: standard deviation of empirical transfer functions, Bottom middle: standard deviation of observed and predicted *PS*A amplification residuals.

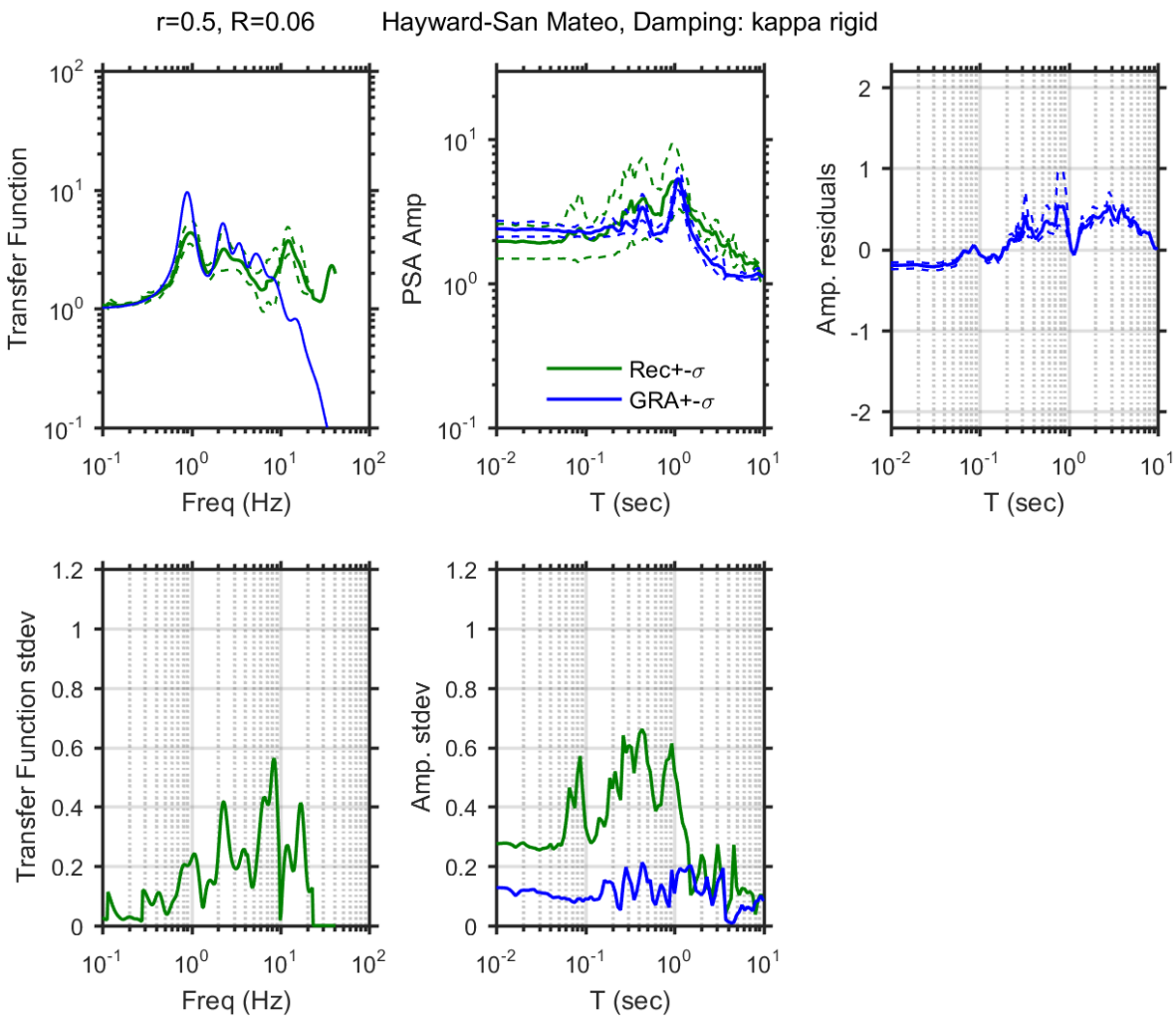

Figure A 40. Observed and simulated site response for Hayward - San Mateo Br site with κ-informed model for damping; Top left: Theoretical and median ± standard deviation of empirical transfer functions, Top middle: observed and predicted median ± standard deviation of *PS*A amplification, Top right: median ± standard deviation of *PS*A amplification residuals, Bottom left: standard deviation of empirical transfer functions, Bottom middle: standard deviation of observed and predicted *PS*A amplification residuals.

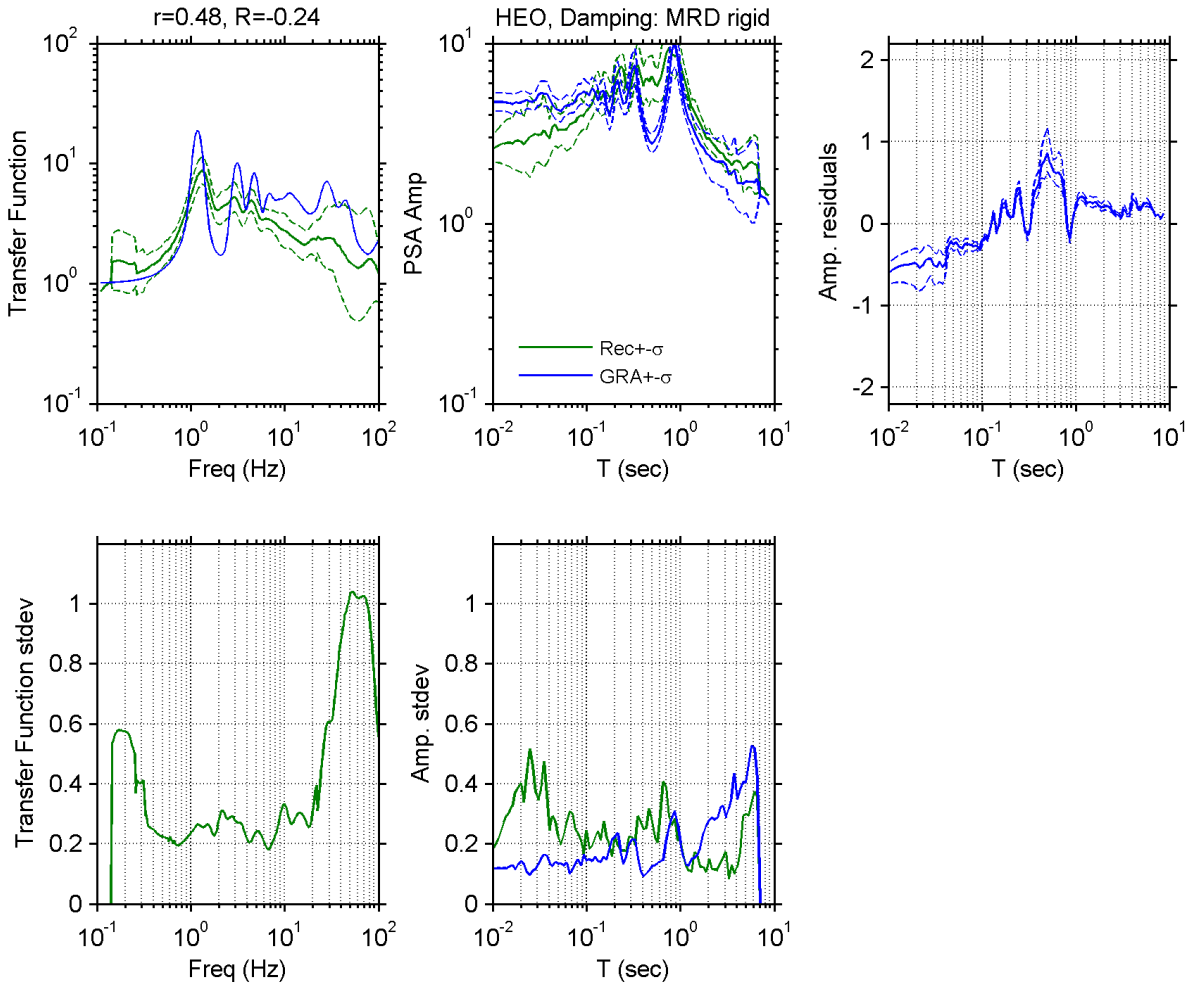

Figure A 41. Observed and simulated site response for Hollister Digital Array (HEO) site with $D_{\min}^{L}$ model for damping; Top left: Theoretical and median ± standard deviation of empirical transfer functions, Top middle: observed and predicted median ± standard deviation of *PS*A amplification, Top right: median ± standard deviation of *PS*A amplification residuals, Bottom left: standard deviation of empirical transfer functions, Bottom middle: standard deviation of observed and predicted *PS*A amplification residuals.

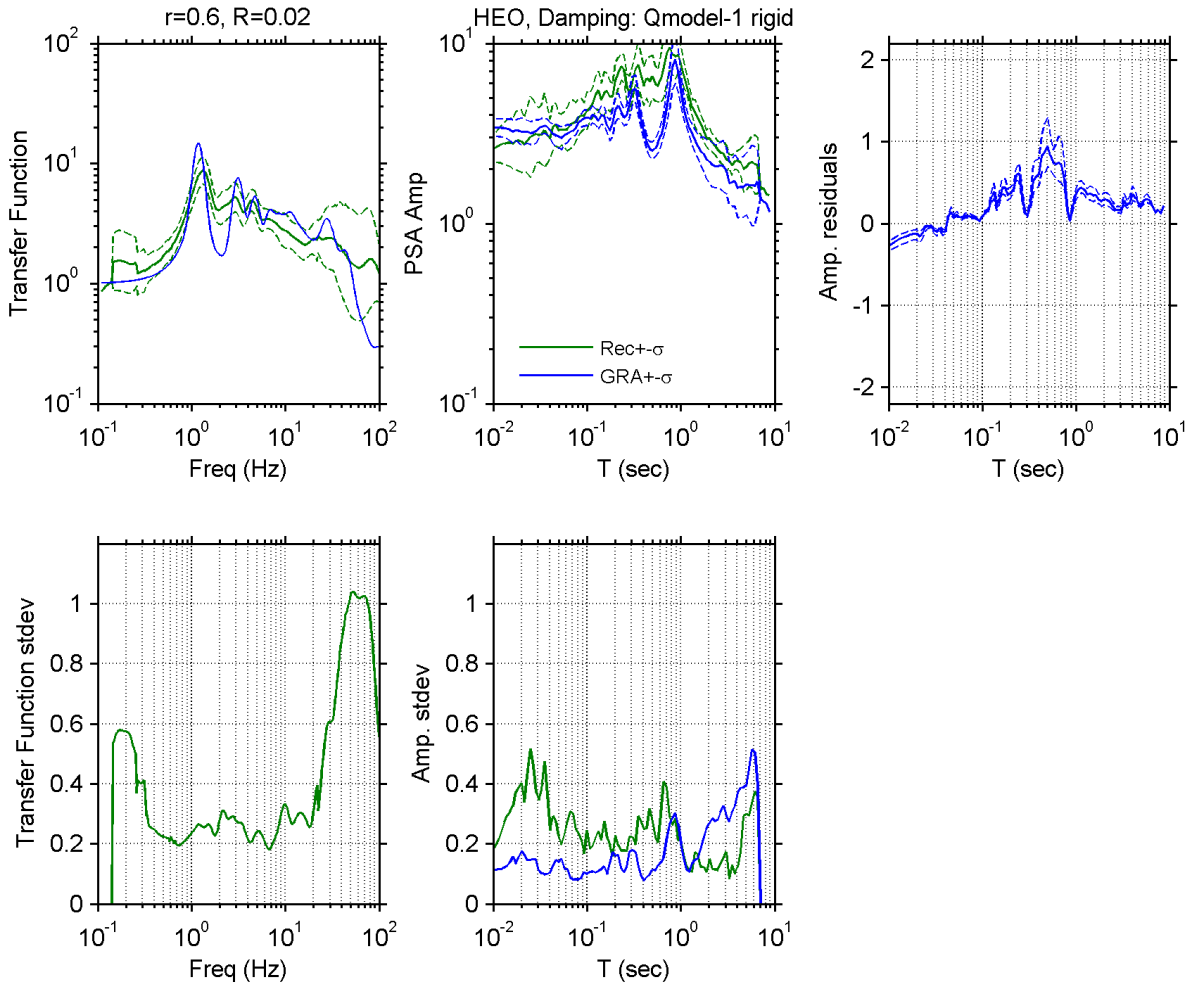

Figure A 42. Observed and simulated site response for Hollister Digital Array (HEO) site with V_S-based model for damping; Top left: Theoretical and median ± standard deviation of empirical transfer functions, Top middle: observed and predicted median ± standard deviation of *PS*A amplification, Top right: median ± standard deviation of *PS*A amplification residuals, Bottom left: standard deviation of empirical transfer functions, Bottom middle: standard deviation of observed and predicted *PS*A amplification residuals.

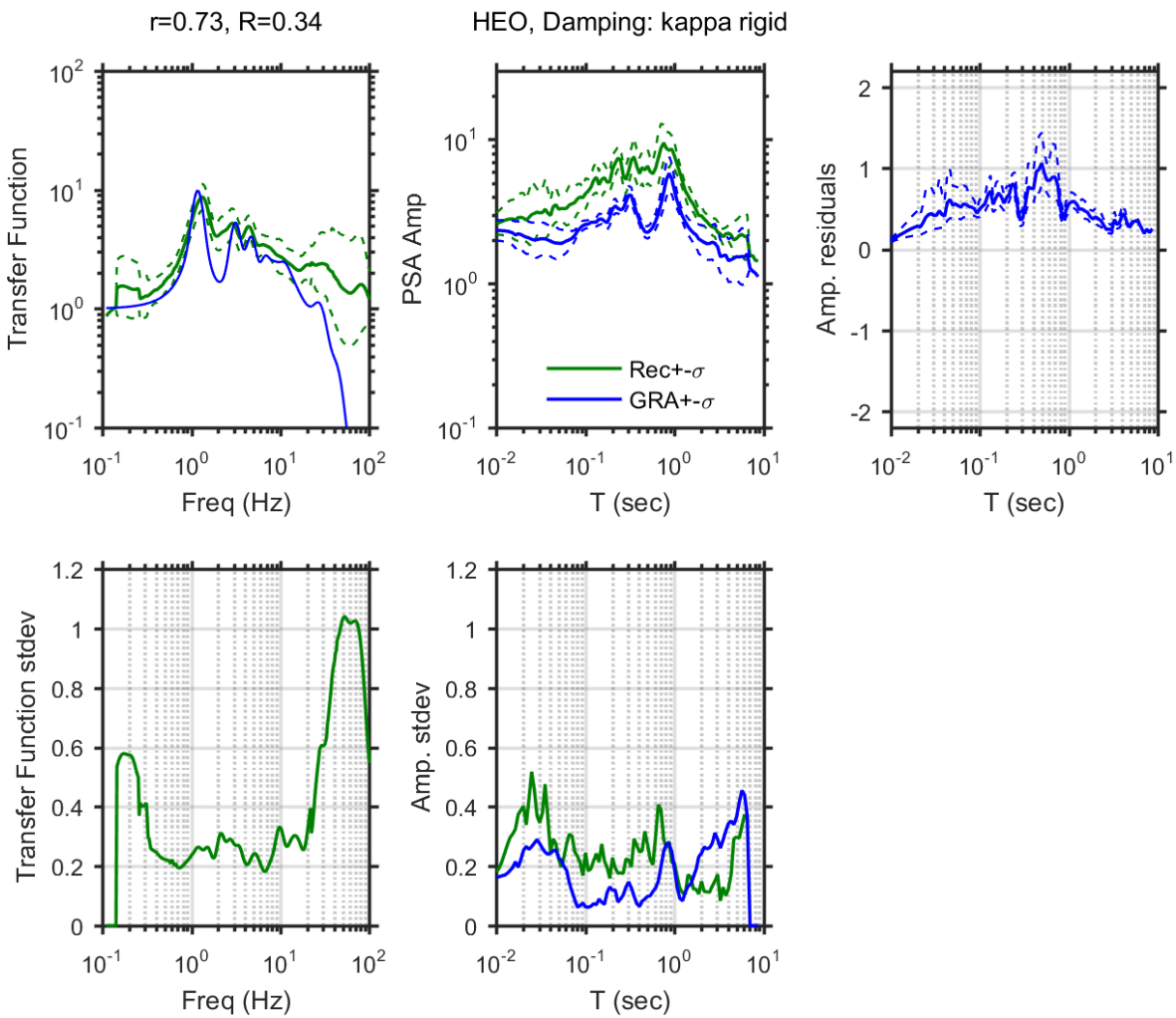

Figure A 43. Observed and simulated site response for Hollister Digital Array (HEO) site with κ-informed model for damping; Top left: Theoretical and median ± standard deviation of empirical transfer functions, Top middle: observed and predicted median ± standard deviation of *PS*A amplification, Top right: median ± standard deviation of *PS*A amplification residuals, Bottom left: standard deviation of empirical transfer functions, Bottom middle: standard deviation of observed and predicted *PS*A amplification residuals.

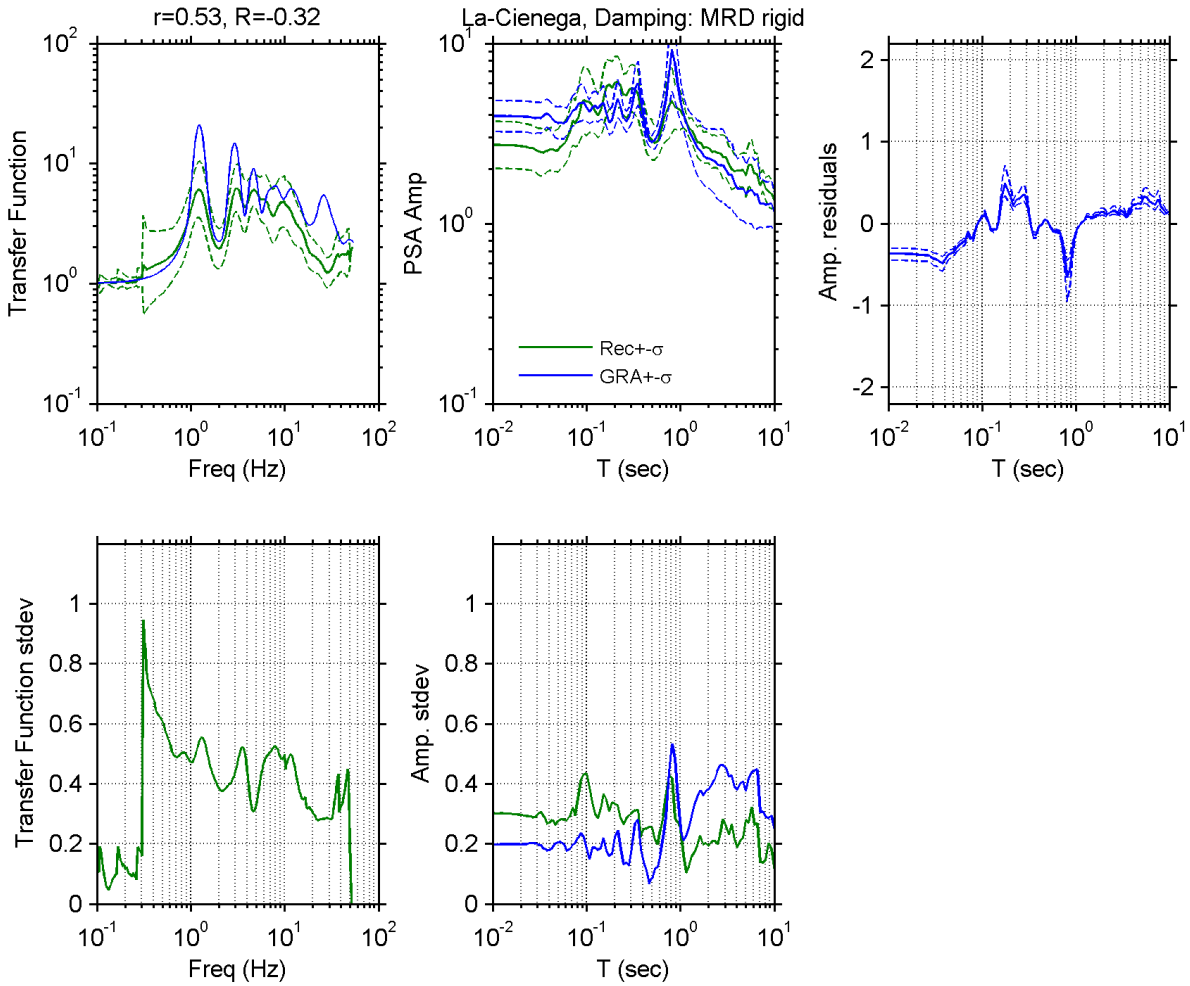

Figure A 44. Observed and simulated site response for La-Cienega site with $D_{\min}^{L}$ model for damping; Top left: Theoretical and median ± standard deviation of empirical transfer functions, Top middle: observed and predicted median ± standard deviation of *PS*A amplification, Top right: median ± standard deviation of *PS*A amplification residuals, Bottom left: standard deviation of empirical transfer functions, Bottom middle: standard deviation of observed and predicted *PS*A amplification residuals.

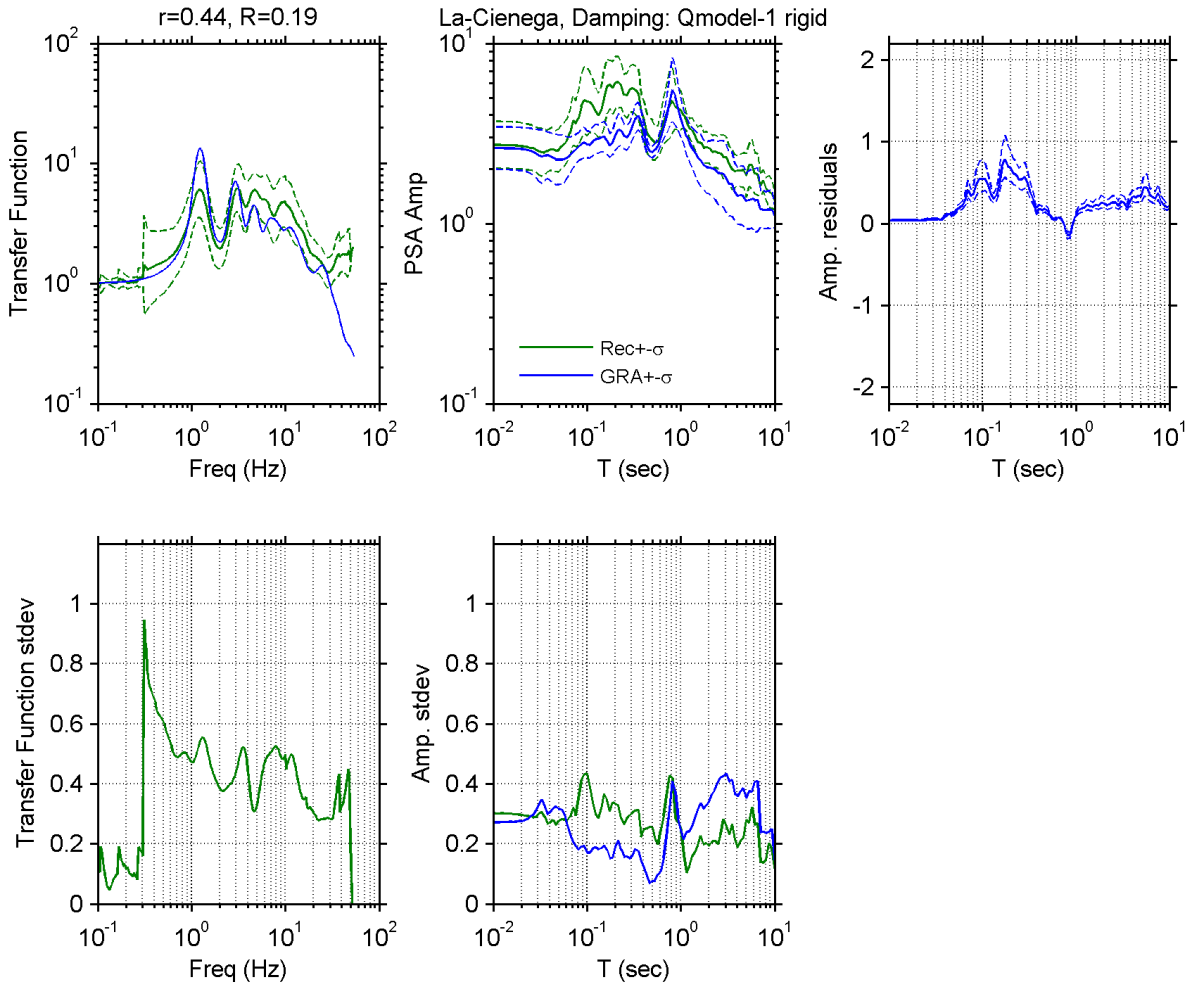

Figure A 45. Observed and simulated site response for La-Cienega site with V_S-based model for damping; Top left: Theoretical and median ± standard deviation of empirical transfer functions, Top middle: observed and predicted median ± standard deviation of *PS*A amplification, Top right: median ± standard deviation of *PS*A amplification residuals, Bottom left: standard deviation of empirical transfer functions, Bottom middle: standard deviation of observed and predicted *PS*A amplification residuals.

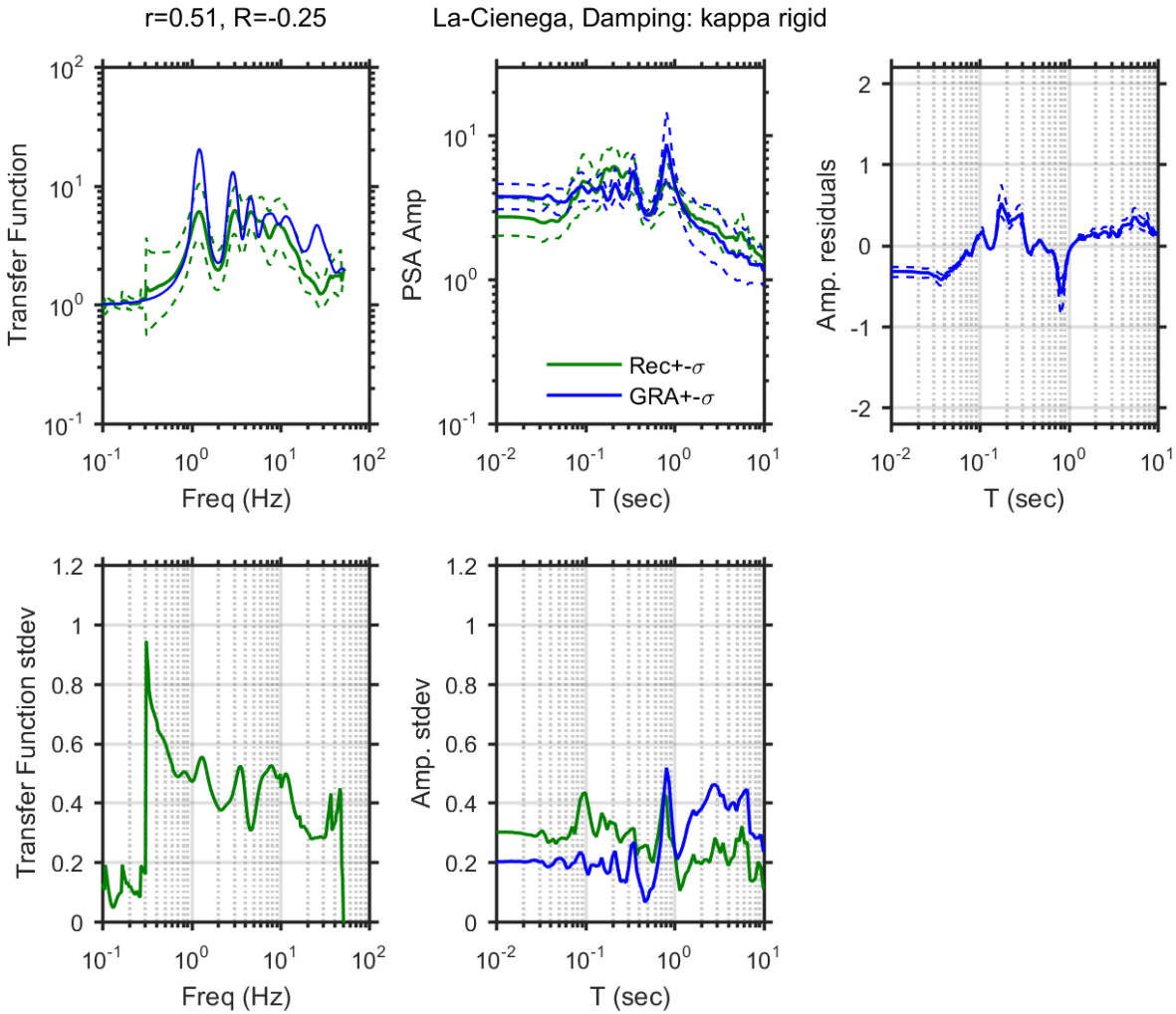

Figure A 46. Observed and simulated site response for La-Cienega site with κ-informed model for damping; Top left: Theoretical and median ± standard deviation of empirical transfer functions, Top middle: observed and predicted median ± standard deviation of *PS*A amplification, Top right: median ± standard deviation of *PS*A amplification residuals, Bottom left: standard deviation of empirical transfer functions, Bottom middle: standard deviation of observed and predicted *PS*A amplification residuals.

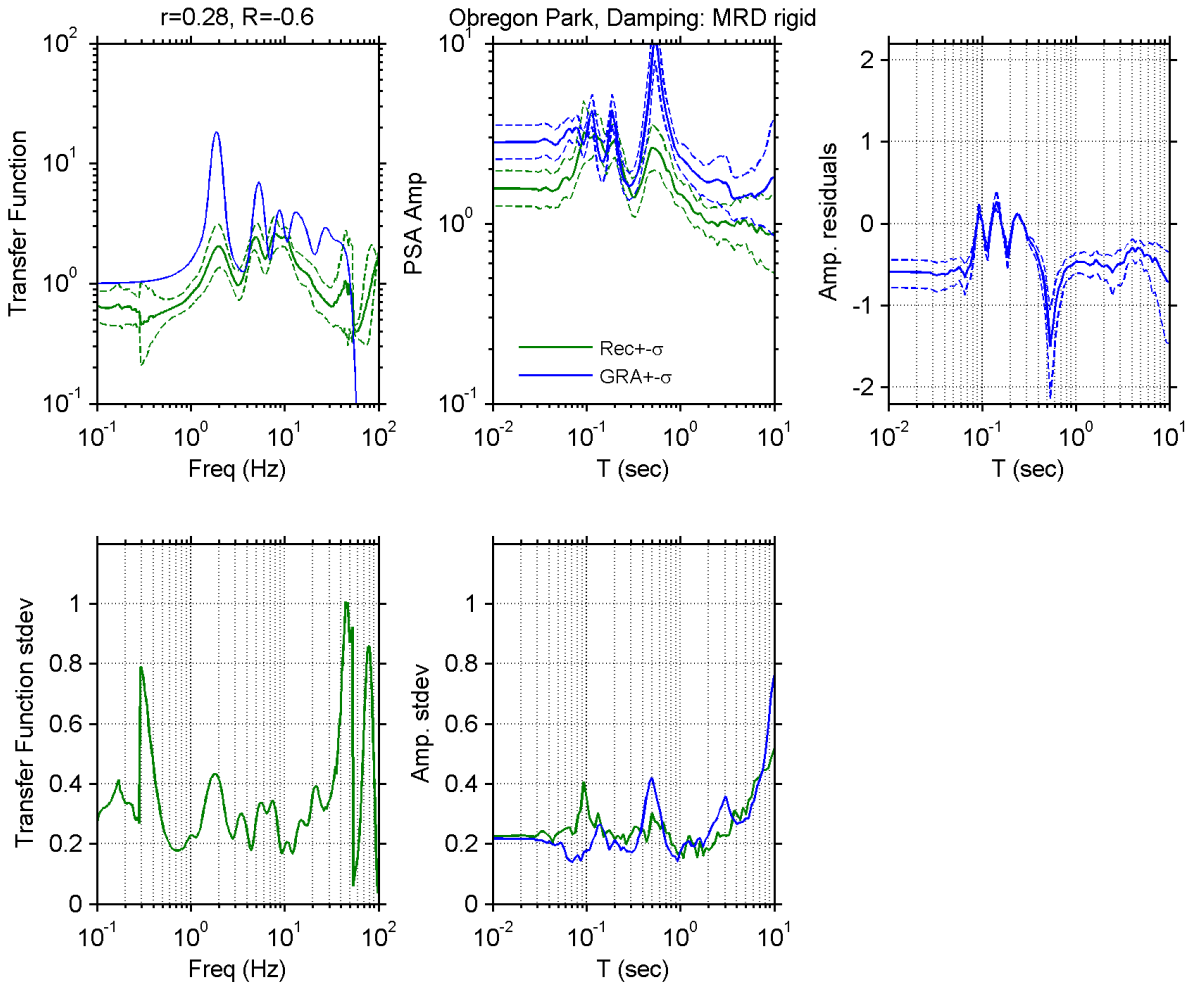

Figure A 47. Observed and simulated site response for Obregon Park site with $D_{\min}^{L}$ model for damping; Top left: Theoretical and median ± standard deviation of empirical transfer functions, Top middle: observed and predicted median ± standard deviation of *PS*A amplification, Top right: median ± standard deviation of *PS*A amplification residuals, Bottom left: standard deviation of empirical transfer functions, Bottom middle: standard deviation of observed and predicted *PS*A amplification residuals.

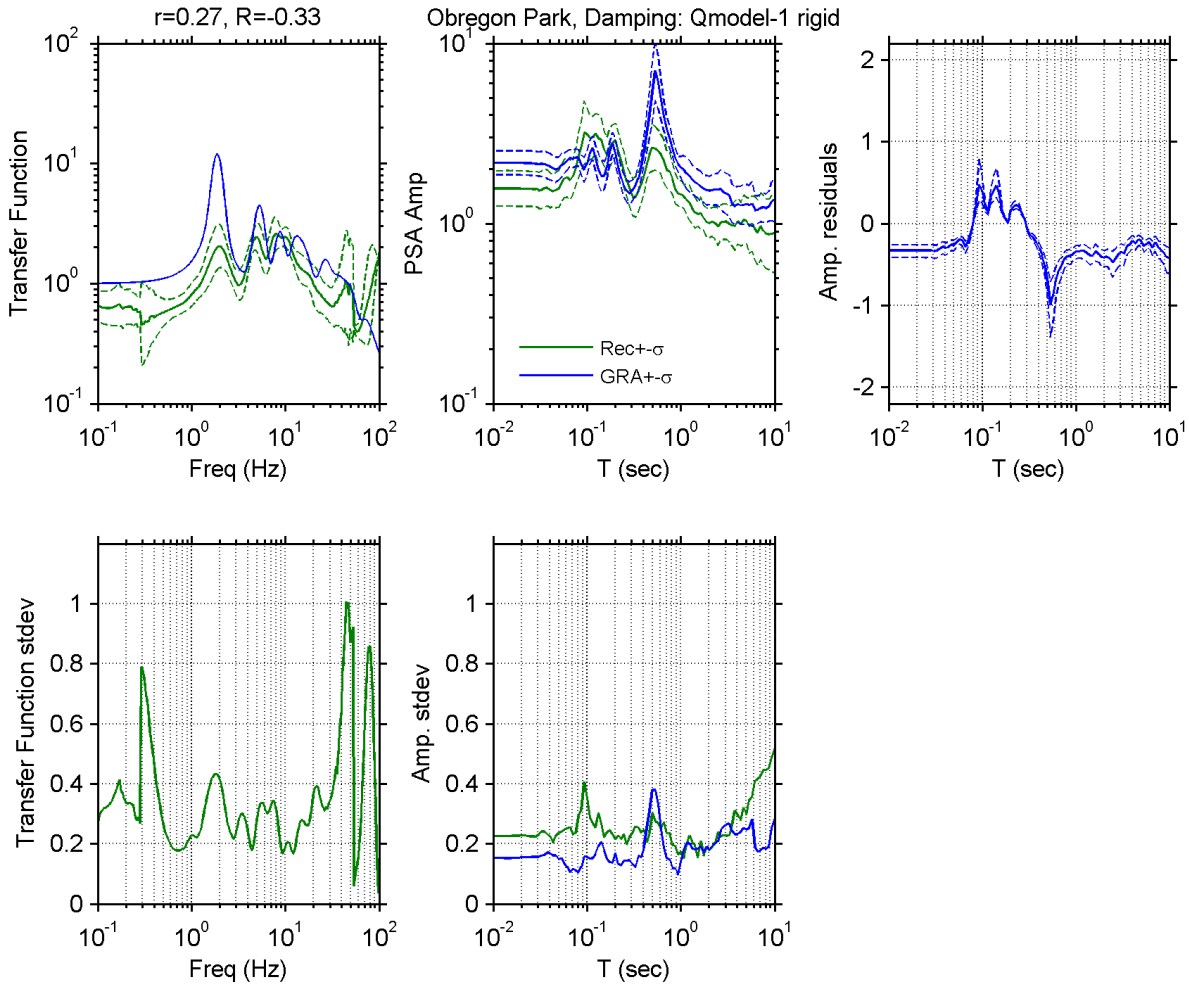

Figure A 48. Observed and simulated site response for Obregon Park site with V_S-based model for damping; Top left: Theoretical and median ± standard deviation of empirical transfer functions, Top middle: observed and predicted median ± standard deviation of *PS*A amplification, Top right: median ± standard deviation of *PS*A amplification residuals, Bottom left: standard deviation of empirical transfer functions, Bottom middle: standard deviation of observed and predicted *PS*A amplification residuals.

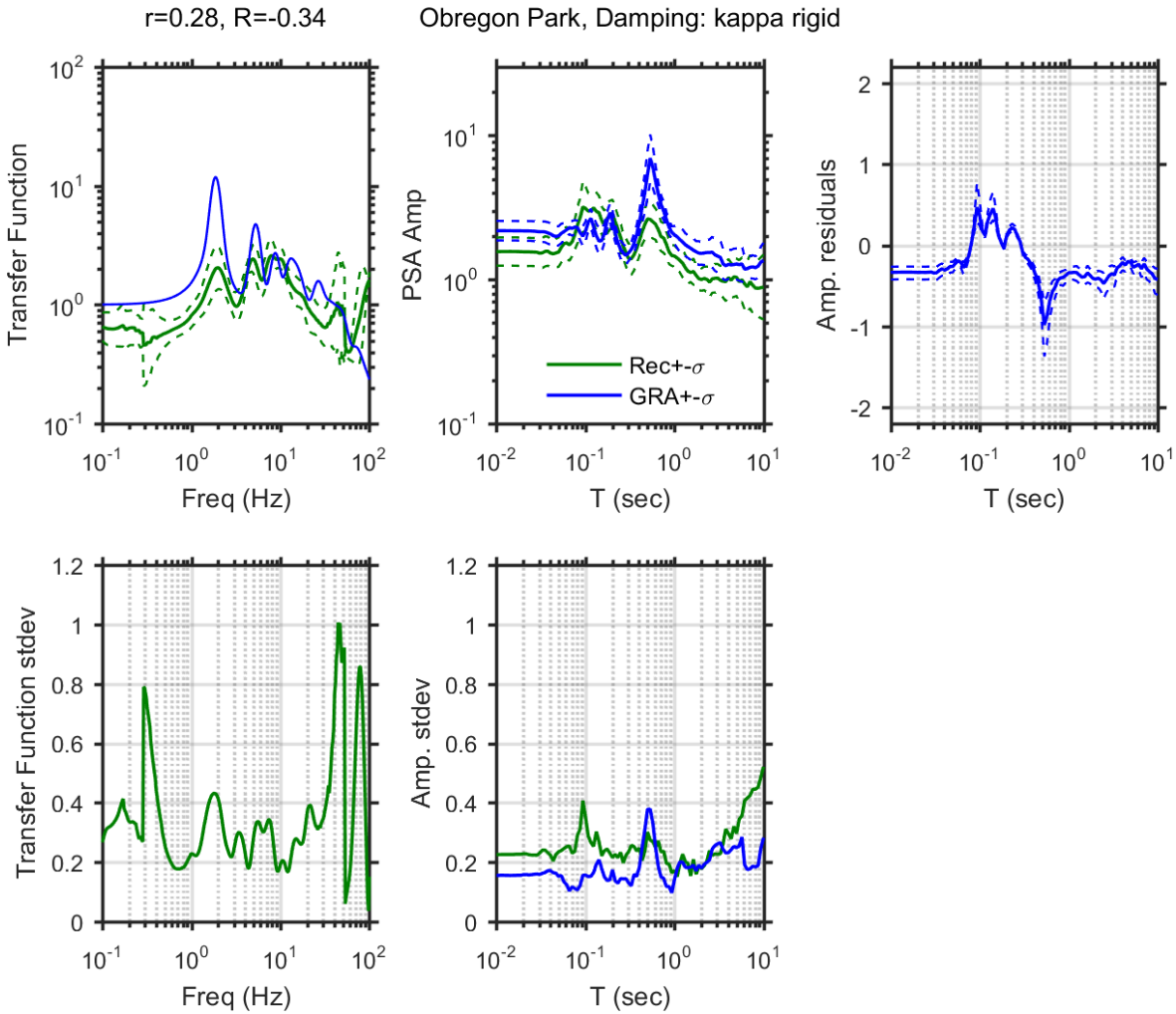

Figure A 49. Observed and simulated site response for Obregon Park site with κ-informed model for damping; Top left: Theoretical and median ± standard deviation of empirical transfer functions, Top middle: observed and predicted median ± standard deviation of *PS*A amplification, Top right: median ± standard deviation of *PS*A amplification residuals, Bottom left: standard deviation of empirical transfer functions, Bottom middle: standard deviation of observed and predicted *PS*A amplification residuals.

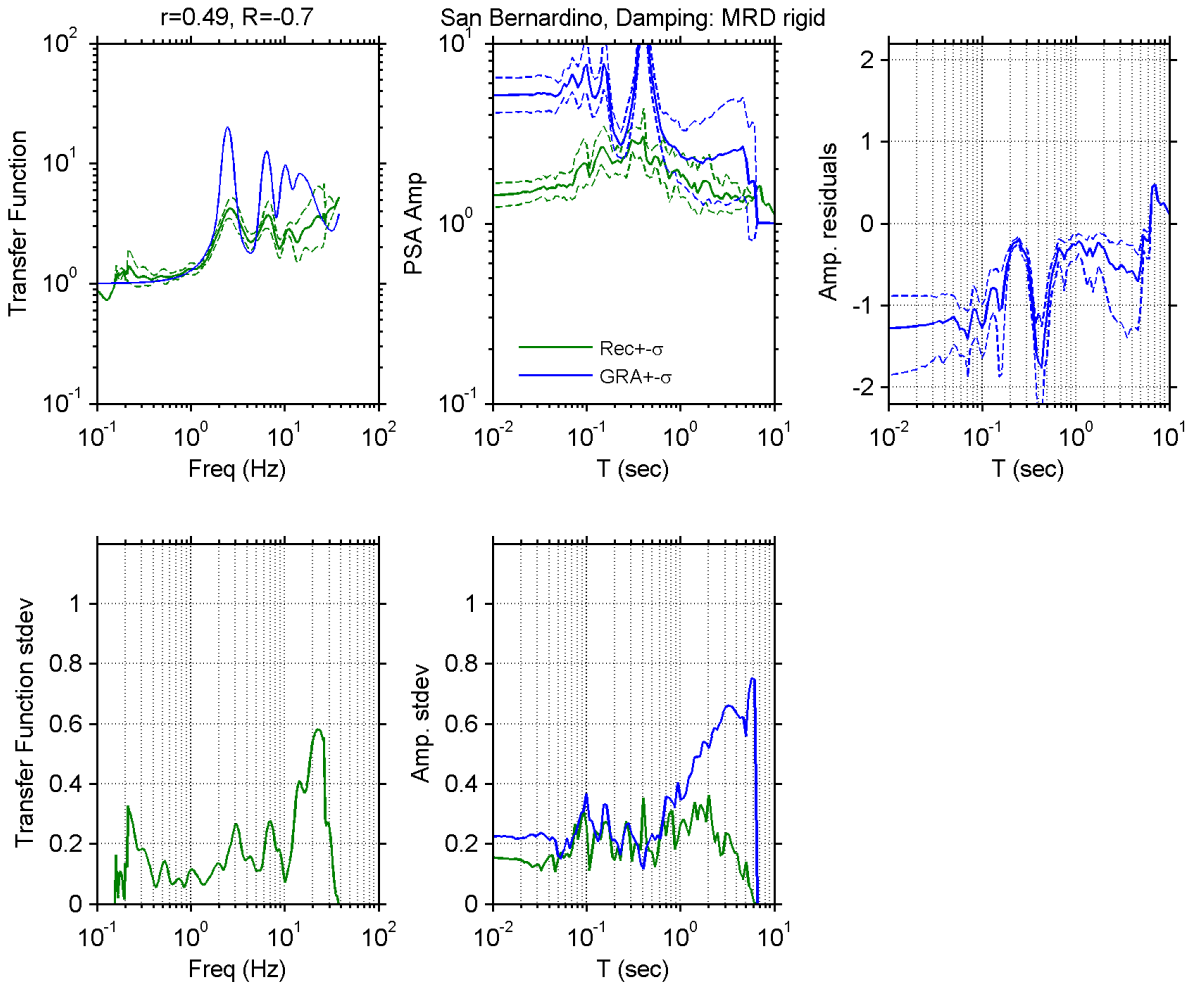

Figure A 50. Observed and simulated site response for San Bernardino site with $D_{\min}^{L}$ model for damping; Top left: Theoretical and median ± standard deviation of empirical transfer functions, Top middle: observed and predicted median ± standard deviation of *PSA* amplification, Top right: median ± standard deviation of *PSA* amplification residuals, Bottom left: standard deviation of empirical transfer functions, Bottom middle: standard deviation of observed and predicted *PSA* amplification residuals.

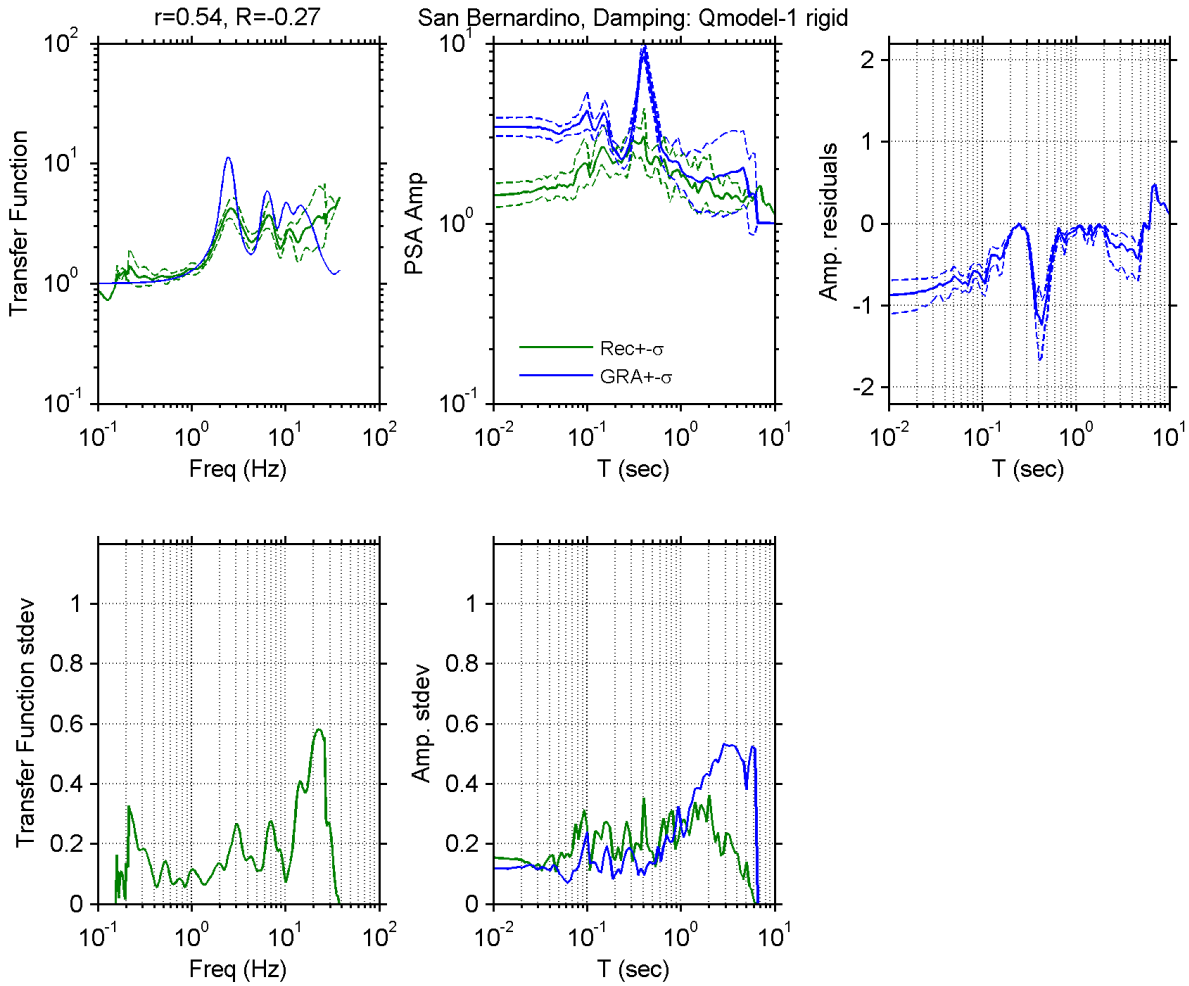

Figure A 51. Observed and simulated site response for San Bernardino site with V_S-based model for damping; Top left: Theoretical and median ± standard deviation of empirical transfer functions, Top middle: observed and predicted median ± standard deviation of *PS*A amplification, Top right: median ± standard deviation of *PS*A amplification residuals, Bottom left: standard deviation of empirical transfer functions, Bottom middle: standard deviation of observed and predicted *PS*A amplification residuals.

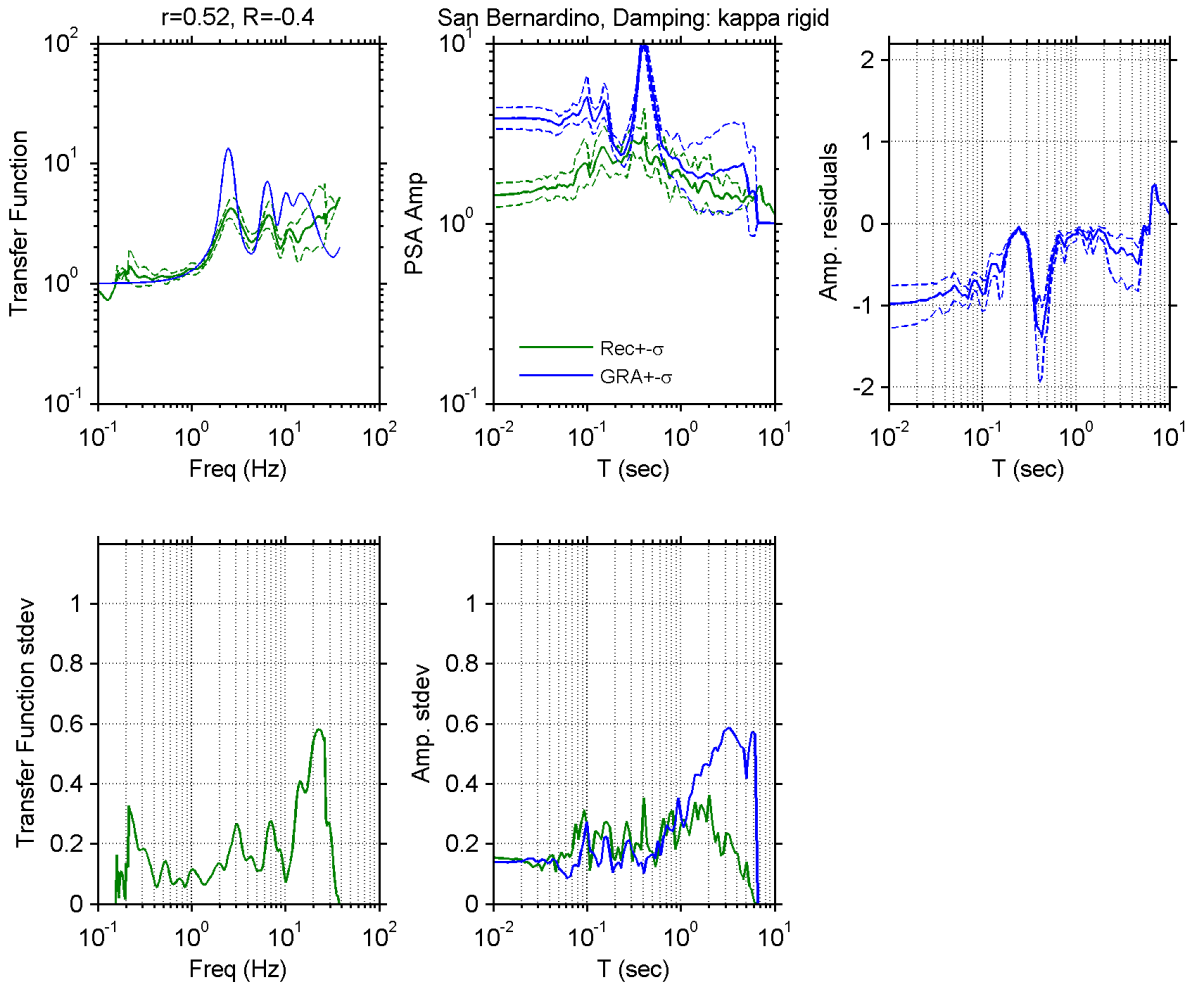

Figure A 52. Observed and simulated site response for San Bernardino site with κ-informed model for damping; Top left: Theoretical and median ± standard deviation of empirical transfer functions, Top middle: observed and predicted median ± standard deviation of *PS*A amplification, Top right: median ± standard deviation of *PS*A amplification residuals, Bottom left: standard deviation of empirical transfer functions, Bottom middle: standard deviation of observed and predicted *PS*A amplification residuals.

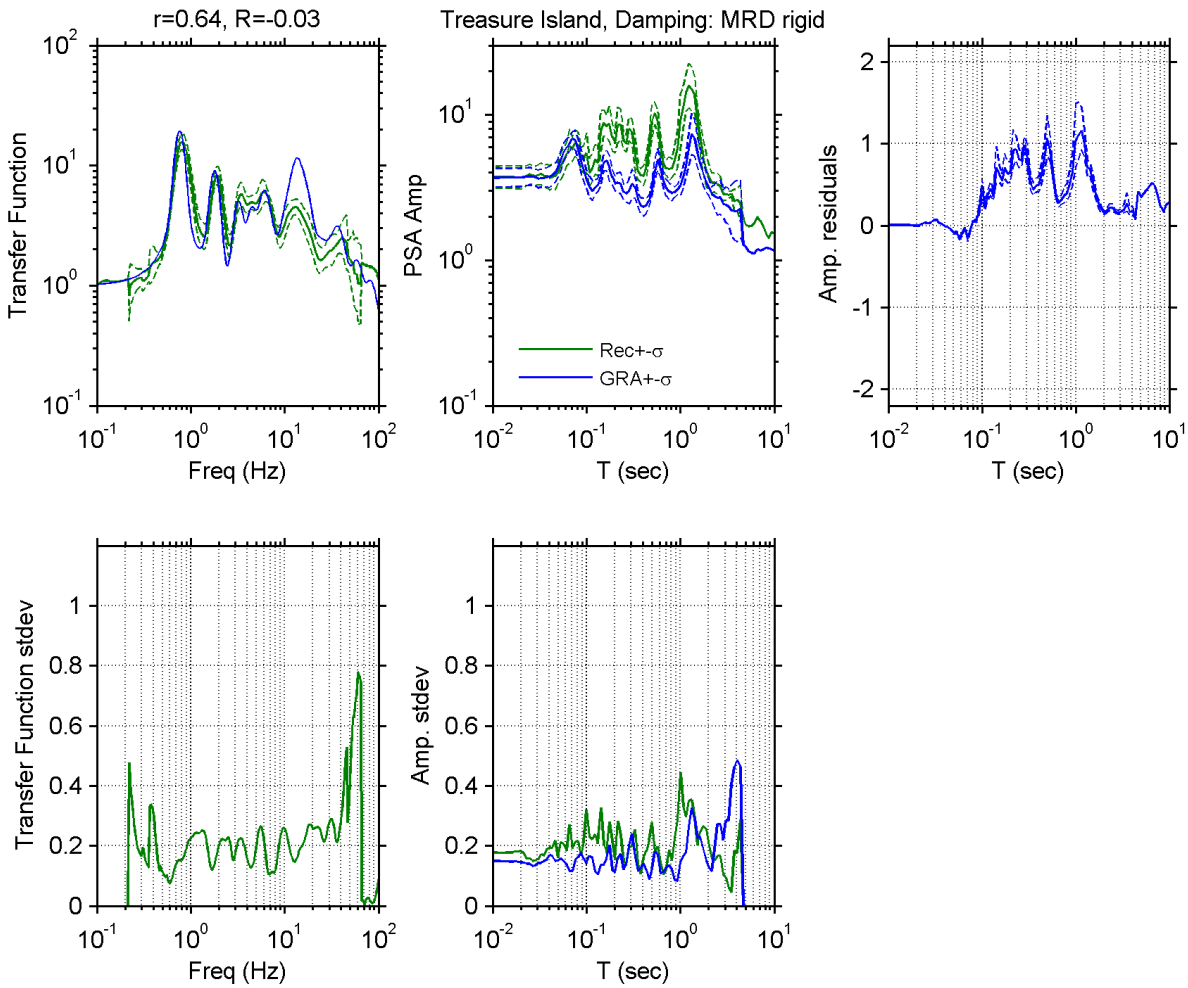

Figure A 53. Observed and simulated site response for Treasure Island site with $D_{\min}^{L}$ model for damping; Top left: Theoretical and median ± standard deviation of empirical transfer functions, Top middle: observed and predicted median ± standard deviation of *PS*A amplification, Top right: median ± standard deviation of *PS*A amplification residuals, Bottom left: standard deviation of empirical transfer functions, Bottom middle: standard deviation of observed and predicted *PS*A amplification residuals.

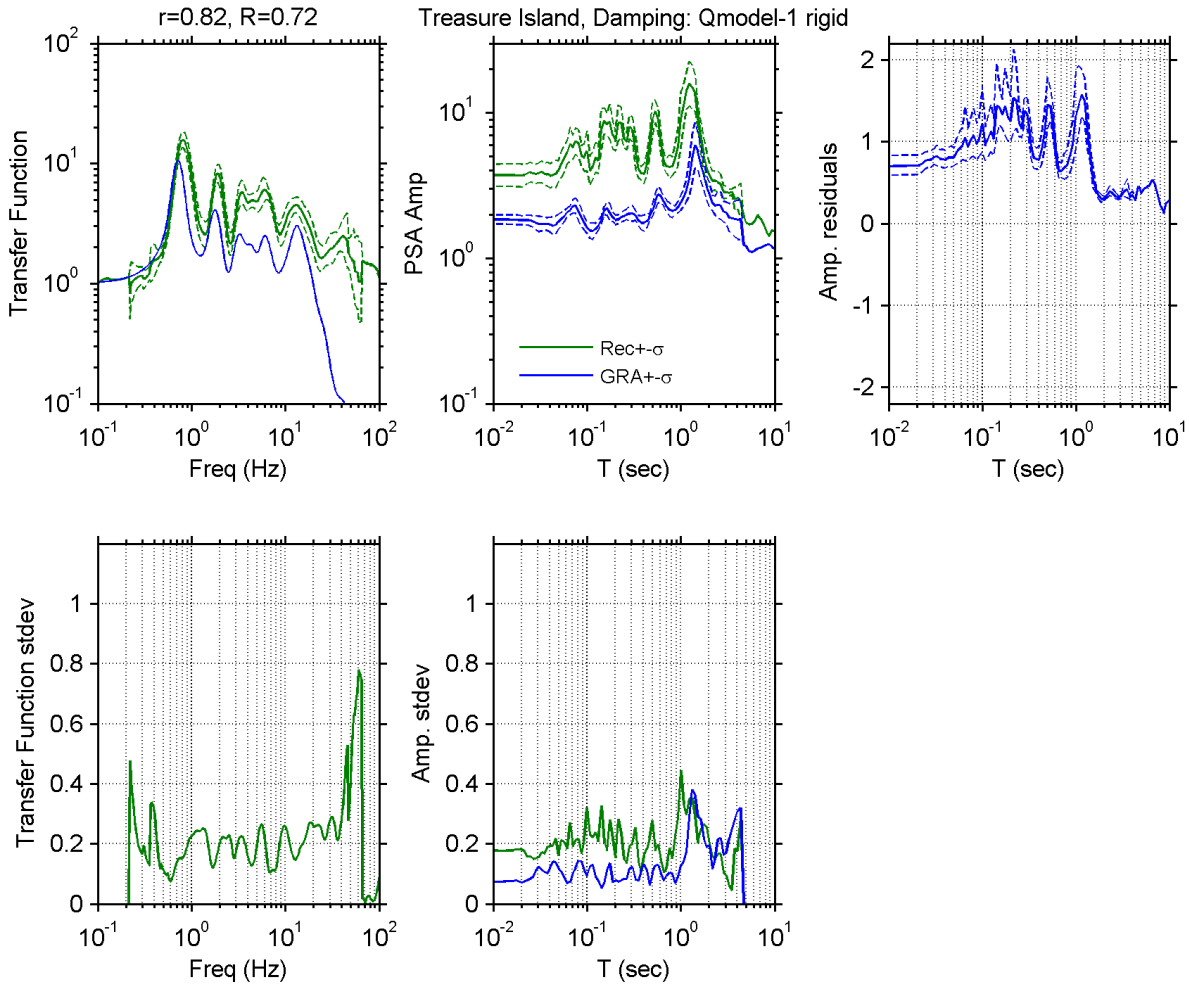

Figure A 54. Observed and simulated site response for Treasure Island site with V_S-based model for damping; Top left: Theoretical and median ± standard deviation of empirical transfer functions, Top middle: observed and predicted median ± standard deviation of *PS*A amplification, Top right: median ± standard deviation of *PS*A amplification residuals, Bottom left: standard deviation of empirical transfer functions, Bottom middle: standard deviation of observed and predicted *PS*A amplification residuals.

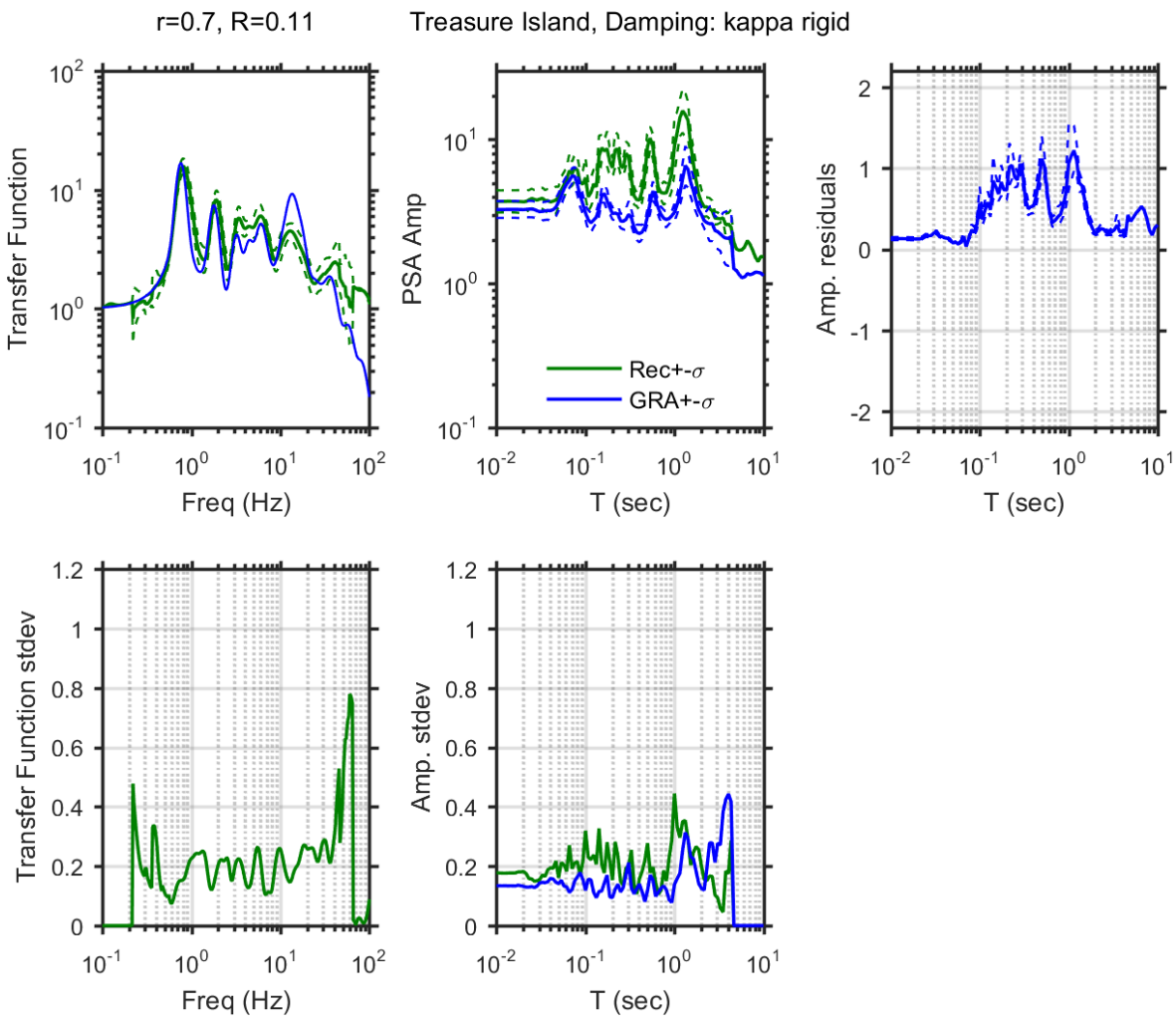

Figure A 55. Observed and simulated site response for Treasure Island site with κ-informed model for damping; Top left: Theoretical and median ± standard deviation of empirical transfer functions, Top middle: observed and predicted median ± standard deviation of *PS*A amplification, Top right: median ± standard deviation of *PS*A amplification residuals, Bottom left: standard deviation of empirical transfer functions, Bottom middle: standard deviation of observed and predicted *PS*A amplification residuals.

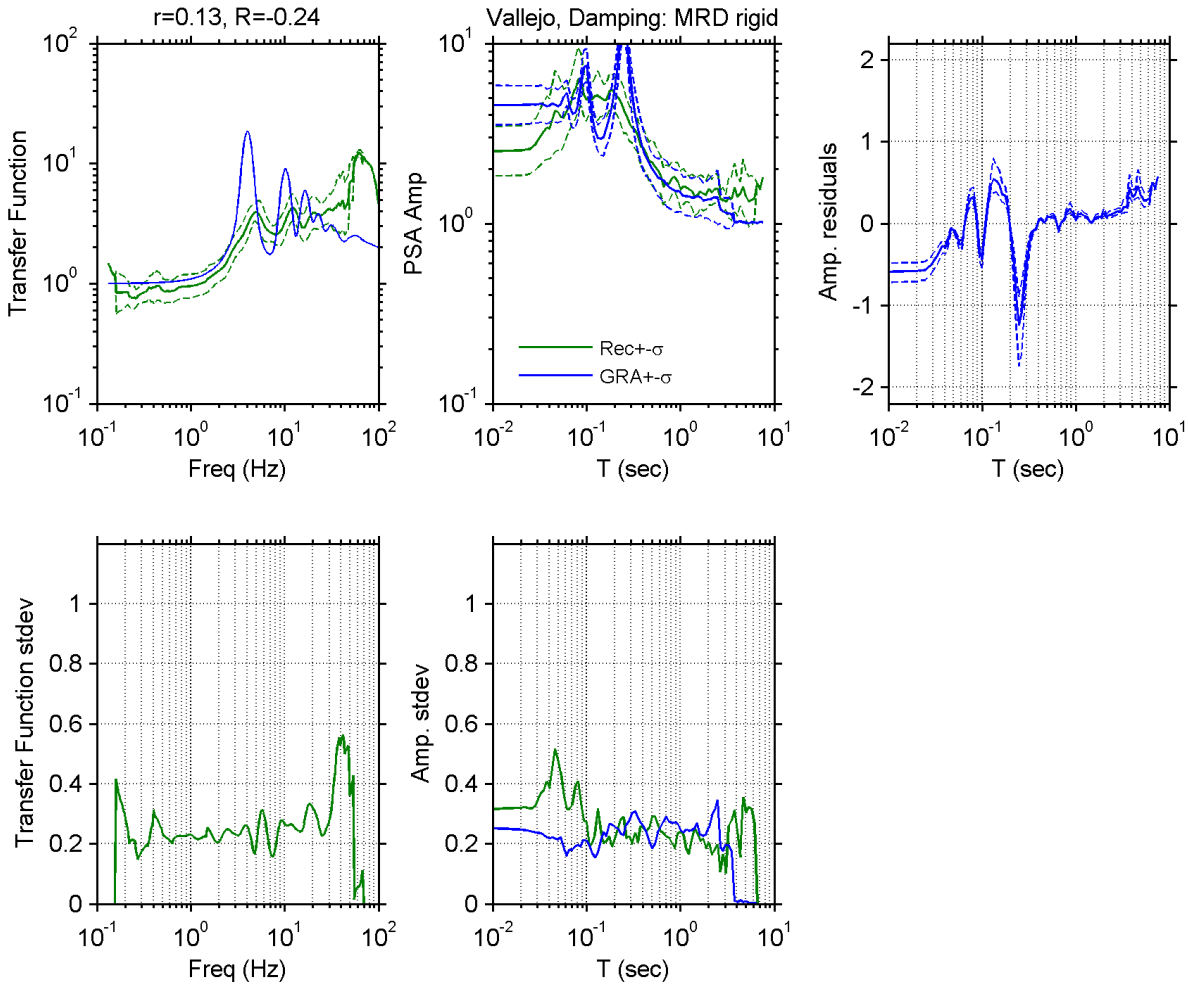

Figure A 56. Observed and simulated site response for Vallejo - Hwy 37/Napa River E site with $D_{\min}^{L}$ model for damping; Top left: Theoretical and median ± standard deviation of empirical transfer functions, Top middle: observed and predicted median ± standard deviation of *PS*A amplification, Top right: median ± standard deviation of *PS*A amplification residuals, Bottom left: standard deviation of empirical transfer functions, Bottom middle: standard deviation of observed and predicted *PS*A amplification residuals.

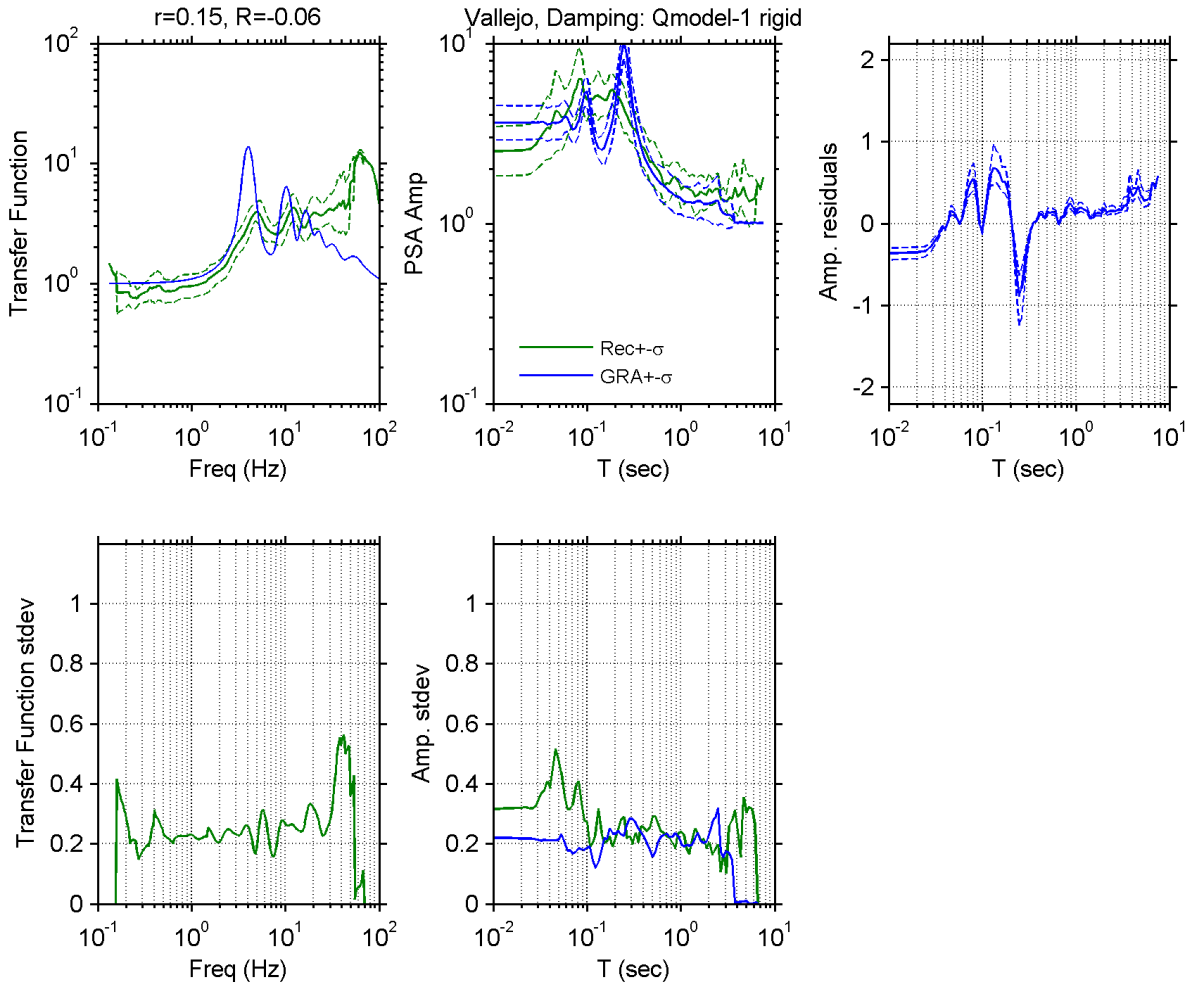

Figure A 57. Observed and simulated site response for Vallejo - Hwy 37/Napa River E site with V_S-based model for damping; Top left: Theoretical and median ± standard deviation of empirical transfer functions, Top middle: observed and predicted median ± standard deviation of *PS*A amplification, Top right: median ± standard deviation of *PS*A amplification residuals, Bottom left: standard deviation of empirical transfer functions, Bottom middle: standard deviation of observed and predicted *PS*A amplification residuals.

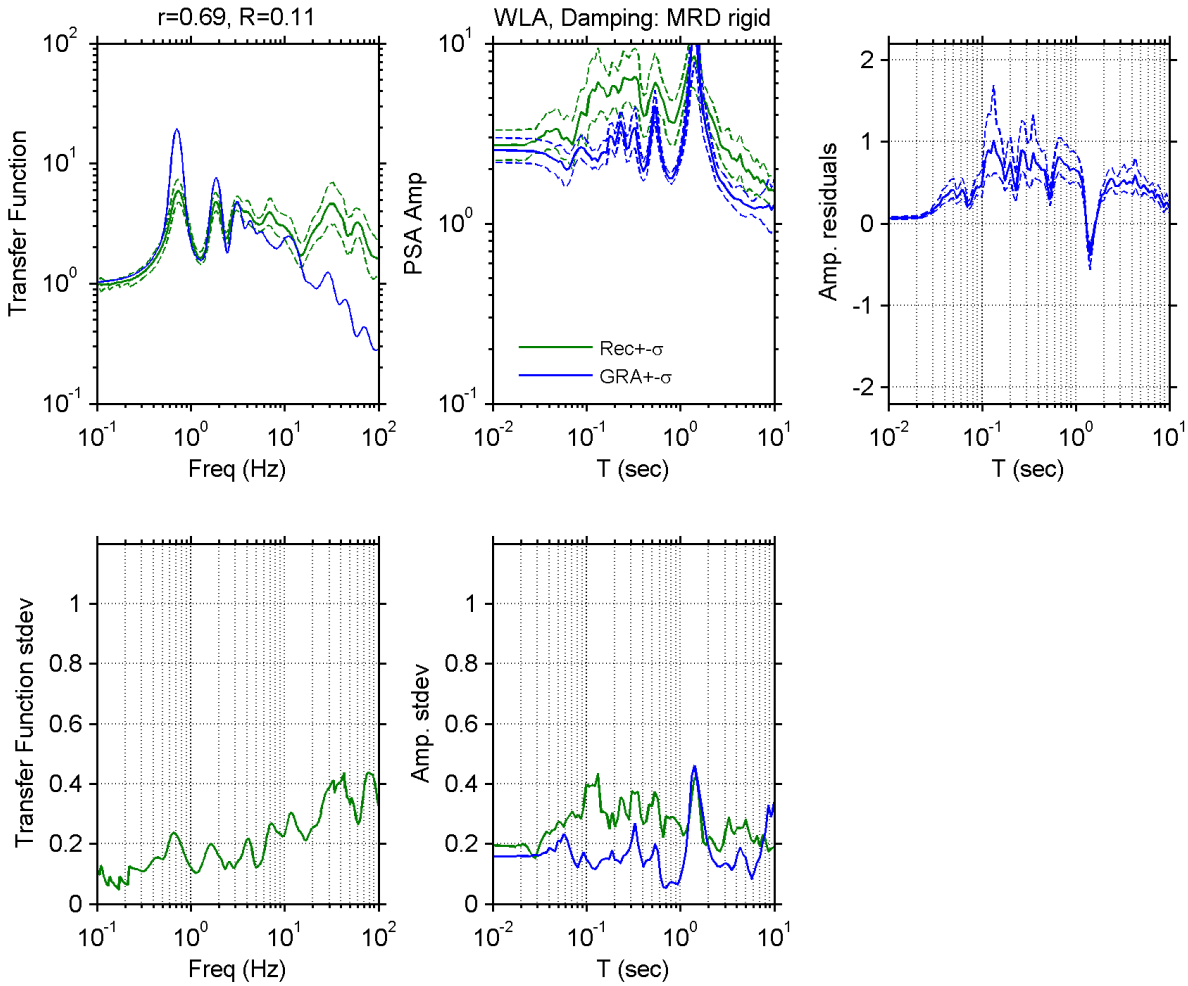

Figure A 58. Observed and simulated site response for Wildlife Liquefaction Array (WLA) site with $D_{\min}^{L}$ model for damping; Top left: Theoretical and median ± standard deviation of empirical transfer functions, Top middle: observed and predicted median ± standard deviation of *PS*A amplification, Top right: median ± standard deviation of *PS*A amplification residuals, Bottom left: standard deviation of empirical transfer functions, Bottom middle: standard deviation of observed and predicted *PS*A amplification residuals.

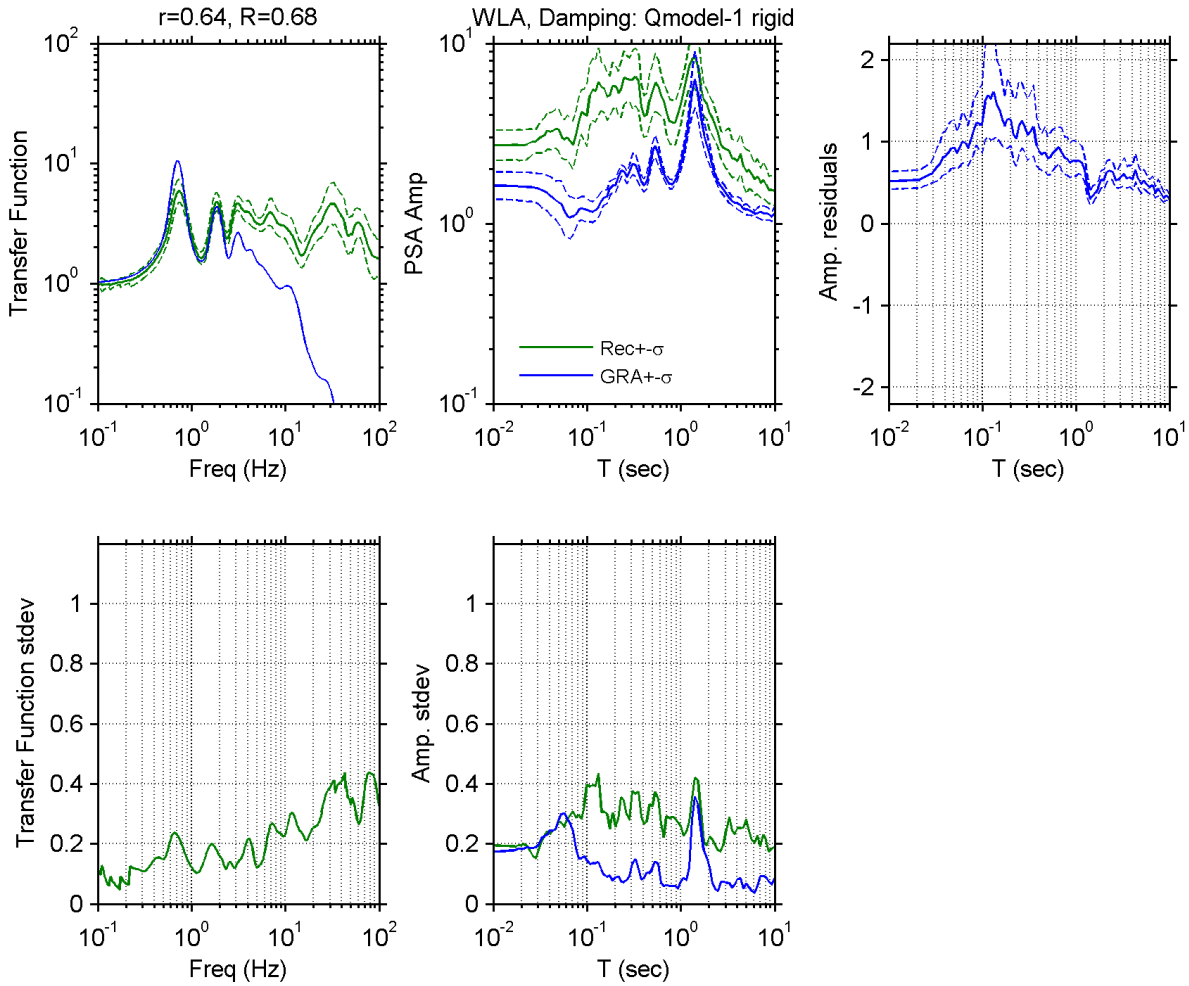

Figure A 59. Observed and simulated site response for Wildlife Liquefaction Array (WLA) site with V_S-based model for damping; Top left: Theoretical and median ± standard deviation of empirical transfer functions, Top middle: observed and predicted median ± standard deviation of *PS*A amplification, Top right: median ± standard deviation of *PS*A amplification residuals, Bottom left: standard deviation of empirical transfer functions, Bottom middle: standard deviation of observed and predicted *PS*A amplification residuals.

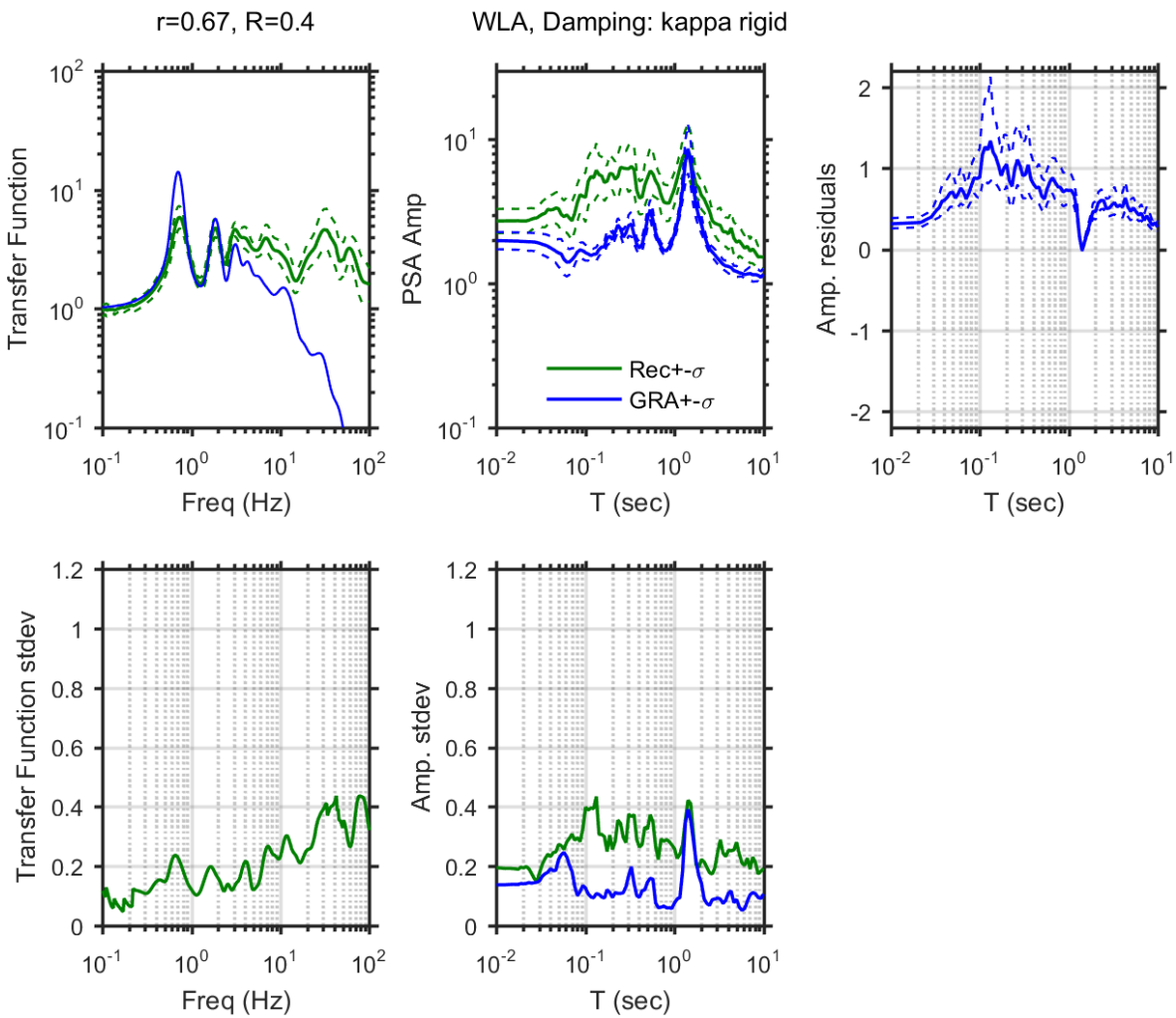

Figure A 60. Observed and simulated site response for Wildlife Liquefaction Array (WLA) site with κ-informed model for damping; Top left: Theoretical and median ± standard deviation of empirical transfer functions, Top middle: observed and predicted median ± standard deviation of *PS*A amplification, Top right: median ± standard deviation of *PS*A amplification residuals, Bottom left: standard deviation of empirical transfer functions, Bottom middle: standard deviation of observed and predicted *PS*A amplification residuals.

References

Abrahamson, N. A. and Bommer, J. J., 2005. Probability and uncertainty in seismic hazard analysis, *Earthquake Spectra*, **21**, 603–607.

Abrahamson, N. A., and Silva, W. J., 1996. Empirical Ground Motion Models, Report to Brookhaven National Laboratory.

Abrahamson, N. A., Silva, W. J., and Kamai, R., 2014. Summary of the ASK14 ground motion relation for active crustal regions, *Earthquake Spectra*, **30**, 1025–1055.

Abrahamson, N. A., and Youngs, R. R., 1992. A stable algorithm for regression analyses using the random effects model. *Bulletin of the Seismological Society of America*, **82,** 505–510.

Afshari, K. and Stewart, J. P., 2015a. Effectiveness of 1D ground response analyses at predicting site response at California vertical array sites, *Proc. SMIP2015 Seminar on Utilization of Strong Motion Data*, California Strong Motion Instrumentation Program, Sacramento, CA.

Afshari, K. and Stewart, J. P., 2015b. Uncertainty of site amplification derived from ground response analysis, *Proc. 6th Int. Conf. Earthquake Geotech. Eng.*, Christchurch, New Zealand, Paper No. 227.

Afshari, K. and Stewart, J. P., 2016. Physically parameterized prediction equations for significant duration in active crustal regions, *Earthquake Spectra*, **32**, 2057-2081.

Afshari, K. and Stewart, J. P., 2016. Validation of duration parameters from SCEC Broadband Platform simulated ground motions, *Seism. Res. Lett.* **86,** DOI: 10.1785/0220160086

Akkar, S., Sandıkkaya, M. A., Şenyurt, M., Azari Sisi, A., Ay, B. Ö., Traversa, P., Douglas, J., Cotton, F., Luzi, L., Hernandez, B., and Godey, S., 2014. Reference database for seismic ground-motion in Europe (RESORCE), *Bull. Earthquake Eng*. **12**, 311–339.

Al Atik, L. and Abrahamson, N. A., 2010. Nonlinear site response effects on the standard deviations of predicted ground motions, *Bull. Seismol. Soc. Am*., **100**, 1288–1292.

Al Atik, L., Abrahamson, N. A., Bommer, J. J., Scherbaum, F., Cotton, F., and Kuehn, N., 2010. The variability of ground motion prediction models and its components, *Seism. Res. Lett.*, **81** 794–801.

Allman, B., and Shearer, P., 2007. Spatial and temporal stress drop variations in small earthquakes near Parkfield, California. *J. Geophisical Res*. **112**, doi: 10.1029/2006JB004395.

Allman, B., and Shearer, P., 2009. Global variations of stress drop for moderate to large earthquakes, *J. Geophisical Res*. **114**, doi: 10.1029/2008JB005821.

Amir-Faryar, B., Aggour, M. S., and McCuen, R. S., 2016. Universal model forms for predicting the shear modulus and material damping of soils. *Geomechanics and Geoengineering*. 1-12. 10.1080/17486025.2016.1162332.

Ancheta, T. D., Darragh, R. B., Stewart, J. P., Seyhan, E., Silva, W. J., Chiou, B. S.-J., Wooddell, K. E., Kottke, A. R., Boore, D. M., Kishida, T., and Donahue, J. L., 2014. NGA-West2 database, *Earthquake Spectra* **30**, 989–1005.

Atkinson, G. M., and Assatourians, K., 2015. Implementation and validation of EXSIM (a stochastic finite-fault ground-motion simulation algorithm) on the SCEC Broadband Platform, *Seism. Res. Lett.* **86,** no. 1, 48–60.

Anderson, J. G., 1991. A preliminary descriptive model for the distance dependence of the spectral decay parameter in Southern California, *Bull. Seismol. Soc. Am*. 74, 1969-1993.

Anderson, J. G. and Brune, J. N., 1999. Probability seismic hazard analysis without the ergodic assumption, *Seismol. Res. Let*., **81**, 2186–2193.

Anderson, J. G., and Hough, S. E., 1984. A model for the shape of the Fourier amplitude spectrum of acceleration at high frequencies, *Bull. Seismol. Soc. Am*. **74**, 1969-1993.

Aoi, S. ,Obara, K., Hori, S., Kasahara, K., Okada, Y., 2000. New Japanese uphole–downhole strong-motion observation network: KiK-Net, Seismological Research Letters *Seism. Res. Lett.* 72:239.

Atkinson, G.M. and Beresnev, I., 1997. Don't call it stress drop, *Seism. Res. Letters* **68**, 3–4.

Atkinson, G. M., 2006. Single-station sigma, *Bull. Seism. Soc. Am.*, **96**, 446–455.

Baker, J. W. and Cornell, C. A., 2006. Which spectral acceleration are you using? *Earthquake Spectra*, **22**, 293–312.

Baker, J. W. and Jayaram, N., 2008. Correlation of spectral acceleration values from NGA ground motion models, *Earthquake Spectra*, **24**, 299–317.

Baturay, M. B. and Stewart, J. P., 2003. Uncertainty and bias in ground motion estimates from ground response analyses, *Bull. Seism. Soc. Am*., **93**, 2025-2042.

Bazzurro, P. and Cornell, C. A., 2004a. Nonlinear soil-site effects in probabilistic seismic-hazard analysis, *Bull. Seismol. Soc. Am*., **94**, 2110–2123.

Bazzurro, P. and Cornell, C. A., 2004b. Ground motion amplification in nonlinear soil sites with uncertain properties, *Bull. Seismol. Soc. Am*., **94**, 2090–2109.

Boore, D.M., 2003. Simulation of ground motion using the stochastic method, *Pure and Applied Geophysics*, **160**, 635-675.

Boore, D. M., 2005. SMSIM—Fortran programs for simulating ground motions from earthquakes: Version 2.3—A Revision of OFR 96- 80-A, *Open-File Rpt. 00-509*, U.S. Geological Survey, revised 15 August 2005, 55 pp.

Boore, D.M., 2008. Some thoughts on relating density to velocity <http://quake.wr.usgs.gov/boore/daves_notes/daves_notes_on_relating_density_to_velocity_v1.2.pdf>

Boore, D. M., 2010. Orientation-independent, nongeometric-mean measures of seismic intensity from two horizontal components of motion, *Bull. Seismol. Soc. Am*., **100**, 1830–1835.

Boore, D. M., 2013. The uses and limitations of the square-root-impedance method for computing site amplication. *Bull. Seismol. Soc. Am*. **103**, 2356-2368.

Boore, D. M. and Bommer, J. J., 2005. Processing of strong-motion accelerograms: needs, options and consequences, *Soil Dyn. Eqk. Eng.*, **25**, 93–115.

Boore, D. M., and W. B. Joyner, 1991. Estimation of ground motion at deep-soil sites in eastern North America, *Bull. Seismol. Soc. Am.* **81**, 2167–2185.

Boore, D. M., Stewart, J. P., Seyhan, E., and Atkinson, G. M, 2014. NGA-West 2 equations for predicting PGA, PGV, and 5%-damped PSA for shallow crustal earthquakes, *Earthquake Spectra*, **30**, 1057–1085.

Boore, D. M., Stewart, J. P., Seyhan, E., and Atkinson, G. M., 2013. *NGA-West2 Equations for Predicting Response Spectral Accelerations for Shallow Crustal Earthquakes*, PEER Report No. 2013/05, Pacific Earthquake Engineering Research Center, UC Berkeley, CA.

Boore, D. M., Thompson, E. M, and Cadet, H., 2011. Regional correlations of V_{S30} and velocities averaged over depths less than and greater than 30 m, *Bull. Seism. Soc. Am*. 101, 3046-3059.

Boore, D. M., and Thompson, E. M., 2014. Path durations for use in the stochastic-method simulation of ground motions, *Bull. Seism. Soc. Am.* **104**, 2541–2552.

Bommer, J. J. and Scherbaum, F., 2008. The use and misuse of logic trees in probabilistic seismic hazard analysis. *Earthquake Spectra*, **24**, 997–1009.

Bommer, J. J., Stafford, P. J, and Alarcón, J. E., 2009. Empirical equations for the prediction of the significant, Bracketed, and uniform duration of earthquake ground motion, *Bull. Seism. Soc. Am.* **99**, 3217–3233.

Bommer, J. J., Coppersmith, K. J., Coppersmith, R. T., Hanson, K. L., Mangongolo, A., Neveling, J., Rathje, E.M, Rodriguez-Marek, A., Scherbaum, F., Shelembe, R., Stafford, P. J., and

Strasser, F. O., 2015. A SSHAC Level 3 probabilistic seismic hazard analysis for a new-build nuclear site in South Africa. *Earthquake Spectra*, **31**, 661–698.

Bora, S. S., Scherbaum, F., Kuehn, N., and Stafford, P., 2014. Fourier spectral- and duration models for the generation of response spectra adjustable to different source-, propagation-, and site conditions, *Bull. Earthquake Eng*. **12**, 467–493.

Borja, R. I., Chao, H.-Y., Montans, F. J., and Lin, C.-H., 1999. Nonlinear ground response at Lotung LSST site, *J. Geotech. Geoenviron. Eng.*, **125**, 187–197.

Bozorgnia, Y., Abrahamson, N. A., Al Atik, L., Ancheta, T. D., Atkinson, G. M., Baker, J. W., Baltay, A., Boore, D. M., Campbell, K. W., Chiou, B. S.-J., Darragh, R., Day, S., Donahue, J., Graves, R. W., Gregor, N., Hanks, T., Idriss, I. M., Kamai, R., Kishida, T., Kottke, A., Mahin, S. A., Rezaeian, S., Rowshandel, B., Seyhan, E., Shahi, S., Shantz, T., Silva, W., Spudich, P., Stewart, J. P., Watson-Lamprey, J., Wooddell, K., and Youngs, R., 2014. NGA-West2 research project, *Earthquake Spectra*, **30**, 973–987.

Bradley, B. A., 2011. Correlation of significant duration with amplitude and cumulative intensity measures and its use in ground motion selection, *J. Earthquake Eng.*, **15**, 809–832.

Bradley, B. A., 2015. Systematic ground motion observations in the Canterbury Earthquakes and region-specific non-ergodic empirical ground motion modeling, *Earthquake Spectra*, **31,** 1735-1761.

Bray, J. D., Rathje, E. R., 1998. Earthquake-induced displacements of solid-waste landfills. *J. Geotech. & Geoenviron. Eng.* **124**, 242–253.

Brune, J. N., 1970. Tectonic stress and the spectra of seismic shear waves from earthquakes, *J. Geophys. Res.* **75**, 4997–5009.

Brune, J. N., 1971. Seismic sources, fault plane studies and tectonics; *EOS*. **52**, 178–187.

Burks, L. S., and Baker, J. W., 2014. Validation of ground-motion simulations through simple proxies for the response of engineered systems, *Bull. Seismol. Soc. Am.* **104,** no. 4, 1930-1946.

Campbell, K.W., 2009. Estimates of shear-wave Q and κ_0 for unconsolidated and semiconsolidated sediments in Eastern North America, *Bull. Seismol. Soc. Am*. 99, 2365-2392.

Campbell, K. W. and Bozorgnia, Y., 2014. NGA-West2 ground motion model for the average horizontal components of PGA, PGV, and 5% damped linear acceleration response spectra, *Earthquake Spectra*, **30**, 1087–1115.

Chavez-Garcia, F. J., Raptakis, D., Makra, K., Pitilakis, K., 2000. Site effects at Euroseistest—II. Results from 2D numerical modeling and comparison with observations, *Soil Dyn & Earthquake Eng*, **19**, 23–39.

Chandramohan, R., Baker, J. W., and Deierlein, G. G., 2015. Quantifying the influence of ground motion duration on structural collapse capacity using spectrally equivalent records. *Earthquake Spectra*, **32**, 927–950.

Chiou, B. S.-J., Darragh R. B., Gregor N., and Silva W. J., 2008. NGA project strong-motion database, *Earthquake Spectra* **24**, 23–44.

Chiou, B. S.-J. and Youngs, R. R., 2014. Update of the Chiou and Youngs NGA model for the average horizontal component of peak ground motion and response spectra, *Earthquake Spectra*, **30**, 1117–1153.

Cook, R. D., and Weisberg S., 1999. *Applied Regression Including Computing and Graphics*, Wiley & Sons, Hoboken, NJ.

Coppersmith, K., Bommer, J., Hanson, K., Coppersmith, R., Unruh, J., Wolf, L, Youngs, B., Al Atik, L, Rodriguez-Marek, A., Toro, G., 2014. Hanford Sitewide Probabilistic Seismic Hazard Analysis, Prepared for the U.S. Department of Energy Under Contract DE-AC06076RL01830, and Energy Northwest, Pacific Northwest National Lab Report PNNL-23361, November.

Cramer, C. H., 2003. Site-specific seismic-hazard analysis that is completely probabilistic, *Bull. Seismol. Soc. Am.*, **93**, 1841–1846.

Cramer, C. H., Gomberg, J. S., Schweig, J. S., Waldron, B. A., and Tucker, K., 2004. The Memphis, Shelby Country, Tennessee, seismic hazard maps, *U.S. Geol. Surv.* Open-File Rept. 04-1294.

Crempien, G. J. F., and Archuleta, R. J., 2015. UCSB Method for simulation of broadband ground motion from kinematic earthquake sources, *Seism. Res. Lett.* **86,** no. 1, 61–67.

Darendeli, M. B., 2001. Development of a New Family of Normalized modulus reduction and material damping curves, PhD Thesis, Department of Civil Engineering, University of Texas, Austin, TX.

Dawood, H., Rodriguez-Marek, A., Bayless, J., and Thompson, E. M., 2015. A Flatfile for the KiK-net Database Processed Using an Automated Protocol, *Earthquake Spectra*, **32**, 1281-1302.

De Martin, F., Matsushima, S., Kawase, H., 2013. Impact of geometric effects on near-surface Green's functions, *Bull. Seismol. Soc. Am.*, **6**, 3289-3304

Dreger, D. S., Beroza, G. C., Day, S. M., Goulet, C. A., Jordan, T. H., Spudich, T. H., and Stewart, J. P., 2015. Validation of the SCEC broadband platform V14.3 simulation methods using pseudospectral acceleration data, *Seism. Res. Lett.* **86,** no.1, 39–47.

Du, W., and Wang, G., 2016. Prediction equations for ground motion significant durations using the NGA-West2 database, *Bull. Seismol. Soc. Am.*, **107**, 319-333.

Elgamal, A., Lai, T., Yang, Z., He, L., 2001. Dynamic soil properties, seismic downhole arrays and applications in practice, *Proceedings, 4th International Conference on Recent Advances in Geotechnical Earthquake Engineering and Soil Dynamics*, S. Prakash, ed., San Diego, CA.

Everitt, B. S., 2002. *The Cambridge Dictionary of Statistics*, CUP ISBN 0-521-81099-X

Field, E. H., Jordan, T. H., and Cornell, C. A., 2003. OpenSHA: A Developing Community-Modeling Environment for Seismic Hazard Analysis, *Seismol. Res. Lett.*, **74**, 406–419.

Field, E. H., Arrowsmith, R. J., Biasi, G. P., Bird, P., Dawson, T. E., Felzer, K. R., Jackson, D. D., Johnson, K. M., Jordan, T. H., Madden, C., Michael, A. J., Milner, K. R., Page, M. T., Parsons, T., Powers, P. M, Shaw, B. E., Thatcher, W. R., Weldon, R. J., and Zeng, Y., 2014. Uniform California earthquake rupture forecast, version 3 (UCERF3): The time-independent model, *Bull. Seismol. Soc. Am*. **104**, 1122–1180.

Frankel, A., D., Stephenson, W., J., Carver, D., L., Williams, R., A., Odum, J., K., and Rhea, S., 2007. Seismic hazard maps for Seattle, Washington, incorporating 3D sedimentary basin effects, nonlinear site response, and rupture directivity: USGS Open-File Report 2007–1175, 77p.

Galasso, C., Zhong, P., Zareian, F., Iervolino, I, and Graves, R. W., 2013. Validation of ground-motion simulations for historical events using MDoF systems, *Earthquake Engng Struct. Dyn*. **42,** no.2, 1395–1495.

Gelman, A., Carlin, J. B., Stern, H. S., Dunson, D. B., Vehtari, A., and Rubin, D. B., 2014. *Bayesian Data Analysis*, 3rd edition, CRC Press.

GeoPentech, 2015. Southwestern United States ground motion characterization SSHAC level 3 – *technical report rev. 2*, March 2015.

Gomberg, J., Waldron, B., Schweig, E., Hwang, H., Webbers, A., Van Arsdale, R., Tucker, K., Williams, R., Street, R., Mayne, P., Stephenson, W., Odum, J., Cramer, C., Updike, R., Hutson, S., and Bradley, M., 2003. Lithology and shear-wave velocity in Memphis, Tennessee, *Bull. Seismol. Soc. Am*. **93**, 986–997.

Goulet, C. A., 2008. Improving the characterization of seismic hazard for performance-based earthquake engineering design, PhD Thesis, Department of Civil Engineering, University of California, Los Angeles.

Goulet, C. A. and Stewart, J. P., 2009. Pitfalls of deterministic application of nonlinear site factors in probabilistic assessment of ground motions, *Earthquake Spectra*, **25**, 541–555.

Goulet, C. A., Abrahamson, N. A., Somerville, P. G., and Wooddell, K. E., 2015. The SCEC Broadband Platform validation exercise: methodology for code validation in the context of seismic-hazard analyses, *Seism. Res. Lett.* **86,** no. 1, 17–26.

Graves, R. W., Jordan, T. H., Callaghan, T. H., Deelman, E., Field, E., Juve, G., Kesselman, C., Maechling, P., Mehta, G., Milner, K., Okaya, D., Small, P., and Vahi, K., 2010. CyberShake: A Physics-Based Seismic Hazard Model for Southern California, *Pure and Applied Geophysics*, **168,** 367–381.

Graves, R. W., and Pitarka, A., 2010. Broadband ground-motion simulation using a hybrid approach, *Bull. Seismol. Soc. Am.* **100,** no. 5A, 2095–2123.

Graves, R. W., and Pitarka, A., 2015. Refinements to the Graves and Pitarka (2010) Broadband ground-motion simulation method, *Seism. Res. Lett.* **86,** no. 1, 75–80.

Hancock, J., and Bommer, J. J., 2007. Using spectral matched records to explore the influence of strong-motion duration on inelastic structural response, *Soil Dyn. Earthquake Eng.* **27**, 291–299.

Hanks, T. C., and Kanamori, H., 1979. A moment magnitude scale, *J. Geophys. Res*. **84**, 2348–2350.

Hanks, T. C., and McGuire, R. K., 1981. The Character of High-frequency Strong Ground Motion, *Bull. Seismol. Soc. Am.* **71**, 2071–2095.

Hough, S. E., and Anderson, J. G., 1988. High-frequency spectra observed at Anza, California: Implications of *Q* structure, *Bull. Seismol. Soc. Am*. 78, 692-707.

Hashash, Y. M. A., Kottke, A. R., Stewart, J. P., Campbell, K. W., Kim, B., Moss, C., Nikolaou, S., Rathje, E. M., Silva, W. J., 2014. Reference rock site condition for central and eastern North America, *Bull. Seismol. Soc. Am*., **104**, 684-701.

Hashash, Y. M. A., Musgrove, M. I., Harmon, J. A., Groholski, D. R., Phillips, C. A., and Park, D., 2016. DEEPSOIL 6.1, User Manual.

Jayaram, N., and Baker, J. W., 2009. Correlation model for spatially distributed ground-motion intensities, *Earthquake Engng Struct. Dyn*, **38**, 1687–1708.

Joyner, W. B., Warrick, R. E., Fumal, T. E. (1981). The effect of Quaternary alluvium on strong ground motion in the Coyote Lake, California, earthquake of 1979, *Bull. Seismol. Soc. Am*., **71**, 1333-1349.

Kaklamanos, J., Bradley, B. A., Thompson, E. M., and Baise, L. G., 2013. Critical parameters affecting bias and variability in site-response analyses using KiK-net downhole array data, *Bull. Seismol. Soc. Am*., **103**, 1733–1749.

Kaklamanos, J., Baise, L. G., Thompson, E. M., and Dorfmann, L., 2014. Comparison of 1D linear, equivalent-linear, and nonlinear site response models at six KiK-net validation sites, *Soil Dyn. Eqk. Eng.*, **69**, 435–460.

Kaklamanos, J., Baise, L. G., Thompson, E. M., Dorfmann, L., 2015. Comparison of 1D linear, equivalent-linear, and nonlinear site response models at six KiK-net validation sites, *Soil Dyn. Earthq. Eng.* 69, 207-215.

Kaklamanos, J., Bradley, B. A., Thompson, E. M., and Baise, L. G., 2013. Critical parameters affecting bias and variability in site-response analyses using KiK-net downhole array data, *Bull. Seismol. Soc. Am*. 103, 1733–1749.

Kempton, J. J., and Stewart, J. P., 2006. Prediction equations for significant duration of earthquake ground motions considering site and near-source effects, *Earthquake Spectra* **22**, 985–1013.

Kim, B., and Hashash, Y. M. A., 2013. Site response analysis using downhole array recordings during the March 2011 Tohoku-Oki Earthquake and the effect of long-duration ground motions." *Earthquake Spectra* **29**, S37–S54.

Kim, B., Hashash, Y. M. A., Stewart, J. P., Rathje, E. M., Harmon, J. A., Musgrove, M. I., Campbell, K. W, and Silva, W. J., 2015. Relative differences between nonlinear and equivalent-linear 1D site response analyses, *Earthquake Spectra*, **32**, 1845-1865.

Kotha, S.R., D. Bindi, and F. Cotton, 2016. Partially non-ergodic region specific GMM for Europe and Middle-East, *Bull. Earthq. Eng.*, **14**, 1245-1263.

Kwok, A. O. L., Stewart, J. P., Hashash, Y. M. A, 2008. Nonlinear ground-response analysis of Turkey Flat shallow stiff-soil site to strong ground motion, *Bull. Seismol. Soc. Am.*, **98**, 331–343.

Landwehr, N., Kuehn, N. M., Scheffer, T., and Abrahamson, N.A., 2016. A nonergodic ground-motion model for California with spatially varying coefficients. *Bull. Seismol. Soc. Am.*, **106**, 2574-2583.

Lee, J., and Green, R. A., 2014. An empirical significant duration relationship for stable continental regions, *Bull. Earthquake Eng*. **12**, 217–235.

Lee, C.-P., Tsai, Y.-B., and Wen, K. L., 2006. Analysis of nonlinear site response using the LSST downhole accelerometer array data, *Soil Dyn. Eqk. Eng.*, **26**, 435–460.

Li, W. and Assimaki, D., 2011. Site and motion-dependent parametric uncertainty of site-response analyses in earthquake simulations, *Bull. Seismol. Soc. Am*., **100**, 954–968.

Li X.-S., Wang Z.-L., Shen C-.K. (1992). *SUMDES: A Nonlinear Procedure for Response Analysis of Horizontally-Layered Sites Subjected to Multi-Directional Earthquake Loading*, Department of Civil Engineering, University of California, Davis, CA.

Lin P.-S., Chiou, B. S.-J, Abrahamson, N. A., Walling, M., Lee, C.-T., and Cheng, C.-T., 2011. Repeatable source, site, and path effects on the standard deviation for ground-motion prediction, *Bull. Seismol. Soc. Am*. **101**, 2281–2295.

Matasovic, N., 2006. *D-MOD_2: A Computer Program for Seismic Response Analysis of Horizontally Layered Soil Deposits, Earthfill Dams, and Solid Waste Landfills, User's Manual*, GeoMotions, LLC, Lacey, Washington.

McGuire, R. K., Silva, W. J., and Costantino, C. J., 2001. Technical basis for revision of regulatory guidance on design ground motions: Hazard-and risk-consistent ground motion spectra guidelines. *NUREG/CR-6728*, United States NRC.

McKenna F., Fenves G. L., 2001. *The OpenSees Command Language Manual, Version 1.2*., Pacific Earthquake Engineering Research Center, University of California, Berkeley, CA.

Menq, F. Y., 2003. Dynamic Properties of Sandy and Gravelly Soils, PhD Thesis, Department of Civil Engineering, University of Texas, Austin, TX.

Mikami, M., Stewart, J. P., Kamiyama, M., 2008. Effects of time series analysis protocols on transfer functions calculated from earthquake accelerograms, *Soil Dyn. Earthquake Eng*. 28, 695-706.

Montgomery, D. C. and Runger, G. C., 2005. Applied statistics and probability for engineers, 6th edition, *John Wiley & Sons, Inc*., Hoboken, New Jersey.

NCHRP, 2012. *Practices and Procedures for Site-Specific Evaluations of Earthquake Ground Motions, Synthesis 428* (N Matasovic and YMA Hashash), National Cooperative Highway Research Program, Transportation Research Board, Washington D.C.

Ktenidou, O-J., Cotton, F., Abrahamson, N. A., and Anderson, J. G., 2014. Taxonomy of κ: A review of definitions and estimation approaches targeted to applications. *Seismological Research Letters* **85**, 135-146.

Olsen, K., Day, S., Bradley, C., 2003. Estimation of Q for long-period (> 2 sec) waves in the Los Angeles basin. *Bull. Seismol. Soc. Am.* **93**, 627–638.

Olsen, K., and Takedatsu, R., 2015. The SDSU broadband ground-motion generation module BBtoolbox version 1.5, *Seism. Res. Lett.* **86,** no. 1, 81–88.

Papaspiliou, M., Kontoe, S., and Bommer, J. J., 2012. An exploration of incorporating site response into PSHA-Part II: Sensitivity of hazard estimates to site response approaches. *Soil Dyn & Earthquake Eng*, **42**, 316–330.

Pearson, K., 1900. On the criterion that a given system of deviations from the probable in the case of a correlated system of variables is such that it can be reasonably supposed to have arisen from random sampling, *Philosophical Magazine* **50,** 157–175. doi:10.1080/14786440009463897.

Pinheiro, H., Bates, D., DebRoy, S., Sarkar, D., and the R Development Core Team, 2013. NLME: Linear and Nonlinear Mixed Effects Models, R package version 3.1-108.

Pousse, G., 2005. Analyse des données accélérométriques de K-net et KiK-net implicationspour la prédiction du mouvement sismique‘accélérogrammes et spectres de réponse’et laprise en compte des effets de site non linéaires, Ph.D. Thesis, Université Joseph Fourier,France.

(15) A Flatfile for the KiK-net Database Processed Using an Automated Protocol. Available from: https://www.researchgate.net/publication/283867433_A_Flatfile_for_the_KiK-net_Database_Processed_Using_an_Automated_Protocol [accessed Sep 15, 2017].

Raghunandan, M., and Liel, A. B., 2013. Effect of ground motion duration on earthquake-induced structural collapse, *Structural Safety* **41**, 119–133

Raptakis, D., Chavez-Garcia, F. J., Makra, K., Pitilakis, K., 2000. Site effects at Euroseistest—I. Determination of the valley structure and confrontation of observations with 1D analysis, *Soil Dyn & Earthquake Eng*, **19**, 1–22.

Rathje, E. M., Kottke, A. R., and Trent, W. L., 2010. Influence of input motion and site property variabilities on seismic site response analysis, *J. Geotech. Geoenv. Eng.*, **136**, 607–619.

Rathje, E. M., Pehlivan, M., Gilbert, R., and Rodriguez-Marek, A., 2015. Incorporating site response into seismic hazard assessments for critical facilities: A probabilistic approach. In *Perspectives on Earthquake Geotechnical Engineering*. Springer International Publishing, 93–111.

Rauch, A. F., and Martin, J. R., 2000. EPOLLS model for predicting average displacements on lateral spreads, *J. Geotech. Eng*. **126**, 360–371.

Renault, P., S. Heuberger, and N. A. Abrahamson, 2010. PEGASOS Refinement Project: An improved PSHA for Swiss nuclear power plants, *Proc. 14th European Conference of Earthq. Engin.*, Ohrid, Republic of Macedonia, 30 August–3 September 2010, Paper ID 991.

Rezaeian, S., Bozorgnia, Y., Idriss, I. M., Abrahamson, N., Campbell, K., and Silva, W., 2014a. Damping scaling factors for elastic response spectra for shallow crustal earthquakes in active tectonic regions ”Average” horizontal component, *Earthquake Spectra* **30**, 939–963.

Rezaeian, S., Bozorgnia, Y., Idriss, I. M., Abrahamson, N., Campbell, K., and Silva, W., 2014b. Damping scaling factors for vertical elastic response spectra for shallow crustal earthquakes in active tectonic regions, *Earthquake Spectra* **30**, 1335–1358.

Rezaeian, S., Zhong, P., Hartzell, S., and Zareian, F, 2015. Validation of simulated earthquake ground motions based on evolution of intensity and frequency content, *Bull. Seismol. Soc. Am.* **105,** no. 6, 3036–3049.

Rodriguez-Marek, A., Montalva, G. A., Cotton, F., and Bonilla, F., 2011, Analysis of single-station standard deviation using the KiK-net data, *Bull. Seismol. Soc. Am*. **101**, 1242–1258.

Rodriguez-Marek, A., Cotton, F., Abrahamson, N. A., Akkar, S., Al Atik, L., Edwards, B., Montalva, G. A., and Dawood, H. M., 2013. A model for single-station standard deviation using data from various tectonic regions, *Bull. Seismol. Soc. Am*. **103**, 3149–3163.

Rodriguez-Marek, A., Rathje, E. M., Bommer, J. J., Scherbaum, F., and Stafford, P. J., 2014. Application of single-station sigma and site response characterization in a probabilistic seismic hazard analysis for a new nuclear site, *Bull. Seismol. Soc. Am*., **104**, 1601-1619.

Seyhan, E. and Stewart, J. P., 2014. Semi-empirical nonlinear site amplification from NGA-West2 data and simulations, *Earthquake Spectra* **30**, 1241–1256.

Seyhan, E., Stewart, J. P., Ancheta, T. D., Darragh, R. B., and Graves, R. W., 2014. NGA-West 2 site database, *Earthquake Spectra,* **30**, 1007–1024.

Shahi, S. K. and Baker, J.W., 2014. NGA-West2 models for ground motion directionality, *Earthquake Spectra,* **30**, 1285–1300.

Small, P., Gill, D., Maechling, P. J., Taborda, R., Callaghan, S., Jordan, T. H., Ely, G. P., Olsen, K. B., and Goulet, C. A., 2017. The SCEC Unified Community Velocity Model Software Framework. *Seismological Research Letters*. **88**, 1469–1478.

Stafford, P. J, 2012 Evaluation of structural performance in the immediate aftermath of an earthquake: a case study of the 2011 Christchurch earthquake, *Int. J. Forensic Engineering*, **1**, 58–77.

Stafford, P. J., Mendis R., and Bommer, J. J., 2008. The dependence of spectral damping ratios on duration and number of cycles. *J. Structural Eng.* **134**, 1364–1373.

Stafford, P. J., 2012. Evaluation of structural performance in the immediate aftermath of an earthquake: A case study of the 2011 Christchurch earthquake, *Int. J. Forensic Engrg.*, **1**, 58-77.

Star, L. M., Stewart, J. P., and Graves, R. W., 2011. Comparison of ground motions from hybrid simulations to NGA prediction equations, *Earthquake Spectra* **27,** no. 2, 331–350.

Stewart, J.P., Afshari, K., and Hashash, Y. M. A., 2014. Guidelines for performing hazard-consistent one-dimensional ground response analysis for ground motion prediction, *PEER Report No. 2014/16*, Pacific Earthquake Engineering Research Center, UC Berkeley, CA.

Stewart, J.P., Afshari, K., and Goulet, C. A., 2017. Non-Ergodic site response in seismic hazard analysis, *Earthquake Spectra***,** doi:10.1193/081716EQS135M

Thompson, E. M., Baise, L. G., Tanaka, Y., and Kayen, R. E., 2012. A taxonomy of site response complexity, *Soil Dyn. Earthq. Eng.*, **41**, 32–43.

Toro, G. R., 1995. Probabilistic models of site velocity profiles for generic and site-specific ground-motion amplification studies, *Technical Report No. 779574*, Brookhaven National Laboratory, Upton, NY.

Trifunac, M. D., and Brady, A. G., 1975. A study on duration of strong earthquake ground motion, *Bull. Seismol. Soc. Am*. **65**, 581–626.

Tsai, C. C. and Hashash, Y. M. A., 2009. Learning of dynamic soil behavior from downhole arrays, *J. Geotech. Geoenv. Eng.*, **135**, 745–757.

Van Houtte, C., Drouet, S., Cotton, F., 2011. Analysis of the origins of κ (kappa) to compute hard rock to rock adjustment factors for GMMs, *Bull. Seismol. Soc. Am.* 101, 2926-2941.

Vucetic, M. and R. Dobry, 1991. "Effect of soil plasticity on cyclic response," *J. Geotech. Geoenv. Eng.*, **117**, 89-107.

Wang, C.-Y., Lee, Y.-H., Ger, M.-L., and Chen, Y.-L., 2004. Investigating Subsurface Structures and P- and S-wave Velocities in the Taipei Basin, *Terrestrial, Atmospheric and Oceanic Sciences (TAO)* **15**, 609–627.

Wooddell, K. E., and Abrahamson, N. A., 2014. Classification of main shocks and aftershocks in the NGA-West 2 database, *Earthquake Spectra* **30**, 1257–1267.

Yee, E., Stewart, J. P., and Tokimatsu, K., 2013. Elastic and large-strain nonlinear seismic site response from analysis of vertical array recordings, *J. Geotech. Geoenv. Eng.*, **139**, 1789–1801.

Youngs, R. R., 2004. Software validation report for SHAKE04, Geomatrix Consultants, Oakland, CA.

Zalachoris, G., and Rathje E. M., 2015. Evaluation of one-dimensional site response techniques using borehole arrays, *J. Geotech. Geoenviron. Eng.*, 10.1061/(ASCE)GT.1943-5606.0001366, 04015053.

Zhang, S., Wang, G., Pang, B., and Du, C., 2013. The effects of strong motion duration on the dynamic response and accumulated damage of concrete gravity dams, *Soil Dyn. Earthquake Eng.* **45**, 112–124.

Zhong, P., Zareian, F, 2016. Applicability of simulated ground motion waveforms for building-code applications, *Earthquake Spectra* **31**, 71–95.